Atmospheric Sounding using IASI

Lucy Jane Ventress
Wadham College

Submitted for the Degree of Doctor of Philosophy

Trinity Term 2013

Atmospheric, Oceanic and Planetary Physics
Department of Physics
University of Oxford

Abstract

Atmospheric Sounding using IASI
Lucy Ventress, Wadham College
Submitted for the Degree of Doctor of Philosophy in Atmospheric, Oceanic and Planetary Physics
Trinity Term 2013

The Infrared Atmospheric Sounding Interferometer (IASI) provides atmospheric observations with high spectral resolution and its data have been shown to have a significant positive impact on global Numerical Weather Prediction (NWP) and trace gas retrievals.

A fundamental component of the retrieval of atmospheric composition is the radiative transfer model used to simulate the observations. An accurate representation of the expected emission spectrum measured by the satellite is essential given that differences in the reproduced atmospheric spectra propagate through a retrieval procedure and produce an altered estimate of the atmospheric state.

The importance of the assumptions within the forward model are discussed and it is established that in the simulation of spectra from satellite-borne instruments the choice of the model parameters can have a large impact upon the resulting output. These assumptions are explored in the context of the Reference Forward Model (RFM), which is further configured to optimise its output for simulating the IASI spectrum in the troposphere.

In order to ascertain the consistency of different radiative transfer models, comparisons are carried out between the RFM and the Radiative Transfer model for TOVS (RTTOV) in order to quantify any discrepancies in the reproduction of IASI measurements. Good agreement is shown across the majority of the spectrum, with exceptions caused by CO_2 line mixing effects and the H_2O continuum. Alongside model comparisons, the RFM is validated against real IASI measurements.

Being a Fourier Transform Spectrometer, there are a large number of channels available from the IASI instrument, which leads to a very large quantity of data. However, this can lead to problems within retrievals and data assimilation. Choosing an optimal subset of the channels is an established method to reduce the amount of data; maintaining the information contained within it whilst eliminating spectral regions with large uncertainties. The method currently used at the UK Met Office to select their spectral channels is re-assessed and a modified method is presented that improves upon the modelling of spectrally correlated errors.

Acknowledgements

There are so many people that I would like to thank for helping me get to the end of my thesis in one piece that it is difficult to know where to begin.

Firstly I must thank Paul and all my family for their love and support throughout everything. I must thank all my friends outside of work for the fun times we always had and for being there for me to rant and moan to (especially my W1 girls who had to watch me morph into 'Grumpy Lucy' towards the end of the thesis).

Both my time in AOPP and my sanity would not have been the same without the people there; always on hand to cheer me up, make me laugh, wear moustaches, and of course, always ready for a pub lunch that we never come back from.

For their offers of help and knowledge to aid my progress I must thank all the members of EODG as well as Fiona Smith, Andrew Collard, Roger Saunders, and Marco Matricardi to name but a few. All your help was truly appreciated.

I now come to my supervisors, to whom I am eternally grateful. Thank you to John Eyre for taking over as my co-supervisor at the Met Office and for always being willing to offer advice and insight into my work. Lastly, but perhaps most importantly, I must thank Anu. As my supervisor he has always been there to help me out, raise his eyebrows when I say something stupid, and set me off back in the right direction if I veered off course. I will always be so unbelievably thankful for the time he has put in and that he never turned me away when I appeared at his door asking for help. Above all, Anu has always been there to make sure I know my limits: 'When you start to sound northern, it's time to go home!'

Contents

List of Figures **xi**

List of Tables **xvii**

1 Motivation **1**

2 The Infrared Atmospheric Sounding Interferometer **5**

2.1 Instrument details 5

2.2 Current applications of IASI data 13

3 Inverse Methods **17**

3.1 Optimal Estimation 17

3.2 The Averaging Kernel 21

3.3 Retrieval Error 22

3.4 Smoothing Error 22

3.5 The Forward Model Jacobian 23

3.6 Figures of Merit 24

3.7 Conversion to column amount 25

4 Radiative Transfer Models **29**

4.1 Radiative Transfer 29

4.2 The Modelling of Radiative Transfer 31

4.2.1 Reference Forward Model 33

4.2.2 RTTOV 36

5 Configuring the RFM to model IASI spectra 39

5.1 Spatial Modelling 46

5.1.1 Field of View Size 46

5.1.2 Refraction 52

5.1.3 Plane-parallel approximation 53

5.2 Modelling the atmosphere 57

5.2.1 Top of atmosphere 58

5.2.2 Stratospheric Vertical Grid 60

5.2.3 Tropospheric vertical grid 62

5.2.4 Comparison to standard altitude grids 64

5.2.5 ‘Linear in tau’ approximation 67

5.3 Spectral Modelling 72

5.3.1 Spectral grid 72

5.3.2 Instrument Line Shape 73

5.3.3 Line Mixing 77

5.3.4 Line Shape 79

5.3.5 Molecular Continua 80

5.3.6 Non-LTE Effects 82

5.4 Atmospheric Composition 85

5.4.1 Atmospheric variability 85

5.4.2 Trace Gases 87
5.4.3 Enhanced absorbers 89
5.4.4 Spectroscopic databases 93
5.5 Summary 99

6 Selection of IASI Channels **103**
6.1 Channel selection algorithms 104
6.1.1 Optimal Estimation Framework 105
6.1.2 Conventional algorithm 106
6.1.3 Application to IASI 107
6.1.4 Spectrally Correlated Errors 108
6.1.5 Linear Error Propagation 110
6.1.6 Modified Selection Algorithm 111
6.2 Selection of IASI Channels 114
6.2.1 Reproducing Original Selection 115
6.2.2 Modified Channel Selection 117
6.3 Results 119
6.3.1 Temperature channels 119
6.3.2 Main Channels 123
6.3.3 Ozone Channels 126
6.4 Maximum DFS 128
6.5 Channel selection for trace gases 131
6.5.1 Ozone 132
6.5.2 Methane 134
6.5.3 Carbon monoxide 136

6.5.4 Nitrous oxide 138

6.6 Column amount retrievals for trace gases 140

6.7 Summary 148

7 Forward Model Comparisons 151

7.1 Configuring the Radiative Transfer Models 152

7.1.1 RTTOV 152

7.1.2 RFM 154

7.2 Model Comparison 156

7.2.1 Dependent Profile Data Set 156

7.2.2 Independent Profile Data Set 164

7.2.3 Forward Model Error Propagation 172

7.3 Comparison to IASI measurements 176

7.3.1 Estimating the atmospheric state 176

7.3.2 Retrieval Theory 177

7.3.3 Selection of IASI data 178

7.3.4 Reproducing IASI spectra 179

7.4 Summary 194

8 Conclusion and Future Work 199

Bibliography 204

List of Figures

2.1 A schematic diagram of a Michelson Interferometer 6

2.2 Internal view of IASI components - Top view 8

2.3 Internal view of IASI components - Bottom view 9

2.4 Typical IASI brightness temperature and transmission (from the ground) spectra illustrating the spectral bands 11

2.5 Example of IASI's daily coverage and single orbit 12

2.6 The IASI field of view 13

5.1 The vertical profiles of temperature and water vapour in the 6 FASCODE atmospheres 41

5.2 The radiometric noise associated with the IASI spectrum 43

5.3 The absorption spectra from IASI for the standard mid latitude daytime atmosphere from different altitudes to space (taken as 120 km). . 45

5.4 A projection to the ground of the IASI and IIS FOV's 47

5.5 The IASI Point Spread Function 48

5.6 The geometry of assessing the finite FOV size 49

5.7 The residual from ignoring the field of view convolution at increasing viewing angles 50

5.8 The residual due to ignoring refraction effects 53

5.9 The geometry when (a) including the curvature of the Earth, (b) assuming a plane parallel atmosphere and (c) the improvement to the viewing angle in the plane parallel atmosphere that accounts for the Earth's curvature. 55

5.10 The residual from ignoring the curvature of the Earth at increasing viewing angles. 56

5.11 As figure 5.10 but considering the zenith angle, ϕ. 57

5.12 The residual due to reducing the altitude of the top of the atmosphere. 59

5.13 The residual from increasing the grid spacing in $\ln(p)$. 62

5.14 The residual due to increasing the grid spacing in pressure. 63

5.15 The altitude spacings for the US Standard atmosphere, the Met Office 1d Var pressure grid, the RTTOV IASI coefficients pressure grid, and the 'optimum' and 'high resolution' grids established in the previous section. The top panel shows the altitude spacing in the upper atmosphere and the bottom panel shows the altitude spacing in the lower atmosphere. 65

5.16 The residuals from comparisons of standard altitude grids to the high resolution grid. 66

5.17 The residual from including the 'linear in τ' approximation for different altitude grids. 68

5.18 The residual from using varying fine grid spacings of 0.001, 0.003, 0.005, and 0.01 cm^{-1} compared to the RFM's default spacing of 0.0005 cm^{-1}. 73

5.19 The apodised IASI ILS with the internal RFM ILS width limit. The IASI ILS is also shown magnified by 100 to emphasise the side lobes. 74

5.20 The residual between convolving the IASI spectra with the full 10 cm^{-1} wide Apodised Instrument Line Shape and truncated versions of the AILS. 76

5.21 The residual error caused by neglecting the CO_2 line mixing effects within the IASI spectrum. 78

5.22 The residual error caused by neglecting the sub-Lorentzian effects in the CO_2 line shape and assuming the Voigt lineshape for all molecules. 80

5.23 The residual caused by neglecting the continua for the molecules H_2O, CO_2, N_2, and O_2. 82

5.24 The residual caused by considering the addition of the Non-LTE effects for CH_4, CO_2, CO, H_2O, HCN, HNO_3, N_2O, NO_2, NO, and O_3, using the daytime values at 200 km. 83

5.25 The residual caused by the 1σ atmospheric variability of the primary atmospheric absorbers; O_3, CO_2, CO, H_2O, N_2O, and CH_4. 86

5.26 The atmospheric absorbers causing the largest residuals by their inclusion. 87

5.27 The atmospheric absorbers causing the smallest residuals by their inclusion. 88

5.28 The U.S Standard and enhanced vertical profiles for each atmospheric absorber. 91

5.29 The residual caused by enhancements of atmospheric absorbers. . . . 92

5.30 The residual, relative to HITRAN 2008, caused due to the differences in spectroscopic databases. 93

5.31 The radiance residuals, as in figure 5.30, for each of the major absorbers. 96

6.1 A typical IASI spectrum indicating the channels blacklisted due to the atmospheric variability of H_2O, O_3, CH_4, CO and N_2O along with those affected by non-LTE effects and solar irradiance. 114
6.2 The error in IASI brightness temperature due to the climatological variability, in a mid latitude daytime atmosphere, of each minor species included in $\mathbf{S}_y$ in the original selection and included as an independent error source in the modified selection. 116
6.3 The additional error spectra (to those in figure 6.2) included in the modified channel selection algorithm. 118
6.4 The locations of the 267 channels selected by the original and modified algorithms. 120
6.5 Temperature error profiles for the U.S standard atmosphere viewed at nadir from 66 channels. 122
6.6 As in figure 6.5 but showing the temperature error profiles after a joint retrieval with water vapour using 252 channels 124
6.7 Water vapour error profiles from 252 channels. 126
6.8 Ozone error profiles from 267 channels. 127
6.9 The evolution of the DFS during the channel selection, applying the systematic error component to both channel sets. 130
6.10 The locations of the 15 channels selected by the original and modified algorithms for ozone. 134
6.11 The locations of the 15 channels selected by the original and modified algorithms for methane. 136
6.12 The locations of the 15 channels selected by the original and modified algorithms for carbon monoxide. 138

6.13 The locations of the 15 channels selected by the original and modified algorithms for nitrous oxide. 139

6.14 Averaging kernels for ozone profiles with different *a priori* assumptions 146

6.15 Averaging kernels for methane profiles with different *a priori* assumptions 147

7.1 The diverse reference profile set of 83 profiles used in the forward model comparisons for a)temperature, b)H_2O and c)O_3. The extreme profiles and the profile mean are indicated in red. 157

7.2 The diverse reference profile set of 83 profiles used in the forward model comparisons for a)CO_2, b)CH_4, c)CO and d)N_2O. The extreme profiles and the profile mean are indicated in red. 158

7.3 The variation in sea surface emissivity with wavenumber at different path angles. 160

7.4 a)The mean value (bias) and b)the standard deviation of the differences between the RFM and RTTOV for 80 profiles at 5 viewing angles are shown in red. The IASI noise is shown in black for reference. 161

7.5 The percentage of channels with given RMS errors for all viewing angles combined and at each separate viewing angle. 163

7.6 The independent profile data set of 100 profiles used in the forward model comparisons for a)temperature, b)H_2O and c)O_3. The extreme profiles and the profile mean are indicated in red. 166

7.7 The mean value (bias) of the differences between the RFM, RTTOV and LBLRTM for 100 independent profiles at 5 viewing angles are shown in red. The IASI noise is shown in black for reference. 167

7.8 The standard deviation of the differences between the RFM, RTTOV and LBLRTM for 100 independent profiles at 5 viewing angles are shown in red. The IASI noise is shown in black for reference. 168

7.9 The percentage of channels with given RMS errors for all viewing angles combined and at each separate viewing angle. 171

7.10 The effect of including an error due to forward model differences on the vertical error profiles of temperature, water vapour and ozone. . . 175

7.11 The mean value of the differences between observed and simulated IASI measurements for IASI band 1 182

7.12 The difference between observed and computed IASI measurements for IASI band 1 after retrieval 183

7.13 The difference between the retrieved vertical profiles and the *a priori* profile for each of the retrieved variables 186

7.14 The mean value of the differences between observed and simulated IASI measurements for IASI band 2 187

7.15 The difference between observed and computed IASI measurements for IASI band 2 after retrieval 188

7.16 The mean value of the differences between observed and simulated IASI measurements for IASI band 3 190

7.17 The difference between observed and computed IASI measurements for IASI band 3 after retrieval 191

7.18 The percentage of channels with given residual errors for the whole spectrum and for each IASI band. 194

List of Tables

2.1 IASI Instrumental Characteristics 10

5.1 Impact of ignoring the finite field of view size 51

5.2 Impact of ignoring refraction 52

5.3 Impact of the plane parallel approximation 54

5.4 Impact of reducing the altitude of the top of the atmosphere 58

5.5 Impact of varying the vertical grid spacings within the atmosphere between 1000–0.002 mb 61

5.6 The impact of alternative standard altitude grids 67

5.7 Impact of ‘linear in τ’ approximation 70

5.8 Impact of varying spectral fine grid spacings 73

5.9 Impact of using truncated versions of the ILS 76

5.10 Impact of neglecting the effects of line mixing and shape 78

5.11 Impact of neglecting the continua for the molecules H_2O, CO_2, N_2, and O_2 81

5.12 Impact due to non-LTE effects. 84

5.13 Impact of the 1σ variability of the primary atmospheric absorber. . . . 87

5.14 Impact of excluding atmospheric absorbers 89

5.15 Impact of enhancing atmospheric absorbers 92

5.16 Impact of different spectroscopic databases relative to HITRAN 2008. 95

5.17 Percentage of spectral points that significantly contribute to the absorption of each molecule and that disagree by $\xi > 0.1$ in comparisons of spectroscopic databases for the primary absorbers. 98

5.18 The recommended forward model settings for simulation of the IASI spectrum in the troposphere 101

6.1 Degrees of Freedom for Signal per profile of 43 levels plus surface term from 66 temperature channels selected by Collard, and by the original and modified algorithms. 121

6.2 Degrees of Freedom for Signal per profile of 43 levels from 252 temperature and water vapour channels selected by the original, reproduced, and modified algorithms. 125

6.3 Degrees of Freedom for Signal per profile of 43 levels from the 267 channels selected by the original, reproduced, and modified algorithms. 127

6.4 Maximum Degrees of Freedom for Signal available from the spectral region 645–2200 cm^{-1} per profile of 43 levels plus surface term considering an $\mathbf{S}_y^{\mathrm{tot}}$ with and without the systematic error components. . 129

6.5 Degrees of Freedom for Signal per profile of 43 levels from the 15 'trace gas' and 252 pre-selected channels selected by the original and modified algorithms, along with the maximum DFS available for the spectral region 645–2200cm^{-1}. 133

6.6 The DFS and percentage errors in retrieved total, tropospheric, and stratospheric column amounts with different retrieval assumptions for O_3, CH_4, CO, N_2O, and CO_2 142
6.7 Percentage of total column amount contained within the troposphere and stratosphere 145

7.1 The features included in comparisons of the RFM and RTTOV. For RTTOV, the settings include the relevant features of its training model, LBLRTM. 155
7.2 The *a priori* assumptions for each retrieved absorber 181

Chapter 1

Motivation

Atmospheric observations are vital in the process of weather forecasting (It is only with a large range of observational data monitoring the Earth's atmosphere, land and ocean that forecasts can be produced). Presently observations come from several sources: radiosondes, surface data, aircraft and satellites. Satellites have become the prevalent source of data due, in part, to the quantity they produce, providing measurements of atmospheric properties such as pressure, temperature, humidity and wind with almost global coverage, but also due to the impact such observations have upon short–range global forecast error reduction. Satellite data has been found by Sangwon et al. (2013) to account for 64% of the global forecast error reduction, with the Metop–A platform having the largest impact of any individual satellite platform ($\sim 25\%$).

Although satellites provide almost global coverage, there are still data gaps within numerical weather prediction windows (typically 6hrs for global NWP). To overcome this problem the process of data assimilation is used. This involves combining the observations available with a forecast of what the conditions are expected to be to form a best estimate of the current state of the atmosphere. This best estimate, or analysis, is the starting point for numerical weather forecasts, which simulate the Earth's atmospheric processes that can affect the weather, and it is this analysis that is propagated forward in time to create the forecast. It is therefore essential to be able to produce an accurate estimate of the current atmospheric state. The aim of the work presented here is to investigate improvements in the use of satellite measurements to accurately determine atmospheric variables.

Infrared sounding instruments, such as the Infrared Atmospheric Sounding Interferometer (IASI), which will be discussed in chapter 2, can provide data with high spectral resolution. Weather centres across the globe use the spectral data from IASI and it has been shown to have a significant positive impact on global NWP. This impact became apparent shortly after IASI's launch despite its data initially having a fairly conservative weighting during the assimilation process (Hilton et al., 2012). Its high absolute radiometric accuracy has been demonstrated through comparisons with data from AIRS (Atmospheric InfraRed Sounder) and the 11 micron AATSR (Advanced Along-Track Scanning Radiometer) channel, in both cases agreement being better than 0.1 K (Illingworth et al., 2009; Strow et al., 2010).

IASI measures the radiance emitted from the surface and atmosphere. In a cloud free region the radiance from the atmosphere can be measured and this allows vertical information to be derived for certain species, assuming surface variables, such as temperature and emissivity, and the atmospheric temperature are known or simultaneously retrieved. The mathematical basis behind such retrievals is described in chapter 3.

A fundamental part in the retrieval of atmospheric composition is the use of radiative transfer models to simulate observations. An accurate representation of the expected emission spectrum measured by the satellite, for a given atmospheric state, is essential in ascertaining the correct atmospheric composition providing the observed satellite radiances. Differences in the reproduced atmospheric spectra can propagate through a retrieval procedure, involving the inversion of radiance measurements to obtain atmospheric profiles, and hence produce an alternative estimate of the atmospheric state.

There are a large number of different radiative transfer models available, which are usually one of two types: a monochromatic line-by-line model or a fast band model, whose differences are explained in chapter 4. Fundamentally, line-by-line models, although more accurate are computationally expensive and are therefore too slow for use in operational, near real time analyses. For this reason, band models, which are much faster, are required in operational situations. The Reference Forward Model (RFM) developed at the University of Oxford (Dudhia, 2002) originally for use with the limb-viewing Michelson Interferometer for Passive Atmospheric Sounding (MIPAS) instrument has been developed into a general purpose line-by-line model, allowing it to be used for nadir-viewing spectroscopic calculations. It is important to understand the assumptions made within radiative transfer models, and be able to characterise the impact they have upon the radiance output. These assumptions are explored in detail in chapter 5, where the RFM is configured to optimise its output for simulating the IASI spectrum.

Being a Fourier Transform Spectrometer (FTS), there are a large number of channels available from the IASI instrument, which leads to a very large quantity of data. However, this can lead to problems within retrievals and data assimilation. Choosing an optimal subset of the channels is an established method to reduce the amount of data, whilst maintaining the information contained within it (Collard, 2007).

Although the number of IASI's spectral channels used in NWP has increased since its launch, the maximum is still at approximately 200 channels (out of the 8461 available). The majority of these lie in the long wave CO_2 band and provide atmospheric temperature information, whilst the IASI water vapour band is currently under used: only a few tens of the water vapour channels are assimilated. Reasons suggested for this limite d use include difficulties with the observation error correlations and biases in the assimilating NWP models (Hilton et al., 2012).

In selection of channels, the amount of information retrieved needs to be optimised whilst also eliminating spectral regions with large uncertainties. The method currently used at the UK Met Office to select their channels is discussed in chapter 6 along with a modified method with potential to improve upon the influence of spectrally correlated errors.

In order to ascertain the validity of each radiative transfer model, comparisons between different models must be carried out in order to quantify any discrepancies in the reproduction of IASI measurements. Alongside model comparisons, it is also imperative that radiative transfer models are able to recreate real IASI observations. The validity of the RFM to reproduce IASI measurements is explored in chapter 7 through comparisons with the fast radiative transfer model, Radiative Transfer model for TOVS (RTTOV) and comparisons to IASI measurements from different geographical locations. The propagation of errors, caused by the differences in radiative transfer models, through a retrieval is also examined for the set of channels selected by the modified method in chapter 6.

Chapter 2

The Infrared Atmospheric Sounding Interferometer

2.1 Instrument details

The Infrared Atmospheric Sounding Interferometer (IASI) is one of eleven instruments on board the Metop-A satellite that was launched on 19th October 2006. It was developed by CNES (Centre National d'Etudes Spatiales) of France for use as part of the EUMETSAT (European Organisation for the Exploitation of Meteorological Satellites) European Polar System. The second in the Metop series of satellites, Metop-B, was launched on 17th September 2012 with a second IASI instrument (IASI-B) on board and a third instrument is planned to be mounted onboard Metop-C, due to be launched in 2018. This will allow the IASI instruments to provide observations over more than a decade. There is also a 'Next Generation' series of instruments planned from about 2020 called IASI-NG, which aims to improve both spectral resolution and radiometric noise.

The IASI instrument is an infrared Fourier transform spectrometer associated with an Integrated Imaging Subsystem (IIS), which uses nadir viewing geometry passively to measure the radiance from Earth. The radiation emitted from both Earth and the atmosphere is affected by the emission, absorption and scattering of the atmospheric molecules along its optical path. It is the radiation resulting from these interactions that IASI measures as the atmospheric spectrum, containing atmospheric emission/absorption features (Turquety et al., 2004). The instrument concept is based on a Michelson interferometer: a schematic of which can be seen in figure 2.1.

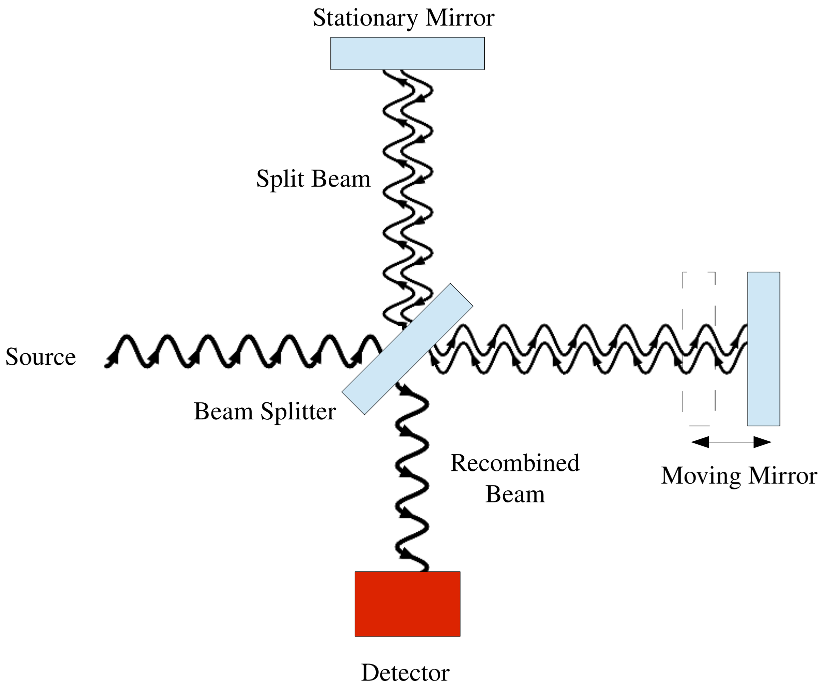

Figure 2.1: A schematic diagram of a Michelson Interferometer

The incident radiation is split into two beams: one beam follows a path of constant length, while the other is reflected by a moving mirror, giving it a variable path length. When the beams recombine on the detectors, their energy varies with the path difference between the two beams creating an interferogram. This interferogram is a Fourier Transform of the incident radiation's spectral distribution. To recover the radiation spectrum an inverse Fourier transform and radiometric calibration are applied.

The essential components of the instrument, shown in figures 2.2 and 2.3 are discussed in detail elsewhere, (Siméoni et al. (1997), Chalon et al. (2001) and Hébert et al. (2004)), but include:

- A scanning mirror to direct the incident radiation into the instrument
- An afocal telescope to transfer the image onto the scan mirror
- The Michelson interferometer, including a beam splitter and corner cube mirrors that are designed to create the optical path difference necessary for the specified spectral resolution.
- The cold box, which the recombined beams are directed into, containing refractive optics that divides the spectral range into three bands and three detector packages (B1/B2/B3). For each band, the detector package consists of a monolithic 2×2 element detector array behind four micro lenses. However, the signals from each detector have different electrical characteristics and a preamplifier is required to normalise the signals. B2 and B3 contain photovoltaic detectors and the output impedance is very high compared to the output signal, therefore, the preamplifier must be in close proximity to the detector

and is contained within the cold box. B1 contains photoconductive detectors and had the requirement for very low noise. In order to achieve this, bipolar transistors were used, which need to achieve a minimum ambient temperature, and so the preamplifier is located within the following aquisition system.

- The Main Aquisition System (MAS), whose principal function is to digitalise the analog signal from the detectors. The MAS amplifies, filters, polarises and applies any gain/offset correction to the signal before finally converting it into digital data.

- The Digital Processing Subsystem that carries out the inverse Fourier transform and calibration on the interferograms before being transmitted to the ground. This is an unusual aspect of IASI, given that this procedure is not normally carried out on-board, but necessitated by the high data volume.

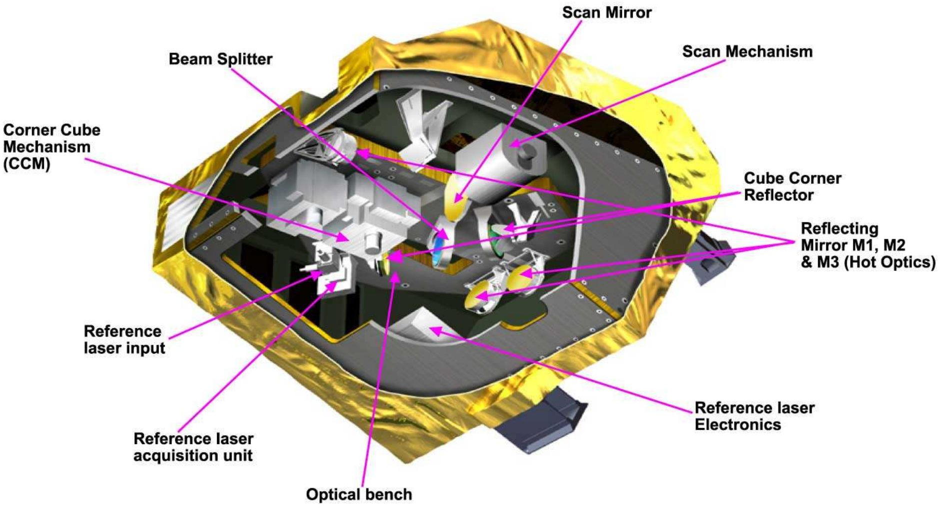

Figure 2.2: An internal view of IASI components - Top view. (Picture by CNES (2009))

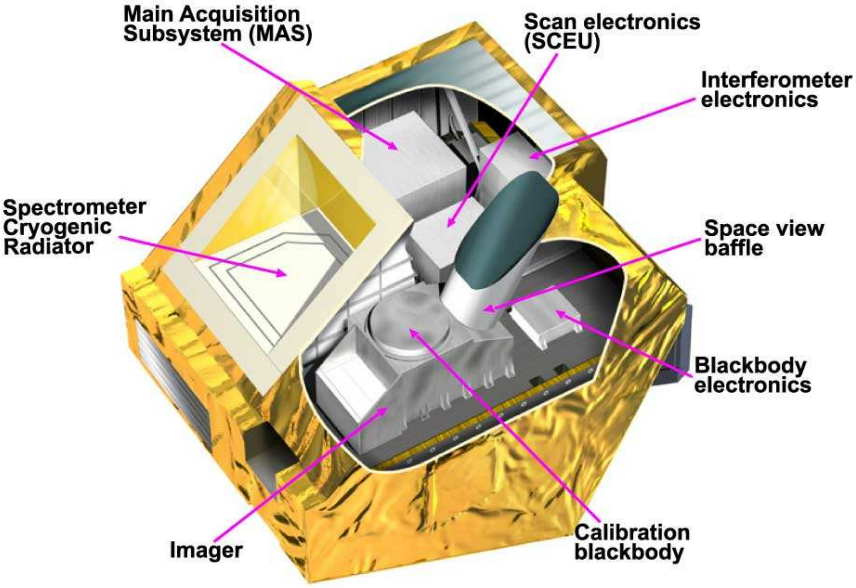

Figure 2.3: An internal view of IASI components - Bottom view. (Picture by CNES (2009))

The main characteristics of the IASI instrument are summarised in Table 2.1. IASI covers the spectral range 645–2760 cm^{-1} with a spectral sampling of 0.25 cm^{-1} (0.5 cm^{-1} apodized spectral resolution) resulting in a total of 8461 channels in each IASI spectrum. Apodisation is the process of removing side lobes from the interferogram, which would cause irregularities in the spectrum. The apodisation function, a truncated Gaussian in the case of IASI, brings the interferogram slowly to zero at the edge of the field. This reduces the side lobes but at the expense of the central peak width; introducing correlations between neighbouring spectral channels. The spectral range is divided into three bands as shown in figure 2.4. 'Band 1', from 645–1210 cm^{-1}, is primarily for temperature and ozone sounding; 'Band 2', from 1210–2000 cm^{-1}, is primarily for water vapour sounding and retrieving N_2O and CH_4 column amounts; and 'Band 3', from 2000–2760 cm^{-1}, is for temperature sounding and the retrieval of N_2O and CO column amounts.

Table 2.1: IASI Instrumental Characteristics (taken from Clerbaux et al. (2007))

	Characteristics
Spectral Range	645–2760 cm^{-1} (15.5–3.62 μm)
Spectral Resolution	0.5 cm^{-1} (apodized)
Instrumental Noise	0.2 to 0.35 K (NEDT at 280 K)
Pixel Size	Diameter of 12 km, 4 pixels matrix, across-track scanning
Data Rate	1.5 megabits per second
Lifetime	5 years
Altitude	$\sim$ 817 km
Orbit	polar sun-synchronous
Inclination	98.7 $^\circ$ to the equator
Local time	$\sim$ 09:30 descending
Orbital Period	101 min

IASI achieves daily global coverage as shown in figure 2.5 and provides measurements twice a day at most locations, with a local equator crossing time of 09:30 for the descending node. The instrument scans perpendicularly to the motion of the satellite between angles $\pm 47.85^\circ$ with respect to the nadir. Within each scan there are 30 steps at which measurements are taken, as well as views to the calibration targets: an internal hot black body and cold deep space. Each view consists of a 2×2 matrix containing independent circular pixels with diameters of 12 km as shown in figure 2.6. This provides an increased probability of obtaining cloud-free views compared to a single continuous FOV of $\sim$ 25 km . The IASI scan pattern provides measurement locations collocated with other instruments on board the METOP satellite such as AVHRR, the Advanced Very High Resolution Radiometer, AMSU-A, the Advanced Microwave Sounding Unit and MHS, the Microwave Humidity Sounder.

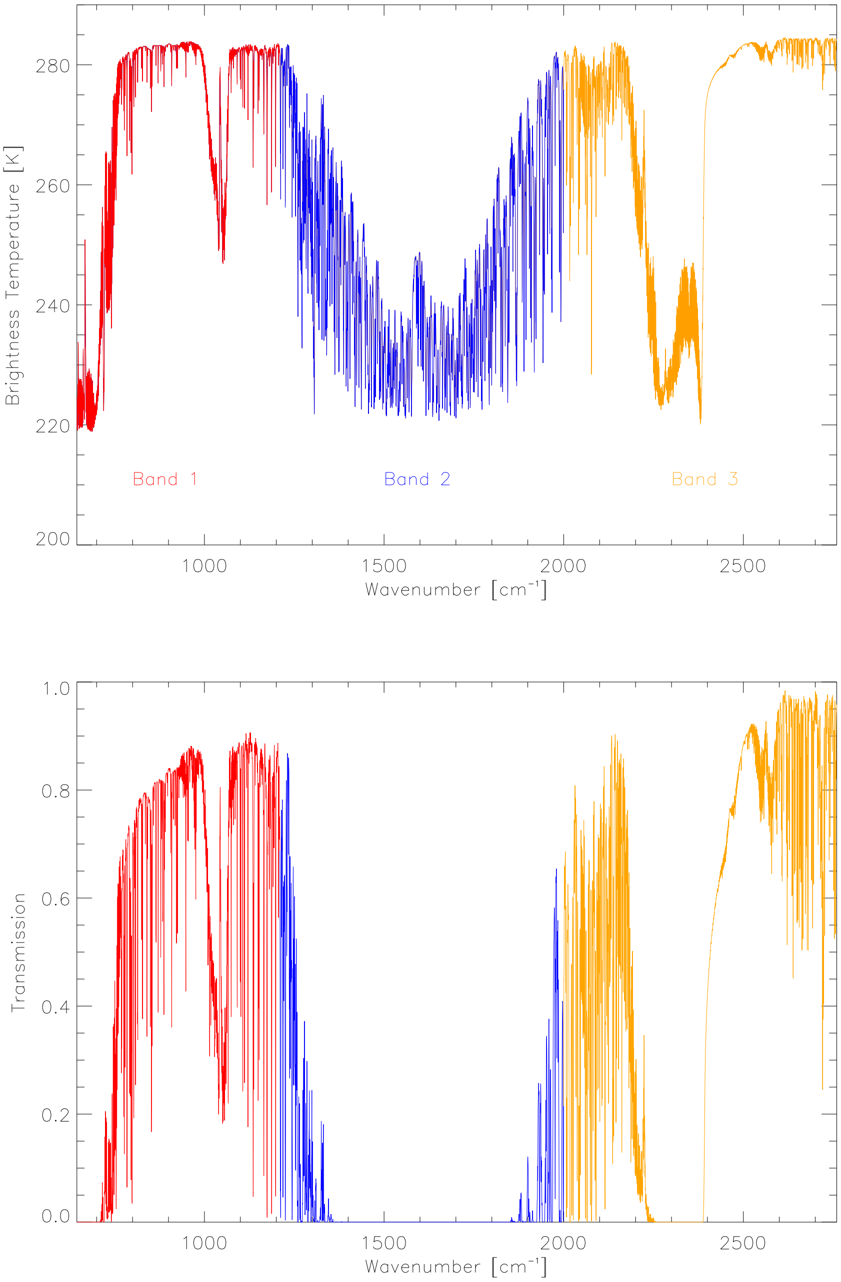

Figure 2.4: Typical IASI brightness temperature and transmission (from the ground) spectra illustrating the spectral bands

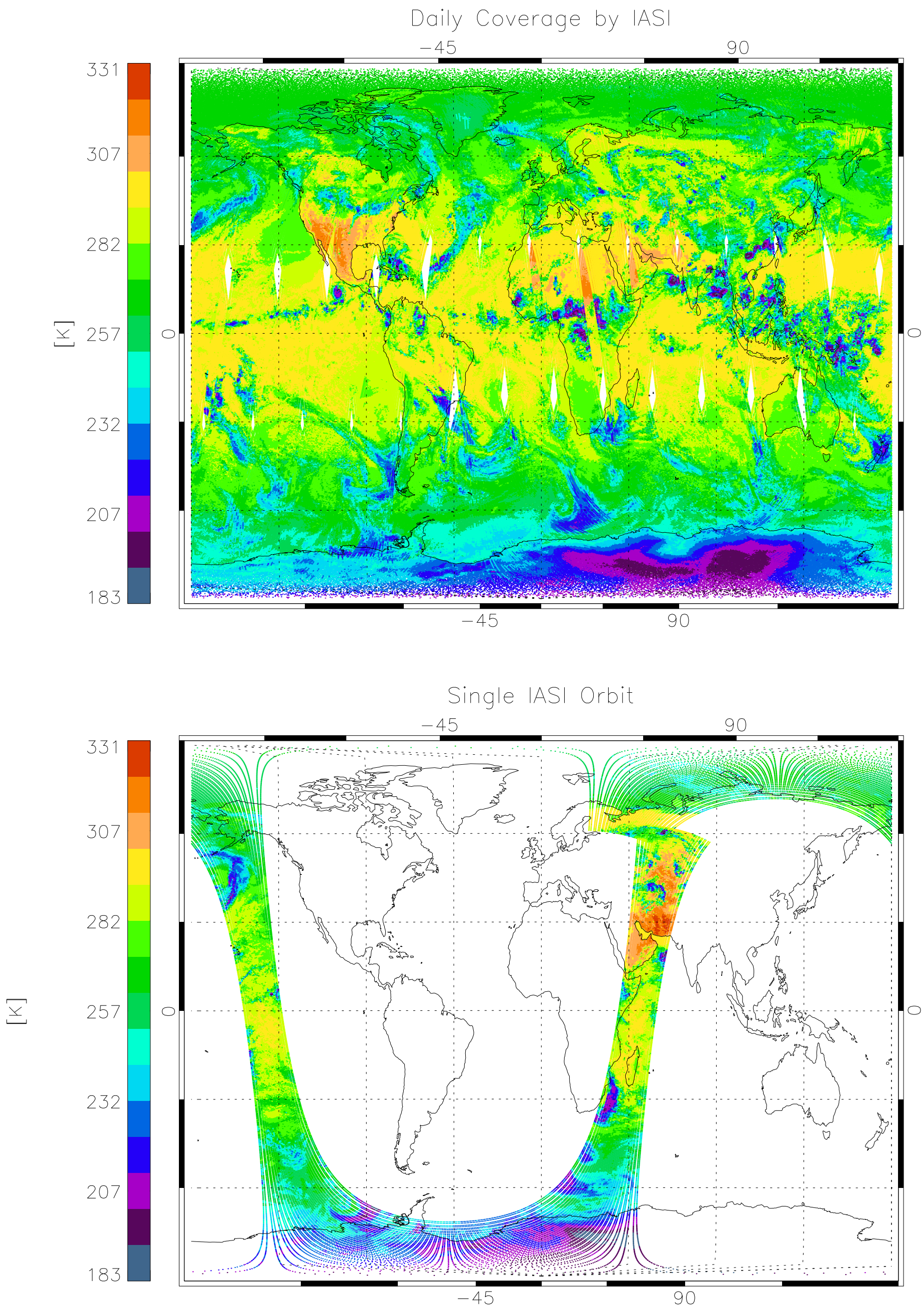

Figure 2.5: Example of the daily coverage available from IASI and the measurements from a single orbit. Measurements show the brightness temperature in the window channel at 961 cm^{-1}.

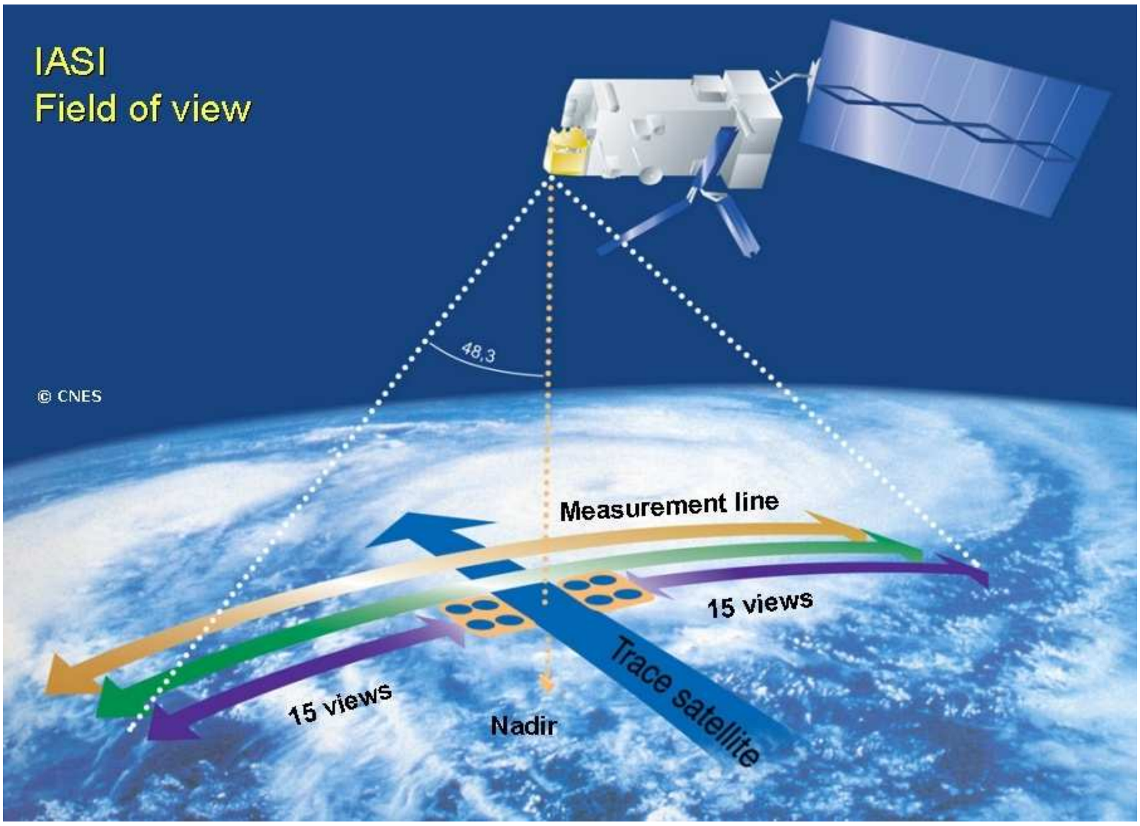

Figure 2.6: The IASI field of view. (Picture by CNES (2009))

2.2 Current applications of IASI data

The primary goal of the IASI mission is to provide accurate measurements that enable estimates of temperature and humidity profiles for use in NWP. However, since its launch it has also provided significant improvement to the monitoring of atmospheric composition, including the detection of some species that were initially not expected, such as ammonia. A summary of the use of IASI observations has been compiled by Hilton et al. (2012) and some of the applications are discussed below.

In NWP a forecast is created by propagating a 'best estimate' of the current atmospheric state forward in time through a model which simulates the Earth's atmospheric processes that can affect the weather. The 'best estimate', or analysis, is created through the combination of observations with existing forecasts using the process of data assimilation. Essentially, the more accurately we know the current atmospheric state the better the forecast output will be. Satellite observations have been shown to have the largest impact upon improving forecast errors and IASI, with its high resolution and large information content has had a large positive impact within NWP (see Hilton et al. (2009a) and Sangwon et al. (2013)) . Despite this, the number of IASI's spectral channels assimilated into NWP systems is only ~ 200; although the number has increased since its launch, this maximum exists due to the computational expense of the assimilation process. Therefore, the maximum amount of information must be gained from each chosen measurement. The method for selecting the subset of IASI channels is discussed in chapter 6 and a modified algorithm is proposed.

An alternative method to channel selection is Principal Component Analysis (PCA), a method of projecting spectra onto a principal component basis and retaining only the largest modes of variability, which has shown powerful properties of noise filtering whilst minimizing the loss of information on trace species (Prunet et al., 2010). Using the leading principal components, reconstructed radiances can be calculated. The instrumental noise associated with these radiances is greatly reduced, however, the method introduces error correlations between channels. Alongside use as a method of data compression (the compressed PC spectra are disseminated in parallel with the full IASI radiance spectra), the potential for the assimilation of principal components and reconstructed radiances within NWP and their implementation in trace gas detections is currently being explored (Collard et al. (2010), Atkinson et al. (2010)).

On top of the contribution to NWP, IASI has shown itself able to provide remarkable improvements to the monitoring of atmospheric composition and the detection of trace reactive species. Retrievals of trace gases, such as carbon monoxide and ozone, have been shown to have excellent agreement with other infrared sounders such as AIRS, whilst also it has been possible to provide global distributions of more minor species such as nitric acid (HNO_3).

Although not IASI's primary purpose, one of the pleasantly surprising capabilities it has demonstrated is its ability to contribute to the monitoring of tropospheric chemistry. Given the complex and non-linear nature of radiative transfer, much has been achieved in the retrieval of trace species through relatively simple methods. Using basic brightness temperature difference detection techniques, described by Clarisse et al. (2008) and a more rigorous version by Walker et al. (2011), the detection of emission sources of short-lived trace species, such as ammonia (NH_3), methanol (CH_3OH) and formic acid (HCOOH) has been possible. These techniques have also been extended to be able to retrieve and trace sulphur dioxide (SO_2) plumes ejected in volcanic explosions, as described by Carboni et al. (2012) and Clarisse et al. (2012). Due to the twice daily near-global coverage IASI provides, plumes can be monitored and tracked in each sequential IASI orbit. In particular the ease of the detection of fires has been shown by Turquety et al. (2009) through CO retrievals and the detection of the volatile organic compounds released within large fires. Detection and classification of aerosol types (including volcanic ash, desert dust and biomass burning) within plumes has also become possible due to the high spectral resolution of IASI and its sensitivity to various aerosol properties (Clarisse et al., 2010).

Although IASI has yet to significantly contribute to the monitoring of long term climate trends, given the expected lifespan of IASI and its successors, the data from IASI is expected to have a large contribution in the future. Its observations of mid/upper tropospheric carbon dioxide and methane columns have already been included within the greenhouse gas Essential Climate Variable (ECV) study within the ESA Climate Change Initiative (CCI) program described by Buchwitz (2013), and the ability to monitor the atmosphere at high spectral resolution will be crucial in the observation of global climate trends.

Chapter 3

Inverse Methods

This chapter explains the mathematical basis of the inverse models contained in this thesis.

3.1 Optimal Estimation

This study implements the use of optimal estimation as described by Rodgers (2000). Here the notation and definitions are briefly explained.

The atmospheric profile, in terms of temperature or the concentration of a particular atmospheric molecule, at a given location, is represented by the state vector $\mathbf{x}$, containing n variables to be retrieved. The satellite measurements, such as a brightness temperature spectrum, are represented by the vector $\mathbf{y}$, of size m. These two vectors can be related by the following equation:

$$\mathbf{y} = \mathbf{F}(\mathbf{x}) + \boldsymbol{\epsilon}, \tag{3.1}$$

where $\boldsymbol{\epsilon}$ is a combination of the measurement and forward model errors whose resulting error covariance matrix is given by $\mathbf{S}_y$ (dimension $m \times m$), and $\mathbf{F}(\mathbf{x})$ is the forward model function that contains our understanding of the physics of the situation. Assuming the radiative transfer equation to be weakly non-linear, this can be linearised around a reference state, $\mathbf{x}_0$, becoming

$$\mathbf{y} - \mathbf{F}(\mathbf{x}_0) = \frac{\partial \mathbf{F}(\mathbf{x})}{\partial \mathbf{x}}(\mathbf{x} - \mathbf{x}_0) + \boldsymbol{\epsilon} = \mathbf{K}(\mathbf{x} - \mathbf{x}_0) + \boldsymbol{\epsilon} \tag{3.2}$$

where $\mathbf{K}$ ($m \times n$) is known as the weighting function matrix, or Jacobian matrix, and contains the partial derivatives of each forward model element with respect to each state vector element, i.e.

$$K_{ij} = \frac{\partial F_i(\mathbf{x})}{\partial x_j}. \tag{3.3}$$

The inverse problem is concerned with retrieving a 'best' estimate of $\mathbf{x}$ given the gathered measurements, $\mathbf{y}$. Remote sensing is usually an ill-posed problem and cannot be entirely defined by the measurements, hence optimal estimation includes the use of *a priori* values. These can be any previously known information about the atmospheric conditions that are unrelated to the measurements taken, such as climatology or model prediction.

Assuming that Gaussian statistics are an appropriate approximation for the errors in the measurements (i.e. $P(\mathbf{y}) \propto \exp\left[-\frac{1}{2}(\mathbf{y} - \bar{\mathbf{y}})^{\mathrm{T}}\mathbf{S}_y^{-1}(\mathbf{y} - \bar{\mathbf{y}})\right]$, where $\bar{\mathbf{y}}$ is the mean value of the probability density function $P(\mathbf{y})$) we can use Bayesian statistics to express the probability of the measurements given a state $\mathbf{x}$ as

$$-2\ln P(\mathbf{y}|\mathbf{x}) = [\mathbf{y} - \mathbf{F}(\mathbf{x})]^{\mathrm{T}}\mathbf{S}_y^{-1}[\mathbf{y} - \mathbf{F}(\mathbf{x})] + c_1 \tag{3.4}$$

where c_1 is an undetermined constant independent of $\mathbf{x}$. Although usually less realistic, it is convenient to also express the prior knowledge of $\mathbf{x}$ as a Gaussian probability distribution, giving

$$-2 \ln P(\mathbf{x}) = [\mathbf{x} - \mathbf{x}_a]^{\mathrm{T}} \mathbf{S}_a^{-1} [\mathbf{x} - \mathbf{x}_a] + c_2 \tag{3.5}$$

where $\mathbf{x}_a$ is the *a priori* estimate of the solution, $\mathbf{S}_a$ $(n \times n)$ is the associated *a priori* error covariance matrix and c_2 is an undetermined constant independent of $\mathbf{x}$.

Bayes' Theorem can now be applied to obtain the probability of a given $\mathbf{x}$ state given the measurements $\mathbf{y}$, i.e.

$$P(\mathbf{x}|\mathbf{y}) = \frac{P(\mathbf{y}|\mathbf{x}) P(\mathbf{x})}{P(\mathbf{y})} \tag{3.6}$$

Under the assumption that $P(\mathbf{y})$ is merely a normalising constant and can be neglected this gives us

$$\chi^2 = -2 \ln P(\mathbf{x}|\mathbf{y}) = [\mathbf{y} - \mathbf{F}(\mathbf{x})]^{\mathrm{T}} \mathbf{S}_y^{-1} [\mathbf{y} - \mathbf{F}(\mathbf{x})] + [\mathbf{x} - \mathbf{x}_a]^{\mathrm{T}} \mathbf{S}_a^{-1} [\mathbf{x} - \mathbf{x}_a] + c_3 \tag{3.7}$$

where c_3 is an undetermined constant independent of $\mathbf{x}$ and χ^2 is known as the 'cost' function and must be minimised to find the most probable state. Essentially this means that in optimal estimation a solution is found that minimises the square of both the measurement/forward model difference and the *a priori* estimate of the state difference, weighted by the equivalent inverse covariance matrices.

If the inverse *a priori* error covariance matrix, $\mathbf{S}_a^{-1}$, is set to zero then only the measurements are used in the retrieval calculation and no prior knowledge of the system is assumed. This reduces the problem to a weighted least squares fit retrieval. Alternatively, optimal estimation can be considered a particular case of a weighted least squares fit in which the measurements are divided into two uncorrelated subsets where one subset has $\mathbf{K} \equiv \mathbf{I}_n$.

In the weakly non-linear limit the solution to finding the point at which the gradient of equation 3.7 equals zero can be found using Newtonian iteration, which states that for the vector equation $\mathbf{g}(\mathbf{x}) = \mathbf{0}$,

$$\mathbf{x}_{i+1} = \mathbf{x}_i - \left[\nabla_{\mathbf{x}}\mathbf{g}(\mathbf{x}_i)\right]^{-1}\mathbf{g}(\mathbf{x}_i) \tag{3.8}$$

Ignoring second derivative terms under the assumption the problem is moderately linear, leads to the Gauss-Newton method, which gives

$$\mathbf{x}_{i+1} = \mathbf{x}_i + (\mathbf{K}_i^T\mathbf{S}_y^{-1}\mathbf{K}_i + \mathbf{S}_a^{-1})^{-1}[\mathbf{K}_i^T\mathbf{S}_y^{-1}(\mathbf{y} - \mathbf{F}(\mathbf{x}_i)) - \mathbf{S}_a^{-1}(\mathbf{x}_i - \mathbf{x}_a)] \tag{3.9}$$

where $\mathbf{K}_i \equiv \mathbf{K}(\mathbf{x}_i)$. Detailed derivation of this method can be found in Rodgers (2000).

Further, by defining the gain matrices $\mathbf{G}$ and $\mathbf{H}$ as the dependence of the retrieval upon the measurements and the *a priori* respectively, equation 3.9 can be written in the form

$$\mathbf{x}_{i+1} = \mathbf{x}_i + \mathbf{G}(\mathbf{y} - \mathbf{F}(\mathbf{x}_i)) - \mathbf{H}(\mathbf{x}_i - \mathbf{x}_a) \tag{3.10}$$

where

$$\mathbf{G} = (\mathbf{K}_i^{\mathrm{T}}\mathbf{S}_y^{-1}\mathbf{K}_i + \mathbf{S}_a^{-1})^{-1}\mathbf{K}_i^{\mathrm{T}}\mathbf{S}_y^{-1}, \tag{3.11}$$

$$\mathbf{H} = (\mathbf{K}_i^{\mathrm{T}}\mathbf{S}_y^{-1}\mathbf{K}_i + \mathbf{S}_a^{-1})^{-1}\mathbf{S}_a^{-1}. \tag{3.12}$$

3.2 The Averaging Kernel

The averaging kernel matrix, $\mathbf{A}$, relates the sensitivity of the retrieval to the true state. Its elements are defined to be

$$A_{ij} = \frac{\partial x_i}{\partial x_j^t}, \tag{3.13}$$

where $\mathbf{x}^t$ is the true value of the state.

Rearranging equation 3.10 and expressing $\mathbf{x}_{i+1}$ as a departure from the the *a priori* rather than the previous iteration gives

$$\mathbf{x}_{i+1} = \mathbf{x}_a + \mathbf{G}\left[\mathbf{y} - \mathbf{F}(\mathbf{x}_i) + \mathbf{K}_i(\mathbf{x}_i - \mathbf{x}_a)\right] \tag{3.14}$$

which in the limit of $i \rightarrow \infty$ and $\mathbf{x}_i \rightarrow \mathbf{x}$ becomes

$$\mathbf{x} = \mathbf{x}_a + \mathbf{G}\left[\mathbf{y} - \mathbf{F}(\mathbf{x}) + \mathbf{K}(\mathbf{x} - \mathbf{x}_a)\right]. \tag{3.15}$$

Through the substitution of $\mathbf{y} = \mathbf{F}(\mathbf{x}^t) + \boldsymbol{\epsilon}$ and the linearisation of $\mathbf{F}(\mathbf{x}^t)$ around $\mathbf{x}$, this can be expressed as

$$\mathbf{x} = \mathbf{x}_a + \mathbf{G}\left[\mathbf{K}(\mathbf{x}^t - \mathbf{x}_a) + \boldsymbol{\epsilon}\right] \tag{3.16}$$

which gives rise to

$$\mathbf{x} - \mathbf{x}^t = (\mathbf{A} - \mathbf{I}_n)(\mathbf{x}^t - \mathbf{x}_a) + \mathbf{G}\boldsymbol{\epsilon} \tag{3.17}$$

where $\mathbf{I}_n$ is the identity matrix and $\mathbf{A}$ can be defined as

$$\mathbf{A} = \mathbf{GK}. \tag{3.18}$$

3.3 Retrieval Error

Under the optimal estimation assumption that the measurements and *a priori* are uncorrelated with each other, equation 3.17 has the corresponding *a posteriori* error covariance matrix, $\mathbf{S}_x$, which, given that $\mathbf{H} = \mathbf{I}_n - \mathbf{A}$, can be written as

$$\mathbf{S}_x = \mathbf{G}\mathbf{S}_y\mathbf{G}^{\mathrm{T}} + \mathbf{H}\mathbf{S}_a\mathbf{H}^{\mathrm{T}}, \tag{3.19}$$

and reduces to:

$$\mathbf{S}_x = (\mathbf{K}^{\mathrm{T}}\,\mathbf{S}_y^{-1}\mathbf{K} + \mathbf{S}_a^{-1})^{-1}. \tag{3.20}$$

In the limit $\mathbf{S}_a^{-1} \to 0$ equation 3.20 tends to a least squares fit. However, given that the problem is usually ill–posed, this rarely works. To solve this we must define $\mathbf{S}_a^{-1} \neq 0$ and thus, if $\mathbf{S}_a$ is full rank, it guarantees that $\mathbf{S}_x$ (and Eq. 3.11) is also full rank and invertible.

3.4 Smoothing Error

A retrieval is just an estimate of the true state and this has an error contribution due to smoothing. In a weighted least squares fit the retrieval purely depends upon the measurements. In this case the second term in equation 3.19 is absent and $\mathbf{A} = \mathbf{I}$, hence the only contribution to the retrieval error comes from the measurements themselves. However, in the optimal estimation retrieval, there is a contribution from the *a priori* estimate that is independent of the true state. This is the smoothing error, which is given by Rodgers (2000) to be

$$\mathbf{S}_s = (\mathbf{A} - \mathbf{I}_n)\mathbf{S}_m(\mathbf{A} - \mathbf{I}_n)^{\mathrm{T}}, \tag{3.21}$$

where $\mathbf{S}_m$ is the covariance of the ensemble of states about the mean state. The true ensemble covariance matrix is often unknown, which can lead to inaccuracies in calculating this error. However, assuming a linear Gaussian case and that the ensemble of states corresponds to the *a priori*, equation 3.21 becomes

$$\mathbf{S}_s = \mathbf{H}\mathbf{S}_a^{-1}\mathbf{H}^{\mathrm{T}} \tag{3.22}$$

showing that this contribution forms the second term in equation 3.19.

In a well constrained inverse problem, such as limb-sounding, large values of $\mathbf{S}_a$ (where $\mathbf{S}_a \gg \mathbf{S}_m$) are often used as mathematical constraints on the inversion. In an NWP context values of $\mathbf{S}_a$ are small and well characterised. However, for nadir-viewing retrievals, $\mathbf{S}_a$ must be carefully chosen to draw on information from both the *a priori* and the measurements.

3.5 The Forward Model Jacobian

As discussed in Chapter 4 there are many Radiative Transfer Models available to simulate the atmospheric spectra and create the Jacobian matrix, $\mathbf{K}$, which in turn is used to calculate the error covariance matrix of the retrieved state vector as shown in section 3.1. The Jacobian gives the rate of change in the measurement vector (e.g.

radiance or brightness temperature) given a perturbation of the state vector. For example, the RFM calculates the Jacobian for atmospheric temperature as the rate of change due to a 1 K perturbation to the state vector and surface temperature using simple numerical differencing, i.e.

$$\mathbf{K} = \frac{\delta \mathbf{T}_{\mathrm{b}}}{\delta \mathbf{x}} = \mathbf{T}_{\mathrm{b}}(\mathbf{x} + \delta \mathbf{x}) - \mathbf{T}_{\mathrm{b}}(\mathbf{x}). \tag{3.23}$$

The atmospheric state can either be the total column amount of a particular gas or the concentration of a gas at specified levels in the atmosphere, and hence, when running the forward model the perturbation can be applied to the column as a whole or to each individual layer respectively.

3.6 Figures of Merit

The accuracy of a retrieval of the state $\mathbf{x}$ is characterised by the error covariance matrix $\mathbf{S}_x$. A figure of merit is a quantity that compresses the information within the retrieval error covariance matrix into a single scalar quantity allowing easier intercomparison of different covariance matrices (for example, when examining how much information can be gained by the additional use different measurement channels).

Two figures of merit commonly used are the Shannon information content and the degrees of freedom for signal, d_s. The former is defined (e.g. Rodgers (2000)) to be the factor by which knowledge of a quantity is improved by making the measurement and weights the error analysis so that it will select any point in the profile regardless of previous knowledge at that level:

$$H = -\frac{1}{2}\log_2 |\mathbf{I}_n - \mathbf{A}| = -\frac{1}{2}\log_2 |\mathbf{S}_x\,\mathbf{S}_a^{-1}|, \tag{3.24}$$

where $\mathbf{I}_n$ is the identity matrix and $\mathbf{A}$ is the averaging kernel matrix.

Alternatively, the degrees of freedom for signal, d_s, can be used, which weights the analysis to favour levels where there is a lack of knowledge. Essentially, it is the number of independent pieces of information in an estimate of the state and is given by

$$d_s = \mathrm{tr}(\mathbf{A}) \tag{3.25}$$

The DFS is chosen for this study in line with previous studies, such as that by Collard (2007), which will be discussed in more detail in chapter 6.

3.7 Conversion to column amount

Column amount is a measure used to describe the quantity of a specified gas in the atmosphere. It is the amount of the gas (in moles or kg) in a vertical column of unit cross-sectional area that extends from the Earth's surface to the top of the atmosphere. It can be defined as:

$$\int_0^\infty x(z)\,\rho_{\mathrm{air}}\,\mathrm{d}z, \tag{3.26}$$

where $x(z)$ is the state vector (in volume mixing ratio, VMR, or mass mixing ratio, MMR) as a function of height, z, and ρ is the air density (in moles/m^3 or kg/m^3). When discussing the column amount of a gas, most generally ozone, a common unit used is the Dobson unit, DU. This is the thickness of the layer that a column of gas would have if it were compressed to standard temperature and pressure, where 100DU$\sim$1mm, and gives the conversion 1DU $= 2.69 \times 10^{16}$ molecules cm^{-2}.

Atmospheric profile data is usually given with units of ppmv (parts per million per volume). The conversion from ppmv to column amount in Dobson's units, c, is as follows:

$$\begin{aligned} c &= \frac{1}{2.69 \times 10^{16}} \frac{N_a}{10^3 M_{\text{air}}} \int_0^\infty x\, \rho_{\text{air}}\, \mathrm{d}z & (3.27) \\ &= \frac{1}{2.69 \times 10^{16}} \frac{N_a}{10^3 M_{\text{air}}} \int_0^{\mathrm{p}_0} \frac{x}{\mathrm{g}}\, \mathrm{d}p, & (3.28) \end{aligned}$$

where the latter results from hydrostatic equilibrium ($\mathrm{d}p = g\rho_{\text{air}}\,\mathrm{d}z$ and ρ is in kg/m^3), N_a is Avagadro's constant and M_{air} is the Molar mass of air.

The column amount can be calculated from the retrieved VMR profile in layers of a set thickness using the above equation. When carrying out the integral numerically, the extended trapezoidal rule is implemented, i.e.

$$\int_{p_1}^{p_n} x(p)\, dp \approx \Delta p[\frac{1}{2}x_1 + x_2 + ... + x_{n-1} + \frac{1}{2}x_n], \tag{3.29}$$

where n is the number of levels in the profile and Δp is the thickness (in pressure units) of each layer. However, when integrating over pressure co-ordinates, the thicknesses of each of the layers are not necessarily equal and the integral becomes:

$$\int_{p_1}^{p_n} x(p)\, dp \approx \sum_{i=1}^{n} \left(\frac{x_i + x_{i+1}}{2} \right) (p_{i+1} - p_i). \tag{3.30}$$

Following from the above equations, an alternative way of calculating the column amount, c, and its associated scalar covariance error, $\mathrm{S}_{\mathrm{col}}$, is to express it as

$$
\begin{aligned}
c &= a_1x_1 + a_2x_2 + \ldots + a_nx_n && (3.31)\\
&= \mathbf{a}^{\mathrm{T}}\mathbf{x} && (3.32)\\
\mathrm{S}_{\mathrm{col}} &= \sigma_{\mathrm{c}}^2 && (3.33)\\
&= \mathbf{a}^{\mathrm{T}}\mathbf{S}_x\mathbf{a} && (3.34)
\end{aligned}
$$

where the a_i values are constants that represent the transformation from the concentrations in different layers to column amount from equation 3.30. Thus the retrieval can be described by a VMR profile and subsequently converted to a column retrieval without loss of generality (obviously this is not the case in the reverse).

Chapter 4

Radiative Transfer Models

4.1 Radiative Transfer

The equation of radiative transfer describes how radiation propagating through the atmosphere is both attenuated and enhanced due to absorption, scattering and thermal emission. This forms the basis for modelling atmospheric radiances and interpreting remote sensing measurements.

Consider a beam of radiation passing through a layer of the atmosphere containing an absorbing (or scattering) gas, of thickness dz. The fractional decrease in radiance, L_ν, for a given wavenumber, ν, is given by Beer-Lambert's Law,

$$\mathrm{dL}_\nu = -k_\nu(z)\rho_a(z)\mathrm{L}_\nu(z)\,\mathrm{d}z, \tag{4.1}$$

where ρ_a is the density of the gas and hence $\rho_a\mathrm{d}z$ gives the mass of gas in the beam, per unit cross-sectional area. The constant of proportionality is k_ν, the extinction coefficient, which is the sum of the absorption and scattering coefficients defining their respective contributions to dL_ν.

The layer of atmosphere will also be emitting radiation, the amount depending upon its temperature. Assuming local thermodynamical equilibrium (LTE) and no scattering, Kirchoff's Law can be applied and the emitted radiation becomes

$$\mathrm{dL}_\nu = k_\nu(z)\rho_a(z)\mathrm{J}_\nu(z)\,\mathrm{d}z \tag{4.2}$$

where $\mathrm{J}_\nu(z)$ is the source function, which is assumed, because of LTE, to be the Planck black body function, $\mathrm{B}_\nu(T)$. The Planck function gives the power radiated by a black body in $\mathrm{W}/(\mathrm{cm}^2.\mathrm{sr}.\mathrm{cm}^{-1})$ as

$$\mathrm{B}_\nu(T) = \frac{2hc^2\nu^3}{\exp(hc\nu/k_\mathrm{B}T) - 1} \tag{4.3}$$

where h is the Planck constant, c is the speed of light and k_B is the Boltzmann constant.

Combining both extinction and emission, the radiative transfer equation (or Schwarzschilds's equation), is obtained

$$\frac{\mathrm{dL}_\nu}{\mathrm{d}z} = -k_\nu\rho_a(\mathrm{L}_\nu - \mathrm{B}_\nu(T)). \tag{4.4}$$

Integrating this equation from a source point, z_s, to an observation point, z_{obs} leads to the integral equation of transfer

$$\mathrm{L}_\nu(z_{obs}) = \mathrm{L}_\nu(z_s)\tau_\nu(z_s, z_{obs}) + \int_{z_s}^{z_{obs}} \mathrm{B}_\nu(T(z))\frac{\mathrm{d}\tau}{\mathrm{d}z}\mathrm{d}z, \tag{4.5}$$

where τ is the transmittance between z_s and z_{obs}, given by

$$\tau(z_s, z_{obs}) = \exp\left(-\int_{z_s}^{z_{obs}} k_\nu(z)\rho_a(z)\mathrm{d}z\right). \tag{4.6}$$

Solving equation 4.5 is the main aim of radiative transfer models (Edwards, 1992).

For nadir viewing, brightness temperature is commonly used instead of radiance. From equation 4.3, the brightness temperature, $\mathrm{T_b}$, is the temperature a black body would have to give the observed radiance at a particular wavenumber:

$$\mathrm{T_b^{-1}} = \frac{k_\mathrm{B}}{hc\nu}\ln\left(1 + \frac{2hc^2\nu^3}{\mathrm{L}_\nu}\right) \tag{4.7}$$

4.2 The Modelling of Radiative Transfer

Radiative transfer models attempt to calculate accurate top of atmosphere radiances given vertical profiles of temperature and atmospheric absorbers . As mentioned in section 4.1, their aim is to solve the equation of radiative transfer. This is multiplied by an appropriate spectral response function to obtain the simulated radiance expected from a particular instrument.

The atmosphere is divided into horizontal layers, which are assumed to be homogeneous and given in either height or pressure co-ordinates. For each layer and atmospheric absorber present, characteristic values are determined for the temperature and pressure that should give the same transmittance values as the ‘real’ inhomogeneous layer. These values are usually calculated using the Curtis-Godson approximation, which states that an equivalent pressure, $\overline{p}_a$, can be defined as

$$\overline{p}_a = \frac{\int_z p\rho_a(z)\mathrm{d}z}{\int_z \rho_a(z)\mathrm{d}z} \tag{4.8}$$

and an equivalent temperature, $\overline{T}_a$, as

$$\overline{T}_a = \frac{\int_z T\rho_a(z)\mathrm{d}z}{\int_z \rho_a(z)\mathrm{d}z} \tag{4.9}$$

Essentially, the quantities are weighted along the atmospheric path by the amount of absorber. These quantities allow the calculation of the layer emission and absorption coefficients, the essential components under local thermodynamic equilibrium.

There are three main types of radiative transfer models: monochromatic models, band models and correlated-k models (the latter will not be discussed here). The fundamental distinction between the monochromatic and band models is the use of Beer's Law in the calculation of the atmospheric transmission; a monochromatic model can implement Beer's Law, whereas a band model, which deals which spectrally averaged transmittances, cannot. These model types are more commonly referred to as line-by-line radiative transfer models and fast radiative transfer models respectively (although a line-by-line model is in fact only a particular case of a monochromatic model).

Although line-by-line models produce more accurate results they are computationally expensive and cannot be run in near real time. For this reason, fast radiative transfer models were developed for use in applications that require near real time processing, such as NWP. In the following sections, a model of each type is discussed explaining their methodology and their differences.

4.2.1 Reference Forward Model

The Reference Forward Model, or RFM, is a line-by-line model developed at the University of Oxford (Dudhia, 2002). Based on GENLN2 (Edwards, 1992), it was developed originally for use with the Michelson Interferometer for Passive Atmospheric Sounding, MIPAS, but has since evolved into a general purpose code for many spectroscopic calculations including nadir viewing measurements.

The line-by-line model first calculates the monochromatic absorption coefficient, $k(\nu)$, at wavenumber ν for every local spectral line using the parameters supplied by a database containing spectroscopic parameters. The line strengths and widths at standard temperature and pressure must be adjusted to the temperature and pressure of the path through the atmosphere.

The actual line-by-line calculation comes from expressing the absorption coefficient at wavenumber ν as the sum of the contributions to absorption from all spectral lines, i, in range, i.e.

$$k(\nu)_j = \sum_i S_{ij}\, g(\nu - \nu_i)_j, \tag{4.10}$$

where S_{ij} is the strength of line i for gas path j and $g(\nu - \nu_i)_j$ is the line shape function, all adjusted to local path conditions. At different altitudes the spectral line shape is dominated by either Lorentz or Doppler broadening. The Lorentz line shape is given by

$$g_{\mathrm{L}}(\nu - \nu_0) = \frac{1}{\pi} \frac{\alpha_{\mathrm{L}}}{((\nu - \nu_0)^2 + \alpha_{\mathrm{L}})} \tag{4.11}$$

with the half width, α_{L} defined as

$$\alpha_{\mathrm{L}} = \alpha_0 \left(\frac{p}{p_0}\right) \left(\frac{T_0}{T}\right)^{1/2} \tag{4.12}$$

where ν_0 is the line centre and α_0 is the half width at standard temperature, T_0, and pressure, p_0. Alternatively, the Doppler line shape is given by

$$g_{\mathrm{D}}(\nu - \nu_0) = \frac{1}{\alpha_{\mathrm{D}}\pi^{1/2}}\exp\left[\left(\frac{\nu - \nu_0}{\alpha_{\mathrm{D}}}\right)^2\right] \tag{4.13}$$

with the $1/e$ width, α_{D} defined as

$$\alpha_{\mathrm{D}} = \frac{\nu_0}{c}\left(\frac{2k_{\mathrm{B}}T}{m}\right)^{1/2}. \tag{4.14}$$

The Voigt line shape, which is a convolution of the Lorentz and Doppler line shapes is appropriate for most infrared atmospheric cases and is given by

$$g_{\mathrm{V}}(\nu - \nu_i) = g_{0i}\,K(x_i, y_i) \tag{4.15}$$

where

$$g_{0i} = \frac{1}{\alpha_{\mathrm{D}i}}\left(\frac{\ln 2}{\pi}\right)^{1/2} \qquad K(x_i, y_i) = \frac{y_i}{\pi}\int\limits_{-\infty}^{+\infty}\frac{e^{-t^2}}{y_i^2 + (x_i - t)^2}dt \tag{4.16}$$

and

$$y_i = \frac{\alpha_{\mathrm{L}i}}{\alpha_{\mathrm{D}i}}(\ln 2)^{1/2} \qquad x_i = \left(\frac{\nu - \nu_i}{\alpha_{\mathrm{D}i}}\right)(\ln 2)^{1/2} \tag{4.17}$$

The Voigt function must be evaluated numerically and the specified spectral grid for the calculation must be sufficiently fine to capture the spectral structure of the atmospheric absorption features. However, for a few atmospheric absorbers, such as CO_2, the Voigt lineshape is inadequate due to the effects of line mixing, sub-Lorentzian line wings or continuum absorption. Line mixing accounts for the collisionally induced transitions between rotational-vibrational molecular states that occur when the Q-branch line structures overlap, causing a decrease in the absorption coefficient in the branch wings. The observed sub-Lorentzian behaviour in the line wings caused by the time-dependence of collisions is accounted for through the inclusion of empirical correction functions known as χ-factors (Clarmann et al., 2003). Essentially they represent the difference between observed measurements and Lorentzian line wing theory. Currently the RFM only provides the ability to apply the χ-factor correction to CO_2 and uses the method described by Doucen et al. (1985) and Cousin et al. (1985). Finally, continuum absorption must also be included along with the line-by-line absorption. This varies slowly with wavelength across the infrared spectral region and is far less well understood than individual molecular transitions. It represents any observed absorption that is not accounted for by simple collision theory. These features can be included within the RFM and their effects upon the radiance output will be discussed further in chapter 5.

Having expressed $k(\nu)$ in this way allows the application of Beer's Law to calculate the transmittances from each layer to the top of the atmosphere as in equation 4.6. Further, using the properties of Beer's Law, the total transmittance becomes the product of the transmittances of each absorber; i.e. $\tau = \prod_n \tau_n$, where n is the number of absorbers. The total transmittances over the spectral range for each gas, in a number of atmospheric layers can be approximated using equation 4.6 as

$$\begin{aligned} \tau(\nu) &= \exp(-\Sigma_j\, k(\nu)_j\, u_j), && (4.18) \\ &= \exp(-\chi(\nu)), && (4.19) \end{aligned}$$

where $\chi(\nu)$ is the optical depth and $u_j = \int_j \rho_a(z)\mathrm{d}z$ is the amount of absorber in the atmospheric path, j. The total optical depth can be calculated as the sum of the optical depths of each individual path, and the transmittance can subsequently be evaluated.

Non line-by-line monochromatic models can, as an alternative to the summation in equation 4.10, pre-calculate look-up tables for $k(\nu)$ using a variety of of pressure and temperature conditions. These can then be interpolated to the appropriate Curtis-Godson conditions.

This now allows the latter part of equation 4.5 to be solved and the radiance at each observation point can be calculated:

$$\mathrm{R}_\nu(z_{obs}) = \int_\nu \mathrm{L}_\nu(z_{obs})\phi(\nu)\,\mathrm{d}\nu \tag{4.20}$$

$$\mathrm{R}_\nu(z_{obs}) = \int_\nu \int_{z_s}^{z_{obs}} \mathrm{B}_\nu(T(z))\phi(\nu)\frac{\mathrm{d}\tau}{\mathrm{d}z}\,\mathrm{d}z\,\mathrm{d}\nu \tag{4.21}$$

where $\phi(\nu)$ is the normalised instrument spectral response function.

4.2.2 RTTOV

The RTTOV model is the Radiative Transfer model for TOVS, where TOVS is the Television InfraRed Observation Satellite (TIROS-N) Operational Vertical Sounder. It was originally developed for use with TOVS but, as with the RFM, has subsequently been developed and adapted for use with other instruments. The latest version is RTTOV-11 (Saunders et al., 2013), which includes all the scientific features of the fast Radiative Transfer model for IASI, RTIASI (Matricardi and Saunders, 1999), a model developed for pre-launch simulation studies of IASI data.

In RTTOV the radiances are not calculated as described for the RFM in equation

4.21, rather they are expressed as a function of profile dependent predictors as explained by Matricardi (2009). The difference arises from the use of spectrally averaged transmittances and Planck function. The calculation, in this case, is only a single integration over the atmospheric path (cf. equation 4.21):

$$\mathrm{R}(z_{obs}) = \int_{z_s}^{z_{obs}} \overline{\mathrm{B}}(T(z)) \frac{\mathrm{d}\overline{\tau}}{\mathrm{d}z}\, \mathrm{d}z, \tag{4.22}$$

where $\overline{\mathrm{B}} = \int_{\nu} \mathrm{B}\phi \, \mathrm{d}\nu$ and $\overline{\tau} = \int_{\nu} \tau\phi \, \mathrm{d}\nu$. This form of calculation increases the computer efficiency by avoiding the line-by-line summation in equation 4.10 and the integral over wavenumber in equation 4.21. Thus allowing the model to be used in near real time to monitor and assimilate satellite radiances as is needed for NWP. Accuracy can however be lost through the assumptions made.

For high spectral resolution instruments, such as IASI, B_{ν} varies only slowly with wavenumber across the instrument spectral response function (ISRF) and can therefore be adequately represented by $\overline{\mathrm{B}}$. However, problems arise when replacing τ_{ν} with $\overline{\tau}$ since it has a much larger variation across the ISRF, and on a much finer scale. In this instance Beer's Law can no longer be applied and instead $\overline{\tau}$ must be calculated empirically.

Accurate line-by-line transmittances are calculated for a diverse training set of atmospheric profiles, which represent the range of variation in atmospheric absorbers, at each defined atmospheric level and at several viewing angles. (The exact settings for the line-by-line calculations are discussed in greater detail in chapter 7.) These transmittances, convolved with the appropriate instrument spectral response function (ISRF), are converted to layer modified optical depths, which become the data points used to calculate channel specific regression coefficients using a set of profile dependent predictors. The regression is carried out on the layer optical depths, and not the level-to-space transmittances, as this has been shown to give more accurate results (Matricardi and Saunders, 1999). Currently the training set of transmittances are calculated using the Line-By-Line Radiative Transfer Model, LBLRTM (Clough et al. (1992),Clough et al. (2005)).

Essentially, for given atmospheric profiles and parameters the effective optical depth, $\chi^{\text{eff}}_{j,\nu}$ (or convolved transmittance, $\overline{\tau}_{j,\nu} = \exp(-\chi^{\text{eff}}_{j,\nu})$), can be written as a function of the profile dependent predictors and regression coefficients (or fast transmittance coefficients) as described by Matricardi et al. (2004). For the layer from pressure level j to space

$$\chi^{\text{eff}}_{j,\nu} = 0, \quad j = 1 \tag{4.23}$$

$$\chi^{\text{eff}}_{j,\nu} = \chi^{\text{eff}}_{j-1,\nu} + \sum_{k=1}^{M} a_{j-1,\nu,k} X_{k,j-1}, \quad j = 2, l \tag{4.24}$$

where the functions $X_{k,j}$ are the M profile dependent predictors of the model and $a_{j-1,\nu,k}$ are the regression coefficients. The coefficients are computed through a linear regression of $\chi^{\text{eff}}_{j,\nu} - \chi^{\text{eff}}_{j-1,\nu}$ versus the predictor values, $X_{k,j}$. The predictors' functional dependence are on factors such as the spectral region and the absorbing gas and are calculated from profile variables for each training profile at each viewing angle. The profile variables are defined from ratios of reference temperature, water vapour and ozone profiles. The calculations and variables are explained in detail in Matricardi and Saunders (1999) and Matricardi et al. (2004).

This method of radiative transfer calculation is extremely efficient and allows near-real time calculations to be carried out. The implications on the spectral accuracy of the assumptions made by RTTOV are assessed through comparisons with the RFM in chapter 7 .

Chapter 5

Configuring the RFM to model IASI spectra

This chapter describes configuring the RFM (described in chapter 4) in its nadir, or more accurately plane parallel, mode for the simulation of the IASI spectrum. Here we explain the assumptions made in this mode and assess any errors they induce.

Similar investigations have been carried out into the KLIMA-IASI line by line model by Cortesi et al. (2009) and also previous RFM studies by Walker and Dudhia (2009).

This study was performed using a pre-release version of the RFM, RFM v 4.3, and unless otherwise stated, the settings below were consistently applied to the calculations:

- The scene was assumed to be cloud free and over the ocean.
- Use of the HITRAN 2008 spectroscopic database.
- The following atmospheric absorbers were included; O_3, CO_2, CO, H_2O, N_2O,

CH_4, NO_2, NH_3, C_2H_6, HCN, CFC–11, CFC–12, HCOOH, SO_2, HNO_3, NO, N_2, O_2, OCS, CCl_4, and CF_4.

- Volume mixing ratios are those from the FASCODE atmospheres. Each calculation was carried out for the 6 atmospheres (U.S. standard, mid-latitude winter, mid-latitude summer, sub-arctic winter, sub-arctic summer and tropical) and the case with the largest residual is shown. Figures 5.1a and 5.1b show the temperature and water vapour vertical profiles for each of these atmospheres.

- The altitude grid is the 50 level U.S. standard atmosphere height grid from 0 km to 120 km.

- The Voigt line shape is assumed suitable for all absorbers except CO_2, for which the χ–factor correction and line mixing effects are included.

- The inclusion of continua for H_2O, CO_2, N_2, and O_2.

- A spectral fine grid of $0.001\,\mathrm{cm}^{-1}$ is used during the RFM calculations. The resulting spectrum is convolved with a truncated version of the IASI instrument line shape before being interpolated onto a frequency grid of $0.25\,\mathrm{cm}^{-1}$, corresponding to the spectral sampling of IASI.

- A spectrally varying surface emissivity calculated using the zenith angle dependent equation for ocean scenes found in RTTOV (Sherlock, 1999).

- Although the entire IASI spectrum is shown, only the spectral region up to $2200\,\mathrm{cm}^{-1}$ is considered for the residuals. This is to exclude channels affected by solar reflectance that are unlikely to be used in operational applications.

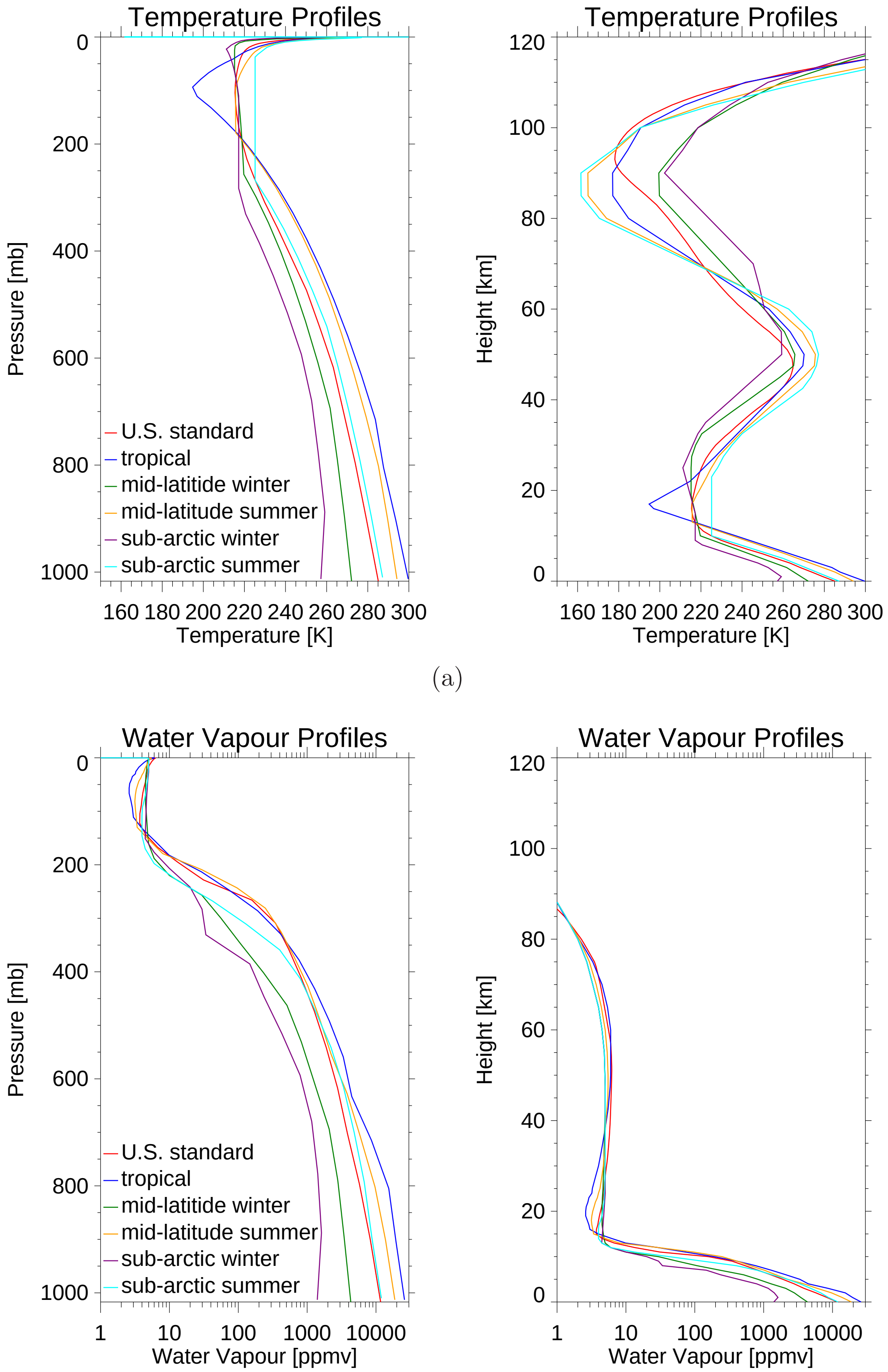

(a)

(b)

Figure 5.1: The vertical profiles of (a) temperature and (b) water vapour in the 6 FASCODE atmospheres that are used in the following comparisons. Profiles shown for both a pressure and height vertical grid.

For each model assumption examined, residuals, which are the differences between the tested assumptions and either the model output without the assumption or a baseline assumed to cause errors below the IASI instrument noise, are calculated. To establish if an approximation is valid, the residuals are compared to the instrument noise associated with the IASI spectrum. As can be seen in figure 5.2 the Noise Equivalent Brightness Temperature (NEΔT) depends on the scene temperature, therefore it can be more useful to view in terms of the Noise Equivalent Spectral Radiance (NESR), which is both smoother and scene independent in radiance space. The 'steps' in the NESR occur at the boundaries between the different IASI spectral bands where the quality of the measurements decreases due to a decrease in detector sensitivity. For each of the following comparisons the differences are plotted in both brightness temperature and radiance, with the errors in radiance shown on a logarithmic axis in order to more easily compare with the noise level. Negative radiance residuals have been projected into the positive domain for plotting purposes. However, in certain spectral regions, despite large residuals, there is little contribution from the atmospheric absorption in the troposphere (the region of most interest in this study) and hence, in these regions, the upper limit for acceptable residuals can be higher. It should be noted that if interested in stratospheric features this would not be the case. The variation in the atmospheric absorption, A, throughout the atmosphere from different altitudes to space is shown in figure 5.3. To account for this variation, an error parameter, ξ, has been introduced that scales the residual in radiance, $\Delta\,\mathrm{L}_\nu$, to the NESR and atmospheric transmission, $\tau = 1 - A$, by

$$\xi_\nu = \frac{\Delta\,\mathrm{L}_\nu \times \tau_\nu}{\mathrm{NESR}_\nu} \tag{5.1}$$

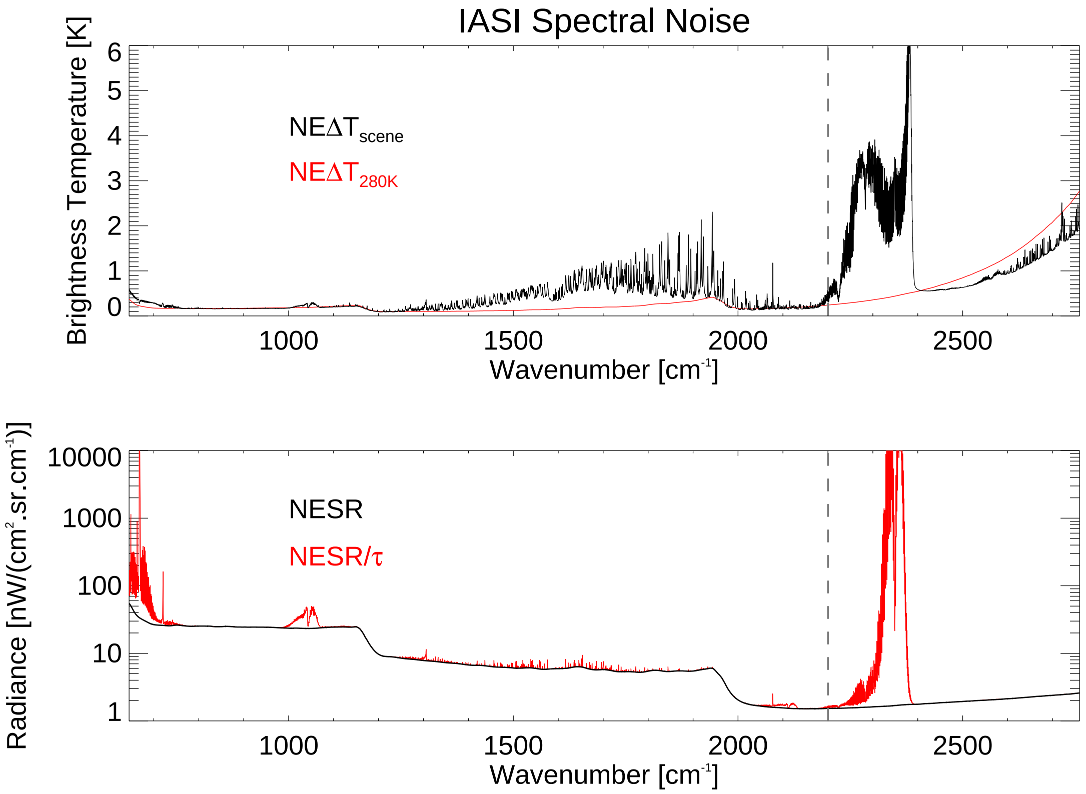

Figure 5.2: The radiometric noise associated with the IASI spectrum from Hilton et al. (2009b). The NEΔT at 280 K is shown with that for the scene temperature of a standard mid-latitude daytime atmosphere. Below is shown the equivalent NESR and the NESR divided by the atmospheric transmission from 20 km to space. The dashed line indicates the region above 2200 cm^{-1} that will be not considered within this chapter.

where τ_ν is the transmittance from 20 km to space, chosen to include all the UTLS (upper troposphere, lower stratosphere) features. Calculated for each spectral point, less weight is attached to spectral regions that are optically thick in the stratosphere. Therefore, for each comparison, the radiance residuals are shown in relation to the error factor, $\mathrm{NESR}_\nu/\tau_\nu$. This error factor can be seen in figure 5.2, which shows its effect upon the NESR for the U.S standard atmosphere. Also plotted for each radiance comparison is the NESR (weighted by the transmission) for 10 and 100 averaged spectra, to see if the assumptions will hold when applied to averaged spectra. In terms of the error factor: if, for the entire spectrum, $\xi < \xi_{NESR} = 1$ the spectrum is deemed within the acceptable noise level, if $\xi < \xi_{NESR\_10} = 1/\sqrt{10}$ the spectrum is within the acceptable level for 10 averaged spectra and if $\xi < \xi_{NESR\_100} = 1/\sqrt{100}$ the spectrum is within the acceptable level for 100 averaged spectra. The maximum ξ value and the corresponding wavenumber it occurs at, $\nu(\xi_{max})$, are shown for each comparison.

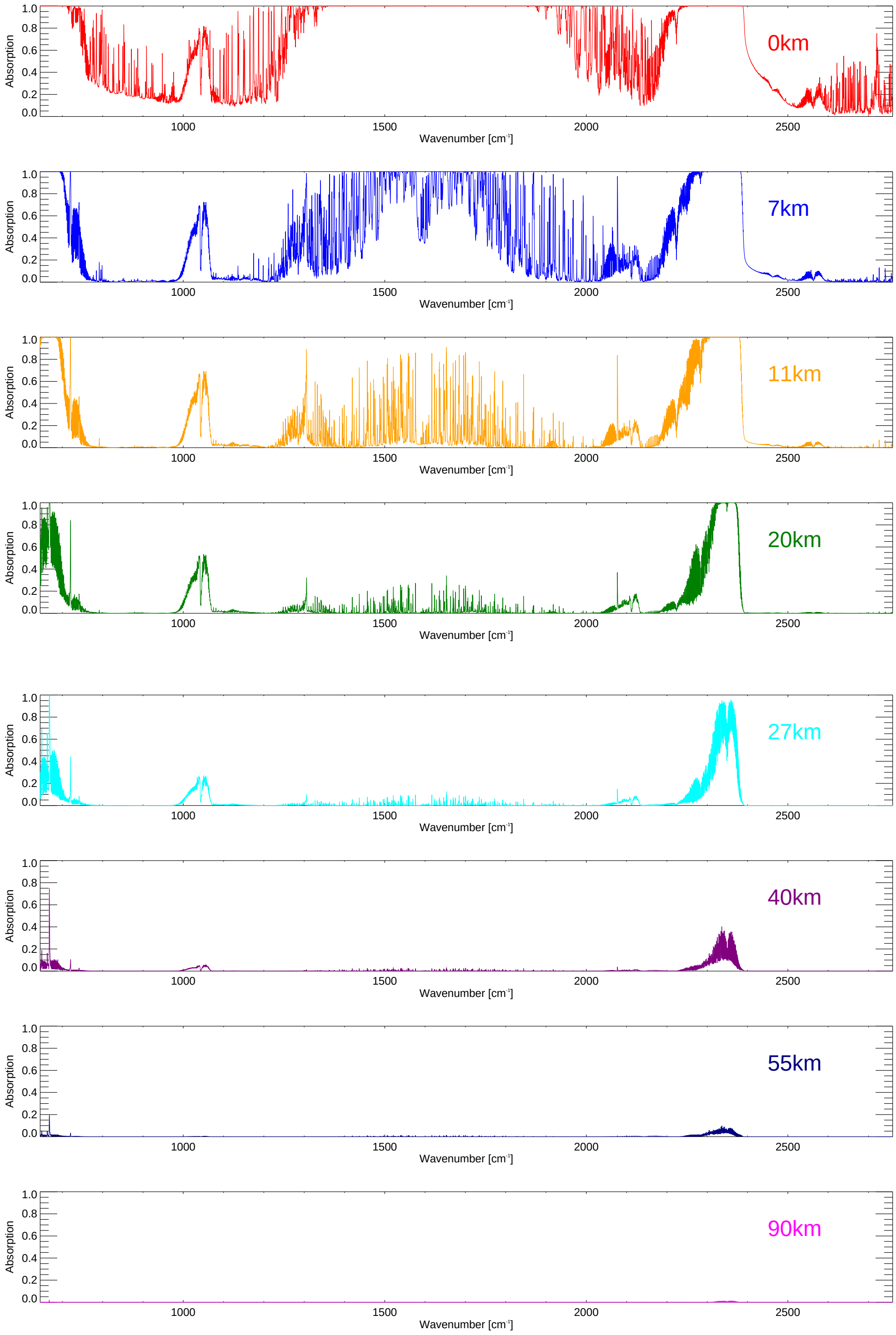

Figure 5.3: The absorption spectra from IASI for the standard mid latitude daytime atmosphere from different altitudes to space (taken as 120 km).

5.1 Spatial Modelling

The assumptions tested in this section are those related to the geometric modelling of the plane parallel viewing mode and how this differs from that in the more general limb viewing mode. In this context, 'limb-viewing' means merely that the full RFM ray tracing calculations are carried out assuming a symmetric curvature to the atmosphere and including refraction and field of view effects. All calculations are carried out purely in the limb-viewing mode of the RFM, modelling the nadir viewing geometry within the limb-viewing construct.

5.1.1 Field of View Size

As mentioned in chapter 2, IASI's effective field of view (FOV), i.e. the angular extent viewed by IASI, consists of a 2 × 2 matrix containing independent circular pixels, or instantaneous fields of view (IFOV), with diameters of 14.65 mrad (12 km at nadir ground resolution). These can be seen schematically in figure 5.4 along with the field of view for the associated imaging system, which encompasses the same effective FOV as IASI but is defined as a square of 64 × 64 pixels and area 59.63 × 59.63 mrad.

Ideally, an instrument's output is proportional to the average radiance within the area bounded by the IFOV. However in reality this is not exactly reproduced. The instrument's point spread function (Φ) is defined as the horizontal sensitivity within each pixel and is given by

$$\mathrm{L}_i^{meas} = \int\int \phi_i(x,y)\mathrm{L}(x,y)\mathrm{d}x\mathrm{d}y \tag{5.2}$$

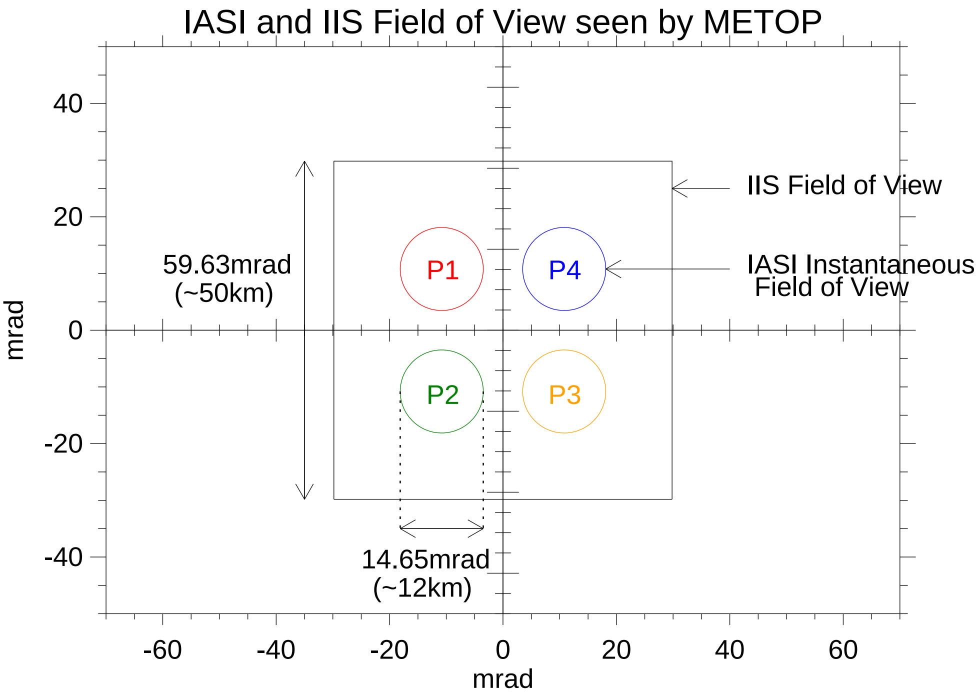

Figure 5.4: A projection to the ground of the IASI and IIS FOV's. Diagram reproduces that by Pequignot (2009).

with

$$\int\int \Phi_i(x, y)\mathrm{d}x\mathrm{d}y = 1 \tag{5.3}$$

where L_i^{meas} is the measured radiance for a given scene radiance, L, and i denotes the pixel. EUMETSAT (2009) explain that for IASI the integral of the PSF across the IFOV is larger than 95% and within the inner 80% of the pixel the inhomogeneity is no larger than ±5%. The PSF can be seen for each pixel in figure 5.5. For a very homogeneous scene, $\mathrm{L}(x, y)$ is a constant and hence, no PSF convolution is required.

In the nadir mode of the RFM there is no allowance for FOV size or shape; it is modelled as purely a single beam at the centre of the field of view. In order to assess

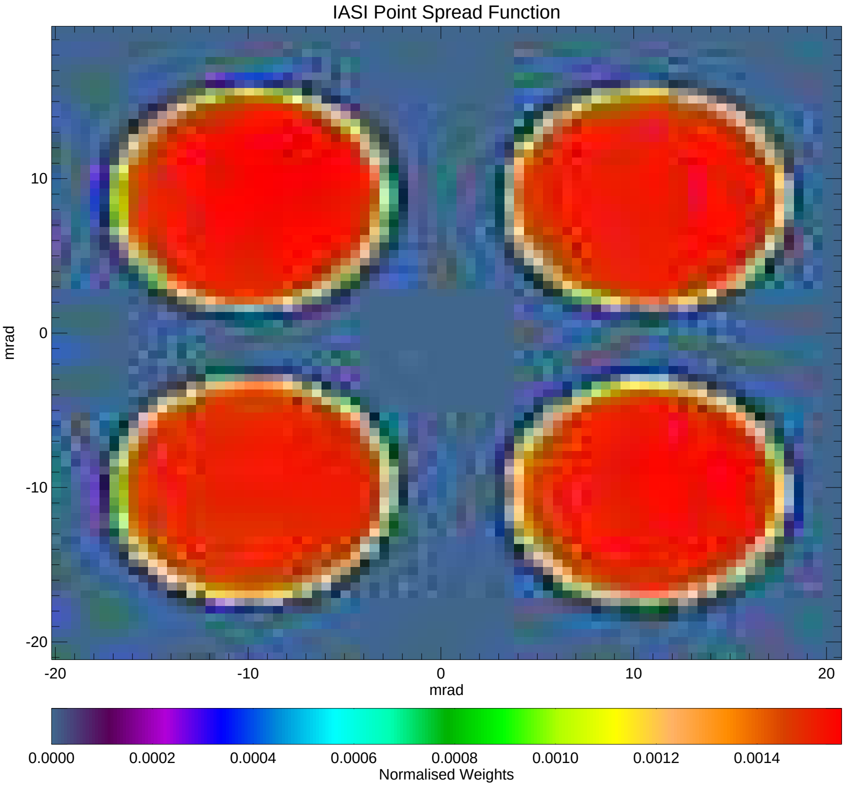

Figure 5.5: The IASI point spread function for each pixel.

the impact of ignoring the finite size of the FOV the RFM is run in its limb viewing mode, where the off-nadir viewing angles can be defined by the elevation angle and the observing altitude. A simple situation is considered, shown in figure 5.6, where the scene radiance is given by the average of the radiances at the two extreme angles of the IFOV, and is compared to the single beam approximation. A more accurate assessment would consist of averaging radiances uniformly distributed throughout the IFOV, but this comparison considers only an upper limit estimate.

Figure 5.7 shows the differences, or residual, from each comparison in terms of brightness temperature and radiance and table 5.1 shows the maximum spectral residual expressed as an error parameter, ξ_{max}, and its spectral location, $\nu(\xi_{max})$,

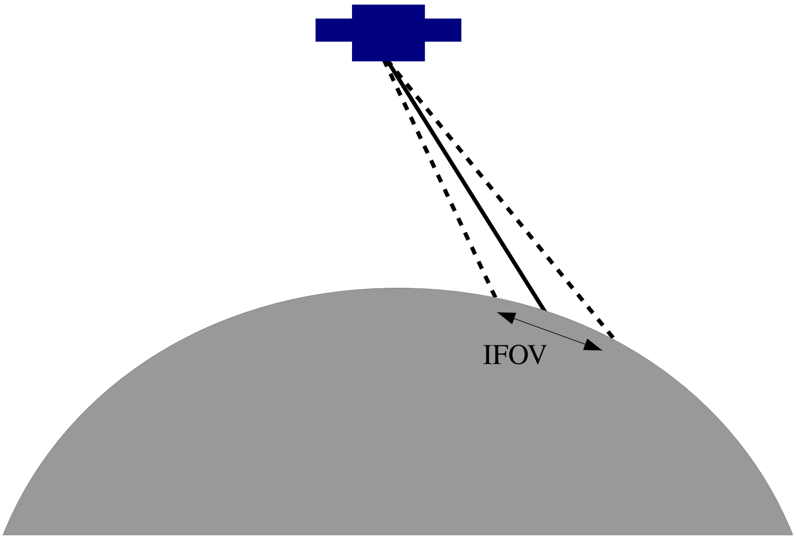

Figure 5.6: The geometry of assessing the finite FOV size

at each viewing angle. It can be clearly seen that even at the largest IASI viewing angle, 48 °, the difference caused by including the FOV convolution is well below the IASI noise, and in fact the NESR for 100 averaged spectra ($\xi < 0.1$). Therefore, the exclusion of a finite FOV size in IASI simulations is considered valid.

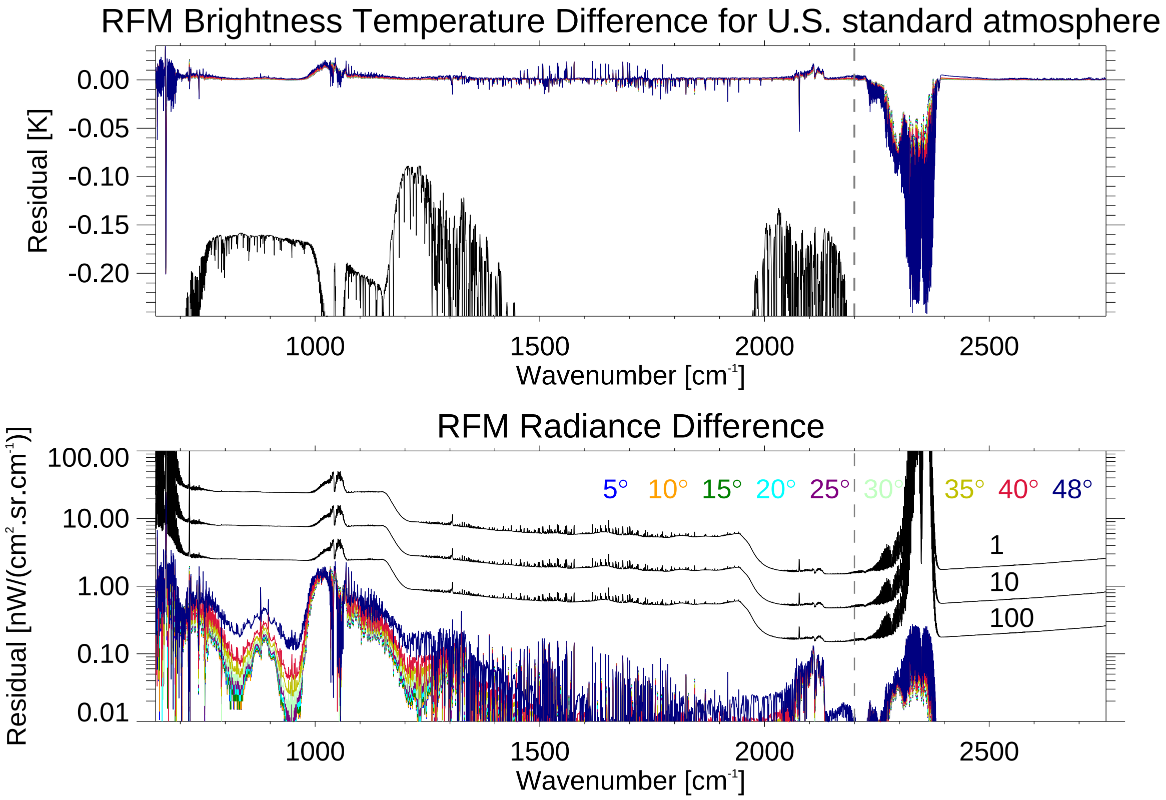

Figure 5.7: The residual from ignoring the field of view convolution at increasing viewing angles. The top plot shows the result in terms of brightness temperature and the IASI noise can be seen in black. The lower plot shows the result in terms of radiance and the NESR for 1, 10 and 100 averaged spectra divided by the atmospheric transmission from 20 km to space can be seen in black.

Table 5.1: Impact of ignoring finite IFOV. The table shows the maximum spectral residual expressed as an error parameter, ξ_{max}, and its spectral location, $\nu(\xi_{max})$.

U.S Standard atmosphere		
Viewing angle	ξ_{max}	$\nu(\xi_{max})$
5°	0.067	1044.75
10°	0.067	1044.75
15°	0.068	1044.75
20°	0.068	1044.75
25°	0.069	1044.75
30°	0.070	1044.75
35°	0.072	1044.75
40°	0.074	1044.75
48°	0.086	1068.75

5.1.2 Refraction

Table 5.2: Impact of ignoring refraction. The table shows the maximum spectral residual expressed as an error parameter and its spectral location.

Tropical atmosphere		
Viewing angle	ξ_{max}	$\nu(\xi_{max})$
0°	0.000	N/A
5°	0.000	978.25
10°	0.001	1236.25
15°	0.002	1278.50
20°	0.004	1276.00
25°	0.006	1276.00
30°	0.010	1278.50
35°	0.015	1278.50
40°	0.022	1250.75
48°	0.048	1230.00

The refraction along an atmospheric path is ignored when using the RFM in the nadir mode. In order to ascertain the validity of this approximation, the RFM is run in its limb viewing mode, for which refraction is assumed by default, but can be switched off. Figure 5.8 shows the residuals at increasing viewing angles. Table 5.2 shows the maximum error parameter at each viewing angle. Even at the largest IASI viewing angle the effect from refraction is negligible, and the residuals are evidently well below the NESR for 100 spectra. The exclusion of refraction in the nadir viewing mode is therefore legitimate.

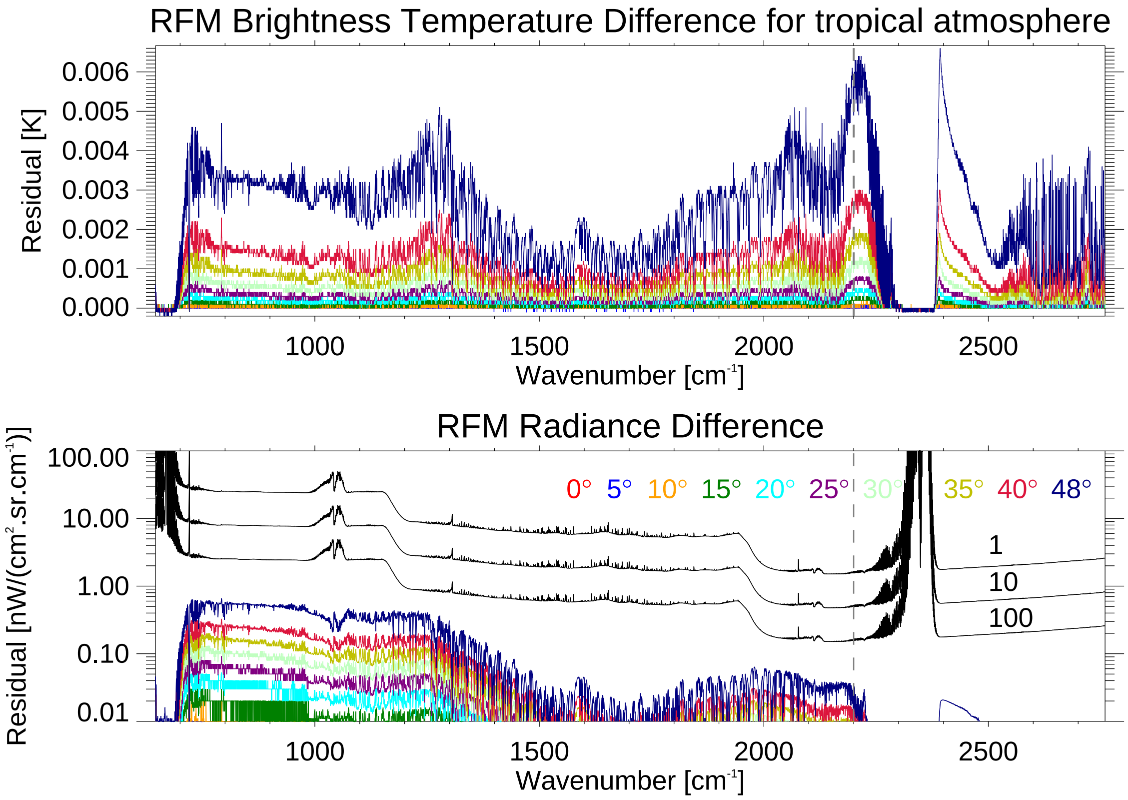

Figure 5.8: The residual from ignoring refraction effects at increasing viewing angles.

5.1.3 Plane-parallel approximation

Assuming a plane parallel atmosphere allows several simplifications to be made. The atmosphere is modelled as a set of flat and parallel layers, with any curvature due to the Earth's surface being ignored. This enables the use of analytical expressions for Curtis-Godson path parameters, whereas these must be numerically integrated for paths through a curved atmosphere. The geometry for a curved atmosphere and a plane parallel atmosphere can be seen in figures 5.9a and 5.9b respectively. At viewing angles, θ, close to zero the Earth's surface will appear approximately flat and the viewing angle equals the zenith angle, ϕ.

The approximation of ignoring the Earth's curvature can be examined by running the RFM in the limb viewing mode as above, where the off-nadir viewing angles can be defined by the elevation angle and the observing altitude, and comparing to the pure nadir function. In the nadir mode, viewing angles are specified as an air mass factor, which relates the slant path to the vertical view by secθ, where θ is the satellite zenith angle. In the plane parallel atmosphere this is the same as nadir viewing angle.

Table 5.3: Impact of the plane parallel approximation using both the scan angle, θ, and the zenith angle, ϕ. The table shows the maximum spectral residual expressed as an error parameter and its spectral location.

Tropical atmosphere				
Viewing angle	ξ_θ	$\nu_\theta(\xi_{max})$	ξ_ϕ	$\nu_\phi(\xi_{max})$
0°	0.018	1214.00	0.018	1214.00
5°	0.156	1282.50	0.019	1213.75
10°	0.610	1282.25	0.020	1213.75
15°	1.406	1282.25	0.022	1223.25
20°	2.614	1276.00	0.030	1230.00
25°	4.353	1276.00	0.050	1276.00
30°	6.801	1276.00	0.080	1298.25
35°	10.250	1276.00	0.127	1298.25
40°	15.202	1276.00	0.200	1298.25
48°	28.899	1276.00	0.432	1276.00

Figure 5.10 shows the difference between the limb viewing mode calculations and the nadir viewing mode and table 5.3 shows the error parameter for each case, where it can be seen that once the viewing angle is greater than 15 ° the residuals become larger than the weighted IASI noise.

An improvement to this approximation can be made with an adjustment to the viewing angle that takes into account the curvature of the Earth. In the nadir mode the zenith angle used in the RFM calculations can be replaced with the angle

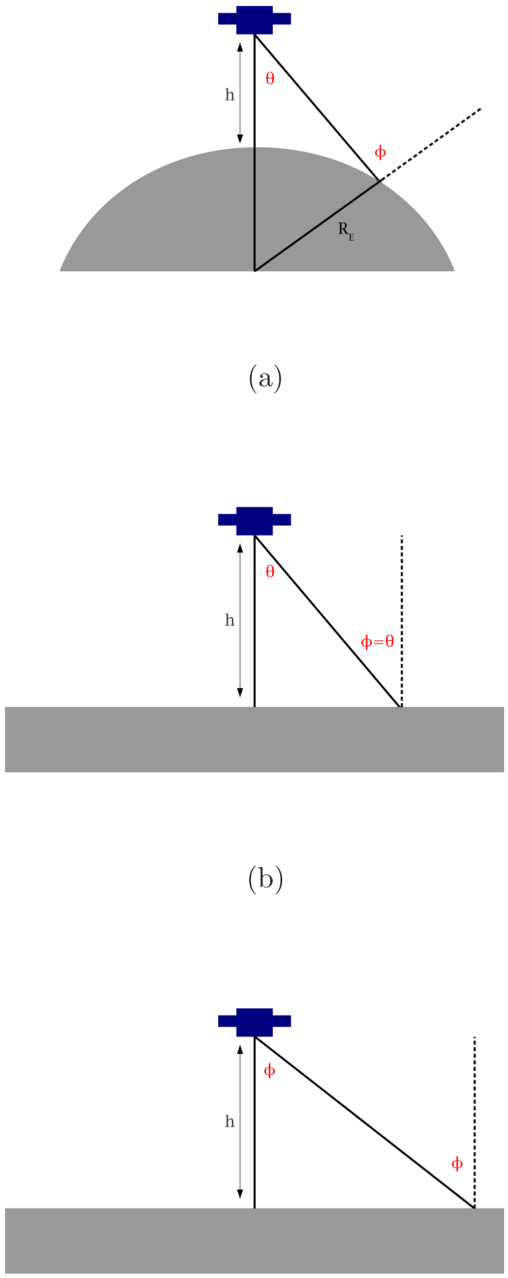

(a)

(b)

(c)

Figure 5.9: The geometry when (a) including the curvature of the Earth, (b) assuming a plane parallel atmosphere and (c) the improvement to the viewing angle in the plane parallel atmosphere that accounts for the Earth's curvature.

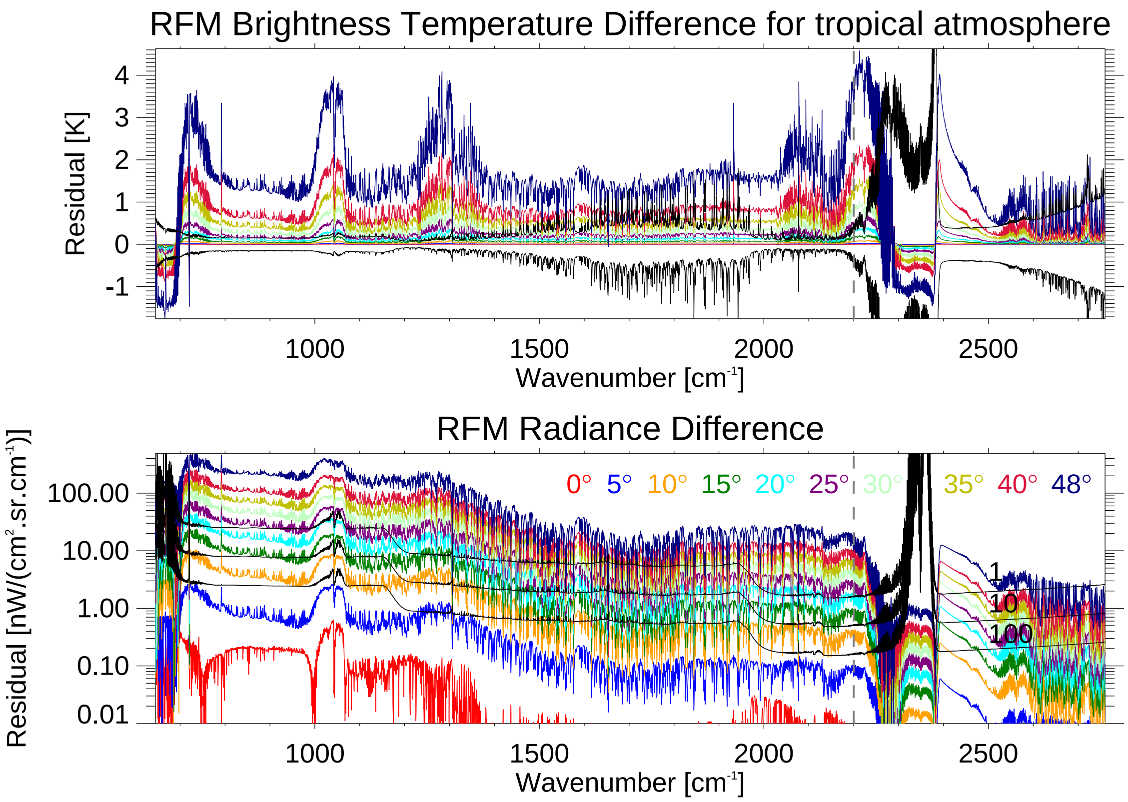

Figure 5.10: The residual from ignoring the curvature of the Earth at increasing viewing angles.

between the satellite and the ground when assuming a spherical Earth, the ground zenith angle ϕ. The geometry is shown in figure 5.9c. This increases the length of the slant path and hence the absorber amount within the path. Especially in the lower layers this causes the path to become much closer to that in the limb viewing mode. Applying the sine rule to the situation in figure 5.9a the ground zenith angle, ϕ, is given by

$$\sin\phi = \left(\frac{\mathrm{R_E} + h}{\mathrm{R_E}}\right)\sin\theta \tag{5.4}$$

where $\mathrm{R_E}$ is the radius of the Earth, h is the satellite altitude and the airmass factor for the nadir viewing mode is now given by $\sec\phi$.

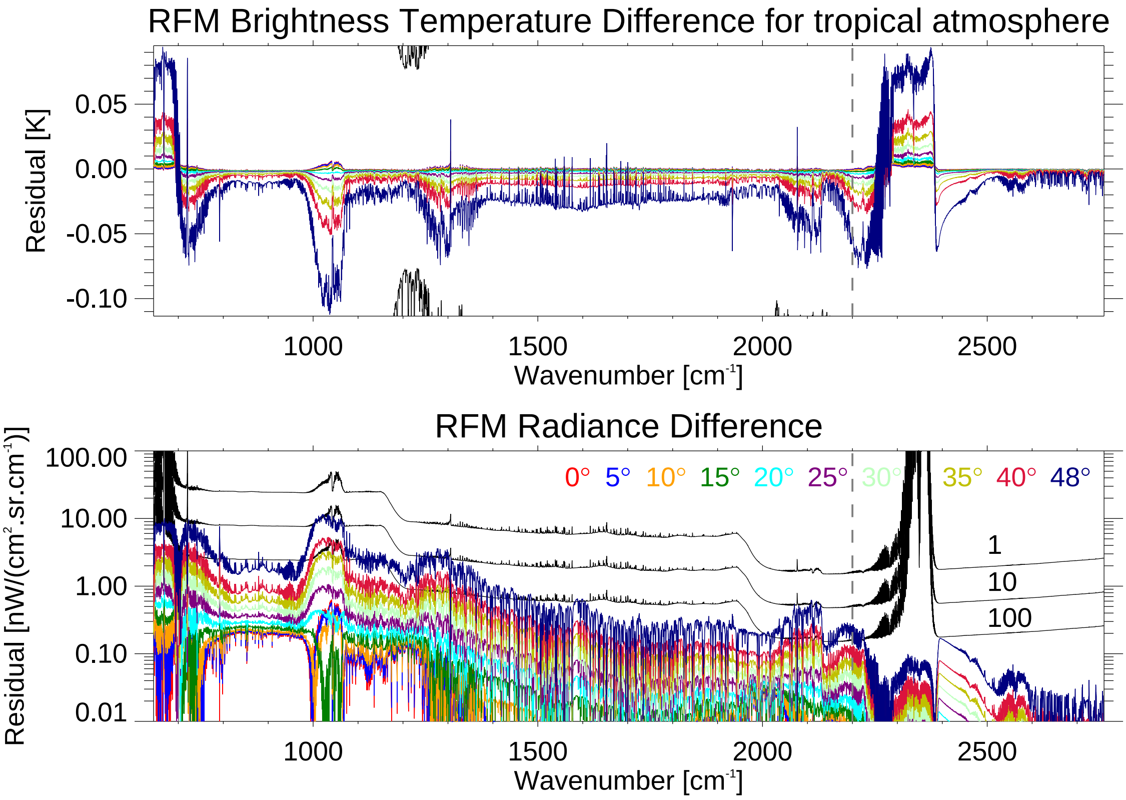

Figure 5.11: As figure 5.10 but considering the zenith angle, ϕ.

The improvement in the residuals from this correction is shown in figure 5.11. Using the ground zenith angle gives a large improvement to the accuracy of the nadir mode and reduces all the residuals to below the IASI noise with only the largest viewing angle now being greater than the NESR for 10 spectra. If using viewing angles greater than 10° the ground angle correction should be implemented.

5.2 Modelling the atmosphere

The user-specified altitude grid that the RFM uses has a large impact upon the computer processing time for each calculation; the coarser the grid the faster the code will run. This is due to having to calculate the absorption coefficients for each path segment, i.e one for each layer and each absorber as shown in equation 4.18. However creating a coarser vertical grid can have large implications on the accuracy of the spectral calculations; for example, the Curtis-Godson approximations for pressure and temperature within the layer will begin to break down the less homogeneous the layer is, as will the radiative transfer integral, whilst also, structural features such as the tropopause or stratopause may not be fully captured.

5.2.1 Top of atmosphere

Before examining how coarse a grid spacing is suitable, first it must be decided where the top level of the atmosphere (TOA) will be defined. Starting at 120 km, the TOA is decreased in 10 km steps and figure 5.12 shows the residuals compared to an atmosphere with TOA of 120 km, which is assumed to have errors well below the IASI noise.

Table 5.4: Impact of reducing the altitude of the top of the atmosphere. The table shows the maximum spectral residual expressed as an error parameter and its spectral location.

Sub arctic summer atmosphere		
TOA height	ξ_{max}	$\nu(\xi_{max})$
50 km	1.598	720.75
60 km	1.482	720.75
70 km	0.384	648.50
80 km	0.077	662.25
90 km	0.010	2176.25
100 km	0.013	2172.75
110 km	0.013	2172.75

As expected, the spectral regions most affected are those containing high-altitude

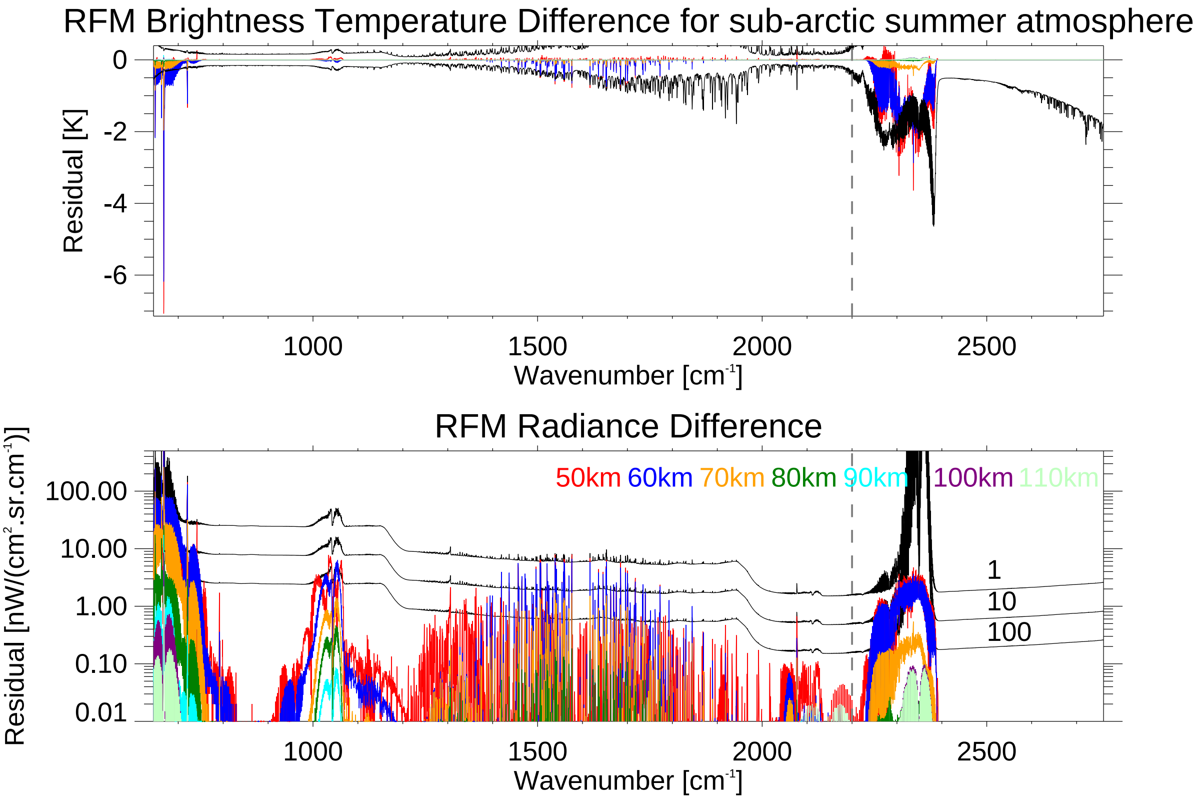

Figure 5.12: The residual due to reducing the altitude of the top of the atmosphere.

CO_2 and O_3 features. The effect of reducing the TOA can be seen in figure 5.12 for the worst atmospheric case of sub arctic winter, which is the coldest of the atmospheres at the mesopause. Reducing the top of the atmosphere to 70 km shows the residuals are almost entirely below the NESR for 1 spectrum except for the high peaking CO_2 lines. However these lie in optically thick regions and hence, as table 5.4 shows, the maximum error parameter lies below ξ_{NESR}. For the entire spectrum to be beneath the noise level for averaged spectra, and to ensure suitability should high altitude lines need to be reproduced and to include the mesopause, the atmosphere must extend upwards to 90 km where the residual lies below the NESR for 100 spectra, $\xi < \xi_{NESR\_100}$.

5.2.2 Stratospheric Vertical Grid

Due to the pressure dependence of Lorentz broadening (shown in equation 4.11) that is not present in Doppler broadening, the spectral line shape at low altitudes and higher pressures is dominated by Lorentz broadening, whereas at higher altitudes, Doppler broadening becomes the dominant process near the line centre. The vertical grid spacing must be fine enough to resolve these line features at their corresponding altitudes. However, working in pressure co-ordinates, equally spaced levels skew the atmosphere in favour of the troposphere and lower altitudes, with the stratosphere and mesosphere contained in just a few levels. Therefore the grid spacing will be considered in two parts; the lower atmosphere will consider equally spaced levels in pressure, and the upper atmosphere will consider equally spaced levels in log pressure, $\ln(p)$, in order to create a finer grid across the upper atmosphere and better resolve the temperature profile at those heights. To ensure a smooth transition between schemes, the altitude at which the grid spacing switches to $\ln(p)$ must be adjusted to where the spacing in pressure is approximately equal to the spacing in $\ln(p)$; this occurs at $\sim 10\,\text{mb}$.

Initially we consider the stratospheric vertical spacing. It is assumed that errors from an altitude grid where the pressure spacing in the lower atmosphere is 10 mb and the spacing in $\ln(p)$ in the upper atmosphere is 0.1 lie significantly below the IASI noise. The changes in altitude spacing are summarised in table 5.5, with the finest grid spacing having nearly 200 levels and the coarsest grid tested having only ~ 50. Maintaining a constant altitude grid in the lower atmosphere, we increase the spacing in $\ln(p)$ and adjust the altitude of the switch in grid spacings to ensure a smooth transition.

Table 5.5: The impact of varying the vertical grid spacings within the atmosphere between 1000–0.002 mb. The top half of the table shows the results for varying the spacing in the upper atmosphere, and the bottom half shows the results for varying the spacing in the lower atmosphere. The table shows the maximum spectral residual expressed as an error parameter and its spectral location. The number of levels, N, within different atmospheric regions is also shown: for the total atmosphere, the troposphere, the stratosphere and the mesosphere.

Δp [mb] (for $p \gtrsim$ 10mb)	$\Delta \ln(p)$ (for $p \lesssim$ 10mb)	N_{tot}	N_{trop} < 15 km	N_{strat} 15–50 km	N_{mes} 50–90 km	ξ_{max}	$\nu(\xi_{max})$
10	0.1	199	139	43	17	N/A	N/A
10	0.2	147	116	22	9	0.022	1063.50
10	0.3	130	110	14	6	0.058	2108.25
10	0.4	122	108	10	5	0.095	2108.25
10	0.5	117	105	9	3	0.124	741.50
10	1.0	109	102	4	3	0.396	741.50
10	1.5	106	101	3	2	1.098	741.50
10	0.4	122	107	10	5	N/A	N/A
15	0.4	90	75	11	5	0.119	1340.25
20	0.4	74	59	11	5	0.289	1457.75
30	0.4	58	43	11	4	0.777	1340.25
40	0.4	50	35	11	4	1.342	1457.75
50	0.4	46	31	10	5	2.250	1457.75

The results can be seen in figure 5.13 and the associated error parameters are in the upper part of table 5.5. For the entire spectrum to be within the noise, and suitable for use with averaged spectra, the ln(p) spacing must be at most 0.4 ($\sim$ 2.5 km); in this case $\xi < \xi_{NESR\_100}$. The most adversely affected spectral regions are those containing high altitudes CO_2 and O_3 features: If working outside these bands, it would be possible to use an even coarser grid spacing.

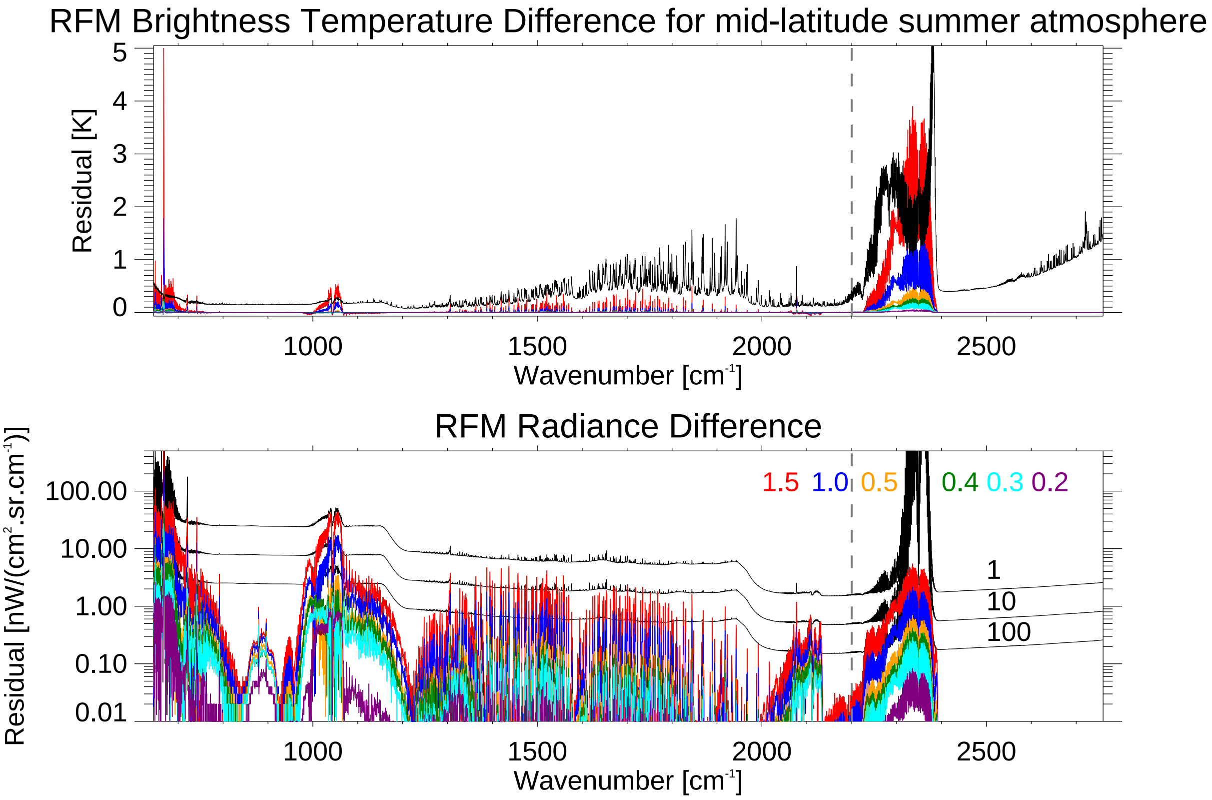
RFM Brightness Temperature Difference for mid-latitude summer atmosphere

RFM Radiance Difference

Figure 5.13: The residual from increasing the grid spacing in $\ln(p)$.

5.2.3 Tropospheric vertical grid

Having fixed the maximum spacing in $\ln(p)$ to 0.4, the pressure spacing in the lower atmosphere is varied. Again, to ensure a smooth transition between schemes, the altitude at which the grid spacing switches to $\ln(p)$ must be adjust to where the spacing in pressure is approximately equal to the spacing in $\ln(p)$, i.e. where $\ln(\Delta p) \sim \Delta \ln(p) = 0.4$. Again the pressure intervals can be seen in table 5.5.

Figure 5.14 shows the residual from varying the pressure spacing in the lower atmosphere and the error parameters are in table 5.5. The most important part of the spectrum when looking at the lower atmosphere is the water vapour ν_2 band, between 1200–2000 cm^{-1}, as this is the dominant tropospheric absorber. In order

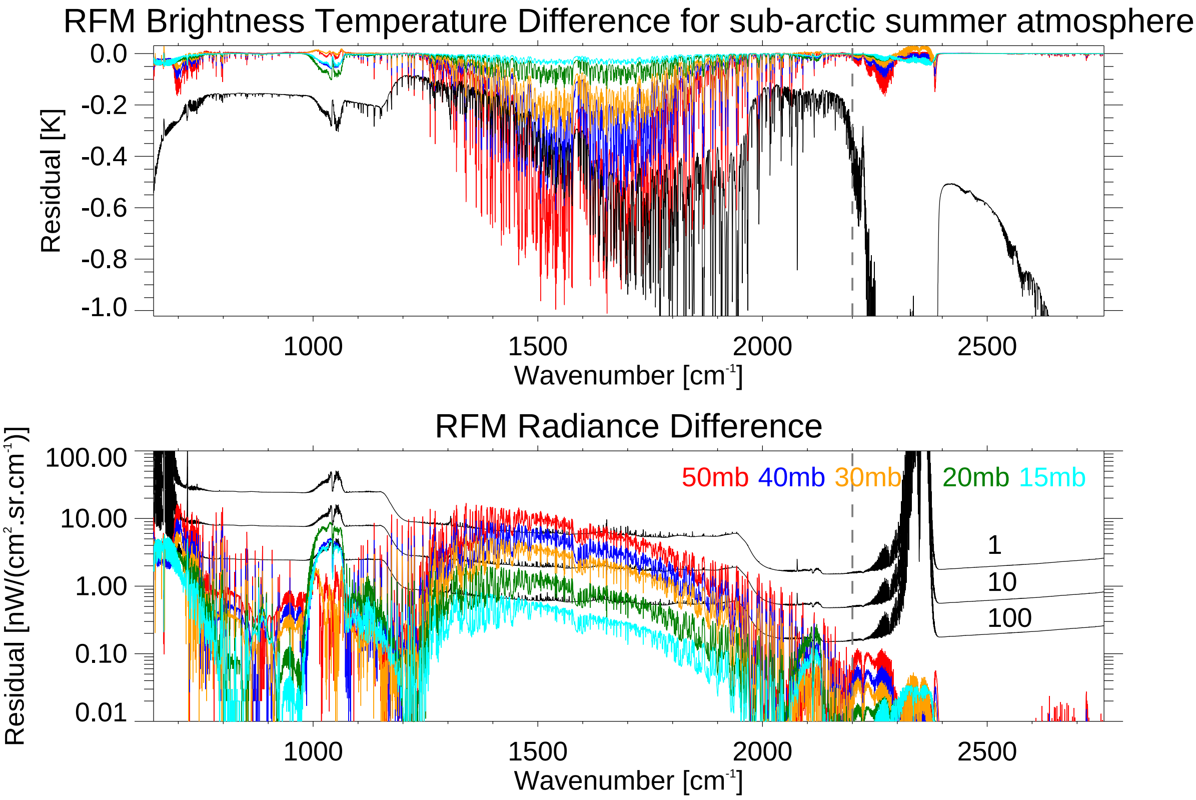

Figure 5.14: The residual due to increasing the grid spacing in pressure.

for this part of the spectrum to be entirely below the IASI noise the spacing must be no coarser than 30 mb and in fact at this spacing the majority of the spectrum is below the NESR for 10 spectra. However, if averaging of data is required a finer grid must be used.

It can be seen in the ozone band that the coarser grids produce smaller errors than the finer grids. However, this is due to the point in the atmosphere at which the change to $\ln(p)$ spacing occurs: at the coarser pressure spacings this is lower in the atmosphere and hence, there is a finer grid covering the higher altitude region where these ozone lines occur.

It is advised that any altitude grid used to reproduce IASI spectra should have an altitude grid with spacing no coarser than 30 mb in the lower atmosphere and no coarser than 0.4 in $\ln(p)$ in the upper atmosphere.

5.2.4 Comparison to standard altitude grids

Having decided upon the coarsest altitude grid that still lies within the IASI noise for a single spectrum (from this point known as the 'optimum grid') it is interesting to compare this to altitude grids commonly used in other retrievals and radiative transfer modelling. The altitude grids considered are:

- the US standard atmosphere of 50 levels starting from 1013 mb
- the Met Office 1dVar v3.3 retrieval grid of 43 starting from 1013 mb
- the RTTOV-9 IASI coefficients altitude grid of 101 levels starting from 1100 mb

The pressure spacings for these altitude grids are shown in figure 5.15 along with the pressure spacings for the 'high resolution' grid used as the baseline in the previous section for which it was assumed that errors due to this altitude grid lie significantly below the IASI noise.

The residuals from comparisons of these grid spacings to the high resolution grid are shown in figure 5.16 and the error parameters are shown in table 5.6. Within the water vapour ν_2 absorption band, between 1300–2000 cm^{-1}, the RTTOV grid produces the smallest residual due to its finer spacing within the troposphere, whereas the residual from the U.S Standard atmosphere, which is fairly coarse in the region of largest water vapour absorption, is well above ξ_{NESR}.

However, in the 'window' regions, the RTTOV grid shows large residuals and the shape indicates that it does not appear to be fully capturing the water vapour

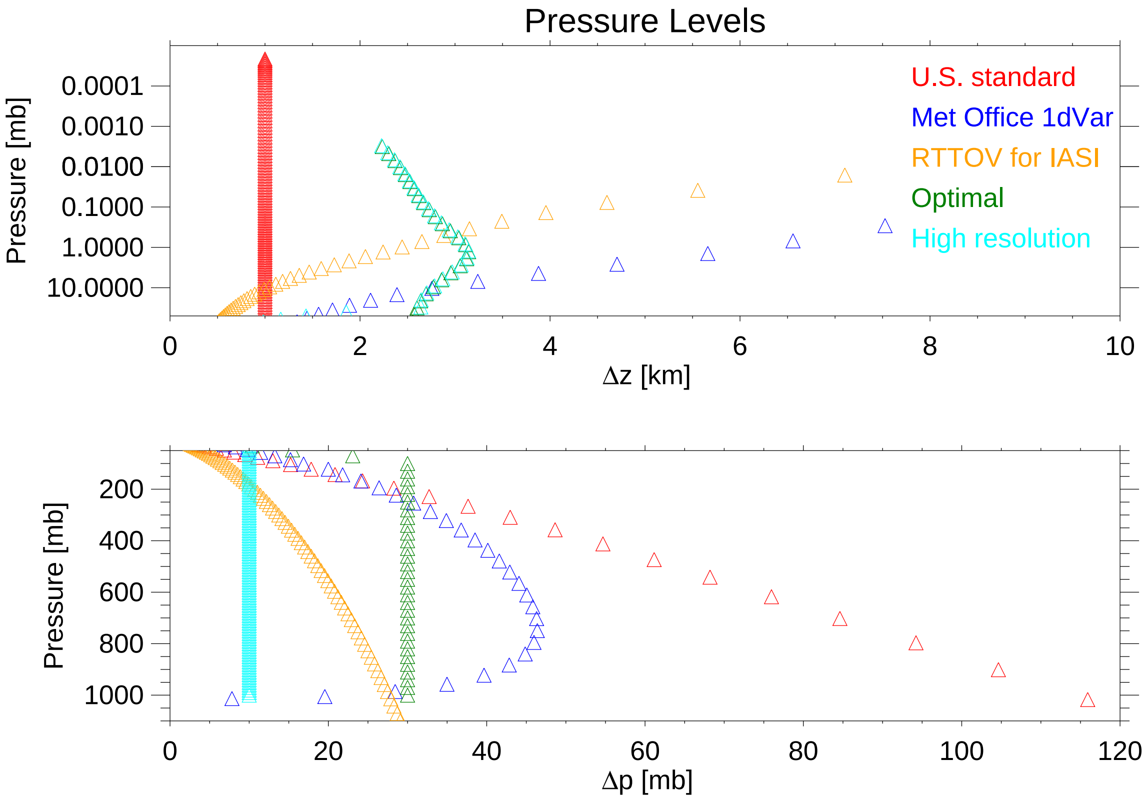

Figure 5.15: The altitude spacings for the US Standard atmosphere, the Met Office 1d Var pressure grid, the RTTOV IASI coefficients pressure grid, and the 'optimum' and 'high resolution' grids established in the previous section. The top panel shows the altitude spacing in the upper atmosphere and the bottom panel shows the altitude spacing in the lower atmosphere.

continuum (discussed in more detail in section 5.3.5). The example shown is for the tropical and most humid atmosphere; when looking at the sub arctic winter atmosphere, the driest atmosphere, the residuals across the entire spectrum are much reduced, almost all grids are completely below the noise value. In table 5.6 the difference in ξ between the two atmospheres can be observed, with all altitude grids able to more accurately reproduce the spectrum, the largest improvement being to RTTOV.

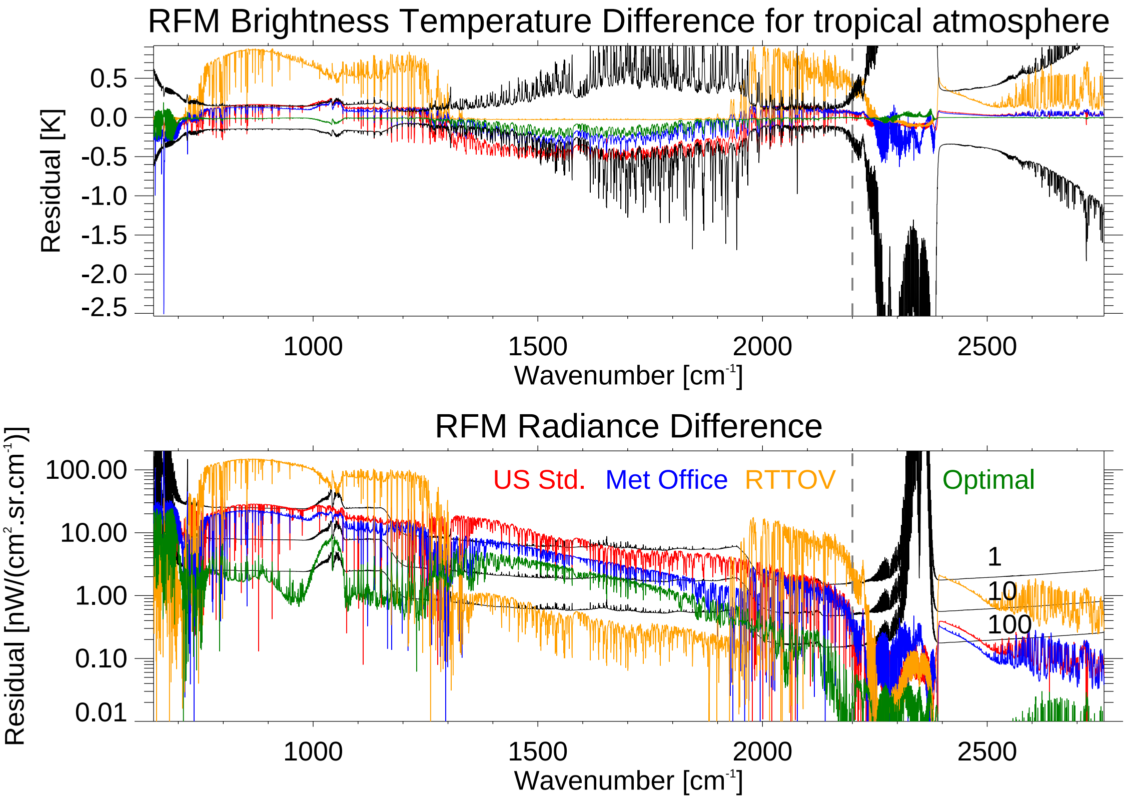

Figure 5.16: The residuals from comparisons of standard altitude grids to the high resolution grid.

In summary, if using the water vapour band then the RTTOV altitude grid would be the best choice, however, outside of this band the Met Office 1dVar v3.3 grid produces results with the lowest residuals (apart from the ‘optimum’ case’) and therefore would be the best choice.

Table 5.6: Impact of different standard altitude grids. The table shows the maximum spectral residual expressed as an error parameter and its spectral location.

Tropical atmosphere		
Altitude grid	ξ_{max}	$\nu(\xi_{max})$
U.S Standard	2.635	1212.50
Met Office 1dVar v3.3	1.699	1213.75
RTTOV–9	10.904	1214.00
Ideal	0.750	1340.25
Sub arctic winter atmosphere		
U.S Standard	1.435	1395.25
Met Office 1dVar v3.3	0.570	1395.00
RTTOV–9	2.668	1353.75
Ideal	0.300	1395.00

5.2.5 'Linear in tau' approximation

By default the RFM assumes that the radiance emitted from an atmospheric layer, at each spectral point, is calculated from an absorption weighted Curtis-Godson emission temperature from all molecules given by

$$\mathrm{T_b}(\nu) = \frac{\sum \mathrm{T}^i_{CG}\chi^i(\nu)}{\sum \chi^i(\nu)} \tag{5.5}$$

where $\chi^i(\nu)$ is the optical thickness of absorber i within the layer and $\mathrm{T_{CG}}$ is the Curtis-Godson temperature as derived in equation 4.9. Whilst this method is valid for homogeneous optically thin layers, in regions of high absorption (optically thick layers) the radiance will tend towards the Planck function of the top of the layer. A method that can be used to adjust for this is the 'linear in τ' approximation described by Clough et al. (1992). This assumes that, for a constant absorption coefficient within the layer, both the Planck function, B, and optical depth, χ, vary

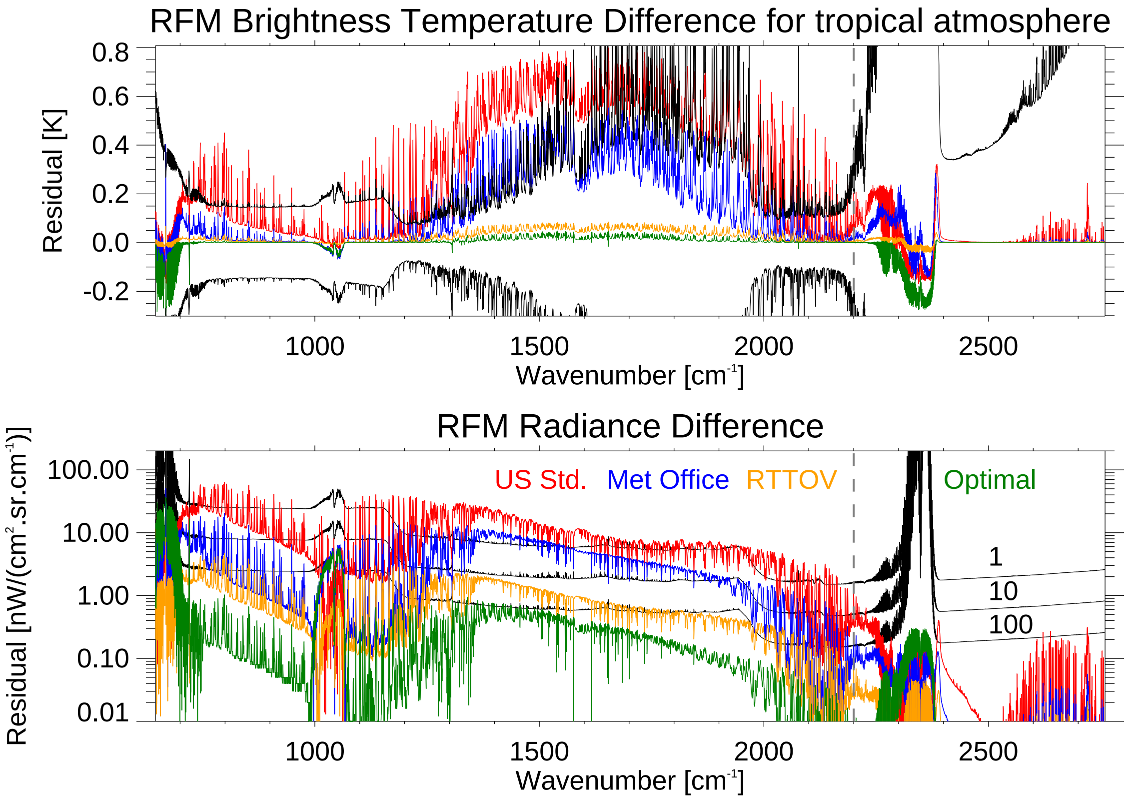

Figure 5.17: The residual from including the ‘linear in τ’ approximation for different altitude grids.

linearly with distance between the top and bottom of the layer.

The contribution from each layer to the total radiance, ΔL, is given by

$$\Delta L = \int_{\text{layer}} B \, d\tau = \tau_0 B_{\text{eff}} \Delta\tau \tag{5.6}$$

where τ is the transmittance from the satellite, τ_0 is the transmittance from the satellite to the ‘near’ boundary of the layer, $\Delta\tau$ is the transmittance across the layer and B_{eff} is an appropriate Planck function for the layer. Making the assumption that B $\propto \ln \tau$, the Planck function can be expressed in terms of optical depth as

$$B = B_0 + \frac{\Delta B}{\chi_1}\chi \tag{5.7}$$

where the subscripts 0 and 1 refer to the 'near' and 'far' boundaries of the layer respectively, $\Delta B = B_1 - B_0$, and χ is the monochromatic optical depth of the layer ($\chi_0 = 0$). The contribution to radiance can now be written as

$$\Delta L = \tau_0 \int_0^{\chi_1} (B_0 + \frac{\Delta B}{\chi_1}\chi) e^{-\chi} \, d\chi \tag{5.8}$$

and integrated to become

$$\frac{\Delta L}{\tau_0} = B_0 \Delta\tau + \Delta B \Delta\tau \left(1 + \frac{1}{\chi_1} - \frac{1}{\Delta\tau}\right) \tag{5.9}$$

where $\Delta\tau = 1 - \exp(-\chi)$.

As Clough et al. (1992) show, this assumption allows an effective Planck function, B_{eff},to be defined as

$$B_{\text{eff}} = \frac{\Delta L}{\tau_0 \Delta\tau} = B_0 + \Delta B \left(1 + \frac{1}{\chi_1} - \frac{1}{\Delta\tau}\right) \tag{5.10}$$

This effective Planck function now tends towards the appropriate regime in each optical limit: $\lim_{\chi\to\infty} B_{\text{eff}} = B_0$ (optically thick) and $\lim_{\chi\to 0} B_{\text{eff}} = \bar{B} = \frac{1}{2}(B_0 + B_1)$ (optically thin). Clough et al. (1992) suggest that a preferred definition for the mean Planck function for the layer, $\bar{B}$, is given using the Curtis-Godson equivalent Planck function and, hence,

$$B_{\text{eff}} = B_0 + 2(B_{CG} - B_0)\left(1 + \frac{1}{\chi_1} - \frac{1}{\Delta\tau}\right). \tag{5.11}$$

Table 5.7: Impact of the 'linear in τ' approximation. The table shows the maximum spectral residual expressed as an error parameter and its spectral location.

Tropical atmosphere		
Altitude Grid	ξ_{max}	$\nu(\xi_{max})$
U.S standard	4.179	1212.75
Met Office 1dVar v3.3	1.728	1339.25
RTTOV	0.311	1212.25
Optimal	0.187	720.75

This treatment of the Planck function can be enabled in the RFM and the difference between the two methods for the altitude grids tested in section 5.2.4 are shown in figure 5.17; for optically thin layers, the two methods converge and the 'linear in τ' method will have only a small effect. It can be seen that across the strongly absorbing parts of the spectrum, mainly the water vapour band and influence of the water vapour continuum, the introduction of the flag has a large effect. However, the effect appears proportional to the altitude spacing in the troposphere. As was shown earlier, the RTTOV grid and the 'optimal' grid are finely spaced within the troposphere and hence the layers are more homogeneous and the approximation has a small impact; the ξ values, shown in table 5.7, are both below ξ_{NESR10}. However, the Met Office 1dVar v3.3 and U.S standard atmosphere grids have much coarser spacing in the lower atmosphere and in both cases the residual is greater than the IASI noise in the water vapour band, with the U.S Standard the most adversely affected and with the largest ξ value. Therefore, if the troposphere is well sampled then the default RFM calculation will be suitable, but if the tropospheric sampling is sparse then using the ‘linear in τ’ method will reproduce the IASI spectrum more accurately.

5.3 Spectral Modelling

5.3.1 Spectral grid

To fully model the IASI spectrum, all spectral features, even those finer than the instrument resolution, must be well captured. In order to do this the model must be run at a sufficiently fine resolution before convolution with an ILS (instrument line shape) function. The RFM defaults to a 'Fine Mesh' calculation prior to the convolution with resolution $0.0005\,\mathrm{cm}^{-1}$. This default is based upon capturing the high altitude Doppler-broadened lines of width $\sim 0.001\,\mathrm{cm}^{-1}$ in its limb viewing mode. The RFM computation time is proportional to the number of fine grid points, hence the desire to use a coarser sampling, if possible.

Assuming that there is no spectral error introduced when using the default $0.0005\,\mathrm{cm}^{-1}$ resolution, figure 5.18 and table 5.8 show the effect of choosing coarser resolutions for the fine mesh. It can be seen that a grid spacing of $0.001\,\mathrm{cm}^{-1}$ is well below the noise for a single spectrum and is also below the noise level (and error parameter) for 100 spectra in all regions, hence its use elsewhere in this section. At a spacing of $0.003\,\mathrm{cm}^{-1}$ the differences are below the NESR (and in fact mostly below the NESR for 100 spectra) except in the spectral regions affected by high altitude CO_2 and O_3 lines around 700 and $1000\,\mathrm{cm}^{-1}$ respectively. At the larger grid spacings more lines begin to cause differences greater than the noise, therefore it is recommended that the coarsest grid to be used is $0.003\,\mathrm{cm}^{-1}$, unless using the CO_2 and O_3 bands, in which case $0.001\,\mathrm{cm}^{-1}$ should be used. Also, if using large numbers of averaged spectra a spacing of $0.001\,\mathrm{cm}^{-1}$ should always be used.

Table 5.8: Impact of varying spectral fine grid spacings. The table shows the maximum spectral residual expressed as an error parameter and its spectral location.

Tropical atmosphere		
Grid Spacing	ξ_{max}	$\nu(\xi_{max})$
$0.010\,\mathrm{cm}^{-1}$	4.809	999.50
$0.005\,\mathrm{cm}^{-1}$	1.154	705.00
$0.003\,\mathrm{cm}^{-1}$	0.691	718.50
$0.001\,\mathrm{cm}^{-1}$	0.029	2102.75

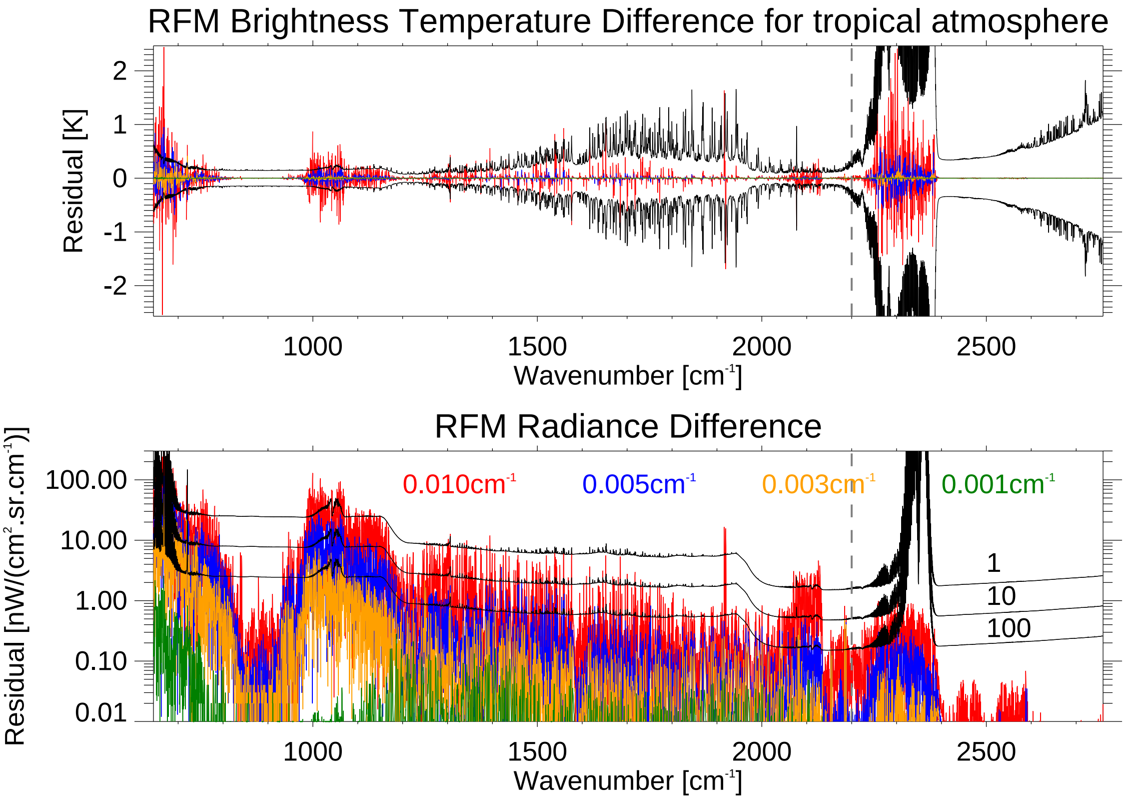

Figure 5.18: The residual from using varying fine grid spacings of 0.001, 0.003, 0.005, and $0.01\,\mathrm{cm}^{-1}$ compared to the RFM's default spacing of $0.0005\,\mathrm{cm}^{-1}$.

5.3.2 Instrument Line Shape

An instrument line shape (ILS) is essentially how the instrument responds to a δ-function spectral input; or rather, the function to describe how the instrument would convolve the input radiance spectrum. In an FTS the ILS is fundamentally determined by the finite optical path difference that causes a truncation of the interferogram. This transforms a δ-function in the real spectrum into a sinc function in the inversion of the truncated interferogram.

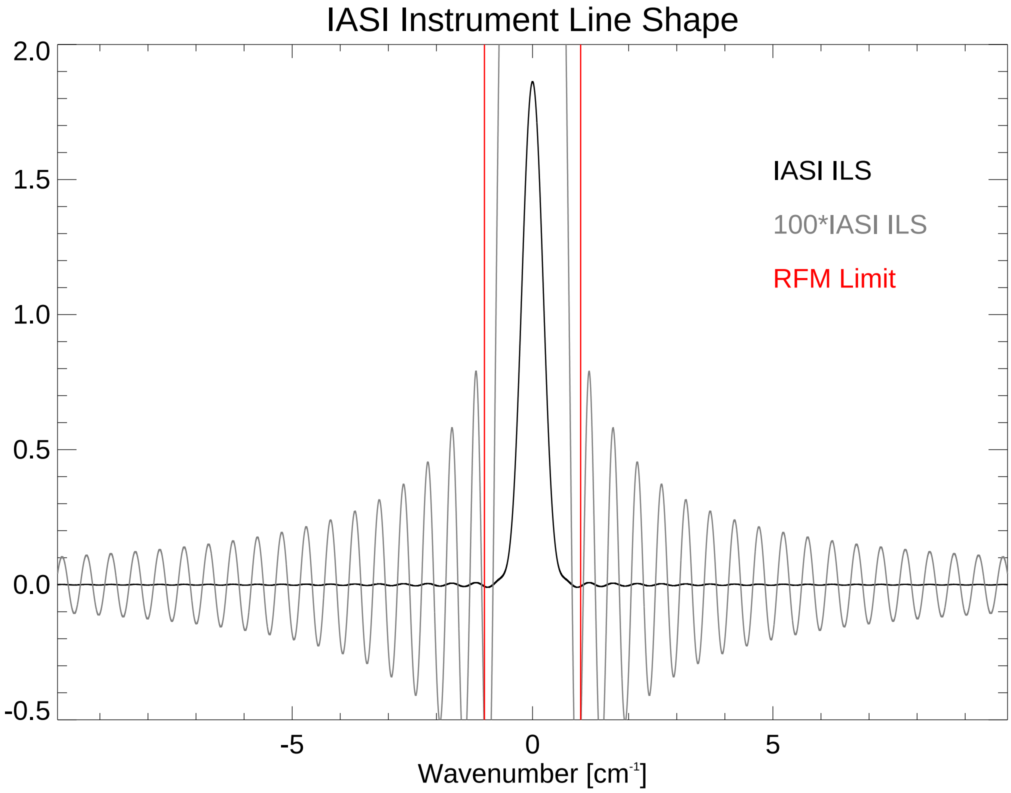

Figure 5.19: The apodised IASI ILS with the internal RFM ILS width limit. The IASI ILS is also shown magnified by 100 to emphasise the side lobes.

To aid spectral modelling, apodisation is a process applied to the interferogram to suppress side-lobes, caused by contributions from distant line features, by smoothly bringing the interferogram to zero at the extent of the sampled region. However, this is at the expense of broadening the central peak and therefore decreasing the spectral resolution. It also introduces noise correlations between neighbouring IASI channels.

The distributed apodised IASI instrument line shape is Gaussian in shape and $10\,\mathrm{cm}^{-1}$ wide as shown in figure 5.19. However, the RFM has limit of $1\,\mathrm{cm}^{-1}$ on the width of the internal ILS convolution. This is due to the widemesh calculation performed by the RFM $1\,\mathrm{cm}^{-1}$ intervals. The RFM only retains spectra from one previous widemesh interval for convolution, therefore allowing an ILS width of only ± 1 widemesh interval.

Truncating the IASI ILS to this width removes many of the side-lobe contributions (see figure 5.19) and may lead to modelling errors. This effect can be estimated by considering the first side lobe, which is $\sim 0.5\%$ the strength of the ILS peak, and comparing it to the IASI signal to noise. In Band A and the window regions, the signal to noise is very low and a reduction in line strength of $\sim 0.5\%$ would have a large impact on absorbing features. Meanwhile, in the strongly absorbing spectral regions (where the impact of an ILS truncation should have the most effect) the signal to noise is higher therefore the impact of eliminating the side-lobes is expected to be less drastic.

The effect of truncating the ILS in this way was examined by externally convolving the RFM output spectra with the ILS truncated at widths of $1, 2, 4, 6$, and $8\,\mathrm{cm}^{-1}$ and comparing to the convolution with the full width ILS. The importance of the ILS width can be seen in figure 5.20 and table 5.9 which show that the residual from a truncation to a width of $1\,\mathrm{cm}^{-1}$ is in fact below the IASI noise and is therefore acceptable to simulate an IASI spectrum. However, in some small regions of the spectrum, the effect of the truncation is larger than the NESR for 10 spectra and hence, if using these regions with averaged IASI spectra, the ILS width limit may not be suitable.

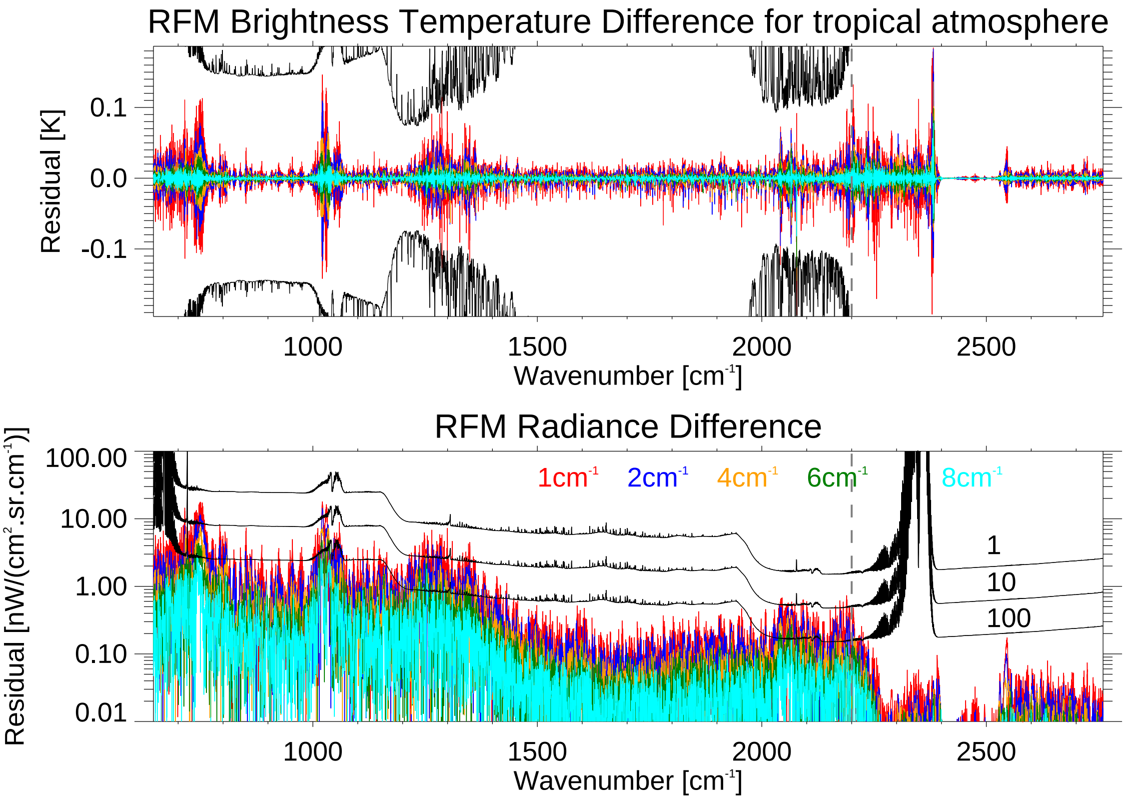

Figure 5.20: The residual between convolving the IASI spectra with the full 10 cm^{-1} wide Apodised Instrument Line Shape and truncated versions of the AILS.

Table 5.9: Impact of using truncated versions of the ILS. The table shows the maximum spectral residual expressed as an error parameter and its spectral location.

Tropical atmosphere		
ILS width	ξ_{max}	$\nu(\xi_{max})$
1 cm^{-1}	0.851	1299.75
2 cm^{-1}	0.496	1256.00
4 cm^{-1}	0.359	1252.00
6 cm^{-1}	0.255	1254.00
8 cm^{-1}	0.209	1254.00

5.3.3 Line Mixing

Line mixing accounts for the collisionally induced transitions between rotational states that occur when the Q-branch line structures overlap. Neglecting line mixing effects, the absorption coefficient is purely the sum of all contributing lines and it has long been known that ignoring line mixing can significantly reduce the accuracy of CO_2 (and CH_4) modelling; shown by Strow and Reuter (1988) and more recently by Hartmann et al. (2009). However, there are methods available to include the effect within radiative transfer models. The RFM currently includes the line-mixing coefficients proposed by Strow et al. (1994), which are calculated, using the Rosenkranz first-order approximation, for the CO_2 ν_2 and ν_3 bands. These coefficients concentrate on correcting the modelling of Q-branch line centres but work carried out by Niro et al. (2005) has produced an improved model suitable for isolated lines, P, Q, and R branches, troughs between transitions and wings. It is intended that this will soon be implemented within the RFM.

There is a significant increase in computation time on the inclusion of line mixing as complete bands must be included and not just local lines.

Figure 5.21 shows the spectral differences between including line mixing in the RFM and assuming no line mixing. Neglecting line mixing only affects the CO_2 ν_2 and ν_3 bands between 645–800 cm^{-1} and 1900–2100 cm^{-1} and in both cases the discrepancy is larger than the noise. As can be seen by the error parameter in table 5.10, ξ is much larger than 1, proving how important line mixing is in the CO_2 affected regions and therefore, if using these spectral regions line-mixing should be included.

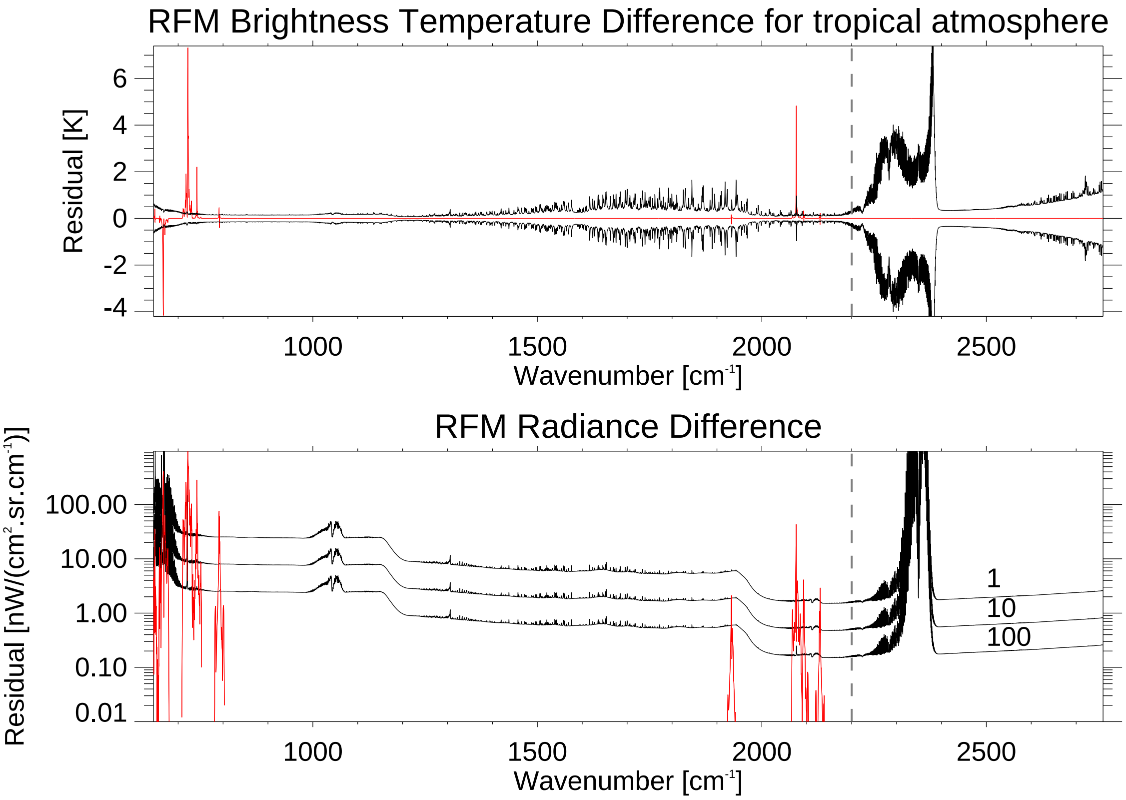

Figure 5.21: The residual error caused by neglecting the CO_2 line mixing effects within the IASI spectrum.

Table 5.10: Impact of including the effects of line mixing and shape. The table shows the maximum spectral residual expressed as an error parameter and its spectral location.

Tropical atmosphere		
Variable	ξ_{max}	ν
Line Mixing	34.412	721.75
Line Shape	4.691	692.75

5.3.4 Line Shape

The Voigt line shape is the default line shape assumed by the RFM for each molecule, unless the user specifies an alternative. As described in section 4.2.1, the Voigt line-shape is a convolution of the Lorentzian and Gaussian line-shape behaviour; however, this does not take into account the observed sub-Lorentzian behaviour in the line wings caused by the time-dependence of collisions. This is accounted for by including empirical correction functions known as χ-factors (Clarmann et al., 2003). Currently the RFM only provides the ability to apply the χ-factor correction to CO_2 and uses the method described by Doucen et al. (1985) and Cousin et al. (1985).

The effect of including the χ-factor for CO_2 can be seen in figure 5.22. The spectral regions most affected are between 645–800 cm^{-1} and 2000–2500 cm^{-1}, with the differences around 700 and 2400 cm^{-1} being well above the spectral noise. Although ξ, from table 5.10, is much less than the effect due to line mixing, it is still much larger than the IASI noise and hence, similarly to line-mixing if using the CO_2 affected ranges, it is necessary to include the χ-factor for CO_2.

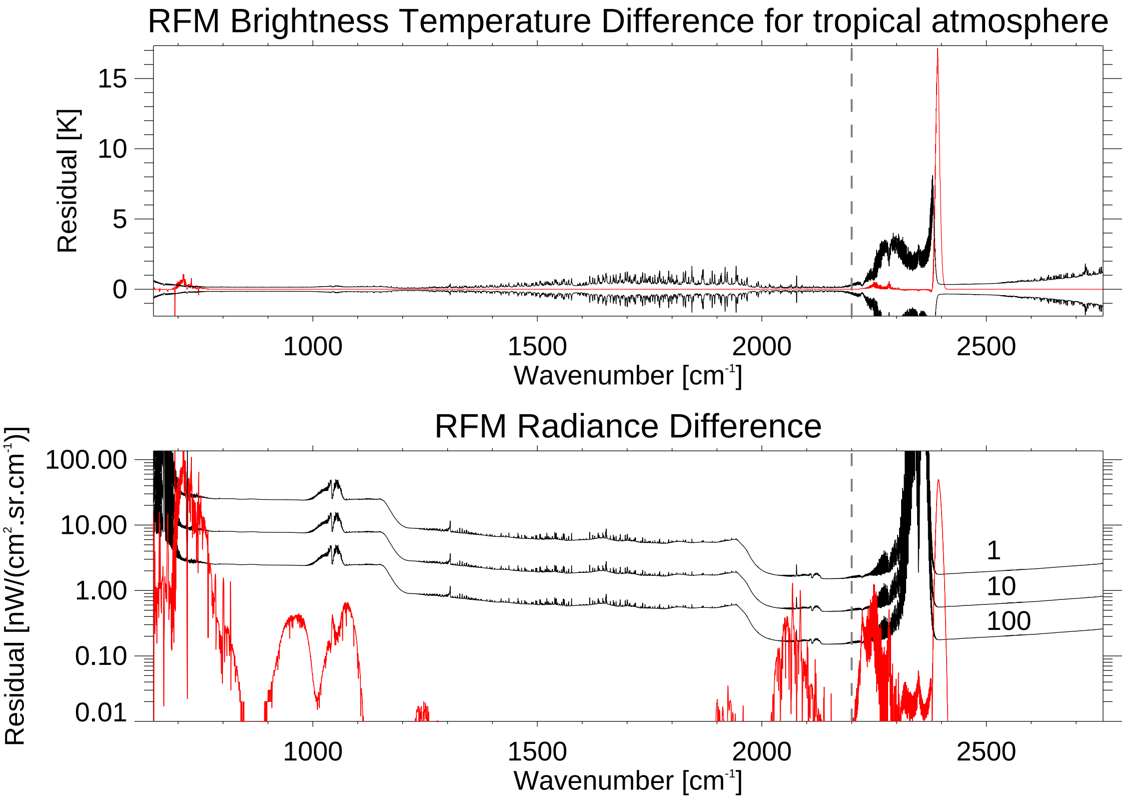

Figure 5.22: The residual error caused by neglecting the sub-Lorentzian effects in the CO_2 line shape and assuming the Voigt lineshape for all molecules.

5.3.5 Molecular Continua

The RFM is currently capable of including the continuum effects from four molecules: H_2O, CO_2, N_2, and O_2. Continuum absorption varies slowly with wavelength across the infrared spectral region and is far less well understood than individual molecular transitions. Especially in the case of water-vapour, it causes the window regions of the spectrum to be less transparent than expected. The MT_CKD_2.5 model maintained by Mlawer et al. (2012) is used to simulate the H_2O continuum and includes both a self broadening (H_2O-H_2O collisions) and a foreign broadened (H_2O-N_2 collisions) continuum model with contributions from two components: a collision-induced component and a line shape component. The N_2 continuum is computed using the model proposed by Lafferty et al. (1996) who measured collision-induced absorption by pure nitrogen near 4.3 μm (2325 cm^{-1}). Similarly, Thibault et al. (1997) measured the collision-induced absorption by O_2 near the 6.4 μm band (1563 cm^{-1}) that is included in the RFM. The effect due to neglecting each molecular continuum across the whole IASI spectrum can be seen in figure 5.23, with the error parameters in table 5.11. The largest difference is due to H_2O, which is significantly above the noise level throughout most of the spectrum and clearly, given its associated ξ, cannot be ignored during calculations using the RFM. The effects due to CO_2, N_2, and O_2 are slightly smaller. However, each causes discrepancies larger than the noise in certain bands and if using these regions should be enabled. Also shown is the difference between the current water-vapour continuum model and an older version, CKD 2.41; the large ξ value shows the need for continued improvements to the continuum models, but emphasises the fact that discrepancies between radiative transfer models could arise due to their handling of the water vapour continuum.

Table 5.11: Impact of neglecting the continua for the molecules H_2O, CO_2, N_2, and O_2. The table shows the maximum spectral residual expressed as an error parameter and its spectral location.

Tropical atmosphere			
Continuum	Model	ξ_{max}	$\nu(\xi_{max})$
H_2O	MT_CKD_2.5 (Mlawer et al., 2012)	58.224	1588.00
H_2O	MT_CKD_2.1 (Mlawer et al., 2012)	58.224	1588.00
H_2O	CKD 2.41 (Clough et al., 1989)	8.365	1234.50
CO_2		1.140	716.00
N_2	(Lafferty et al., 1996)	6.949	2192.00
O_2	(Thibault et al., 1997)	4.857	1588.00

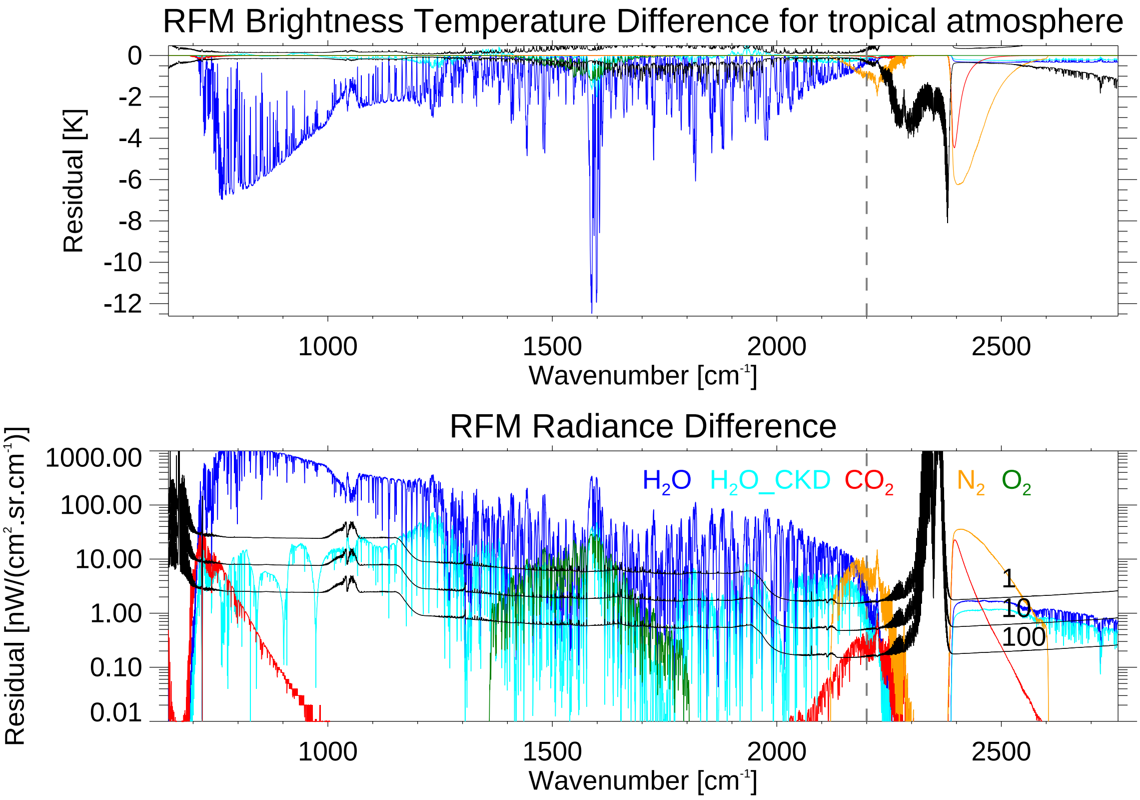

Figure 5.23: The residual caused by neglecting the continua for the molecules H_2O, CO_2, N_2, and O_2.

5.3.6 Non-LTE Effects

The usual treatment of the atmospheric radiative transfer is to assume that it is in local thermodynamic equilibrium (LTE). This assumption allows Kirchoff's Law to be applied to the equation of radiative transfer, as described in section 4.1, and the source function can be replaced by the Planck function at the local kinetic temperature. It is also assumed that this local temperature defines the absorption coefficient. Although the atmosphere is not in thermodynamic equilibrium as there is no closed system, i.e. net radiation can be lost or gained, at the higher pressures of the lower atmosphere it is an appropriate approximation. At high pressures,

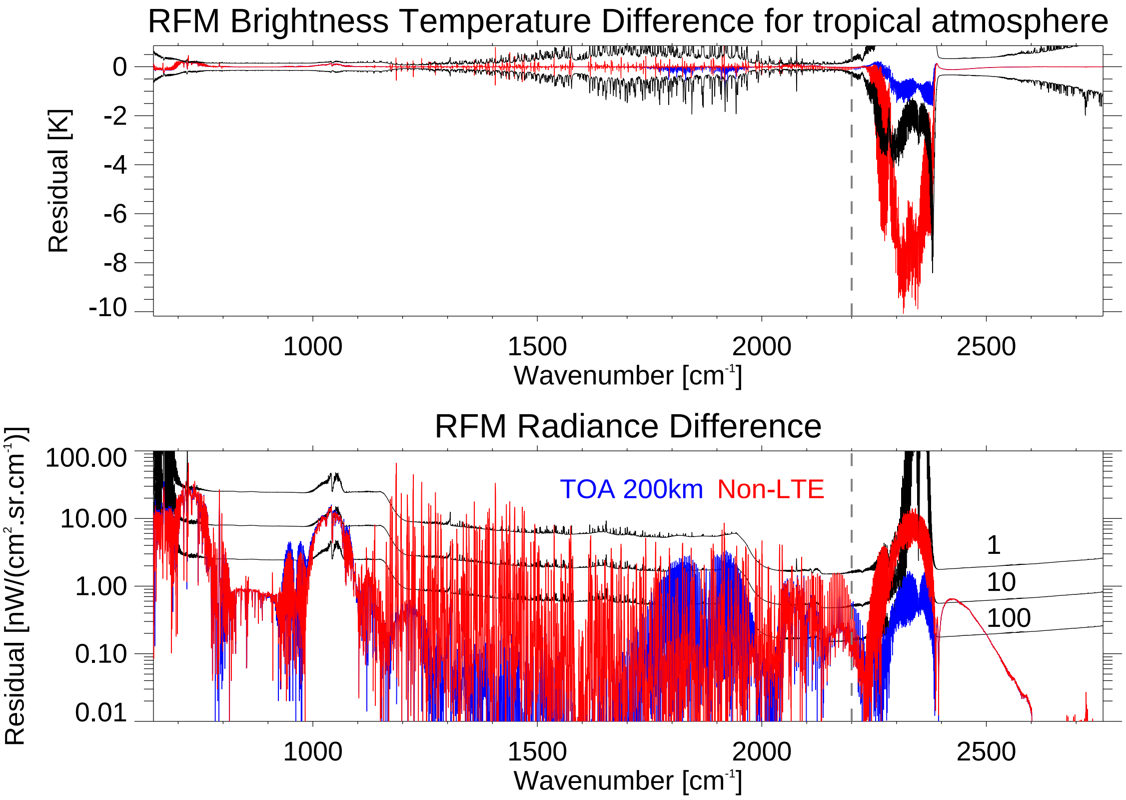

Figure 5.24: The residual caused by considering the addition of the Non-LTE effects for CH_4, CO_2, CO, H_2O, HCN, HNO_3, N_2O, NO_2, NO, and O_3, using the daytime values at 200 km.

the collision rates causing excitation and de-excitation between energy levels within a molecule can be high enough to dominate the radiative loss or gain and this is the assumed LTE situation. However, at higher altitudes, where the collision rate is lower and the probability of emission to space is higher, the absorption and emission rates begin to dominate and the LTE assumption breaks down in the vibrational molecular levels; the Boltzmann distribution is no longer valid.

The inclusion of a modified absorption coefficient and source function in the RFM that account for these non-LTE effects is described by Edwards et al. (1993). The modified quantities relate the general non-LTE situation to the equivalent LTE values by expressing the temperature in terms of user-supplied vibrational temperature profiles (which are both molecule and band specific). It should be noted that the supplied temperatures are 'typical' values and therefore specific to particular atmospheric states.

Table 5.12: Impact due to non-LTE effects. The table shows the maximum spectral residual expressed as an error parameter and its spectral location.

Tropical atmosphere		
Variable	ξ_{max}	$\nu(\xi_{max})$
Non-LTE	5.447	1185.75
TOA at 200 km	0.361	1034.00

The residual due to the inclusion of non-LTE effects for a tropical atmosphere is shown in figure 5.24. In order to fully capture the non-LTE effects the top of atmosphere (TOA) must be increased to a height of 200 km; therefore, to clarify which spectral features are purely non-LTE induced and not artifacts of the increased TOA, the residual due to the increased TOA is also plotted. It can be seen that the large residuals surrounding the O_3 band at 1000 cm^{-1} and CO_2 features around 700 cm^{-1} are caused by the increase in TOA and not due to the non-LTE inclusion. There is also a clear spectral signal from NO between 1800–2000 cm^{-1}, which does not appear in the non-LTE comparison, suggesting that the NO emission temperature is actually lower than the kinetic temperature assumed in the LTE case. The largest non-LTE induced residuals appear across the water vapour band and in the CO band at 2100 cm^{-1}, where they lie above the NESR. It can be seen that the effect of assuming LTE has a large impact, but including non-LTE effects can be impractical, therefore it is advised to screen out channels adversely affected by the LTE assumption.

5.4 Atmospheric Composition

Throughout this chapter, O_3, CO_2, CO, H_2O, N_2O, CH_4, NO_2, NH_3, C_2H_6, HCN, CFC–11, CFC–12, HCOOH, SO_2, HNO_3, NO, N_2, O_2, OCS, CCl4, and CF4 have been included in the atmosphere for each model run. Here, we examine the quality of profile information needed for each atmospheric absorber. In the following cases we have assumed that the six 'primary' absorbers (O_3, CO_2, CO, H_2O, N_2O, and CH_4) are all essential in recreating the IASI spectrum and therefore use this simplified atmosphere as a baseline, adding other species individually.

5.4.1 Atmospheric variability

When representing an atmospheric scene, the atmospheric profiles supplied to the RFM can come from many sources, for example a climatology or a forecast. However, the absorber concentrations are not constant across the globe and therefore a climatology may not capture the correct atmospheric information for the location in question. Assuming the simplified atmosphere, the impact of each of the primary absorbers $1\,\sigma$ climatological variability is tested and the residuals are shown in figure 5.25 for the U.S Standard atmosphere. The error parameters can also be seen in table 5.13. The $1\,\sigma$ variability for each absorber was calculated by Remedios et al. (2007).

It can be seen that the atmospheric variability of CO_2 lies entirely below the weighted NESR, and apart from the long wave CO_2 lines below ξ_{NESR_100}, and therefore a climatological profile would be adequate. Despite this, it should be noted that the $1\,\sigma$ variability of CO_2 is $\sim 1\%$ and it is known that the concentration of CO_2 increases by $\sim 0.5\%$ each year. Therefore, although a climatology would be suitable, after two years this would need to be updated to reflect present day conditions. In all other cases, most noticeably H_2O and O_3, the residuals lie well above the IASI noise and specific atmospheric profiles are necessary. In the case of H_2O, a climatology may be acceptable in the stratosphere but the variation in the troposphere is so great that it must be treated as a retrieval problem for most of the spectrum. It is not always feasible to obtain a location specific profile for each of these absorbers, nevertheless at least a more specific climatology should be used as opposed to only using the standard atmosphere.

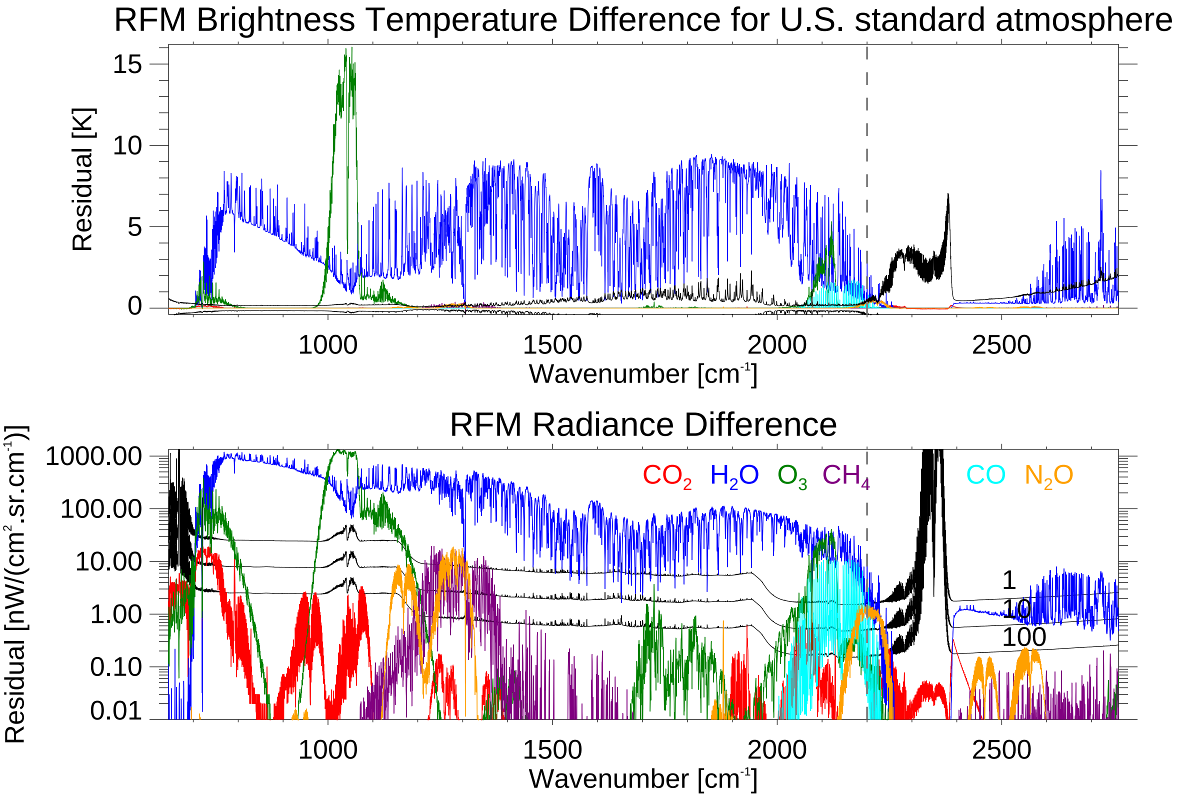

Figure 5.25: The residual caused by the 1σ atmospheric variability of the primary atmospheric absorbers; O_3, CO_2, CO, H_2O, N_2O, and CH_4.

Table 5.13: Impact of the 1σ variability of the primary atmospheric absorbers. The table shows the maximum spectral residual expressed as an error parameter and its spectral location.

U.S Standard atmosphere			
Absorber	1σ variability [%]	ξ_{max}	$\nu(\xi_{max})$
CO_2	1.0	0.721	733.75
H_2O	93.4	68.844	1325.00
O_3	74.8	40.242	1021.75
CH_4	3.9	2.176	1236.00
CO	36.4	7.543	2111.50
N_2O	3.34	2.270	1278.75

5.4.2 Trace Gases

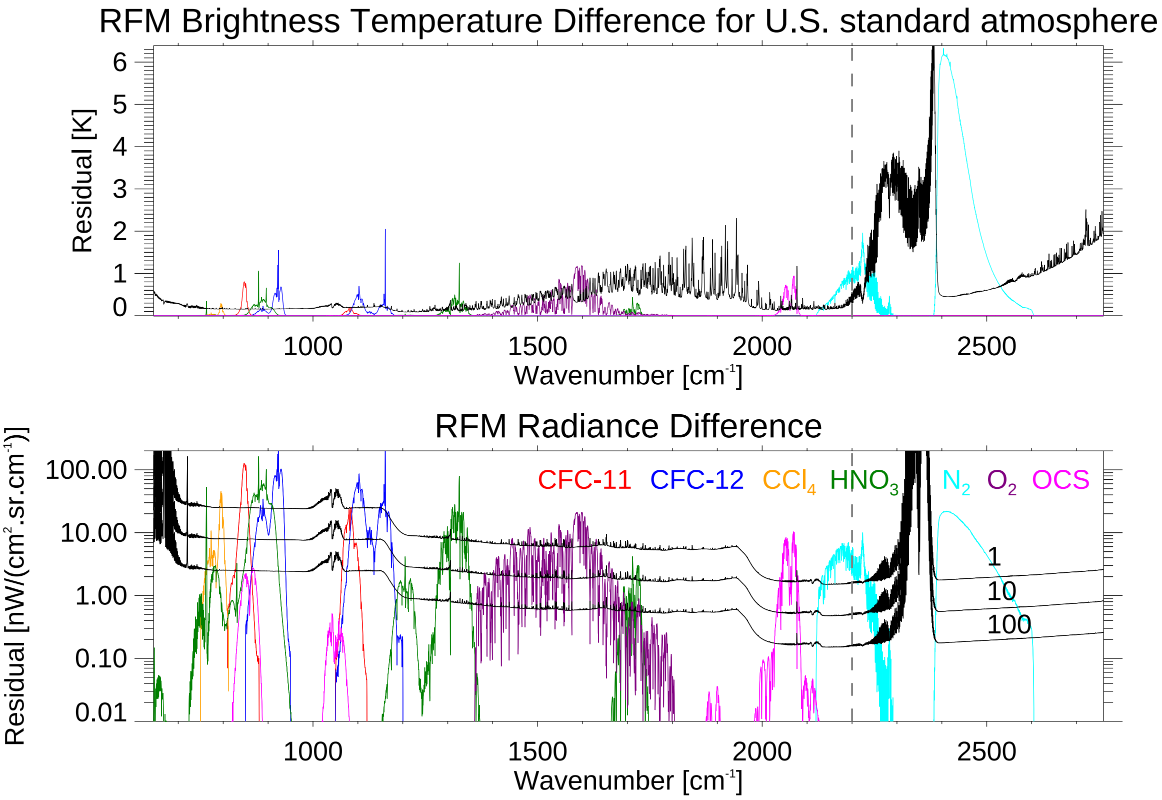

Figure 5.26: The atmospheric absorbers causing the largest residuals by their inclusion.

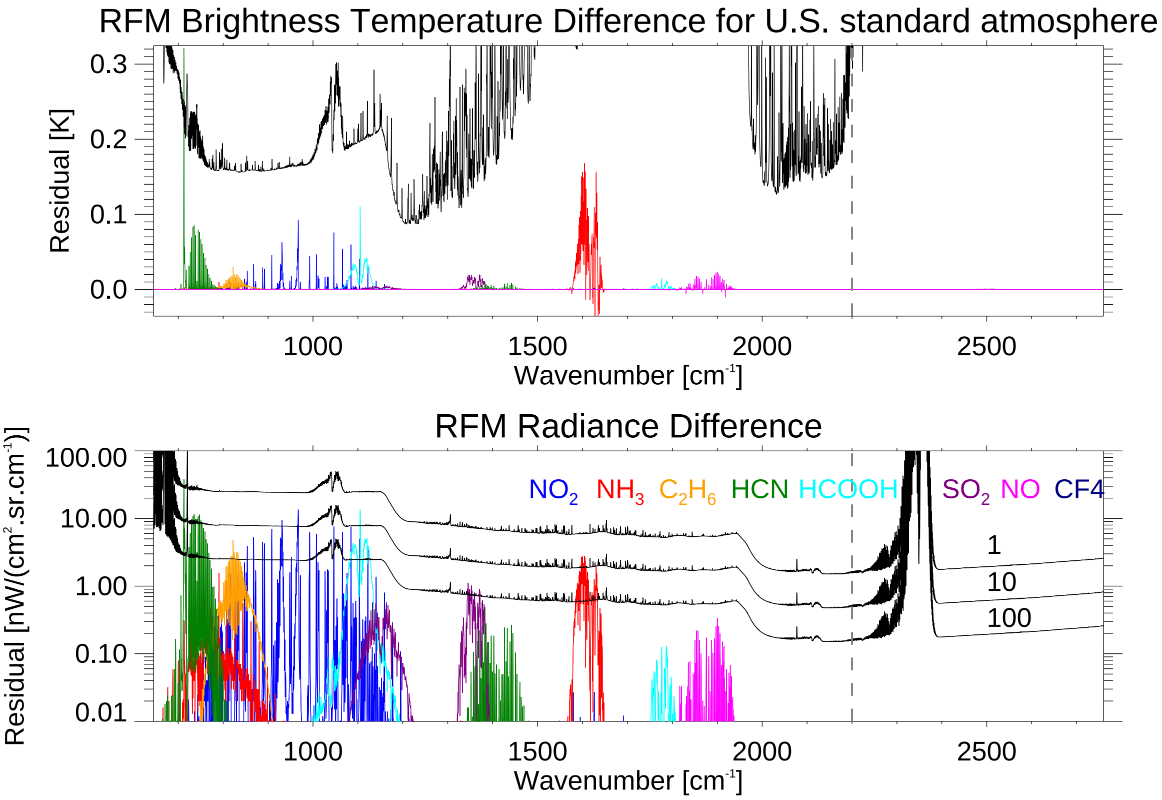

Figure 5.27: The atmospheric absorbers causing the smallest residuals by their inclusion.

Having assumed the use of 21 atmospheric absorbers throughout this chapter, here we ascertain whether each absorber is in fact needed or whether the net contribution of each gas lies below the IASI noise. The effect of adding each of the 'secondary' absorbers to the simplified atmosphere of only the six primary absorbers is examined.

Figure 5.26 shows the secondary absorbers that cause a residual larger than the IASI noise. Their associated error parameters, in table 5.14, are all significantly larger than ξ_{NESR} and hence should all be included in the assumed atmosphere in order to correctly replicate the atmospheric spectrum. The gases in figure 5.27 all

Table 5.14: Impact of excluding atmospheric absorbers. The table shows the maximum spectral residual expressed as an error parameter and its spectral location.

U.S Standard atmosphere		
Absorber	ξ_{max}	$\nu(\xi_{max})$
CFC-11	5.095	847.00
CFC-12	10.353	1161.00
CCl_4	1.800	795.00
HNO_3	10.338	1325.75
N_2	4.570	2192.00
O_2	3.564	1588.25
OCS	6.260	2069.75
NH_3	0.620	967.25
NO_2	0.704	1604.50
C_2H_6	0.307	822.25
HCN	0.572	712.50
HCOOH	0.597	1105.00
SO_2	0.122	1345.50
NO	0.114	1900.00

cause residuals smaller than the IASI noise and so could be excluded from RFM calculations if required. However, they do not all lie below the NESR for 10 spectra and therefore care should be taken when averaging spectra as the weaker absorbers may need to be included.

5.4.3 Enhanced absorbers

The ‘secondary’ absorbers with smaller residuals are those that are naturally found in small concentrations but many are often enhanced through either natural or anthropogenic causes: i.e. volcanic emissions, agricultural processes, biomass burning, and lightning. Therefore, the inclusion of these absorbers will depend upon the scene that needs to be reproduced and if the concentrations are larger, due to an enhancing event.

The standard atmospheric concentrations of NO_2 and HCN are compared to enhanced values provided for the CORSA study to judge the effect of the increased absorber amount. The enhancements for SO_2, provided by E. Carboni, are for several volcanic scenarios, representing ejections of either 10 DU (small plume) or 100 DU (large plume) into the troposphere or stratosphere. Each enhanced profile can be seen in figure 5.28 compared to the U.S standard atmospheric profile assumed throughout this chapter. The results can be seen in figure 5.29. Taking into account the error parameters, in table 5.15, the enhancements due to NO_2 and HCN are entirely below the NESR and therefore seem unlikely to be picked up when viewing a single spectrum. Despite the difficulty in observing HCN, recent work by Duflot et al. (2013) has shown the possibility for retrieving HCN column amounts through careful modelling of the overlapping CO_2 line features.

Meanwhile, in the case of SO_2, all enhancing events produce residuals above the IASI noise in both the ν_1 and ν_3 absorbing bands. Therefore, an enhancement in SO_2 should be detectable, even with only a single spectrum. There have been many studies into both detection and retrieval schemes for SO_2. Initially studies, such as that by Clarisse et al. (2008), were able to detect the presence of SO_2 enhancements using simple two-channel brightness temperature difference methods. These methods were improved upon by Walker et al. (2011) and have been extended to full retrieval schemes using either large parameter look-up tables (Clarisse et al., 2012) or a full optimal estimation framework (Carboni et al., 2012). In both cases the results from IASI have shown good agreement with retrievals from other instruments, such as GOME-2. Therefore, care should be taken in scenes that may be influenced by volcanic emissions and in these cases SO_2 must be included in the modelled atmosphere.

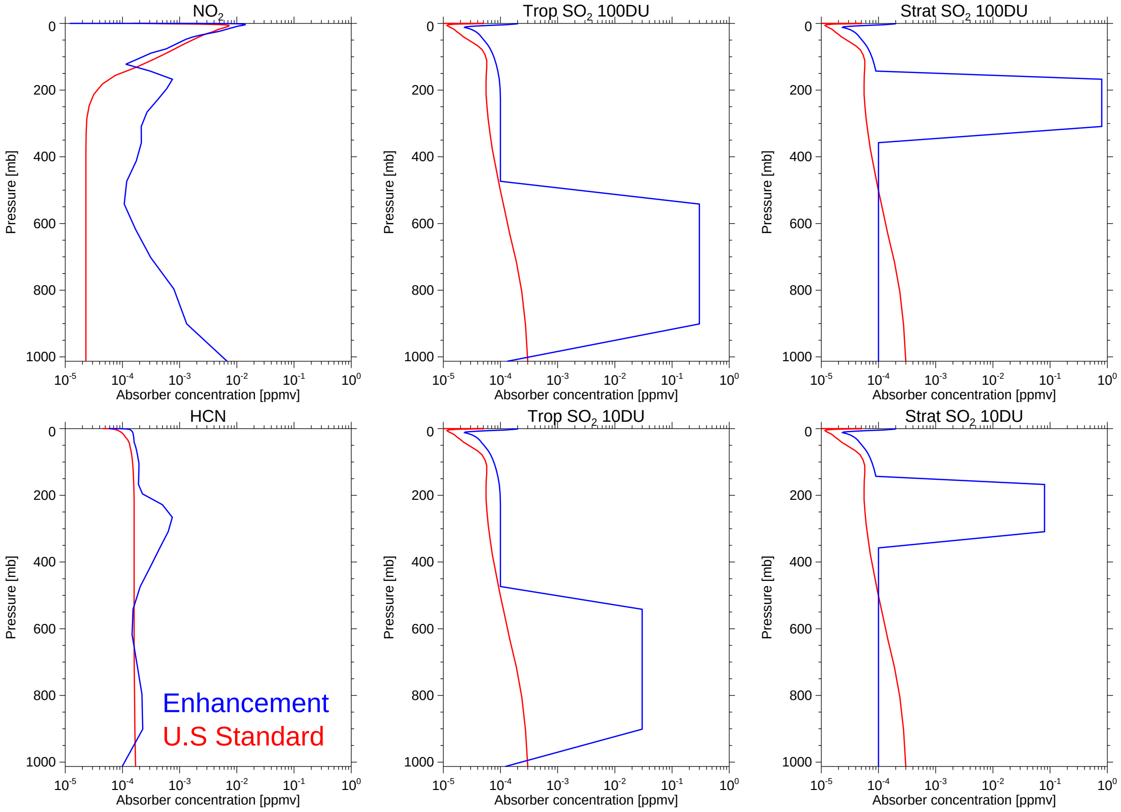

Figure 5.28: The U.S Standard and enhanced vertical profiles for each atmospheric absorber.

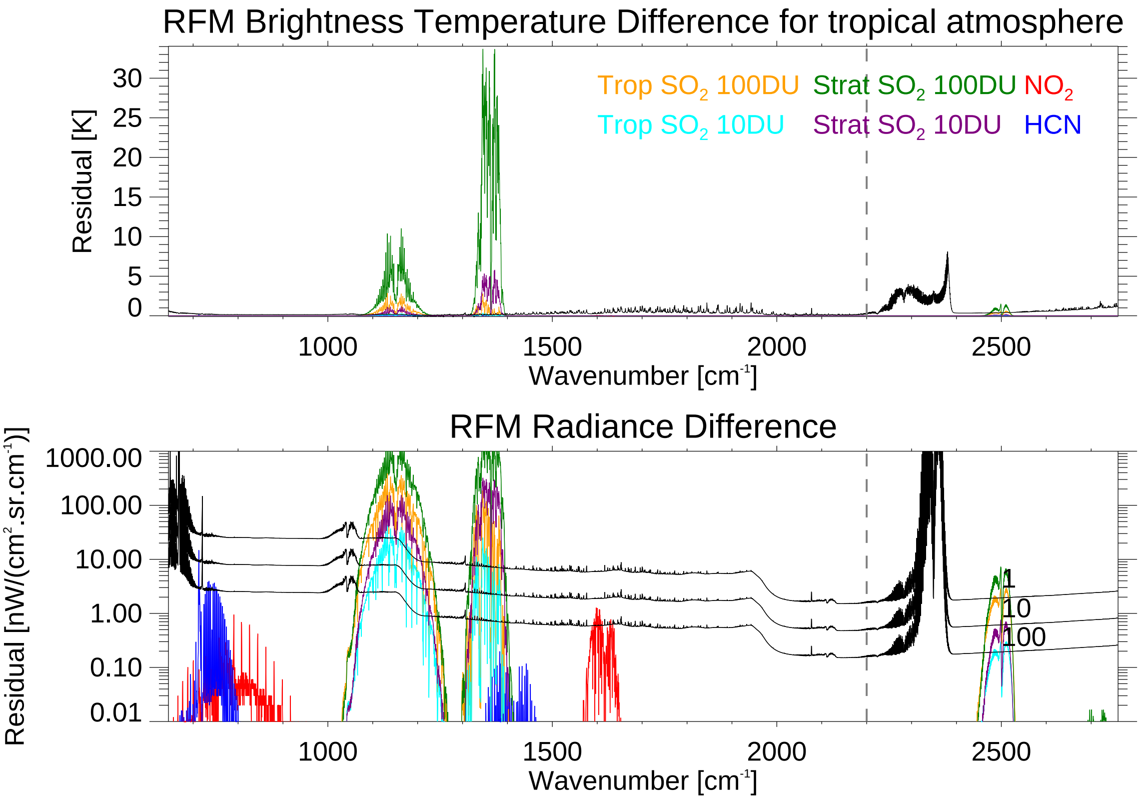

Figure 5.29: The residual caused by enhancements of atmospheric absorbers.

Table 5.15: Impact of enhancing atmospheric absorbers. The table shows the maximum spectral residual expressed as an error parameter and its spectral location.

Tropical atmosphere		
Enhancement	ξ_{max}	$\nu(\xi_{max})$
NO_2	0.213	1598.00
HCN	0.511	712.50
SO_2 - 100DU in troposphere	25.432	1345.25
SO_2 - 100DU in stratosphere	225.157	1345.25
SO_2 - 10DU in troposphere	3.405	1345.25
SO_2 - 10DU in stratosphere	43.735	1345.50

5.4.4 Spectroscopic databases

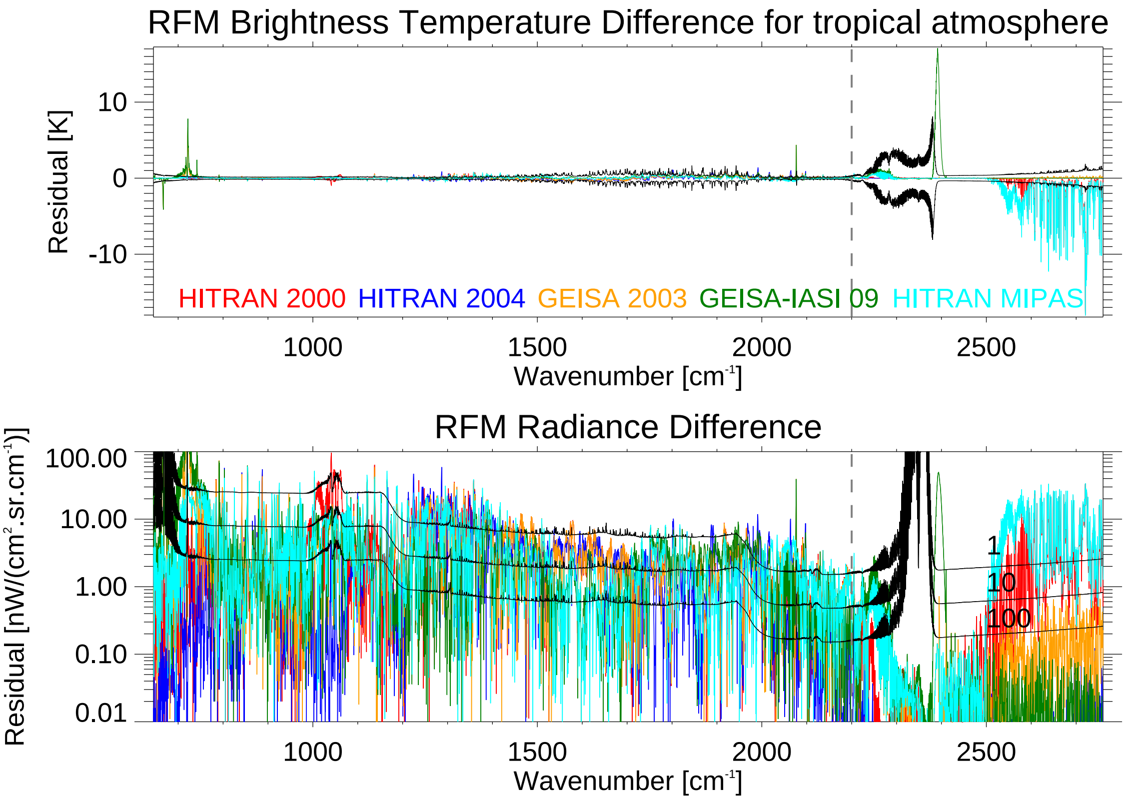

Figure 5.30: The residual, relative to HITRAN 2008, caused due to the differences in spectroscopic databases.

One of the crucial inputs to the RFM is the spectroscopic database, as the simulation of the IASI spectrum depends upon the accuracy of the molecular line parameters. Such databases contain many components used in radiative transfer calculations; for example, individual line parameters for molecules in the gas phase and absorption cross-sections for molecules in which the individual lines cannot be resolved as described by Rothman et al. (2009). This section only considers the line parameters, i.e. line position, strength and shape, as all the primary absorbers are represented as such. There are several databases available, which are updated at regular intervals as new research is carried out. However, these databases do not contain exactly the same data. Hence, the resulting spectrum from a radiative transfer model will differ depending upon the choice of spectroscopic database. The databases compared here are:

1. HITRAN 2000, (Rothman et al., 2003)
2. HITRAN 2004, (Rothman et al., 2005)
3. HITRAN 2008, (Rothman et al., 2009)
4. GEISA 2003, (Jacquinet-Husson et al., 2005)
5. GEISA-IASI 2009, (Jacquinet-Husson, 2009)
6. MIPAS, (Flaud et al., 2003)

where 1, 2 and 3 are versions of HITRAN (HIgh-resolution TRANsmission molecular absorption database) and 4 and 5 are versions of GEISA (Gestion et Etude des Informations Spectroscopiques Atmosphériques). The MIPAS (Michelson Interferometer for Passive Atmospheric Sounding) database is a customised version of the HITRAN databases made specifically for use with the MIPAS instrument, which is truncated at $2500\,\mathrm{cm}^{-1}$ due to the MIPAS spectral range.

Figure 5.30 compares the simulation of the IASI spectrum by each of the above databases to the HITRAN 2008 database used throughout this chapter. In this case, table 5.16 shows the percentage of spectral points ($\nu < 2200\,\mathrm{cm}^{-1}$) where the agreement with HITRAN 2008 gives $\xi < 0.1$. Large discrepancies can be seen between all databases. However, it is difficult to ascertain which absorbers are the cause

Table 5.16: Impact of different spectroscopic databases relative to HITRAN 2008. The table shows the spectral location of the maximum spectral residual expressed as an error parameter and also the percentage of spectral points that have $\xi < 0.1$.

Tropical atmosphere		
Database	$\% \, \xi < 0.1$	$\nu(\xi_{max})$
HITRAN 2000	30.34	1358.00
HITRAN 2004	49.18	1287.00
HITRAN MIPAS	38.04	1358.00
GEISA 2003	30.42	721.75
GEISA-IASI 09	37.65	721.75

of the large residuals. Therefore, for the primary absorbers, assumed in the previous section to be essential in the modelling of the atmosphere, residuals have been calculated to compare the spectroscopic databases by running the RFM for each absorber assuming an atmosphere of purely that gas (i.e the absorbtion coefficients for all other species have been switched off but the VMR of the gas in question remains at normal atmospheric concentration). Again, the residuals are from comparisons to the HITRAN 2008 database and the residuals for O_3, CO_2, CO, H_2O, N_2O, and CH_4 are shown in figure 5.31. However, this assumes that HITRAN 2008 is a ‘truth’, which it is not. Table 5.17 shows intercomparisons between all databases and gives the percentage of spectral points, which are considered to significantly contribute to the absorption of the molecule, that have $\xi > 0.1$ when compared to each database.

The most notable discrepancies between databases occur in the H_2O comparisons where the agreement between any pair of databases is less than 50%. This is due to the continual updates to water vapour line positions and intensities and highlights the uncertainty in the water vapour parameters. There is also noticeable disagreement between the CH_4 parameters between databases (again of order 50%) except

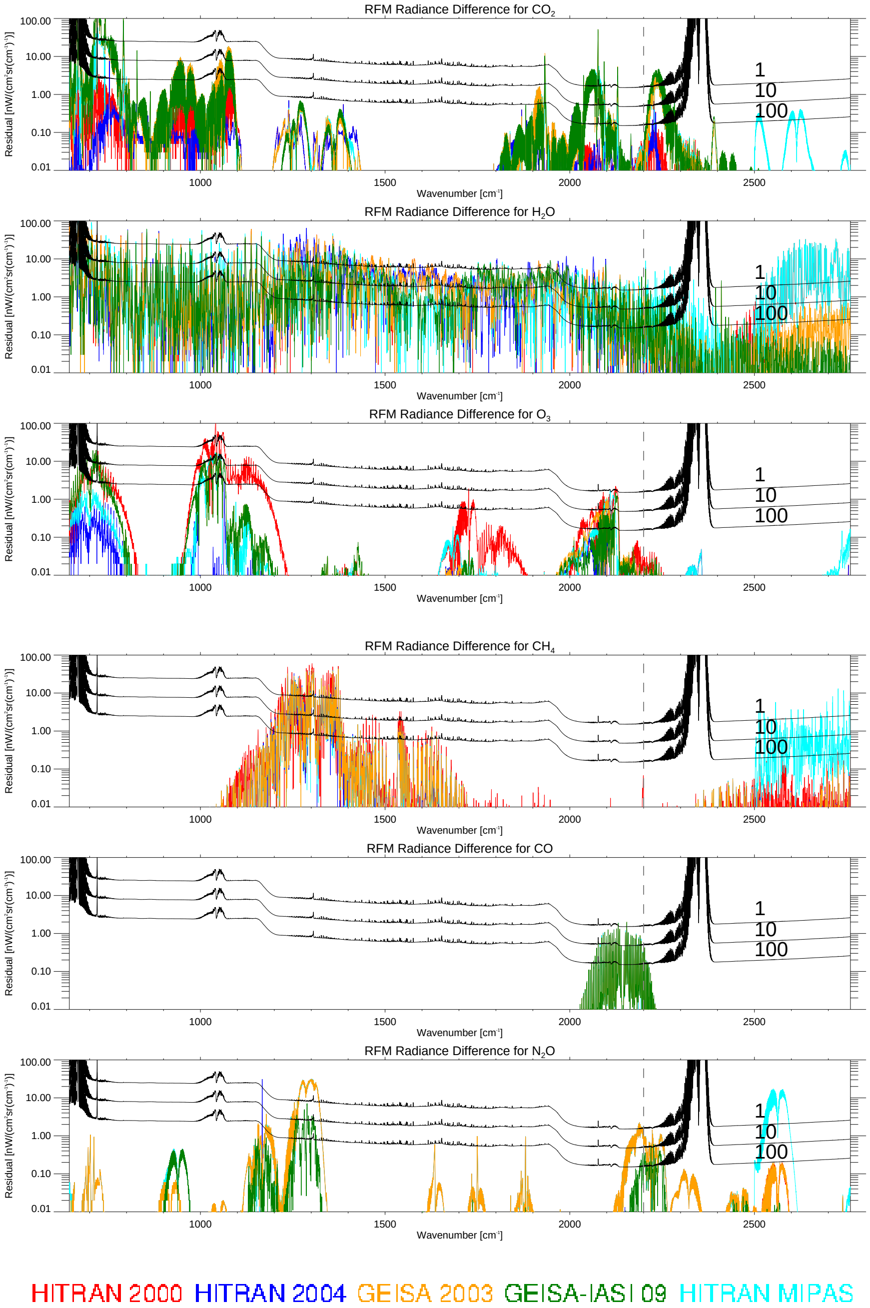

Figure 5.31: The radiance residuals, as in figure 5.30, for each of the major absorbers.

for the most recent editions of the databases, HITRAN 2008 and GEISA-IASI 09, where the values appear to have converged. The difficulty in accurately measuring the CH_4 line parameters in the infrared is due to the overlapping water vapour features, of which there is still large uncertainty as has been mentioned. Despite these large discrepancies, good agreement can be seen between all HITRAN databases for CO_2, although differences do exist between HITRAN and GEISA editions. The absorber with the smallest residuals and most agreement between databases is CO. The discrepancy in parameters is due to an update to the line features in HITRAN 2004 (maintained in HITRAN 2008) that has not been implemented in the GEISA databases.

It is clear that the spectroscopic database chosen for modelling the IASI spectrum significantly affects the output and hence, when comparing different models, these effects must be considered to be one of the largest causes of discrepancies.

Table 5.17: Percentage of spectral points that significantly contribute to the absorption of each molecule and that disagree by $\xi > 0.1$ in comparisons of spectroscopic databases for the primary absorbers.

Absorber	Database	H 2000	H 2004	H 2008	H MIPAS	G 2003	G-I 09
CO_2	H 2000	0.0	0.2	0.3	23.6	25.7	24.3
	H 2004	0.2	0.0	0.1	23.7	26.1	24.3
	H 2008	0.3	0.1	0.0	23.9	26.0	24.1
	H MIPAS	23.6	23.7	23.9	0.0	11.0	12.5
	G 2003	25.7	26.1	26.0	11.0	0.0	3.5
	G-I 09	24.3	24.3	24.1	12.5	3.5	0.0
H_2O	H 2000	0.0	49.5	57.4	60.8	0.6	54.0
	H 2004	49.5	0.0	53.0	60.2	49.4	57.5
	H 2008	57.4	53.0	0.0	51.8	57.6	53.3
	H MIPAS	60.8	60.2	51.8	0.0	60.8	51.0
	G 2003	0.6	49.4	57.6	60.8	0.0	54.0
	G-I 09	54.0	57.5	53.3	51.0	54.0	0.0
O_3	H 2000	0.0	44.8	45.0	46.0	48.7	48.4
	H 2004	44.8	0.0	0.0	13.5	20.1	16.5
	H 2008	45.0	0.0	0.0	13.5	20.3	16.3
	H MIPAS	46.0	13.5	13.5	0.0	14.0	16.1
	G 2003	48.7	20.1	20.3	14.0	0.0	5.8
	G-I 09	48.4	16.5	16.3	16.1	5.8	0.0
CH_4	H 2000	0.0	53.7	52.5	53.6	54.1	52.5
	H 2004	53.7	0.0	46.6	14.1	15.1	46.6
	H 2008	52.5	46.6	0.0	46.8	46.9	0.0
	H MIPAS	53.6	14.1	46.8	0.0	1.8	46.8
	G 2003	54.1	15.1	46.9	1.8	0.0	46.9
	G-I 09	52.5	46.6	0.0	46.8	46.9	0.0
CO	H 2000	0.0	16.9	16.9	0.0	0.0	0.0
	H 2004	16.9	0.0	0.0	16.9	16.8	16.8
	H 2008	16.9	0.0	0.0	16.9	16.8	16.8
	H MIPAS	0.0	16.9	16.9	0.0	0.0	0.0
	G 2003	0.0	16.8	16.8	0.0	0.0	0.0
	G-I 09	0.0	16.8	16.8	0.0	0.0	0.0
N_2O	H 2000	0.0	46.8	46.5	0.0	5.3	47.2
	H 2004	46.8	0.0	0.4	46.8	46.0	13.3
	H 2008	46.5	0.4	0.0	46.5	45.7	13.0
	H MIPAS	0.0	46.8	46.5	0.0	5.3	47.2
	G 2003	5.3	46.0	45.7	5.3	0.0	46.6
	G-I 09	47.2	13.3	13.0	47.2	46.6	0.0

5.5 Summary

In this chapter the importance of the initial assumptions within the forward model has been established and it can be seen that in the simulation of spectra from satellite–borne instruments the choice of the model parameters can have a large impact upon the resulting output. A summary of the key forward model parameters and the suggested settings required for general simulation of the IASI spectrum in the troposphere, along with the settings recommended for more accurate IASI calculations, is shown in table 5.18.

The approximations used in the spatial modelling within the RFM, described in section 5.1, have been shown to be valid at all viewing angles. However, although close to nadir the zenith angle is equal to the viewing angle, at larger scan angles a correction must be made to the zenith angle to fully capture the extended path length due to the curvature of the Earth.

When modelling the atmosphere a vertical altitude grid must be chosen, and the effect of varying the size of the layers in this grid were shown in section 5.2. If wishing to use the high altitude CO_2 or O_3 spectral features, then the assumed top of atmosphere must lie above the altitudes at which they occur: at least 90 km. Again it is these features that are adversely affected by coarse sampling in the stratosphere. The importance of the tropospheric altitude grid spacing for resolving the water vapour band was clear and the use of the 'linear in τ' approximation, as expected, was dependent upon the altitude grid to which it is applied. Therefore, its application is conditional on the chosen grid, and should be enabled if there is only a coarse altitude grid sampling the troposphere.

The optional spectral modelling parameters described in section 5.3 all exhibit large residuals on their exclusion, and it is therefore advised that they be included in any calculations. Despite the increase in processing time, the χ-factor and line mixing are crucial in fully capturing the behaviour of the CO_2 spectral features. Molecular continua must be included in order to correctly model the IASI spectrum. Despite this, it should be noted that there are continuous improvements to the water vapour continuum models available, and as was shown, large differences between versions; therefore discrepancies between radiative transfer models often arise from their handling of the continua.

The essential gases required for infrared modelling are established in section 5.4, providing 13 atmospheric absorbers fundamental to replicating the IASI spectrum to within the IASI noise. A further 7 absorbers are suggested that should be included for more accurate simulations, and the effects of an enhancing event upon a selection of these were shown.

Some of the largest residuals in these comparisons were those between spectroscopic databases, with over 50% of relevant channels for H_2O and CH_4 disagreeing by more than the IASI noise for 100 spectra. This illustrates how significantly the input line parameters can affect the output spectra by radiative transfer models and highlights the importance of taking into account the spectroscopy when comparing such models.

Table 5.18: The recommended forward model settings for simulation of the IASI spectrum in the troposphere

Forward model parameter	Recommended Settings	
	Normal ($\xi < 1$)	Accurate ($\xi < 0.1$)
FOV Convolution	Disabled	Disabled
Refraction	Disabled	Disabled
Plane-parallel Approximation	Valid	Valid
Ground angle correction	Needed above 10°	Needed above 0°
Top of atmosphere	70 km (unless using long wave CO_2 lines)	90 km
Stratospheric vertical grid	$\Delta(\ln p) = 1.0$ ($\Delta z \sim 6$ km)	$\Delta(\ln p) = 0.4$ ($\Delta z \sim 2.5$ km)
Tropospheric vertical grid	$\Delta p = 30$ mb	$\Delta p = 10$ mb
'Linear in τ' Approximation	Enabled for U.S Standard and Met Office grid	Enabled
Spectral grid spacing	$0.003\,\mathrm{cm}^{-1}$	$0.001\,\mathrm{cm}^{-1}$
ILS convolution width	$1\,\mathrm{cm}^{-1}$	$10\,\mathrm{cm}^{-1}$
Line mixing	Enabled if using CO_2 bands	Enabled if using CO_2 bands
Line shape	Enabled if using CO_2 bands	Enabled if using CO_2 bands
Molecular continua	All enabled	All enabled
Non-LTE effects	Enable if using affected lines	Enable if using affected lines
Primary absorbers that need location specific profiles	O_3, H_2O, N_2O, CO, CH_4,	Also CO_2
Trace Gases to include	CFC–11, CFC–12, HNO_3, N_2, O_2, OCS, and CCl4	Also NO_2, NH_3, C_2H_6, HCN, HCOOH, SO_2 and NO
Enhanced absorbers	SO_2	Also NO_2 and HCN

Chapter 6

Selection of IASI Channels

IASI is, in many ways, the successor to the HIRS instrument flown on the NOAA satellites, but while HIRS had just 20 broadband channels each IASI spectrum contains a total of 8461 spectral points, conventionally also designated ‘channels’. As decribed in chapter 2 an important feature of IASI is that it covers the spectral range 645–2760 cm^{-1} (15.5–3.6 μm) sampled at 0.25 cm^{-1}, with 0.5 cm^{-1} resolution after apodisation. This results in a large quantity of data and use of the full IASI spectrum is not feasible for operational retrieval and data assimilation schemes, which typically only deal with a few tens of measurements per location from other satellite instruments. Choosing an optimal subset of the IASI channels is an established method of data reduction, aiming to identify the minimum number of channels that contain all the essential information on the target atmospheric and surface variables. A constant channel set is usually used in operational applications, where the optimal selection is calculated taking an average across the globe.

There are several potential methods for the selection of an optimal channel set. Rabier et al. (2002) discuss various alternative schemes for the selection of IASI channels including iterative statistical schemes and selections based upon the characteristics of the Jacobians. The latter being similar to the channel selection methods implemented for AIRS (Atmospheric Infrared Sounder) by Crevoisier et al. (2003) and for CrIS (Cross-Track Infrared Sounder) by Gambacorta and Barnet (2013), which use physically based sensitivity studies to select channels based purely on their spectral properties. However, Rabier et al. (2002) favour the algorithm originally proposed by Rodgers (1996), which is implemented by Collard (2007) to select IASI channels for NWP (numerical weather prediction). These current channel selection schemes tend to be based on a correct treatment of uncorrelated errors but ignore, or represent only crudely, spectrally correlated errors that often limit the accuracy of the radiative transfer modelling.

Taking the standard algorithm by Collard (2007), this chapter explores a modification that allows the influence of spectrally-correlated errors to be correctly modelled without significant computational overheads. The relative performance of the two algorithms is then compared. The modified scheme is essentially a simplification of a solution developed by Dudhia et al. (2002) for the related, but more complex, problem of microwindow selection for a limb-viewing interferometer.

Throughout this chapter the channel selection is expressed explicitly as a 1D retrieval problem. However, it is assumed to be applicable to channels selected for direct radiance assimilation within a 3D- or 4D-var system.

6.1 Channel selection algorithms

The theoretical background of the following has been introduced in chapter 3 and is explained in detail in Rodgers (2000). Although the work here is in an NWP context, the notation used follows the Rodgers (2000) symbol conventions (instead of the NWP symbol conventions) in order to maintain consistency throughout this thesis.

6.1.1 Optimal Estimation Framework

It was established in chapter 3 that, assuming no correlation between the measurement error covariance $\mathbf{S}_y$ $(m \times m)$, and the *a priori* error covariance, $\mathbf{S}_a$ $(n \times n)$, the *a posteriori* error covariance, $\mathbf{S}_x$ is given by

$$\mathbf{S}_x = \left(\mathbf{K}^T \mathbf{S}_y^{-1} \mathbf{K} + \mathbf{S}_a^{-1}\right)^{-1} \tag{6.1}$$

where $\mathbf{K}$ is the Jacobian matrix $(m \times n)$. Here, the matrix $\mathbf{S}_y$ includes both the inherent measurement errors, such as spectral noise and calibration errors, and also those associated with the radiative transfer model used to predict the measurement from a given state; in this case, the RFM.

The aim of the channel selection is to either find the 'best' subset of m channels from the measurement domain or, alternatively, to find the minimum number of channels required to meet a target retrieval accuracy.

In either case, the impact of each channel upon a figure of merit is calculated in order to compare the channel selections. Information in the state error covariance matrix is compressed into a single scalar quantity allowing the intercomparison of different covariance matrices (e.g. from using different measurement channels). The chosen measure is the 'degrees of freedom for signal' (DFS), which is essentially the number of independent pieces of information available, defined in chapter 3 to be:

$$d_s = \mathrm{Tr}(\mathbf{I} - \mathbf{S}_{\mathrm{x}}\mathbf{S}_{\mathrm{a}}^{-1}) \tag{6.2}$$

where $\mathbf{I}$ is the identity matrix (order n). The DFS is chosen in line with that used by Collard (2007) and because it weights the analysis to favour levels where there is a lack of previous knowledge. A value $d_s = 0$ corresponds to $\mathbf{S}_x = \mathbf{S}_a$, i.e., the case before any measurements have been used or when the measurements have provided no information on the state vector. In the limit of a 'perfect' retrieval $\mathbf{S}_x \to 0$, hence $d_s \to \mathrm{Tr}(\mathbf{I}) = n$, the number of elements in the state vector.

6.1.2 Conventional algorithm

If only selecting two or three channels, it might be feasible to evaluate the DFS for each possible combination of the 8461 IASI channels. However, this is not the case for selecting a hundred channels, or even just ten, and another approach is required. Ideally, the best set of m channels to use would be selected. However, in practice this must be treated in a different, more tractable manner: having already selected $(m-1)$ channels, which of the remaining channels will provide the largest improvement?

Rodgers (1996) exploits a particular property of optimal estimation: provided the matrix $\mathbf{S}_y$ is diagonal (i.e., measurement errors are uncorrelated), equation 6.1 can be evaluated sequentially:

$$\mathbf{S}_x(m) = (\mathbf{k}^T(\sigma^2)^{-1}\mathbf{k} + \mathbf{S}_a^{-1}(m-1))^{-1} \tag{6.3}$$

where $\mathbf{S}_x(m)$ is the solution for equation 6.1 after m measurements have been included, $\mathbf{k}$ is the row of $\mathbf{K}$ corresponding to the mth channel and σ^2 (often just taken as the square of the instrument noise) is the equivalent diagonal element of $\mathbf{S}_y$. Now, the matrix inversion in Eq. 6.3 is of order n, whereas in Eq. 6.1 there is an additional, and expanding, matrix inversion of order m ($\mathbf{S}_y^{-1}$). This is extremely useful when typically n is a few tens but m can exceed 100.

Before beginning the selection, the RFM is used to compute the $\mathbf{K}$ matrix for all channels in the measurement domain, assuming a typical atmospheric profile (or set of profiles).

Initially, for ($m = 1$), we set $\mathbf{S}_x(0) = \mathbf{S}_a$, then equation 6.3 is solved for each channel individually and the corresponding DFS is evaluated. The channel with the largest DFS is selected as the first channel.

Next, ($m = 2$), $\mathbf{S}_a$ is replaced with the solution covariance $\mathbf{S}_x(1)$ from the first selected channel. Eq. 6.3 and the corresponding DFS (still using the original $\mathbf{S}_a$) are re-evaluated for all remaining channels to determine the second channel. This is repeated until the required threshold has been reached, i.e number of channels or target DFS value.

6.1.3 Application to IASI

In the development of the above algorithm into a practical scheme for IASI channel selection, Collard (2007) notes that it contains no mechanism for handling spectrally correlated errors. Such errors are commonly associated with the radiative transfer model. For example, these can arise from assuming an incorrect concentration of an interfering (i.e., a non-retrieved) molecule: an underestimate of the concentration generally leads to an overestimate of the radiance at all spectral points overlapping the molecule's absorption bands. Therefore, Collard (2007) estimated the magnitude of such error contributions at each spectral point and if larger than a given threshold ($\sim$1 K in brightness temperature) then the channel was 'blacklisted', i.e., excluded from possible selection. If the error contribution was smaller, then it was added to the noise as an additional term in $\mathbf{S}_y$ and treated as a random error.

This *ad hoc* approach is unsatisfactory in that it does not properly allow for the cumulative effect of correlated errors in the retrieval accuracy (while the random noise impact reduces as the square root of the number of measurements, the correlated error remains the same so may become dominant when $\sim$100 channels are used). However the alternative, setting the blacklist threshold even lower, may exclude channels whose benefit in signal/noise outweighs their correlated error contribution.

6.1.4 Spectrally Correlated Errors

In principle, all random correlated measurement errors can be represented as additional terms in the measurement covariance matrix, $\mathbf{S}_y$ as described above. This is straightforward for the selection of the first channel since none of these errors are assumed to have any correlation with the *a priori* covariance, $\mathbf{S}_a(0)$. The difficulty occurs after subsequent channel selections ($m \geq 1$) since $\mathbf{S}_a(m)$ now contains some error component that is correlated with the remaining measurements, and hence, the assumption required for equation 3.10 breaks downs.

However, within a set of m spectral measurements $\mathbf{y}$, correlated errors can be represented by a combination of one or more statistically independent error vectors

$\delta\mathbf{y}^j$, each contributing an additive term to the overall error covariance matrix:

$$\mathbf{S}_y^j = (\delta\mathbf{y}^j)(\delta\mathbf{y}^j)^T \tag{6.4}$$

As an example, a 0.1 K radiometric uncertainty in the onboard black-body calibration target would be a single vector containing m values of 0.1 K. In more complex cases, such as a $(i \times i)$ covariance matrix representing the uncertainty in the assumed profile of a contaminating species, it can be decomposed into i eigenfunctions in profile space and, using an appropriate Jacobian matrix, mapped into i independent error vectors in spectral space.

A total measurement error covariance matrix can then be represented as a sum of random spectrally uncorrelated and random spectrally correlated components

$$\mathbf{S}_y^{\mathrm{tot}} = \mathbf{S}_y^{\mathrm{rnd}} + \sum_j (\delta\mathbf{y}^j)(\delta\mathbf{y}^j)^T \tag{6.5}$$

Note that a diagonal $\mathbf{S}_y^{\mathrm{rnd}}$ matrix could also be represented as a set of m error vectors each containing a single non-zero element.

Walker et al. (2011) use this approach to construct a total error covariance as part of a fast linear retrieval scheme for IASI. In their sequential channel selection they simply computed the figure of merit for each potential new channel using the full inversion of Eq. 6.1, with $\mathbf{S}_y^{\mathrm{tot}}$ for $\mathbf{S}_y$ (and in this case without $\mathbf{S}_a$). This is feasible since they only deal with a two element state vector ($n = 2$) and do not consider the entire spectrum ($m \ll 100$).

By assuming a diagonal $\mathbf{S}_y$ matrix the need for repeatedly inverting it is avoided and initially it appears as though a generalisation to include the full correlated covariance $\mathbf{S}_y^{\mathrm{tot}}$ would cause a significant increase in computer processing time. The solution lies in distinguishing between the way the channels are *selected* and the way in which they will be *used* in the retrieval or data assimilation. Although recent work has been carried out to include more realistic $\mathbf{S}_y$ matrices, including correlated errors, within 4d-Var assimilation systems (see Bormann et al. (2010) and Weston (2011)) here we only discuss the use of a diagonal $\mathbf{S}_y$ matrix.

6.1.5 Linear Error Propagation

Established in chapter 3, the linear form of the optimal estimation solution is represented by

$$\mathbf{x} = \mathbf{G}\mathbf{y} + (\mathbf{I} - \mathbf{G}\mathbf{K})\mathbf{x}_a \tag{6.6}$$

where $\mathbf{G}$ (the 'gain matrix') is given by:

$$\mathbf{G} = \left(\mathbf{K}^T\mathbf{S}_y^{-1}\mathbf{K} + \mathbf{S}_a^{-1}\right)^{-1}\mathbf{K}^T\mathbf{S}_y^{-1} \tag{6.7}$$

where the measurement covariance, $\mathbf{S}_y$, is that used by the retrieval, which is not necessarily (and not usually) the total error covariance. It will be assumed that the retrieval just uses the random measurement error covariance $\mathbf{S}_y^{\mathrm{rnd}}$, and hence (using equation 6.1):

$$\mathbf{G} = \mathbf{S}_x^{\mathrm{rnd}}\mathbf{K}^T(\mathbf{S}_y^{\mathrm{rnd}})^{-1} \tag{6.8}$$

where $\mathbf{S}_x^{\mathrm{rnd}}$ is the random error covariance of the solution $\mathbf{x}$. From here it follows that any measurement error vector $\delta\mathbf{y}^j$ can be mapped into a corresponding retrieval error vector $\delta\mathbf{x}^j$ through

$$\delta\mathbf{x}^j = \mathbf{G}\delta\mathbf{y}^j + (\mathbf{I} - \mathbf{GK})\delta\mathbf{a}^j \tag{6.9}$$

where $\delta\mathbf{a}^j$ represent components of the same error j that contribute to the *a priori* estimate (i.e., via a previously incorporated measurement). Since these errors are independent they can then be combined in retrieval space, by analogy with Eq. 6.5, to give a total retrieval error

$$\mathbf{S}_x^{\mathrm{tot}} = \mathbf{S}_x^{\mathrm{rnd}} + \sum_j (\delta\mathbf{x}^j)(\delta\mathbf{x}^j)^T \tag{6.10}$$

Thus, if the retrieval process can be expressed as a sequential application of Eq. 6.6 — which basically means that the retrieval regards the measurement errors as uncorrelated — then correlated errors can be mapped into the solution as vectors without having to invert, or even construct, the full measurement covariance matrix $\mathbf{S}_y^{\mathrm{tot}}$.

6.1.6 Modified Selection Algorithm

The conventional algorithm can be modified by

(a) correctly modelling the measurement error correlations during the selection process itself, while

(b) allowing for (in fact, requiring) the selected channels being subsequently used in a retrieval as if uncorrelated

It is assumed that spectrally correlated errors have been modelled as a set of independent error spectra $\delta\mathbf{y}^j$ and that the initial *a priori* covariance $\mathbf{S}_a$ contains no contributions from these errors.

Starting with $\mathbf{S}_x^{\mathrm{rnd}}(0) = \mathbf{S}_a$ and $\delta\mathbf{x}^j(0) = 0$, the modified channel selection then proceeds from $m = 1$ as follows

$$\begin{aligned}
\mathbf{S}_x^{\mathrm{rnd}}(m) &= (\mathbf{k}^T(\sigma^2)^{-1}\mathbf{k} + (\mathbf{S}_x^{\mathrm{rnd}})^{-1}(m-1))^{-1} && (6.11)\\
\mathbf{g} &= \mathbf{S}_x^{\mathrm{rnd}}(m)\mathbf{k}^T(\sigma^2)^{-1} && (6.12)\\
\delta\mathbf{x}^j(m) &= \mathbf{g}\delta y^j + (\mathbf{I} - \mathbf{gk})\delta\mathbf{x}^j(m-1) && (6.13)\\
\mathbf{S}_x^{\mathrm{tot}}(m) &= \mathbf{S}_x^{\mathrm{rnd}}(m) + \sum_j (\delta\mathbf{x}^j(m))(\delta\mathbf{x}^j(m))^T && (6.14)\\
d_s^{\mathrm{tot}}(m) &= \mathrm{Tr}(\mathbf{I} - \mathbf{S}_{\mathrm{x}}^{\mathrm{tot}}(\mathrm{m})\mathbf{S}_{\mathrm{a}}^{-1}) && (6.15)
\end{aligned}$$

where $\mathbf{g}$ is the Gain Matrix $\mathbf{G}$ from Eq. 6.7 reduced to a $(n \times 1)$ vector for a single measurement. Eqs. 6.12–6.14 are new, but computationally fast compared to the inversion in Eq. 6.11 (which is the same as in the original scheme). As well as the random error covariance $\mathbf{S}_x^{\mathrm{rnd}}(m)$ it is now also necessary to save the set of vectors $\delta\mathbf{x}^j(m)$, representing the various systematic error contributions to the next *a priori* estimate.

At this point it is noted that apodisation introduces noise correlations between IASI channels and therefore the selection described in section 6.2 does not allow for adjacent channels to be chosen. However, if selection of adjacent channels *is* to be allowed the sequential procedure explained above must be modified.

If the retrieval still assumes an uncorrelated $\mathbf{R}$, then the 'true' $\mathbf{A}_m^{\mathrm{rnd}}$ in Eq. 6.14 (as opposed to the uncorrelated version assumed by the retrieval in Eq's 6.11 and 6.12) would have to be modified to

$$\mathbf{S}_x^{\mathrm{rnd}}(m) = (\mathbf{K}^T(\mathbf{S}_y^{\mathrm{rnd}}(m))^{-1}\mathbf{K} + (\mathbf{S}_x^{\mathrm{rnd}})^{-1})^{-1} \qquad (6.16)$$

where $\mathbf{S}_y^{\mathrm{rnd}}(m)$ is the correlated noise covariance matrix for the m measurements selected so far. Given $\mathbf{S}_y^{\mathrm{rnd}}(m)$ is now a sparse tridiagonal matrix (of growing dimension m × m) this could still be practical.

On the other hand, if the retrieval also models correlated errors, it may be adequate to apply the above to select each channel by replacing Eq. 6.11 with Eq. 6.16 and subsequently updating Eq's 6.12 and 6.13 with the equivalent for the full measurement vector so far:

$$\begin{aligned} \mathbf{G} &= \mathbf{S}_x^{\mathrm{rnd}}(m)\mathbf{K}^T(\mathbf{S}_y^{\mathrm{rnd}}(m))^{-1} && (6.17) \\ \delta\mathbf{x}^j(m) &= \mathbf{G}\delta\mathbf{y}^j(m) && (6.18) \end{aligned}$$

where $\delta\mathbf{y}^j(m)$ is the error vector for the m selected measurements.

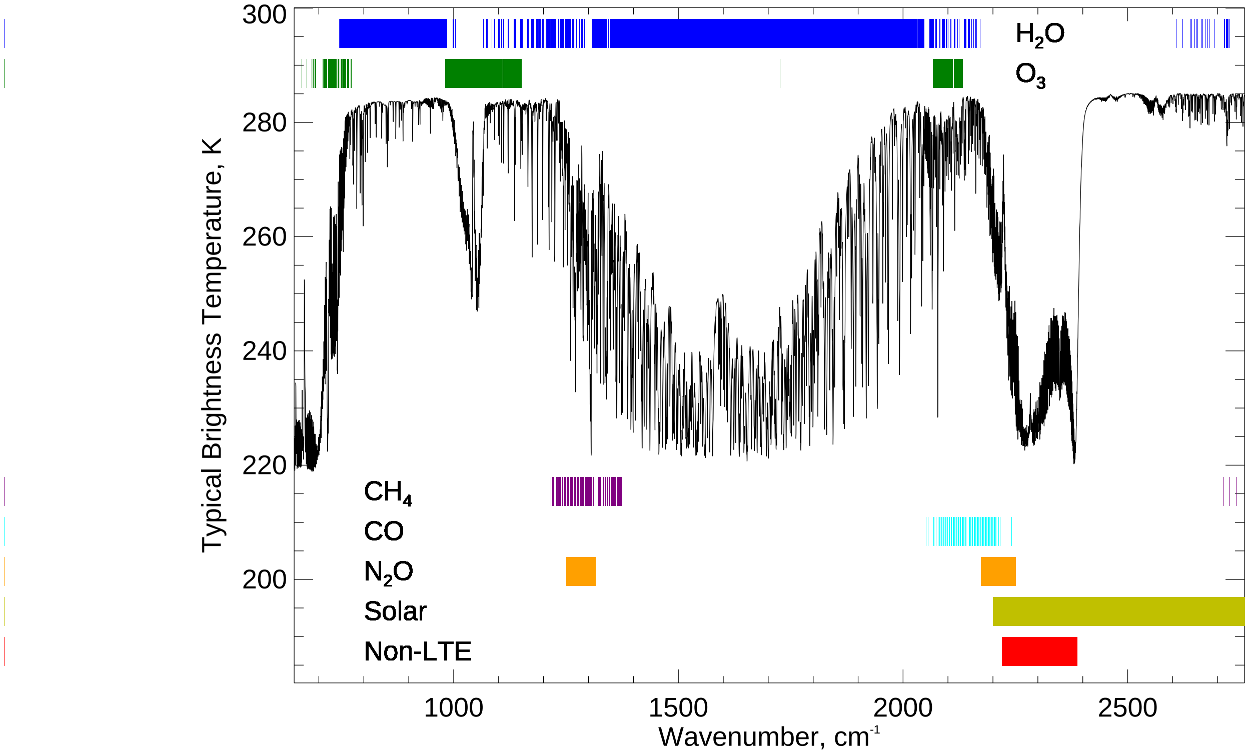

Figure 6.1: A typical IASI spectrum indicating the channels blacklisted due to the atmospheric variability of H_2O, O_3, CH_4, CO and N_2O along with those affected by non-LTE effects and solar irradiance.

6.2 Selection of IASI Channels

In order to compare the original and modified algorithms we first attempt to reproduce the practical selection of 300 channels carried out by Collard (2007) and then repeat the selection using the modified algorithm. This ensures that differences are due to the algorithms themselves and not in the details of the calculations. For example, in this study the radiative transfer calculations are performed using the Reference Forward Model Dudhia (2002) while Collard used RTIASI-4 (Matricardi (2003), Matricardi and Saunders (1999)); the background error covariance matrices are based upon different operational 1 D-Var matrices; different assumptions are made on the variability of minor species. However, the original Collard channels are also included in the comparisons to give some indication of the robustness of the original selection to minor differences in implementation.

Given a set of channels selected by either method, the formalism of the modified algorithm can then be applied to evaluate both DFS for total error, d_s^{tot}, (i.e., the quantity that the modified algorithm aims to maximise) or the DFS for random error, d_s^{rnd} (maximised by the original algorithm).

6.2.1 Reproducing Original Selection

Collard selected 300 channels for distribution to NWP centres in near real time. This means that the only species of interest are water vapour, ozone, carbon dioxide and temperature.

The same flags used by Collard (personal communication) are used to blacklist channels where the climatological variability of CH_4, CO and N_2O cause a brightness temperature uncertainty of > 1 K, as well as channels influenced by non-LTE effects (i.e., where the usual assumption of local thermodynamic equilibrium breaks down, chiefly at shorter wavelengths and high altitudes), solar irradiance and, in certain selection runs, water vapour and ozone. The locations of affected channels are shown in figure 6.1.

The random error on each spectral point is taken as a combination of the following terms (in quadrature)

1. instrument noise from the CNES 2008 post-launch estimate

2. the climatological variability (using MIPAS IG2 data by Remedios et al. (2007))

for each minor species that caused an uncertainty of < 1 K (CCl_4, CFC-11, CFC-12, CFC-14, HNO_3, NO_2, OCS, NO and SO_2)

3. an additional forward modelling uncertainty, assumed to be a constant 0.2 K (in line with the Collard selection)

These terms are plotted in Fig. 6.2.

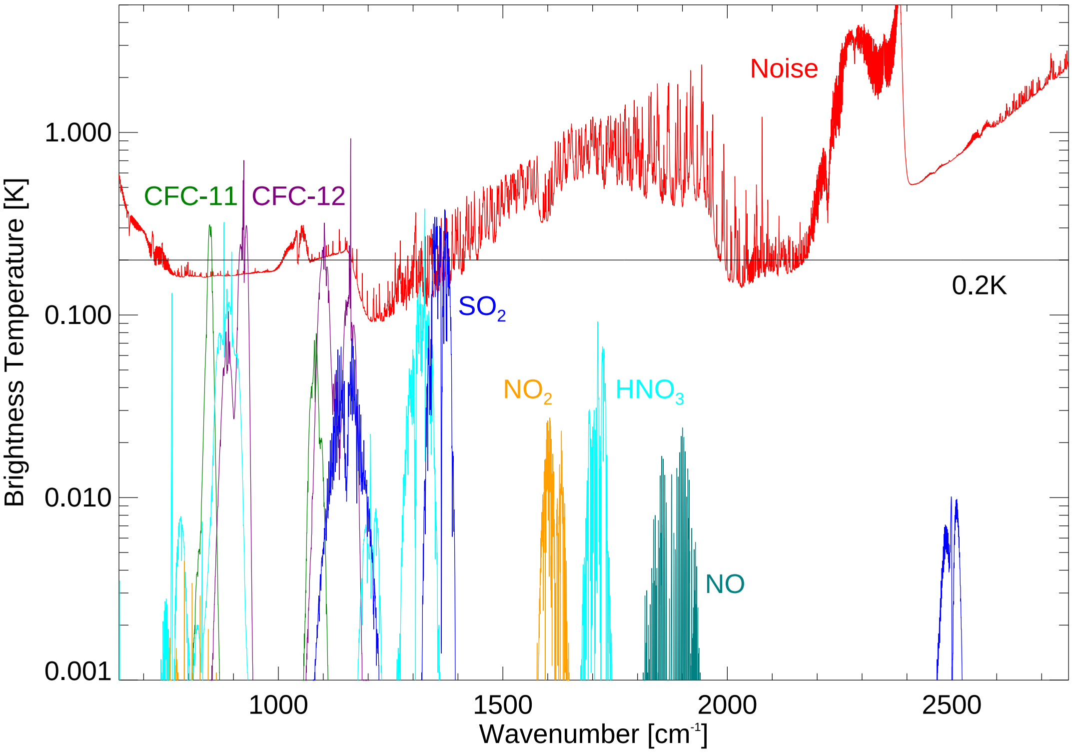

Figure 6.2: The error in IASI brightness temperature due to the climatological variability, in a mid latitude daytime atmosphere, of each minor species included in $\mathbf{S}_y$ in the original selection and included as an independent error source in the modified selection. The instrument noise and 0.2 K assumed forward model uncertainty are also plotted.

In order to create a channel set suitable for use globally rather than specific to one particular location, Jacobian spectra are precomputed for two different viewing angles (nadir and 40 °) and for six different FASCODE atmospheres (US Standard atmosphere, tropics, mid-latitude summer, mid-latitude winter, sub-arctic summer, sub-arctic winter). The DFS is computed for each and the figure of merit d_s^{rnd} taken as the average of the 12 DFS values.

Finally, although each wavenumber channel has a width of $0.25\,\mathrm{cm}^{-1}$, the apodized data has a spectral response function of width $0.5\,\mathrm{cm}^{-1}$ and hence, the signal becomes spectrally correlated between neighbouring channels. Practically, this means that once a channel is selected the adjacent channels are ‘blacklisted’.

6.2.2 Modified Channel Selection

The error contributions representing the uncertainty in concentration for each molecular absorber were created for each species represented by blacklists in the original scheme as well as each of the minor species. In most cases these were defined by a single error spectrum representing the climatological variability, which can be seen in figures 6.2 and 6.3.

However, for water vapour, the relevant components of the Met Office 1D-var background covariance were decomposed into 27 independent error vectors. Non-LTE was also modelled as an error spectrum created by running the RFM with and without non-LTE modelling switched on. As with the original scheme, once a channel was selected the adjacent channels were blacklisted and also, to avoid solar effects, only channels up to 2200 cm^{-1} were considered.

The random component of measurement error was represented by the instrument noise (with the additional 0.2K for consistency).

The DFS, this time based on the total error, d_s^{tot} was again taken as the average

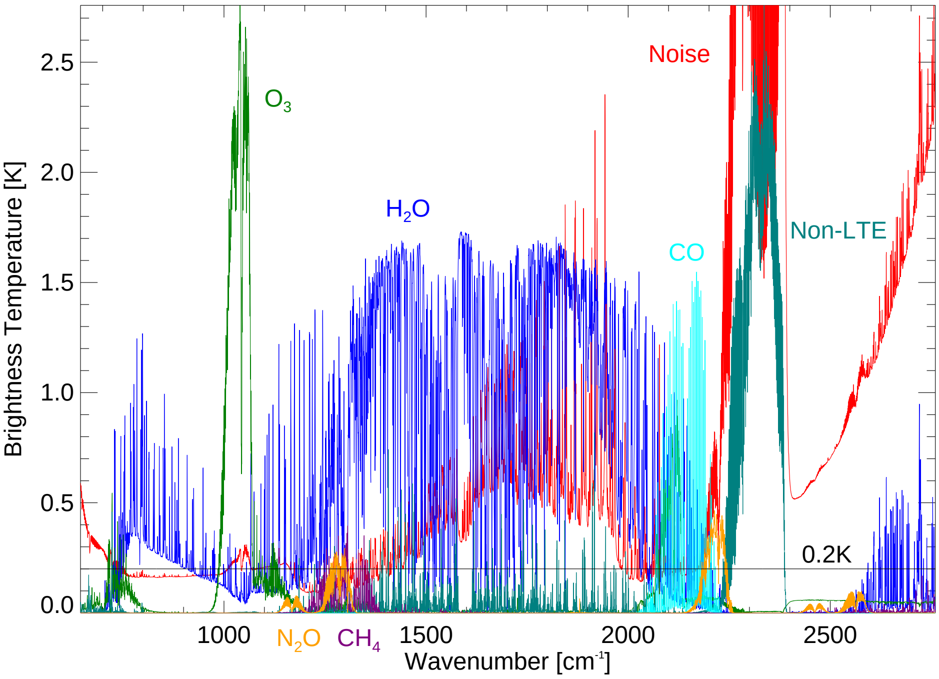

Figure 6.3: The additional error spectra (to those in figure 6.2) included in the modified channel selection algorithm. The largest water vapour error is plotted as an example. The instrument noise and 0.2 K assumed forward model uncertainty are also plotted.

over the same 6 atmospheres and two viewing angles.

6.3 Results

6.3.1 Temperature channels

Following Collard, initially the selection considers channels for a purely temperature retrieval. A state vector is defined containing 44 variables: temperature at 43 atmospheric levels plus the surface temperature (For the calculation of the Jacobians it is assumed that the surface is at the same temperature as the lowest level of each of the 6 modelled atmospheres).

In the original algorithm, the H_2O and O_3 blacklist masks are also applied to ensure that CO_2 features are targeted. The first thirty channels are selected, followed by another 36 limited to the spectral range 707.25–759.75 cm^{-1}, intended to improve the information in the troposphere.

The same state vector was defined for the modified algorithm and the first 66 channels were selected without any restriction. A selection limited to the 707.25–759.75 cm^{-1} region after the first 30 channels was investigated, as well as weighting the figure of merit so that channels with information in the troposphere might be preferentially selected, but negligible improvement was found in the profile error for this region, suggesting that most of the available tropospheric information had already been extracted within the first 30 channels of the modified algorithm.

The locations of the selected channels are shown in Fig. 6.4. The largest difference between the temperature selections is that the channels from the original algorithm are almost entirely between 645–800 cm^{-1} whereas the modified algorithm chooses a large number between 2100–2200 cm^{-1}. This is also the case with the first channel, for the original algorithm this is 1204 cm^{-1} whereas for the modified version the first channel is at 2150 cm^{-1}; in both cases they are obtaining surface information and in fact obtain almost all the surface information in just this one channel. Favouring the shorter wavelength is due to the effect of the water vapour errors. As shown by Collard, the algorithms select a large proportion of the channels in the 670–710 cm^{-1} range, which are sensitive to higher altitudes (upper troposphere and lower stratosphere). This is caused, in part, by the larger *a priori* errors at these altitudes, compared to the troposphere, but also results from the larger errors associated with each channel and, hence, more channels are required to reduce the DFS in this region.

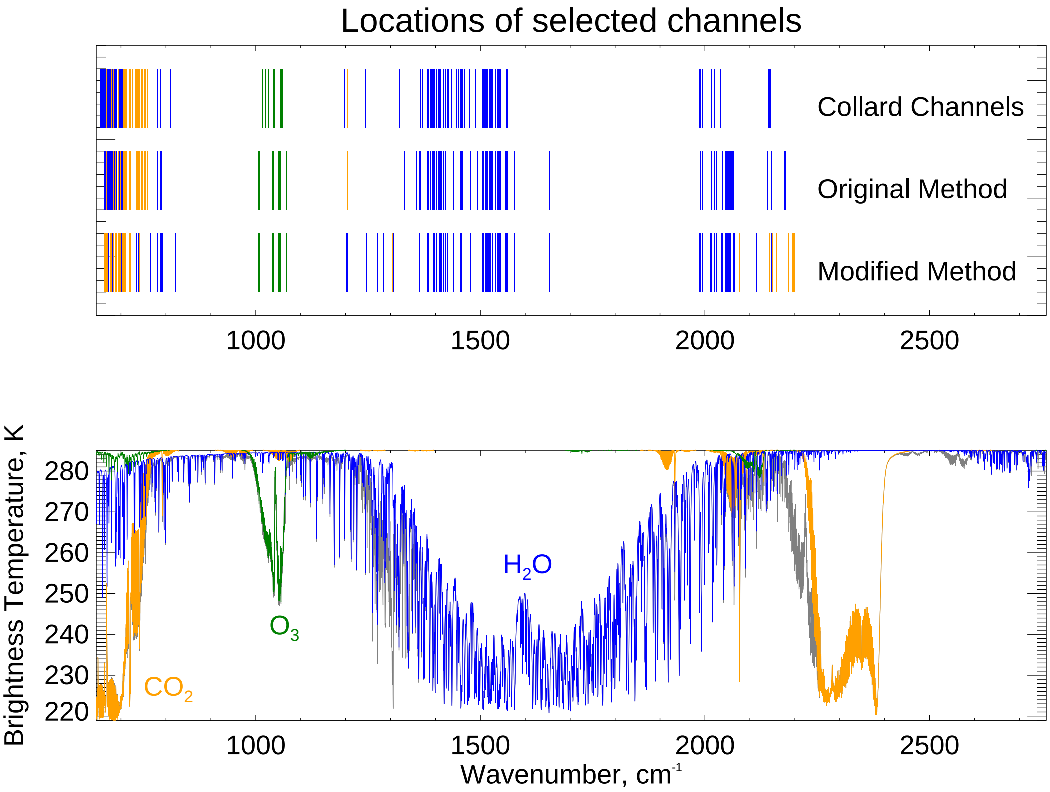

Figure 6.4: The locations of the 267 channels selected by the original and modified algorithms; the 66 temperature channels (orange), 186 temperature and water vapour channels (blue) and 15 ozone channels (green). The lower plot shows a typical IASI spectrum in grey, with the spectral features for CO_2, H_2O and O_3 overplotted. Features at 1300, 2100, and 2200 cm^{-1} are CH_4, CO, and N_2O respectively.

The resulting DFS values for the original and modified algorithms are listed in Table 6.1 alongside the values for the channels selected by Collard for comparison. The Collard values show that the reproduced set of channels manages to provide similar information and select similar channels, as can be seen in figure 6.4. The small discrepancies arise from the unavoidable differences in the reproduction mentioned earlier.

As expected, the original algorithm has a better DFS for random error (since this is the figure which is optimised) but not by much. However the big difference is in the DFS evaluated for total error. For the modified algorithm it is only slightly worse than for the random error, suggesting that the spectrally correlated errors have little net contribution, but for the original algorithm the figure is almost halved. It turns out that most of this is due to the water vapour induced errors so, in principle, recoverable if water vapour is jointly retrieved, as discussed in the next section.

Table 6.1: Degrees of Freedom for Signal per profile of 43 levels plus surface term from 66 temperature channels selected by Collard, and by the original and modified algorithms.

		Collard	Original	Modified
$\mathrm{T}_{\{43\}}$	$\mathrm{d}_s^{\mathrm{rnd}}$	6.22	6.43	6.35
	$\mathrm{d}_s^{\mathrm{tot}}$	3.86	3.71	5.98
T_s	$\mathrm{d}_s^{\mathrm{rnd}}$	0.97	0.99	0.99
	$\mathrm{d}_s^{\mathrm{tot}}$	0.93	0.97	0.97

The vertical profiles of random and total error for the US standard atmosphere, viewed at nadir, are shown in Fig. 6.5. Here it can be seen that the main differences are at altitudes below 200 hPa: the original algorithm has a smaller random error but a larger total error, again consistent with using channels sensitive to uncertainties in the water vapour concentration and, between 200–400 hPa, the ozone uncertainty.

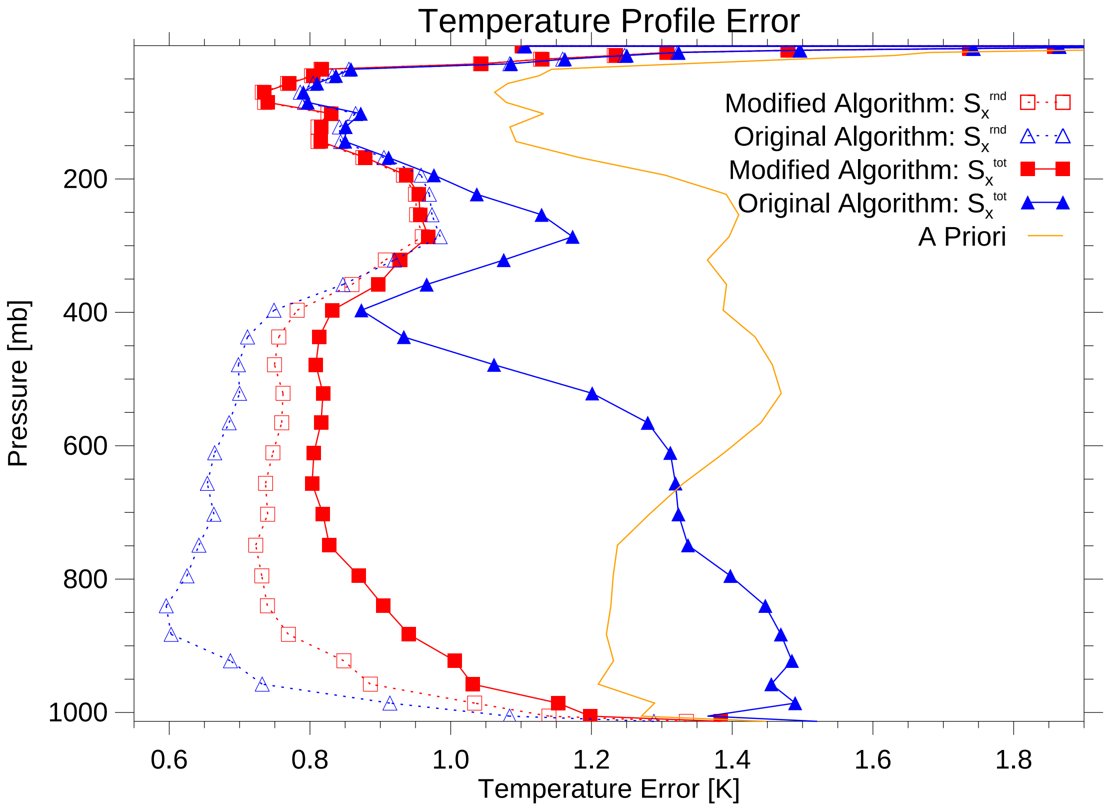

Figure 6.5: Temperature error profiles for the U.S standard atmosphere viewed at nadir from 66 channels for the original algorithm (blue) and the modified algorithm (red). The error due to both the random (dashed line) and total (solid line) errors are shown.

It can also be seen that total error for the original selection algorithm is larger than the *a priori* uncertainty in the lower troposphere: here the measurements are contributing *negative* DFS. Despite the fact that an optimal estimation retrieval aims to minimise the error and, hence, the error should not be able to increase above the *a priori* uncertainty, this assumes that the correct error covariance matrix and optimal gain matrix are used. This is not the case when looking at the total error for the original selection; instead, this examines the effect of introducing additional error sources to an optimised random retrieval (see equation 6.10) and therefore, the total error is able to exceed the *a priori* error.

6.3.2 Main Channels

Once the temperature channels have been selected, the ‘main run’ is carried out. The aim is to find channels mainly sensitive to water vapour but which also provide additional temperature information.

A water vapour volume mixing ratio profile is added to the state vector (an extra 43 elements) and the *a priori* covariance is taken from the Met Office 1D-var scheme. For the original algorithm the channels initially excluded by the water vapour ‘blacklist’ are reinstated, and for the modified algorithm the error vectors representing water vapour uncertainty are removed.

In line with the 2007 Collard example a further 186 channels are selected in this manner, giving a total of 252 channels. The locations of these channels are also plotted in Fig. 6.4. The locations of the channels appear very similar; despite this $\sim 40\%$ of the 252 are in differing locations. This in part depends upon the channels previously chosen and information already gained. Table 6.2 shows the DFS values for the various retrieval components. The addition of the new channels increases the temperature DFS by over 1 but more noticeably the random and total error curves have also converged, as expected if the primary source of correlated error — the water vapour profile — is now jointly retrieved. This can be seen visually in Fig. 6.6, which shows the vertical temperature error profile after the ‘main run’. The difference between the random and total error components is much smaller than previously but nevertheless, the modified algorithm retains a clear advantage in total error over the original algorithm, while the original algorithm has only a small advantage in random error.

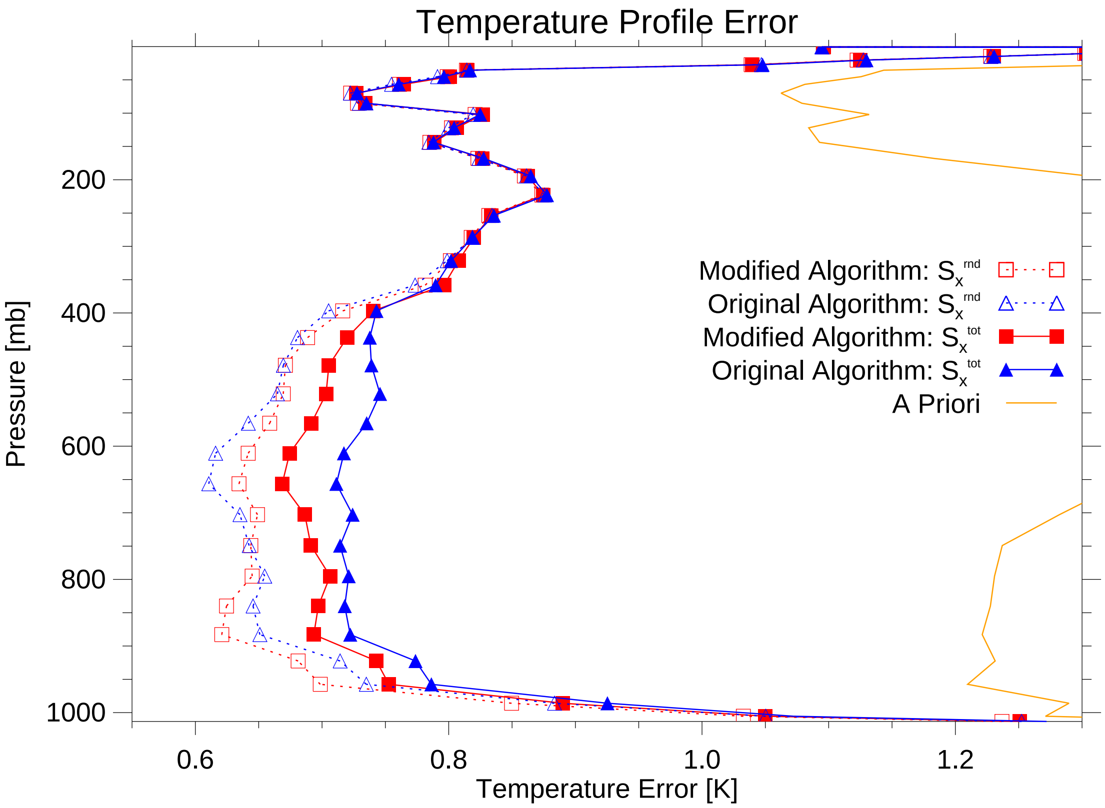

Figure 6.6: As in figure 6.5 but showing the temperature error profiles after a joint retrieval with water vapour using 252 channels

For the water vapour component the conclusions are similar: the original algorithm has a small advantage in random error but the modified algorithm has a large advantage in total error. Again the total error reduction is small. However this is most likely because water vapour has the largest signal in this spectral region so it will not be as adversely affected by the application of the other errors. The vertical water vapour error profile can be seen in Fig. 6.7, which shows that the profile for the modified case is barely changed whereas the original algorithm is worse between 400–800 hPa. This is caused by the second largest contributing error: ozone. Note, however, that there is no improvement at altitudes above the 100 mb surface or in the very lowest levels, where IASI has limited sounding capability (at least for cloud free atmospheres with no surface temperature contrast).

Table 6.2: Degrees of Freedom for Signal per profile of 43 levels from 252 temperature and water vapour channels selected by the original, reproduced, and modified algorithms.

		Collard	Original	Modified
$H_2O_{\{43\}}$	d_s^{rnd}	5.86	6.06	6.04
	d_s^{tot}	5.68	5.67	5.93
$T_{\{43\}}$	d_s^{rnd}	7.53	7.62	7.62
	d_s^{tot}	7.32	7.17	7.44
T_s	d_s^{rnd}	0.99	1.00	1.00
	d_s^{tot}	0.99	0.99	1.00

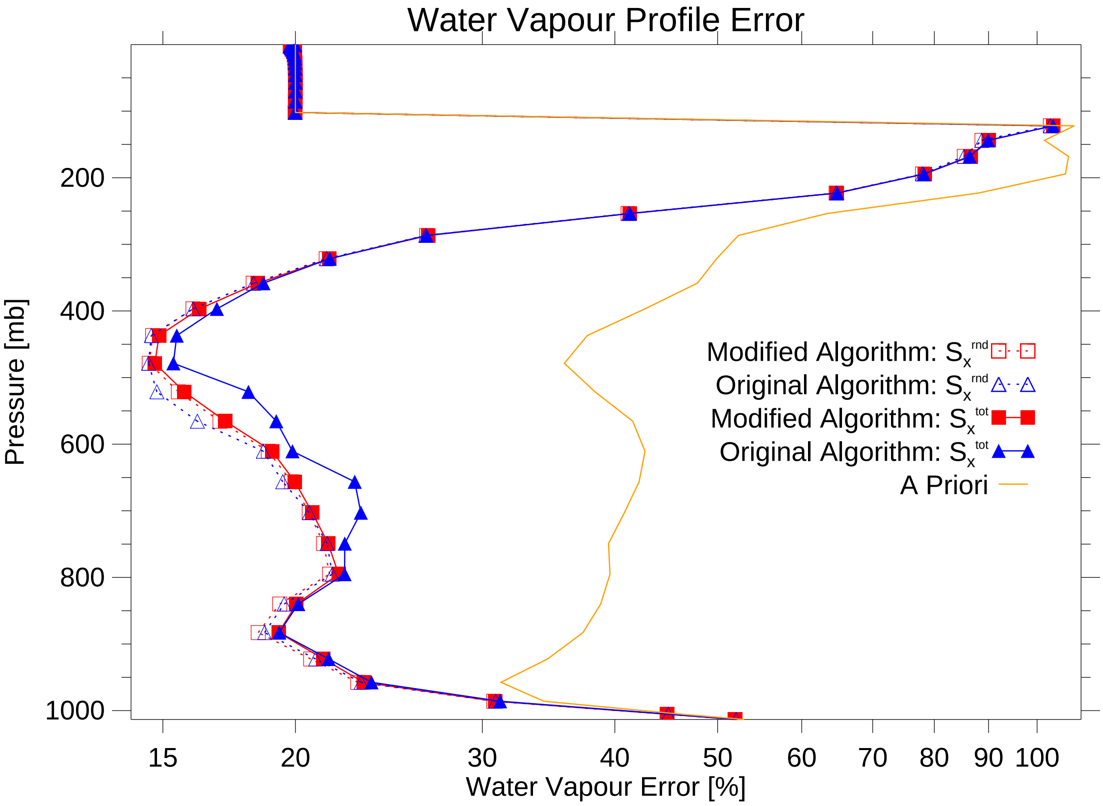

Figure 6.7: Water vapour error profiles from 252 channels for the original algorithm (blue) and the modified algorithm (red). The error due to both the random (dashed line) and total (solid line) errors are shown.

6.3.3 Ozone Channels

Following the selection of temperature and water vapour channels, a further 15 channels are chosen to maximise the ozone information. In this instance, the channel selection is for ozone only and starts from the 252 channels already selected. A correlated background error covariance matrix is assumed with a diagonal of error $(10\,\%)^2$;this value is chosen as it is the upper bound on the accuracy of ozonesondes, which provide vertical profiles with an accuracy of ∼ 5–10% (Boynard et al., 2009). Figure 6.8 shows the expected error profiles for ozone having selected all 267 channels. The two algorithms result in the same 15 ozone channels (although not selected

Table 6.3: Degrees of Freedom for Signal per profile of 43 levels from the 267 channels selected by the original, reproduced, and modified algorithms.

		Collard	Original	Modified
$O_{3\,\{43\}}$	d_s^{rnd}	1.05	1.16	1.15
	d_s^{tot}	1.05	1.16	1.15

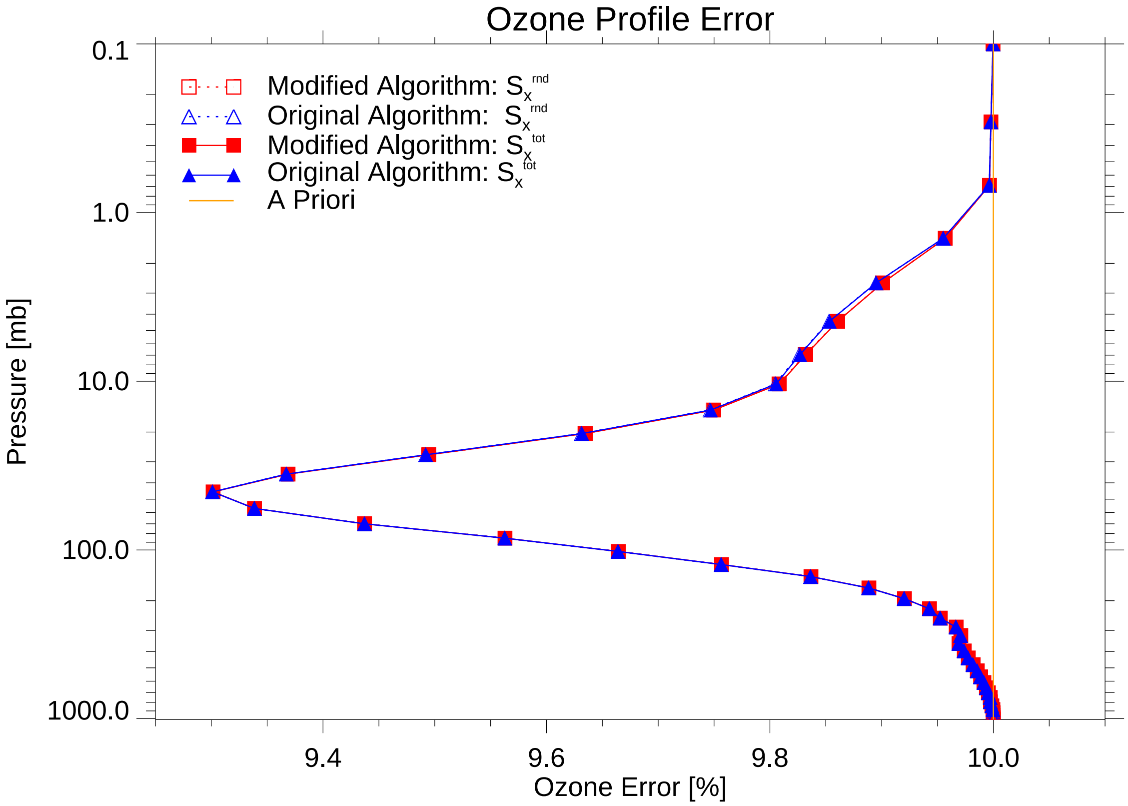

Figure 6.8: Ozone error profiles from 267 channels for the original algorithm (blue) and the modified algorithm (red). The error due to both the random (dashed line) and total (solid line) errors are shown.

in the same order) hence the effect of the total error is the same and the profile errors are almost identical. This is due to there being no large correlated errors (water vapour having been excluded) in the Ozone band between 1000–1100 cm^{-1}. The slightly lower errors seen in the original algorithm between 10–1 mb, and similarly the larger degrees of freedom, are due to the previously selected channels; the modified algorithm reduces the use of channels sensitive to ozone and hence, there is no information already gained on ozone in the selection of the 252 channels.

6.4 Maximum DFS

So far the modified algorithm has been applied on the assumption that the measurements are treated by the retrieval as random, which implies a limit will be reached after which any further channels will start to reduce the DFS for total error. However the question arises: what value DFS could be reached if all the available measurements were combined optimally using the total measurement covariance? This requires solving

$$\mathbf{S}_x^{\mathrm{tot}} = \left(\mathbf{K}^T(\mathbf{S}_y^{\mathrm{tot}})^{-1}\mathbf{K} + \mathbf{S}_a^{-1}\right)^{-1} \tag{6.19}$$

where $\mathbf{S}_y^{\mathrm{tot}}$ (equation 6.5) is now the total measurement error covariance, including the correlated noise between adjacent channels, for the entire set of IASI measurements (or at least all those below 2200 cm^{-1}). This is a large matrix ($m = 6220$) but, for this calculation, it only has to be inverted once.

The resulting maximum DFS available are shown in table 6.4. Both cases achieve similar DFS although Max($\mathrm{d}_s^{\mathrm{tot}}$), which includes the effect of the systematic error components is always slightly reduced.

Figure 6.9 shows the evolution of the DFS as the channel selection progresses. In this case the 'total available DFS' is Max($\mathrm{d}_s^{\mathrm{tot}}$); it is separately calculated for the three runs, accounting for temperature only, the main run of temperature and water vapour, and ozone only. The steep initial curve in all cases shows that most of the

Table 6.4: Maximum Degrees of Freedom for Signal available from the spectral region 645–2200 cm^{-1} per profile of 43 levels plus surface term considering an $\mathbf{R}^{\text{tot}}$ with and without the correlated error components. Separated into the three retrieval types; temperature only, temperature and water vapour, and ozone only.

	Max(d_s^{rnd})	Max(d_s^{tot})
$T_{\{43\}}$	12.63	12.37
T_s	1.00	1.00
$H_2O_{\{43\}}$	7.52	7.50
$T_{\{43\}}$	10.01	9.74
T_s	1.00	1.00
$O_{3\,\{43\}}$	2.25	2.24

information is obtained within the first few channels selected and that towards the end of the selection the channels contain a high fraction of the total information available, with only small improvements being made with the addition of each channel. Similar behaviour is observed for the original algorithm. Initially the algorithms agree very well, but as the selection progresses the original algorithm is adversely affected by its sensitivity to the included error sources and less information is gained (compared to the modified algorithm) on the addition of new channels. This is more pronounced when looking at the original Collard channels, although some of these discrepancies arise from the differences in the reproduction of the original algorithm, such as the forward model and S_a matrices used.

Switching to the 'main run' for temperature and water vapour, both the original algorithm and Collards's channels begin with a larger fractional DFS than the modified version due to no longer considering the errors in water vapour on the previously selected channels. Hence, initially the original algorithm continues to have the greater value but as selection continues the modified algorithm gains more DFS in the first channels and soon has the larger fractional value. Again

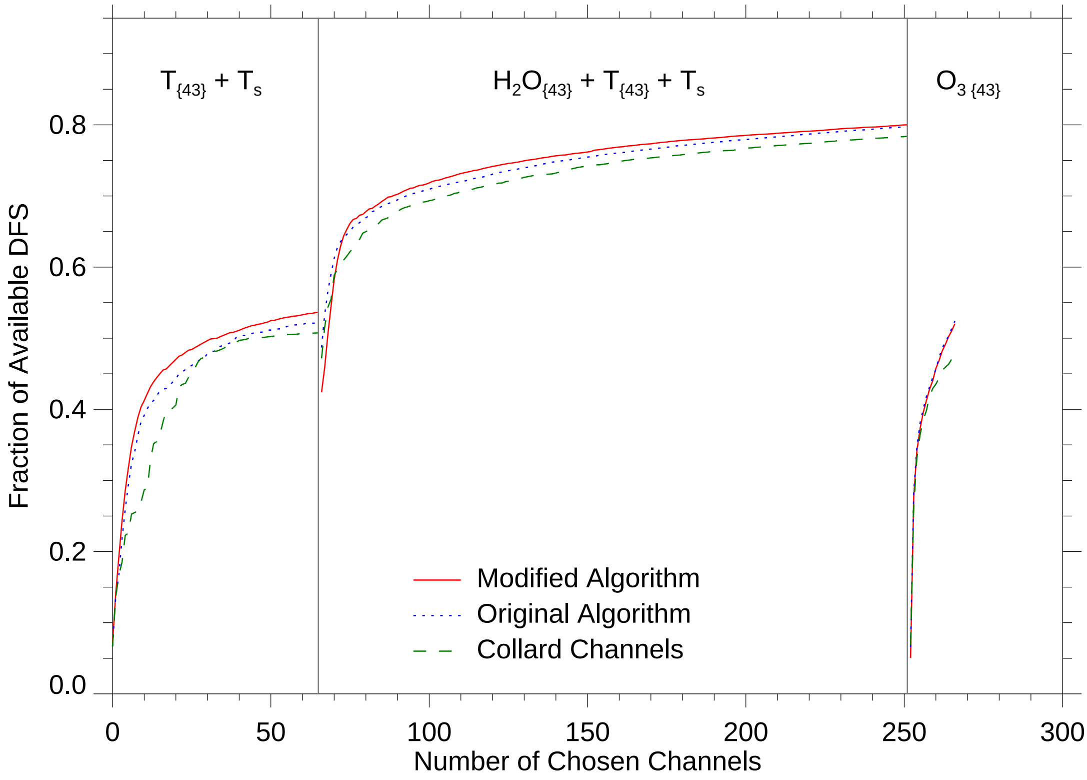

Figure 6.9: The evolution of the DFS during the channel selection, applying the systematic error component to both channel sets. The 'maximum available DFS' is calculated for; purely a temperature analysis, a temperature and water vapour analysis and a purely ozone analysis. The channels selected using the modified algorithm are shown in red, using the original algorithm are shown in blue and the original Collard channels are shown in green.

the Collard channels have a reduced improvement to the DFS, compared to the reproduced channel set, by the selection of certain channels, again highlighting the difference in reproducing the method. However, it can be seen that towards the end of the selection, the improvement to the DFS by all methods by the inclusion of each new channel is approximately the same. Similar behaviour can be seen in the ozone selection, again the original algorithm begins at a larger value than the modified version due to previously considering ozone as a systematic error and therefore there is minimal ozone information already available in the modified case, whereas the channels from the original method have already gained some information from the 252 channels selected. However, after the channel selection both sets contain almost identical amounts of ozone information.

6.5 Channel selection for trace gases

The work of the previous sections has examined optimising channel selection in an NWP context, where the important atmospheric parameters are temperature, water vapour and ozone. It also recreated the method developed by Collard in order to have a baseline with which to compare the modified algorithm. However, the algorithm is not limited to selecting channels for this purpose. A channel set for use in retrievals of trace gases in the atmosphere can be selected that minimises the impact of spectrally interfering species and maximises the information gained on any chosen species, such as was previously carried out for ozone.

The suggested method for choosing such a set of channels implements the same modified algorithm as described previously, with two alterations:

- The selection is carried out as a joint retrieval of the target molecule along with surface temperature, atmospheric temperature and water vapour
- The total DFS for each channel, d_s^{tot}, is only evaluated from the matrix elements associated with the target molecule

The joint retrieval is chosen as it is simpler to implement than including separate error contributions from temperature and water vapour which, having large signals, dominate certain spectral regions, e.g. the methane band, whilst only considering the DFS for the target molecule ensures it is the information on the absorber that is improved and not that of temperature or water vapour. The channels previously selected for temperature and water vapour in section 6.3 are assumed to have been pre-selected, and therefore channels adjacent to these are also initially excluded in the selection. However, it should be noted that in the calculation of the maximum available DFS, $\mathrm{Max}(\mathrm{d}_s^{\mathrm{tot}})$, as described in section 6.4, all IASI channels from 645–2200 cm^{-1} are included.

For the selection of the first new channel the *a priori* error covariance, $\mathbf{S}_a$, is calculated assuming the impact of the pre-selected channels, with the initial background error covariance matrix for the chosen trace gas assumed to have a diagonal of error $(100\%)^2$ and a correlation length of 10 levels in order to account for some realistic vertical correlation within the atmosphere. This large initial error assumption aims to maximise the information contribution from the measurements by assuming we have little prior knowledge of the profile.

In line with the Collard selection for ozone, 15 channels have been selected. Despite the situation not occurring during the following selections, it should be noted that if the contribution to the DFS were to become zero or, in the case of the modified algorithm, negative, the selection would be terminated.

The channel selection has been carried out for ozone (O_3), methane (CH_4), carbon monoxide (CO) and nitrous oxide (N_2O).

6.5.1 Ozone

The first trace gas examined is ozone, as a comparison to the method used previously, where temperature and water vapour are assumed to be known and the retrieval was purely for ozone. All the channels selected by the new method lie within the range 1025–1075 cm^{-1} used in ozone retrievals by both Boynard et al. (2009) and Keim et al. (2009) and can be seen in figure 6.10.

In the previous selection for ozone, both the original and modified algorithms selected identical channels; noticeably, this is not the case this time, although many are the same. Despite this, the DFS gained by both algorithms are almost identical, and can be seen in table 6.5. The total DFS available, as defined in section 6.4, is also shown. The values for DFS are larger than those in the previous selection for ozone due to the *a priori* error estimate being larger in this case, therefore there is relatively more information to be gained. Nevertheless, the values agree well with those found by Boynard et al. (2009) and Eremenko et al. (2008) who expect $\sim$ 3–4 DFS. Keim et al. (2009) compare several ozone retrieval schemes from different research institutes and found the DFS for a total column retrieval varied between 1.5 and 4 across the algorithms. This highlights the variation caused by both retrieval method and *a priori* assumption.

Table 6.5: Degrees of Freedom for Signal per profile of 43 levels from the 15 'trace gas' and 252 pre-selected channels selected by the original and modified algorithms, along with the maximum DFS available for the spectral region 645–2200cm^{-1}.

		Original	Modified	Maximum
$\mathrm{O}_{3\,\{43\}}$	$\mathrm{d}_s^{\mathrm{rnd}}$	3.68	3.70	4.92
	$\mathrm{d}_s^{\mathrm{tot}}$	3.68	3.69	4.90
$\mathrm{CH}_{4\,\{43\}}$	$\mathrm{d}_s^{\mathrm{rnd}}$	3.93	4.18	5.01
	$\mathrm{d}_s^{\mathrm{tot}}$	3.93	4.15	5.22
$\mathrm{CO}_{\{43\}}$	$\mathrm{d}_s^{\mathrm{rnd}}$	1.81	1.87	2.47
	$\mathrm{d}_s^{\mathrm{tot}}$	1.80	1.83	2.47
$\mathrm{N}_2\mathrm{O}_{\{43\}}$	$\mathrm{d}_s^{\mathrm{rnd}}$	3.16	3.30	4.11
	$\mathrm{d}_s^{\mathrm{tot}}$	3.05	3.27	4.22

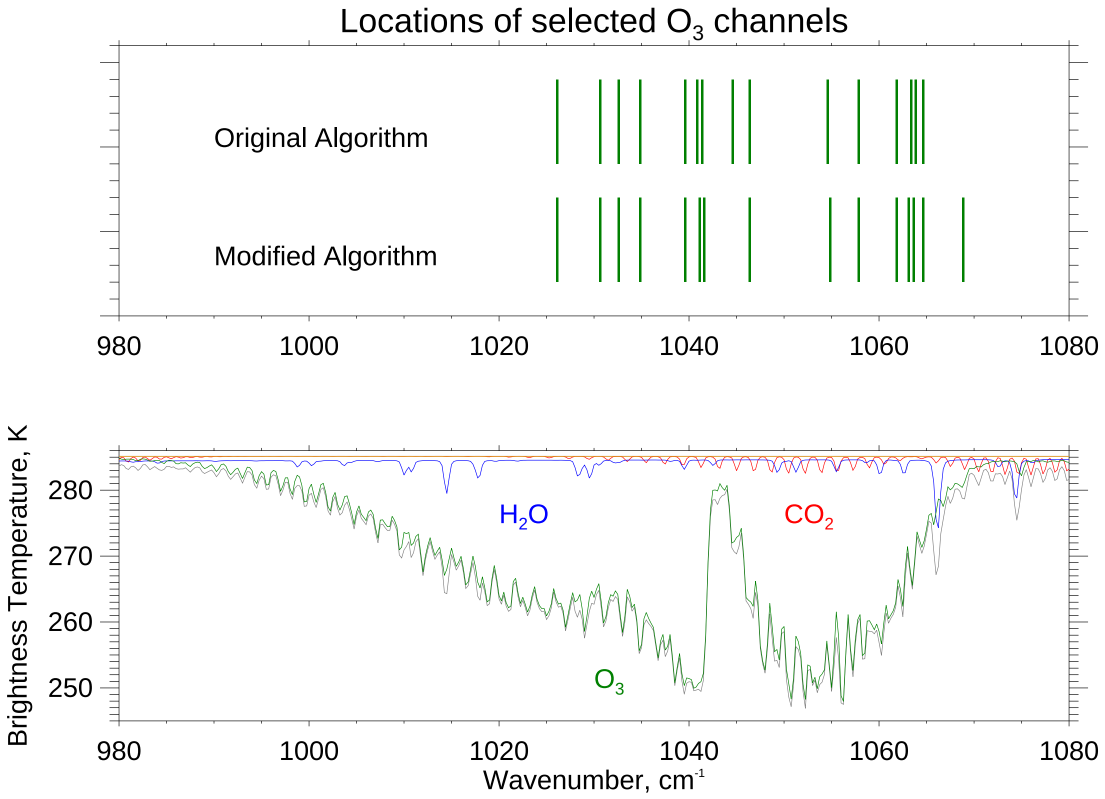

Figure 6.10: The locations of the 15 channels selected by the original and modified algorithms for ozone. The lower plot shows a typical IASI spectrum in grey, with the spectral features for CO_2 and H_2O overplotted

6.5.2 Methane

The selection algorithm was subsequently applied to methane, which has several other primary absorbers, such as H_2O and N_2O, overlapping its spectral features. These can be seen in figure 6.11 along with the selected channels. Again a large proportion of the same channels are selected for both methods. Crevoisier et al. (2009) select the 9 channels between 1301–1305cm^{-1} least sensitive to water vapour for tropospheric methane retrievals, whereas Razavi et al. (2009) exclude the region above 1310cm^{-1} due to water vapour interference and limit their retrieval to the range 1240–1290cm^{-1}. In both cases, the modified algorithm implemented here selects only 3 channels within each specified range. The channels selected by Xiong et al. (2013) are the most similar to those presented here, although that selection extends to 60 channels. The channels lie within the same range, 1230–1370cm^{-1}, and are selected to minimise the impact of H_2O and N_2O by including the uncertainty in assumed parameters as noise, hence the similarity to the modified algorithm.

Table 6.5 shows the DFS obtained by each algorithm for the 15 channels. Surprisingly the modified algorithm claims more DFS than the original algorithm. There are two factors that contribute towards this: firstly, in the selection of the previous 252 channels, the original method would exclude channels affected by methane, whereas if the water vapour contribution was large enough the modified algorithm would have chosen the channel and therefore gained some information. Secondly, the original algorithm excludes channels affected by N_2O, whose spectral features significantly overlap with methane, whereas the modified algorithm is able to select these channels if the contribution to methane DFS outweigh the negative impact from N_2O. The DFS shown for methane are much larger than that shown in the literature of ~ 1 (see Crevoisier et al. (2009), Razavi et al. (2009) and Xiong et al. (2013)) however this is due to the pessimistic *a priori* error assumed: with a more realistic *a priori* error covariance the DFS value would be lower than that shown here.

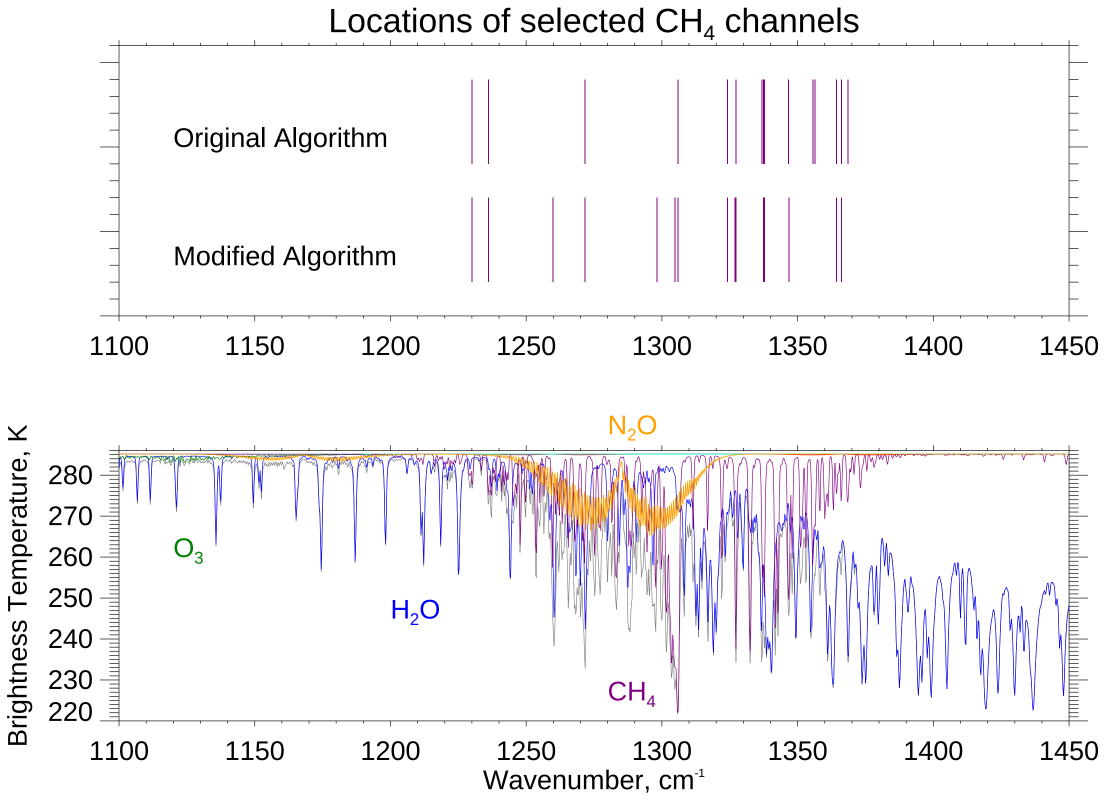

Figure 6.11: The locations of the 15 channels selected by the original and modified algorithms for methane. The lower plot shows a typical IASI spectrum in grey, with the spectral features for H_2O, N_2O and O_3 overplotted

6.5.3 Carbon monoxide

Applying the selection to carbon monoxide whose spectral signature is weaker than those of ozone and methane and, like methane, has several interfering species, results in the channels shown in figure 6.12. As in the previous examples several of the channels selected are the same in both algorithms, however those selected by the modified algorithm can be seen to avoid the peaks in absorbtion due to the other molecules. The similarity in channels is expected for CO given the relatively small number of distinct lines within the CO spectrum. Retrievals of CO by George et al. (2009), Turquety et al. (2009), Kerzenmacher et al. (2012) and Illingworth et al.

(2011) all use the spectral range surrounding the CO R-branch, 2143–2181.25 cm^{-1}, which is also the region that contains the majority of the channels selected here. Nevertheless, several channels are selected outside of this range, where the impact of the interfering species is considered small relative to the CO information.

Comparing the DFS available for CO, shown in table 6.5, it can be seen that it is only half that available for the other trace gases. Despite this, the channel selections still manage to obtain over half of the maximum available information. The values shown are also in good agreement with those given by Turquety et al. (2009) and George et al. (2009) as ~ 1.8–2.2 and ~ 0.8–2.4 respectively.

As with methane, the DFS obtained for the modified algorithm is slightly larger than that for the original algorithm. This occurs for the same reasons as previously mentioned, due to the modified algorithm allowing the selection of channels if the improvement to the DFS of the chosen absorber negates the impact of the interfering species.

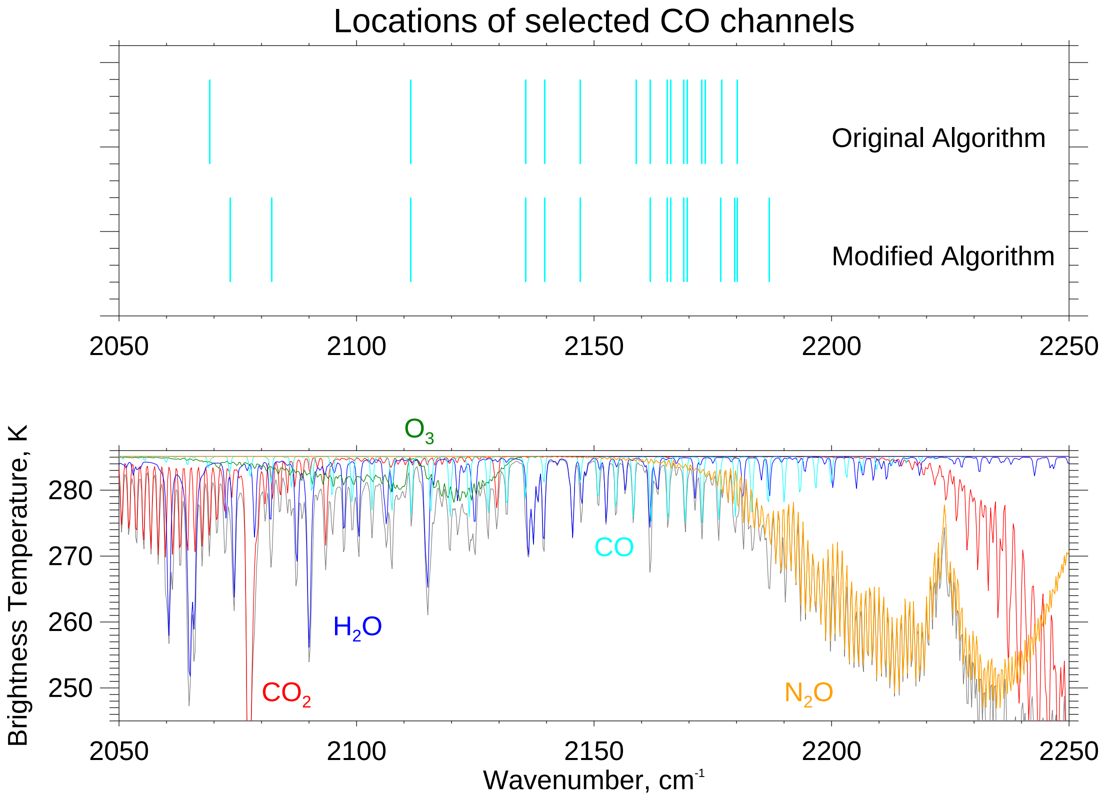

Figure 6.12: The locations of the 15 channels selected by the original and modified algorithms for carbon monoxide. The lower plot shows a typical IASI spectrum in grey, with the spectral features for CO_2, H_2O, N_2O and O_3 overplotted

6.5.4 Nitrous oxide

The selection of 15 channels for the retrieval of N_2O, shown in figure 6.13, exhibit the same behaviour as that of the previous species; the DFS obtained for the modified algorithm is slightly larger than that for the original algorithm. Again this occurs due the ability of the modified algorithm to select a channel if the improvement to the DFS of the target molecule outweighs the impact of an interfering species, as opposed to fully excluding it. In this case the interfering species are mostly CH_4 and H_2O, with the impact of the latter being reduced due to the joint retrieval.

In the selection shown all the channels lie within the ν_1 band centered at 1285 cm^{-1}, with no channels being selected in the ν_3 band centered at 2224 cm^{-1}. This differs significantly compared to the channels suggested by Lubrano et al. (2004) and Ricaud et al. (2009), both of whom prefer use of the ν_3 band to avoid spectral interference from H_2O and CH_4: the former choosing the spectral range of 2195–2215 cm^{-1}, and the latter selecting 30 channels within the ν_3 band and only 4 channels from the ν_1 band. The reason for the difference is due to this method of selection taking into account the interfering species.

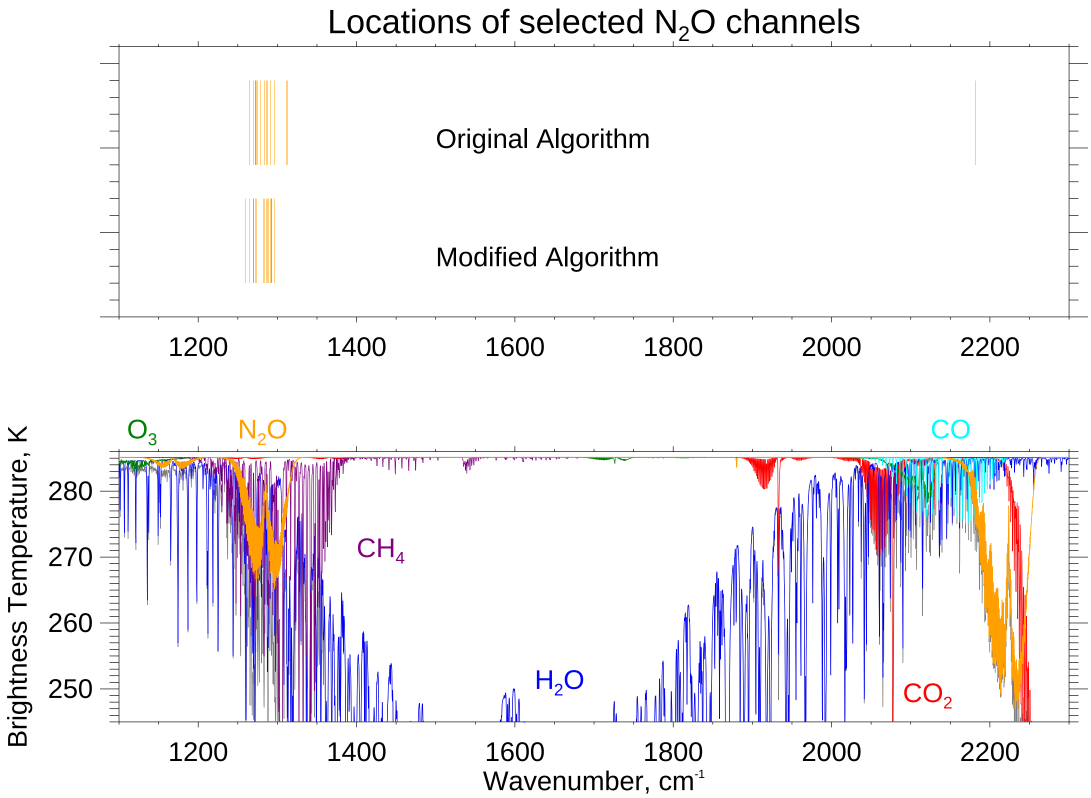
Locations of selected N_2O channels

Figure 6.13: The locations of the 15 channels selected by the original and modified algorithms for nitrous oxide. The lower plot shows a typical IASI spectrum in grey, with the spectral features for CO_2, H_2O, CH_4, O_3 and CO overplotted

6.6 Column amount retrievals for trace gases

Given the low values of the DFS for each absorber, i.e. much smaller than the number of retrieval levels in the state vector, profile retrievals are impractical, therefore it is more useful to consider the effect upon the retrieval of column amount (the transformation from atmospheric profile to column amount was described in section 3.7). The column amount can also be split into partial columns, i.e. a tropospheric column and stratospheric column, where in this case the tropopause height is assumed to be at 15 km.

Many space-borne instruments give information on trace species atmospheric distribution, however they are usually only sensitive to certain levels in the atmosphere. For example, limb viewing instruments such as the Michelson Interferometer for Passive Atmospheric Sounding (MIPAS, Fischer et al. (2008)), the Atmospheric Chemistry Experiment (ACE, Bernath et al. (2005)) and the Halogen Occultation Experiment (HALOE, Russell et al. (1993)) provide good vertical resolution but only in the upper troposphere and stratosphere. Nadir viewing infrared instruments, including IASI and AIRS (the Atmospheric Infrared Sounder), have sensitivity limited to the mid to upper troposphere and lower stratosphere.

The main quantity of interest from IASI, as a nadir-viewing instrument, is the tropospheric column amount. However, thermal contrast at the surface can provide problems in retrieving absorber concentration in the lower troposphere and boundary layer, which, in regions close to emission sources (of for example CH_4 or CO) is highly variable.

Using instruments with sensitivity to different atmospheric regions together might provide the potential to improve our knowledge of this region. Essentially, combining the information retrieved by IASI in the mid-troposphere with that of a limb viewing instrument such as MIPAS, which gives an accurate stratospheric column, could result in an improvement in the accuracy of the tropospheric column. Therefore, alongside the column errors produced using the selected channels, the effect on the tropospheric column from improving the knowledge of the stratospheric column is investigated. Also shown is the impact of a positive 10 K thermal contrast at the surface upon the tropospheric column.

Looking at table 6.5 it can be seen that the DFS achieved through the use of both algorithms is extremely similar in all cases, although the modified algorithm is marginally, but consistently larger. It can also be seen that, for each absorber, $\mathrm{d}_s^{\mathrm{rnd}} \sim \mathrm{d}_s^{\mathrm{tot}}$, which indicates that the dominant error source in each situation is the random noise and there is little performance difference between the two algorithms. Given the similarity of the results for both algorithms, the following section only considers the channels selected by the modified algorithm and the total error contribution.

For interest, on top of the species previously examined, results are shown for carbon dioxide (CO_2), despite no channel selection having been made. Since the temperature retrieval selects channels sensitive to CO_2, the channels needed for a retrieval have already been chosen and negligible new information would be gained by the addition of further CO_2 channels. Therefore, for CO_2 only the 252 channels selected for temperature and water vapour are considered, with CO_2 being added to the state vector.

Table 6.6: The DFS and percentage errors in retrieved total, tropospheric, and stratospheric column amounts with different retrieval assumptions for O_3, CH_4, CO, N_2O, and CO_2

	$\mathbf{S}_a$		Baseline	+ known stratosphere	+10K thermal contrast	+ both
CH_4	100%	$\mathrm{d}_s^{\mathrm{tot}}$	4.37	3.21	4.63	3.47
		$\mathrm{S}_{\mathrm{col}\{strat\}}$ [%]	45.92	–	46.02	–
		$\mathrm{S}_{\mathrm{col}\{trop\}}$ [%]	13.98	13.29	6.42	5.51
		$\mathrm{S}_{\mathrm{col}\{tot\}}$ [%]	12.06	12.05	5.04	4.97
	10%	$\mathrm{d}_s^{\mathrm{tot}}$	1.69	1.52	1.92	1.75
		$\mathrm{S}_{\mathrm{col}\{strat\}}$ [%]	9.69	–	9.69	–
		$\mathrm{S}_{\mathrm{col}\{trop\}}$ [%]	3.55	3.51	2.56	2.51
		$\mathrm{S}_{\mathrm{col}\{tot\}}$ [%]	3.21	3.19	2.32	2.29
O_3	100%	$\mathrm{d}_s^{\mathrm{tot}}$	3.90	1.94	4.03	2.08
		$\mathrm{S}_{\mathrm{col}\{strat\}}$ [%]	7.57	–	6.92	–
		$\mathrm{S}_{\mathrm{col}\{trop\}}$ [%]	21.05	13.67	18.66	8.13
		$\mathrm{S}_{\mathrm{col}\{tot\}}$ [%]	5.50	2.11	4.90	1.32
	10%	$\mathrm{d}_s^{\mathrm{tot}}$	1.68	1.02	1.78	1.06
		$\mathrm{S}_{\mathrm{col}\{strat\}}$ [%]	4.40	–	4.15	–
		$\mathrm{S}_{\mathrm{col}\{trop\}}$ [%]	7.24	3.06	6.65	2.43
		$\mathrm{S}_{\mathrm{col}\{tot\}}$ [%]	2.97	0.46	2.78	0.36
CO	100%	$\mathrm{d}_s^{\mathrm{tot}}$	1.95	1.91	2.10	2.07
		$\mathrm{S}_{\mathrm{col}\{strat\}}$ [%]	97.69	–	98.02	–
		$\mathrm{S}_{\mathrm{col}\{trop\}}$ [%]	20.10	20.10	8.51	8.48
		$\mathrm{S}_{\mathrm{col}\{tot\}}$ [%]	19.73	19.38	8.71	8.25
	10%	$\mathrm{d}_s^{\mathrm{tot}}$	1.01	1.01	1.08	1.08
		$\mathrm{S}_{\mathrm{col}\{strat\}}$ [%]	10.20	–	10.20	–
		$\mathrm{S}_{\mathrm{col}\{trop\}}$ [%]	4.43	4.42	3.23	3.23
		$\mathrm{S}_{\mathrm{col}\{tot\}}$ [%]	4.26	4.25	3.11	3.10
N_2O	100%	$\mathrm{d}_s^{\mathrm{tot}}$	3.45	2.95	3.72	3.22
		$\mathrm{S}_{\mathrm{col}\{strat\}}$ [%]	52.21	–	51.87	–
		$\mathrm{S}_{\mathrm{col}\{trop\}}$ [%]	11.10	10.62	4.45	3.54
		$\mathrm{S}_{\mathrm{col}\{tot\}}$ [%]	9.76	9.69	3.64	3.30
	10%	$\mathrm{d}_s^{\mathrm{tot}}$	1.48	1.45	1.68	1.64
		$\mathrm{S}_{\mathrm{col}\{strat\}}$ [%]	9.78	–	9.77	–
		$\mathrm{S}_{\mathrm{col}\{trop\}}$ [%]	2.51	2.48	1.47	1.43
		$\mathrm{S}_{\mathrm{col}\{tot\}}$ [%]	2.29	2.26	1.38	1.31
CO_2	100%	$\mathrm{d}_s^{\mathrm{tot}}$	6.89	3.91	7.15	4.18
		$\mathrm{S}_{\mathrm{col}\{strat\}}$ [%]	27.37	–	27.26	–
		$\mathrm{S}_{\mathrm{col}\{trop\}}$ [%]	9.90	9.77	4.00	3.48
		$\mathrm{S}_{\mathrm{col}\{tot\}}$ [%]	8.80	8.63	3.37	3.10
	10%	$\mathrm{d}_s^{\mathrm{tot}}$	2.50	1.76	2.73	1.99
		$\mathrm{S}_{\mathrm{col}\{strat\}}$ [%]	8.06	–	8.06	–
		$\mathrm{S}_{\mathrm{col}\{trop\}}$ [%]	3.00	2.95	1.90	1.84
		$\mathrm{S}_{\mathrm{col}\{tot\}}$ [%]	2.63	2.60	1.70	1.63

The DFS obtained for each species, alongside the percentage error in the total, tropospheric ($< 15\,\mathrm{km}$), and stratospheric ($> 15\,\mathrm{km}$) column amount following a joint retrieval of the target molecule with temperature and water vapour can be seen in table 6.6.

In the 'baseline' calculation, the *a priori* error covariance, $\mathbf{S}_a$, as previously assumed, has a correlation length of 10 levels. This correlation is needed due to the inability of nadir viewing instruments to see the boundary layer and therefore to be able to calculate a total tropospheric column a strong *a priori* vertical correlation must be assumed. However, this must be seen as an optimistic case as the boundary layer is often more detached from the free troposphere. The *a priori* error is also weighted appropriately so that both the tropospheric column amount error and stratospheric column amount error equal 100% (or 10% depending upon the test).

Three modifications to this baseline retrieval are then made: $\mathbf{S}_a$ is modified to include an error estimate for the stratosphere that assumes it is perfectly well known. Essentially, the stratospheric components of $\mathbf{S}_a$ are replaced with an error of negligible value. In reality the covariance would be created using the output of a limb viewing instrument such as MIPAS. From this it can be investigated how an improvement in the sounding of the stratosphere may help with the retrieval of the tropospheric column amount. For comparison, the effect of introducing a positive surface thermal contrast of 10K into the retrieval is shown, and the subsequent effect of also having perfect knowledge of the stratosphere. The results can all be seen in table 6.6.

Looking at table 6.6 it is clear that the knowledge gained from a perfect stratosphere has minimal effect upon the error in tropospheric column amount, with the exception of O_3. With an initial column amount error of 100% the improvement is $< 0.5\%$ and with an initial column amount error of 10% the improvement is $< 0.1\%$. In fact for CO the improvement is as small as 0.01%. In these cases the total column amount error is driven by the tropospheric column error. As mentioned, the exception is O_3, where the impact of stratospheric knowledge is large; in the case of an initial error of 10%, the tropospheric column amount error is reduced to only $\sim 0.5\%$. These results must be placed in context with the distribution of the species throughout the atmosphere. Table 6.7 presents the percentage of the total column amount contained with the specified troposphere and stratosphere. As perhaps expected, those unaffected by the additional stratospheric knowledge are the absorbers that are largely concentrated within the troposphere, whereas O_3, which is largely concentrated in the stratosphere is able to improve the estimate of the tropospheric column through better quantification of the bulk of the absorber. However, the reason there is little effect upon the tropospheric column for most species cannot be entirely placed on the location of the absorber as a proportion of each absorber does lie in the stratosphere. Instead it highlights that IASI is not sensitive to the stratospheric absorption lines of the molecules, for example in the case of CH_4, because the lines are too narrow for IASI's spectral resolution. This is demonstrated by the averaging kernels associated with each retrieval. The averaging kernels show the sensitivity of the retrieval to the true state, as described in section 3.2, and the kernels for each retrieval level can be seen in figures 6.14 and 6.15 for ozone and methane respectively. Despite ozone being primarily located within the stratosphere, the altitudes at which there is the greatest sensitivity lie in the troposphere. Similarly, despite methane being well mixed within the troposphere, the region of greatest sensitivity is the upper troposphere, with minimal sensitivity near the surface. In both cases, but most noticeably methane, the averaging kernels are broad and hence resolving information at individual levels is difficult. The effect of including perfect knowledge of the stratosphere is shown for both cases: for methane, the effect is negligible and the sensitivity in the troposphere is unchanged, hence the small difference in tropospheric column amount error whereas for ozone the sensitivity of the levels in the troposphere, especially the upper troposphere, increases leading to the improvement seen in the tropospheric column error.

Table 6.7: Percentage of total column amount contained within the troposphere and stratosphere

	Total Column Amount [DU]	Tropospheric Column	Stratospheric Column
CH_4	1375.96	91.0%	9.0%
O_3	300.09	15.1%	84.9%
CO	80.21	96.2%	3.8%
N_2O	242.14	91.1%	8.9%
CO_2	293410.50	88.1%	11.9%

In comparison, the effect upon the tropospheric column amount due to a thermal contrast of 10K is large for species concentrated in the troposphere and that have large surface emission sources, reducing the errors by over half in most case, whereas it is much reduced when applied to O_3. The improvement is due to being able to better sound the lower atmosphere and boundary layer due to the large temperature difference between the surface and the atmospheric levels. As mentioned before this estimate will be quite optimistic due to the large vertical correlation assumed. The change in sensitivity to the true state can be seen to improve near the surface in the methane averaging kernels, shown in figure 6.15, but have only a small improvement in the ozone averaging kernels, shown in figure 6.14. On applying the assumption of a perfectly known stratosphere the effect is also the same as described previously: there is minimal improvement.

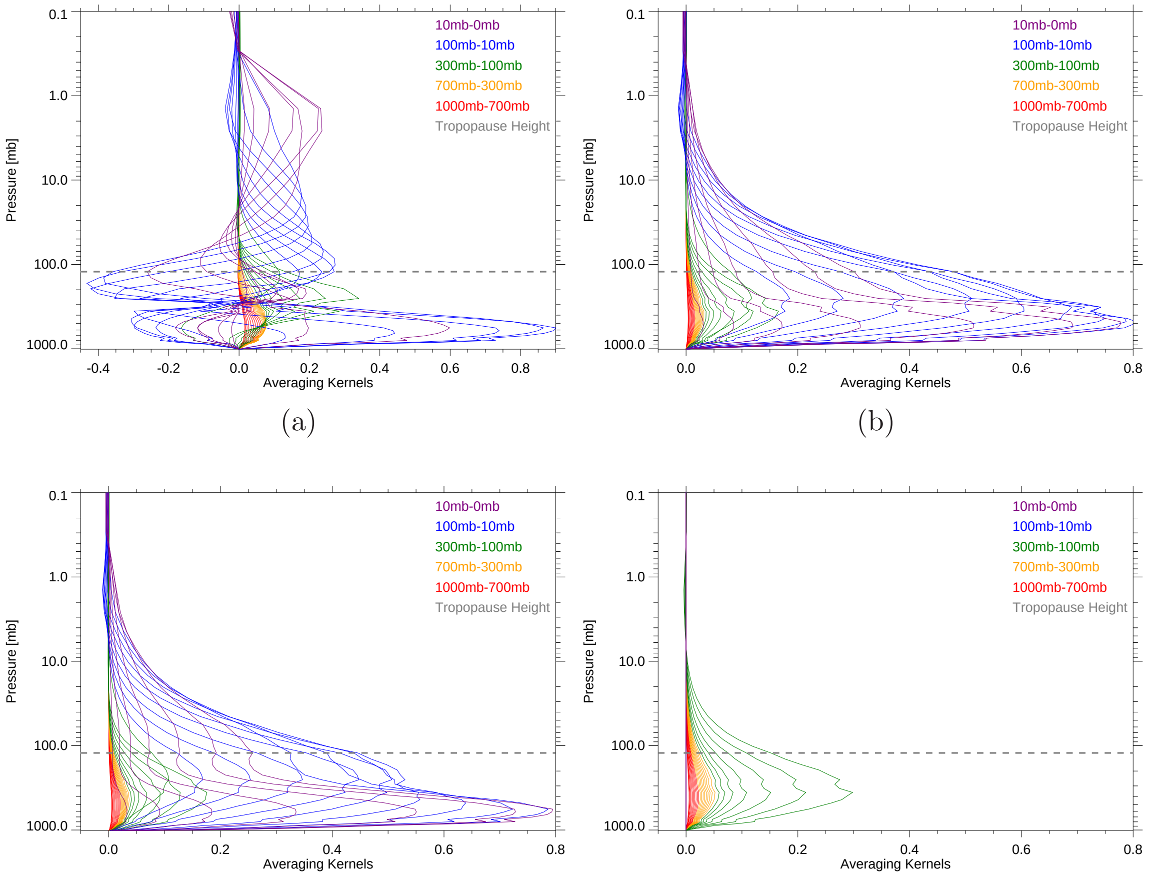

(a) (b) (c) (d)

Figure 6.14: Averaging kernels for ozone profiles assuming (a) tropospheric and stratospheric *a priori* column amount errors of 100%, (b) tropospheric and stratospheric *a priori* column amount errors of 10%, (c) tropospheric and stratospheric *a priori* column amount errors of 10% plus a +10 K thermal contrast at the surface and (d) a tropospheric *a priori* column amount error of 10% plus a perfectly known stratosphere.

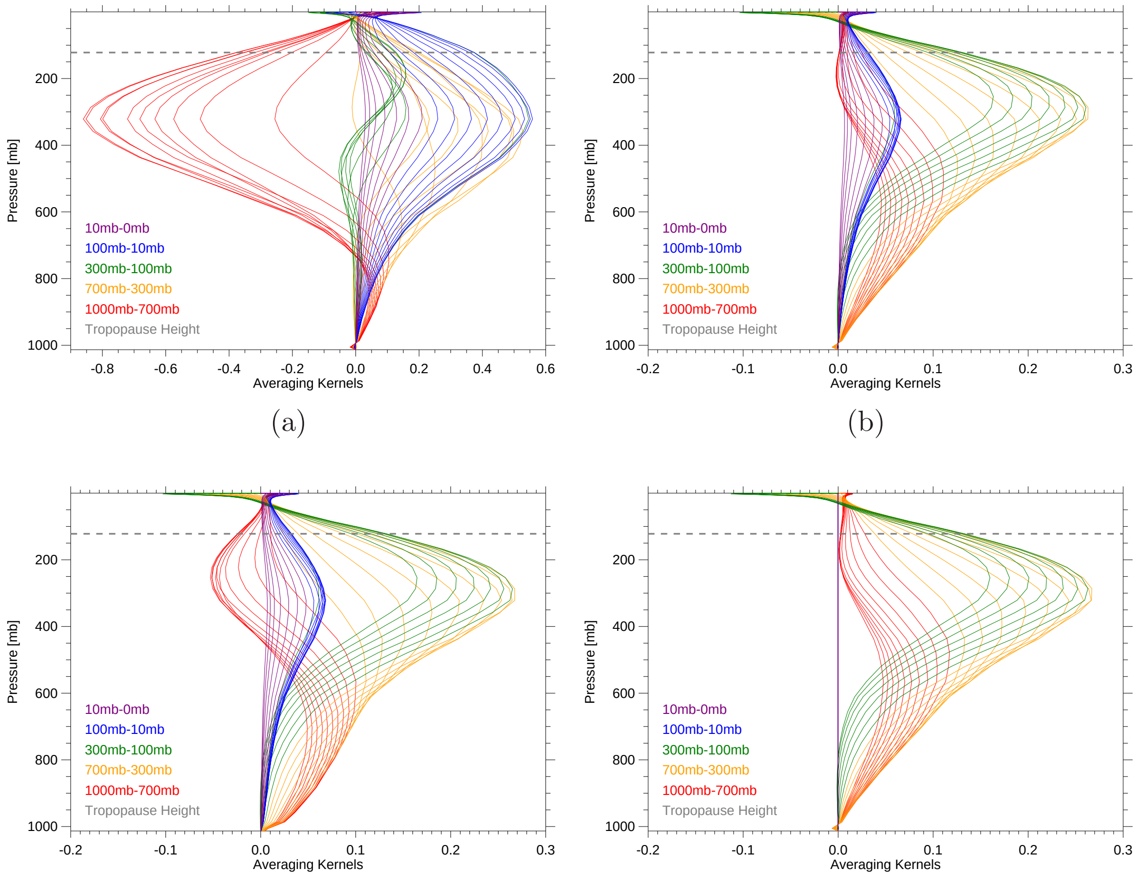

(a) (b)

(c) (d)

Figure 6.15: Averaging kernels for methane profiles assuming (a) tropospheric and stratospheric *a priori* column amount errors of 100%, (b) tropospheric and stratospheric *a priori* column amount errors of 10%, (c) tropospheric and stratospheric *a priori* column amount errors of 10% plus a +10 K thermal contrast at the surface and (d) a tropospheric *a priori* column amount error of 10% plus a perfectly known stratosphere.

6.7 Summary

A new method for the selection of IASI channels has been presented. Through comparison with the algorithm used currently to select the operational NWP channels, it has been shown that the new algorithm maintains the same number of DFS whilst reducing the sensitivity of the channel set to unknown (or unspecified) spectral correlations. The methods are intrinsically the same in that the channels are selected based upon their contribution to the DFS. However, where the previous method only considers the random component of the error and fully excludes certain channels from being chosen, the new method incorporates, for example, the effects of species' atmospheric variability within the selection process as a correlated error.

Although carried out within an NWP context to allow comparison, the new selection method can be generalised to the selection of channels for the retrieval of any species.

In the case of minor species, there is only a small improvement by the modified algorithm due to the dominance of the random noise. However, with the modified algorithm a full error analysis is obtained. Also, in retrievals over large areas, which involve spatial averaging of the IASI data, the noise becomes relatively less important and the benefits of the modified algorithm will be larger.

It has been shown that the tropospheric column retrieval benefits more from a strong thermal contrast at the surface than from improved knowledge of the stratosphere. In essence, combining information from limb and nadir viewing instruments to improve the error in tropospheric column amount does not appear promising for species largely concentrated within the troposphere and that have large variability near the surface. However, for species such as O_3 that are largely concentrated in the stratosphere, greater knowledge of the stratosphere does provide additional information that can improve tropospheric estimates.

Chapter 7

Forward Model Comparisons

Many radiative transfer models (RTM's) are available to simulate IASI spectra. These include line-by-line models such as the RFM or LBLRTM (AER, Atmospheric and Environmetal Research (2012)), and fast radiative transfer models such as RTTOV. The methodology of each model type was described in chapter 4 and the differences between them were outlined.

Ideally the differences between RTM's lie well below the instrument noise level and in chapter 5 we have examined how to optimise the set-up of the RFM and minimise the effects of potential error sources. However, different RTM's will have been optimised for their own purpose, for example using different spectroscopic databases or molecular continuum models. Any differences not removed by bias correction will propagate through retrieval schemes and give rise to discrepancies in the output retrieved parameters.

Previous large scale RTM comparisons have been carried out such as looking at the simulation of AIRS data by Saunders et al. (2007) or simulation of high-resolution spectra, applicable to IASI, by Tjemkes et al. (2003). Here we examine only three radiative transfer models, one fast model, RTTOV, and two line-by-line models, the RFM and LBLRTM. The focus of the comparisons is to ascertain discrepancies between the RFM and RTTOV, using LBLRTM to clarify the results. One fundamental concept of the fast RT model is that it should be able to reproduce, with sufficient accuracy, the results of the line-by-line model in near real time.

7.1 Configuring the Radiative Transfer Models

7.1.1 RTTOV

Section 4.2.2 described how the transmittance, calculated by RTTOV, at each wavenumber is determined as a function of profile dependent predictors and regression coefficients. These coefficients are derived using accurate line-by-line calculated transmittances from a training set of atmospheric profiles. The training set of transmittances are calculated using the LBLRTM (Line-by-line Radiative Transfer Model).

The key settings within the LBLRTM implemented in the generation of the training set of transmittances are summarised in table 7.1 and include:

- Version 11.1 of the LBLRTM (LBLRTM_v_11.1) atmospheric transmittance and radiance model.
- The Voigt line shape is used at all atmospheric levels for all gases except for CO_2, for which the χ-factor correction is used.
- Line mixing parameters are used for the CO_2 P/Q/R branches. The parameters were created using the HITRAN 2000 line data using the method by Niro et al. (2005)

- Continua are included for O_2 and N_2 using the same models as the RFM by Thibault et al. (1997) and Lafferty et al. (1996) respectively.

- The water vapour continuum model MT_CKD_2.1 is used within LBLRTM_v_11.1. However, the H_2O continuum is not included within the main transmittance calculations. Separate water vapour continuum transmittances are generated and regression coefficients are calculated through a linear regression of the model transmittances against the predictor values, generated by the profile variables. The water vapour transmittances are then predicted by RTTOV using these regression coefficients. This follows the method by Matricardi (2003)

- The 'linear in tau' approximation is implemented to handle Planck function variations within the atmospheric layers.

- The following atmospheric constituents were included and their concentrations allowed to vary: H_2O, O_3, CO_2, N_2O, CO and CH_4

- The following atmospheric constituents were included but considered 'fixed', i.e. their profile concentrations were held constant, as the spatial and temporal variation in their concentration is assumed not to affect observed radiances significantly: NO_2, SO_2, NO, N_2, O_2, HNO_3, OCS, CCl_4, CF_4, CFC-11 and CFC-12. The AFGL atmospheric profiles were assumed for all gases except HNO3 and NO for which the profiles were generated using the MOZART chemical transport model. The profiles of CCl_4, CF_4, CFC-11 and CFC-12 were scaled to reflect present day concentrations.

- A merged spectroscopic database containing line parameters from both HITRAN and GEISA databases (listed in table 7.1). The CO_2 line parameters must be from HITRAN 2000 in order to be consistent with the line mixing coefficients by Niro et al. (2005). This database was created after results in Matricardi (2007) show better agreement can be achieved between observations and simulations using alternative line parameters in different regions.

The transmitances used within the regression were calculated:

- from 0.005 hPa to each of the pressure levels in the ‘RTTOV’ altitude grid shown in 5.15
- for each atmospheric profile in the 83 diverse profile dataset, which will be described in more detail in section 7.2.1
- for six different path angles whose secants are equally spaced between 1 and 2.25 (additional angles are also included, to model the solar term in RTTOV, with secants 2.58, 3.94, 3.72, 4.83, 6.1, 7.2 and 9) for a plane-parallel atmosphere, although RTTOV itself allows for the curvature of the Earth.

7.1.2 RFM

The RFM is configured as per the recommendations given in chapter 5 for accurate modelling in order to replicate the IASI spectrum. Some of the optional settings are enabled to ensure the most accurate comparison with RTTOV, shown in table 7.1.

Table 7.1: The features included in comparisons of the RFM and RTTOV. For RTTOV, the settings include the relevant features of its training model, LBLRTM.

Feature	RTTOV	RFM
Altitude Grid	101 pressure levels (1100–0.005 mb)	Same
'Linear in tau' approximation	Included as standard	Enabled
Line Mixing	CO_2 P/Q/R branches (Niro et al., 2005)	CO_2 Q branches (Strow et al., 1994)
Line Shape	CO_2 χ-factor Voigt elsewhere	CO_2 χ-factor (Doucen et al., 1985) Voigt elsewhere
Molecular continua	H_2O: MT_CKD_2.1	H_2O: MT_CKD_2.5 (Mlawer et al., 2012)
	N_2 (Lafferty et al., 1996)	N_2 Same
	O_2 (Thibault et al., 1997)	O_2 Same
	CO_2	CO_2
Composition	H_2O, O_3, CO_2, CO, N_2O, CH_4, NO_2, SO_2, HNO_3, NO, N_2, O_2, CFC–11, CFC–12, OCS, CCl_4, and CF_4	Same
Spectroscopic Database	400–800 cm^{-1} GEISA 2003 800–1000 cm^{-1} HITRAN 2004/06 1000–1100 cm^{-1} HITRAN 2000 1100–1700 cm^{-1} HITRAN 2004/06 1700–2400 cm^{-1} GEISA 2003 2400–3000 cm^{-1} HITRAN 2004/06 All CO_2 line data - HITRAN 2000	Same

7.2 Model Comparison

In order to fully test the capabilities of each model, a diverse profile data set is required that will represent the range of values that can be expected for temperature and absorber amount within the atmosphere.

7.2.1 Dependent Profile Data Set

Initially for these comparisons the profile data set used to train the IASI RTTOV regression coefficients is employed to ascertain the accuracy of the model itself. The profile set contains a selection of 83 profiles, for night time scenes over ocean, and detailed explanations on its formation can be found in Matricardi (2008). Although this will not be independent from the RTTOV training transmittances, it is the profile set that it should be able to recreate accurately. The temperature, water vapour and ozone profiles are a subset taken from the database by Chevallier et al. (2006), which is formulated from profiles generated by the ECMWF forecasting system for the time period July 2006–July 2007 and the spread of the profiles can be seen in figure 7.1. As suggested by Chevallier et al. (2002), the number of profiles can be reduced from the large number in the original database to a manageable quantity for use with line-by-line models through random sampling, as this would still retain the probability distribution of the original dataset.

Other methods were used to formulate the trace gas profile data. In the case of carbon dioxide, carbon monoxide and methane, the profiles were created from archived data co-located with the previously selected profiles of temperature, water vapour and ozone. These profile concentrations were then scaled by appropriate rates of increase to the year 2009. The profiles included can be seen in figure 7.2.

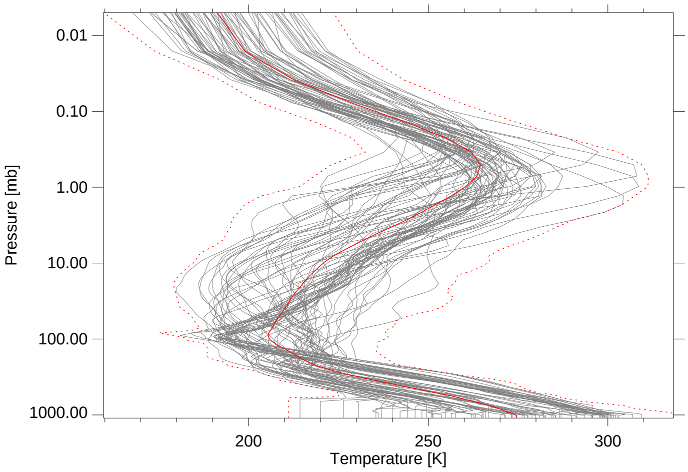

(a)

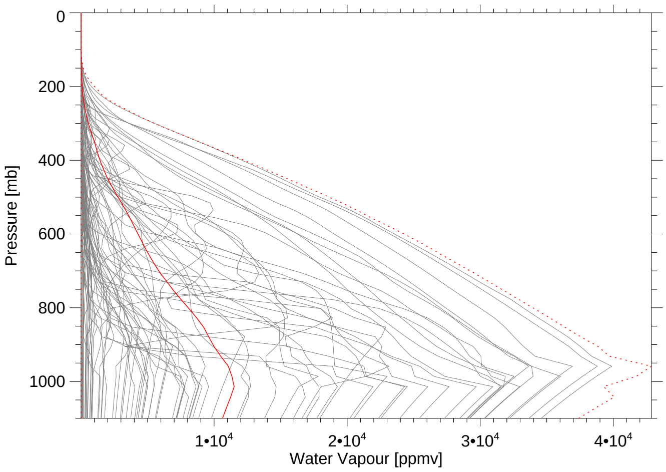

(b)

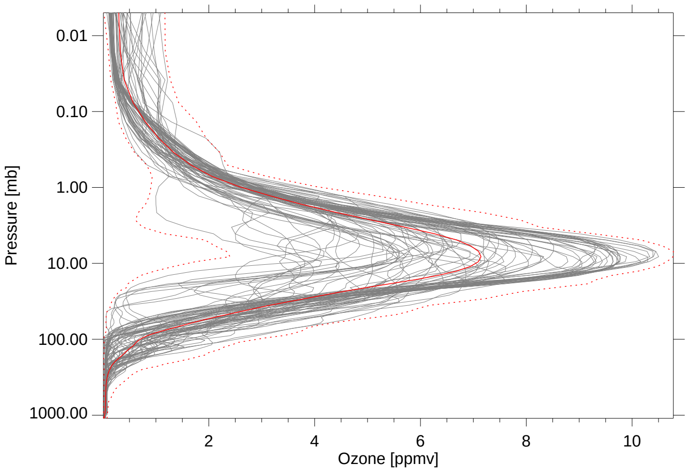

(c)

Figure 7.1: The diverse reference profile set of 83 profiles used in the forward model comparisons for a)temperature, b)H_2O and c)O_3. The extreme profiles and the profile mean are indicated in red.

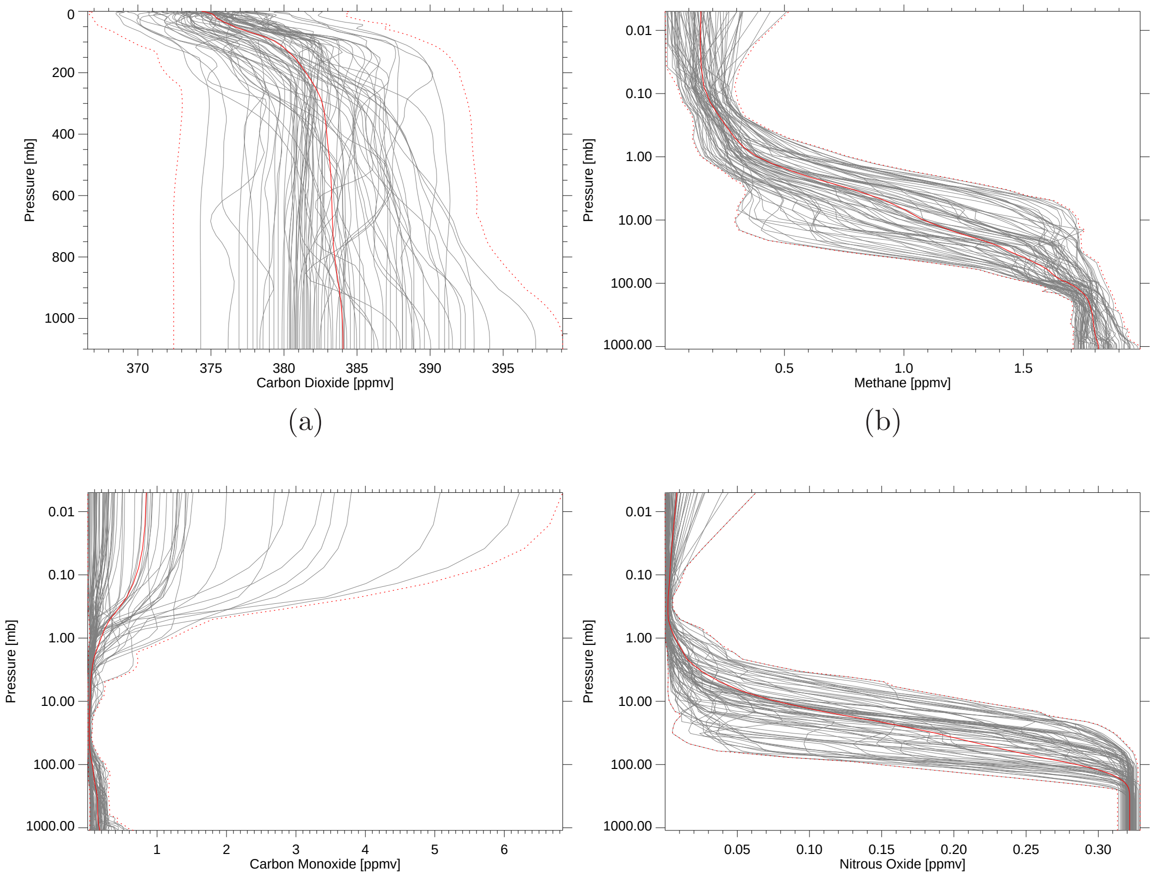

(a) (b)

(c) (d)

Figure 7.2: The diverse reference profile set of 83 profiles used in the forward model comparisons for a)CO_2, b)CH_4, c)CO and d)N_2O. The extreme profiles and the profile mean are indicated in red.

However, for nitrous oxide the profiles were generated using data from CLAES (Cryogenic Limb Array Etalon Spectrometer) and ground based measurements from the CMDL (Climate Monitoring and Diagnostics Laboratory) and AGAGE (Advanced Global Atmospheric Gas Experiment) programs using the method described in Matricardi (2003), which were also scaled to reflect the appropriate concentration in 2009 and are shown in figure 7.2d. All 83 profiles and their corresponding surface parameters can be found at the following website: `http://research.metoffice.gov.uk/research/interproj/nwpsaf/rtm/profile_datasets.html`. The ‘fixed’ trace gases use the atmospheric profiles as described in section 7.1.1.

Although the fast model coefficients are trained to reproduce transmittance, the following comparisons are shown in terms of both radiance, as this is the quantity produced by IASI, and brightness temperature, for ease of visualising discrepancies.

Spectra are calculated using the RFM and RTTOV for each atmospheric profile and at five different path angles whose secants are equally spaced between 1 and 2. Given that the RFM does not have an internal surface emissivity calculation and in order to maintain as much consistency as possible, the sea surface emissivity calculated by RTTOV is fed into the RFM so that both models assume the same spectrally varying values. An example of how the emissivity varies with wavelength and viewing angle can be seen in figure 7.3. The emissivity is a function of wavelength, zenith angle and surface roughness (caused by wind speed), however, it has been shown that emissivity is approximately independent of wind speed at zenith angle $< 60°$ and therefore it is not included in the model used here. The zenith angle dependence is caused by the change in refractive index between different mediums and is given by the Fresnel equations, explained in more detail by Sherlock (1999).

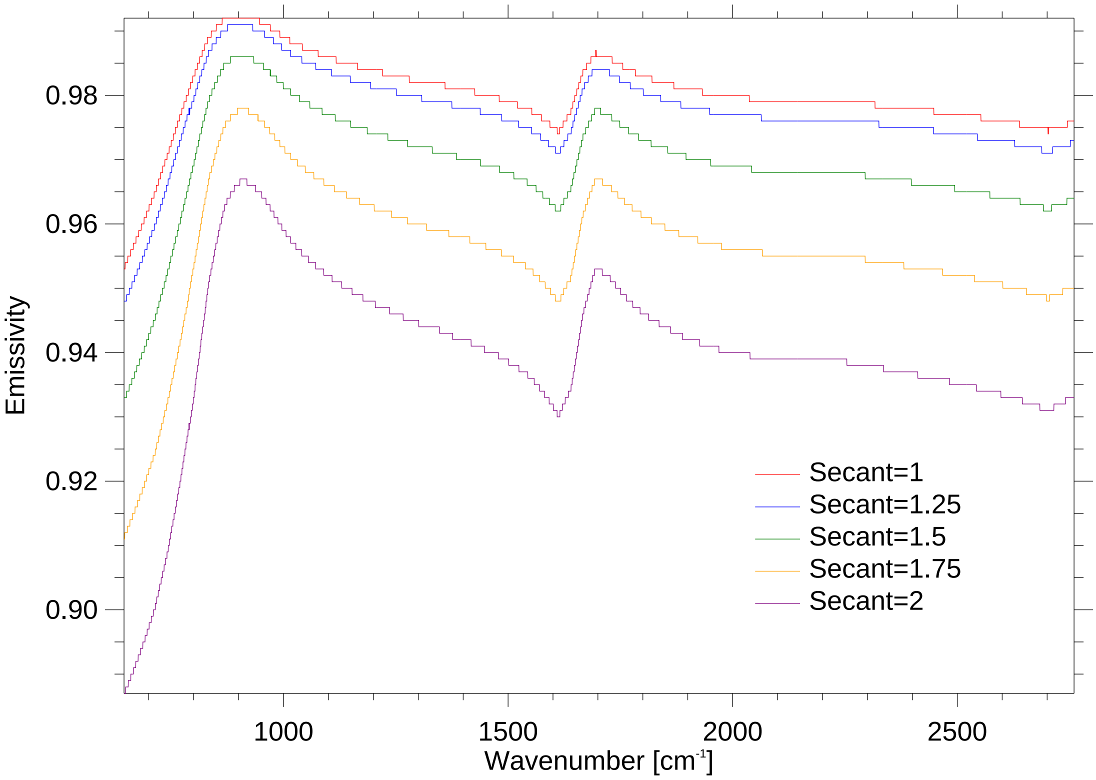

Figure 7.3: The variation in sea surface emissivity with wavenumber at different path angles.

Results can be seen in figures 7.4a and 7.4b where the mean value (bias) and standard deviation of the differences between spectra produced by the RFM and RTTOV for the 80 profiles at 5 viewing angles are shown. Three of the profiles are excluded from comparisons as they represent the maximum, minimum and mean profiles of the dataset and are therefore not necessarily realistic. As expected, the model differences are larger than those between the LBLRTM and RTTOV shown by Matricardi (2008). However the bias values are similar to those found by Tjemkes et al. (2003) and Matricardi (2007). Good agreement can be seen across the ν_2 water vapour band with biases of $\sim 0.1\,\mathrm{K}$ and, outside of the CO_2 bands, the biases lying

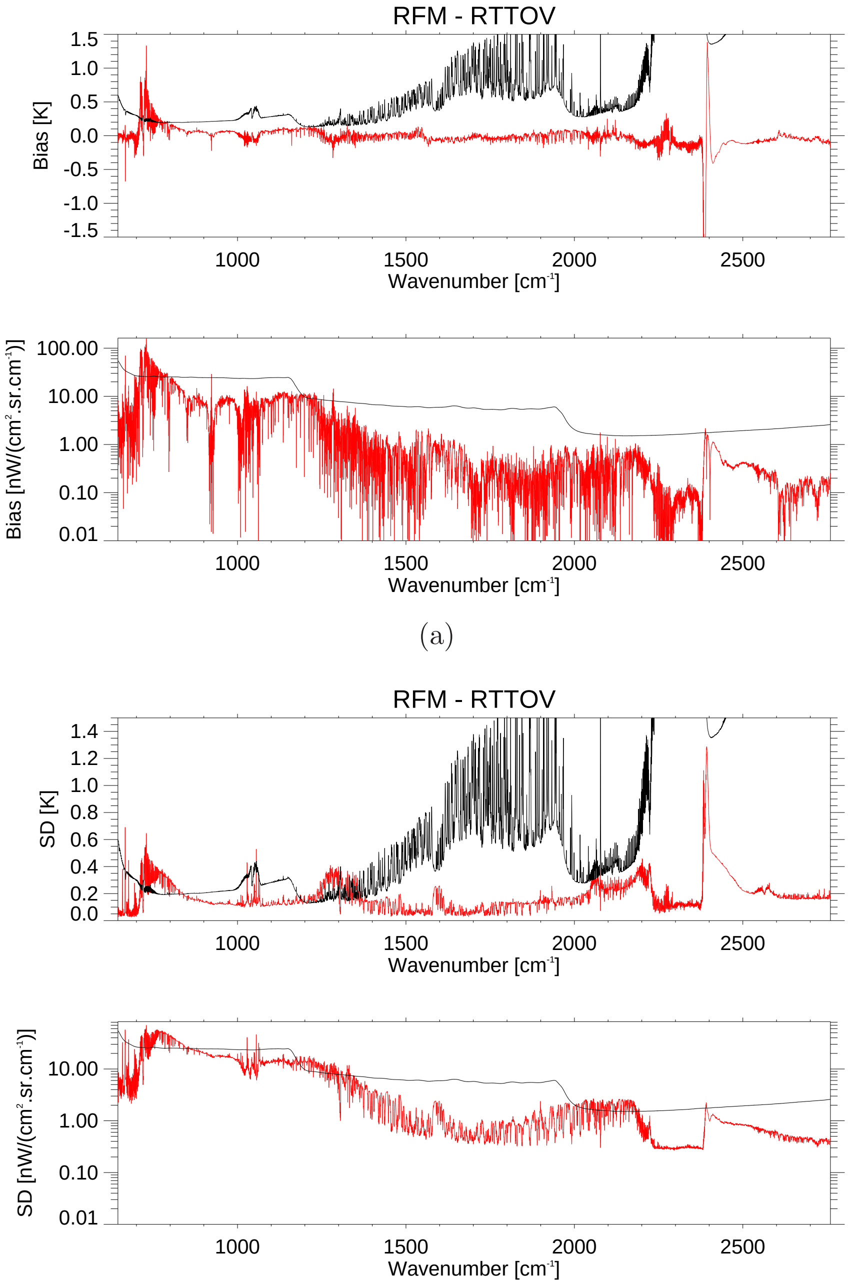

(a)

(b)

Figure 7.4: a)The mean value (bias) and b)the standard deviation of the differences between the RFM and RTTOV for 80 profiles at 5 viewing angles are shown in red. The IASI noise is shown in black for reference.

below the IASI noise. Despite this agreement, large standard deviations can be observed in the regions surrounding 750 cm^{-1}, 1050 cm^{-1}, 1300 cm^{-1} and between 2000–2500 cm^{-1}.

In the CO_2 ν_2 band (640–800cm $^{-1}$) the large bias and standard deviation are probably due to the inclusion of the P- and R- branch line coupling by Niro et al. (2005) within the LBLRTM, which also causes a recalculation of the CO_2 continuum. This has been demonstrated by Alvarado et al. (2013) to cause a large residual between updates of the LBLRTM model where these line parameters have been introduced, and their impact can clearly be seen here. This difference in line shape assumption is also responsible for the large peak in the bias at 2400 cm^{-1}.

Small biases are observed in the O_3 ν_3 band at 1050 cm^{-1} but the standard deviation in this region is relatively large. Each of the remaining spectral regions with large standard deviations coincide with regions of interfering species (including the shorter wavelengths within the CO_2 ν_2 band). Surrounding the CH_4 ν_4 band (1250–1350 cm^{-1}) and the fundamental CO band (2050–2250 cm^{-1}) there is interference from both N_2O and H_2O. For the latter, Alvarado et al. (2013) show that an update to the H_2O self continuum in the MT_CKD_2.5 model, used by the RFM, improved the fit to observations near the CO_2 ν_3 bandhead but in doing so degraded the fit within the CO band. It is likely that this change in the continuum is responsible for the spread shown by the comparisons within the CO band

Figure 7.5 shows the percentage of channels at each viewing angle whose RMS error lies within certain binned values. Matricardi (2008) found that $\sim 98\%$ of channels had RMS values less than 0.1K in comparisons between the LBLRTM and RTTOV with weak angular dependence; here, as expected, the results are not as good as this. However there is still agreement of better than 0.4K in $\sim 95\%$ of the channels.

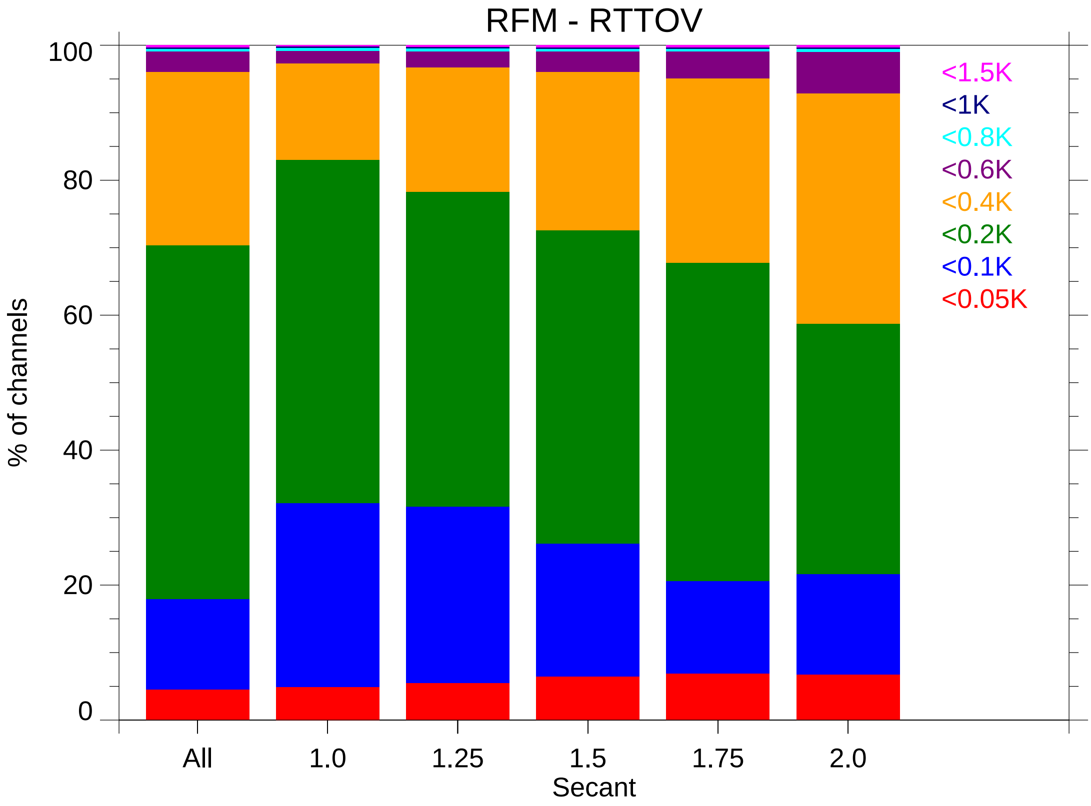

Figure 7.5: The percentage of channels with given RMS errors for all viewing angles combined and at each separate viewing angle.

The next step is to establish the extent to which these discrepancies can be explained by the differences between the RFM and RTTOV's underlying line-by-line model, LBLRTM. Unfortunately the LBLRTM radiances for this profile data set were not available but they were available for an alternative profile set and will be discussed in section 7.2.2.

7.2.2 Independent Profile Data Set

Given that the RTTOV regression coefficients for simulating the IASI spectrum were trained using the previous profile dataset, it is necessary to carry out comparisons with an independent set of profiles in order to ascertain uncertainties caused by the variation between atmospheric profiles. An independent set of profiles, which are again a subset of the profile database by Chevallier et al. (2006), was provided by Marco Matricardi, ECMWF (private communication). The set of 100 profiles is taken from the larger selection used in the training of the the principal component version of RTTOV and is described fully by Matricardi (2010). As before, reducing the number of profiles from those in the original database is possible through random sampling, as this retains the probability distribution of the original dataset. All selected profiles are considered to be clear sky and over the ocean.

In this profile set only temperature, water vapour and ozone are allowed to vary and the spread of the profiles can be seen in figures 7.6a–7.6c.

As previously, the ‘fixed’ trace gases use the AFGL atmospheric profiles as described in section 7.1.1 and in this data set the fixed profiles for carbon dioxide, carbon monoxide, nitrous oxide and methane come from the mean climatological profile described in the previous section and explained by Matricardi (2008).

This profile data set was chosen due to the availability of equivalent LBLRTM spectra, enabling a direct comparison between LBLRTM and the RFM and the ability to ascertain which RFM–RTTOV discrepancies arise due to the fast model approximations and which arise due to differences between the RFM and the LBLRTM line-by-line model used to train RTTOV.

Spectra are calculated using the RFM and RTTOV for each atmospheric profile and at five different path angles whose secants are equally spaced between 1 and 2. As in the previous comparison, the surface emissivity calculated by RTTOV is fed into the RFM to maintain consistency. These are subsequently compared with the equivalent LBLRTM spectra calculated for a plane parallel atmosphere.

The biases and standard deviations of the 3–way comparison can be seen in figures 7.7 and 7.8 respectively. It is immediately apparent that the bias between the RFM and RTTOV is almost entirely due to the bias between the line-by-line models and is caused by, for example, differences in the continua and CO_2 line parameters as described in the previous section.

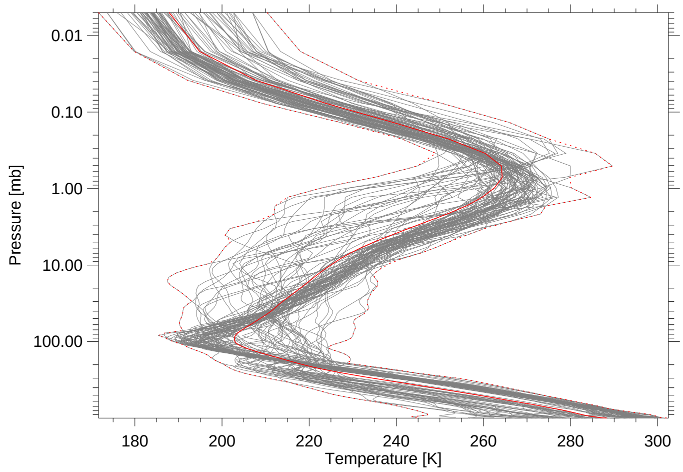

(a)

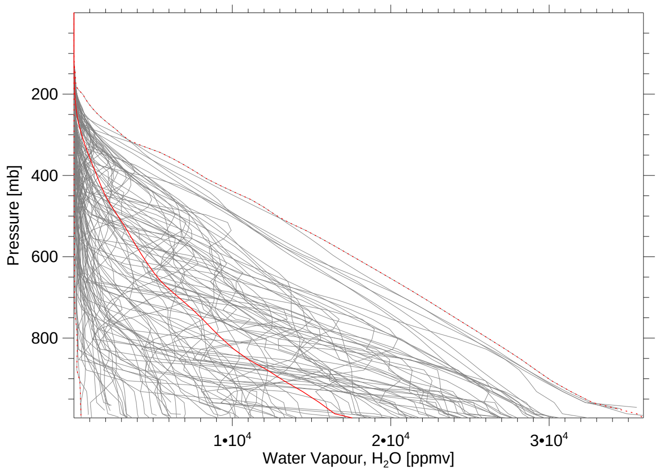

(b)

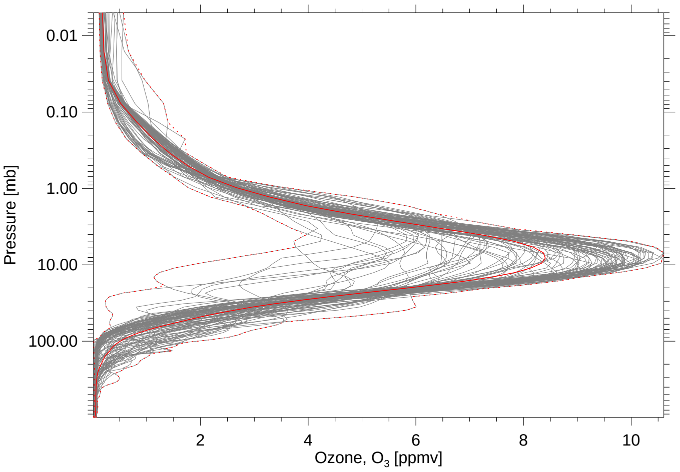

(c)

Figure 7.6: The independent profile data set of 100 profiles used in the forward model comparisons for a)temperature, b)H_2O and c)O_3. The extreme profiles and the profile mean are indicated in red.

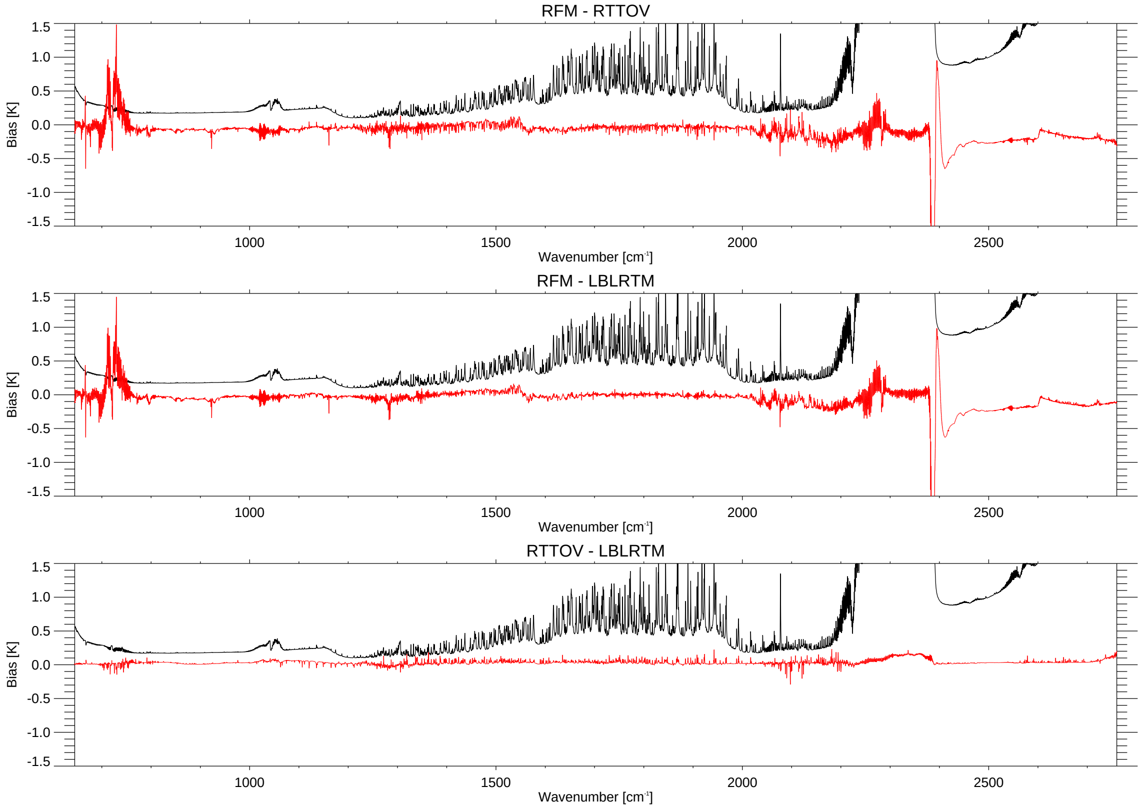

Figure 7.7: The mean value (bias) of the differences between the RFM, RTTOV and LBLRTM for 100 independent profiles at 5 viewing angles are shown in red. The IASI noise is shown in black for reference.

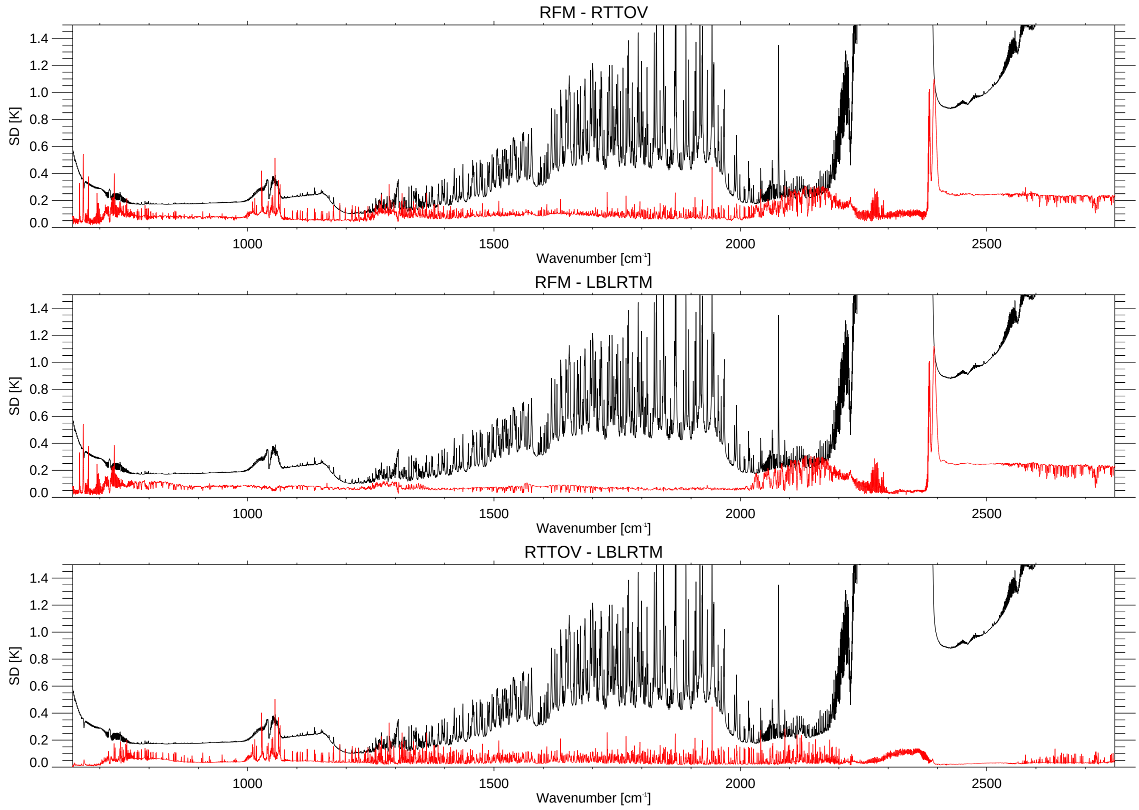
RFM - RTTOV

RFM - LBLRTM

RTTOV - LBLRTM

Figure 7.8: The standard deviation of the differences between the RFM, RTTOV and LBLRTM for 100 independent profiles at 5 viewing angles are shown in red. The IASI noise is shown in black for reference.

The RFM–RTTOV bias is also extremely similar to the bias from the dependent profile set, suggesting it is minimally affected by the profile data set chosen. The RTTOV–LBLRTM bias is, by comparison, small and on a par with that observed by Matricardi (2008) for another independent set of profiles.

Comparing the observed standard deviations enables us to confirm which deviations are caused by the fast model and which are caused by the line-by-line discrepancies. The large deviations in the CO_2 ν_2 and ν_3 band, and across the fundamental CO band can be seen to be due to the line-by-line differences previously mentioned: from updates to the H_2O continuum and the inclusion of P- and R-branch line coupling. However there are certain discrepancies that arise in comparisons between both line-by-line models and RTTOV; within the O_3 ν_3 band and the CH_4 ν_4 band. These larger deviations were observed by Matricardi (2008) and are expected to be caused by the formulation of coefficients in regions of interfering water vapour lines with the respective gases.

The percentage of channels at each viewing angle whose RMS error lies within certain binned values can be seen for each intercomparison in figure 7.9. As in Matricardi (2008), nearly 100% of channels have an rms error below 0.2K in the RTTOV–LBLRTM comparison, with $\sim$ 90% below 0.1K. Agreement between the RFM and LBLRTM is also encouragingly good, with $\sim$ 80% of channels having an rms error less than 0.2K and in the nadir case this value increases to $\sim$ 95%. The results are similar for the RFM–RTTOV comparison, with $\sim$ 80% of channels having an rms error less than 0.2K. However, it can be seen that in this case a larger percentage of the channels lie within the 0.1–0.2K bin than in the LBLRTM comparison. Apart from the clear agreement in the nadir between the RFM and LBLRTM, there is only a weak angular dependence upon the results. The angular dependence is in fact better than that for the dependent profile data set but this is likely to be caused by the use of fixed CO, CO_2, CH_4 and N_2O profiles as their variation will not be having an impact.

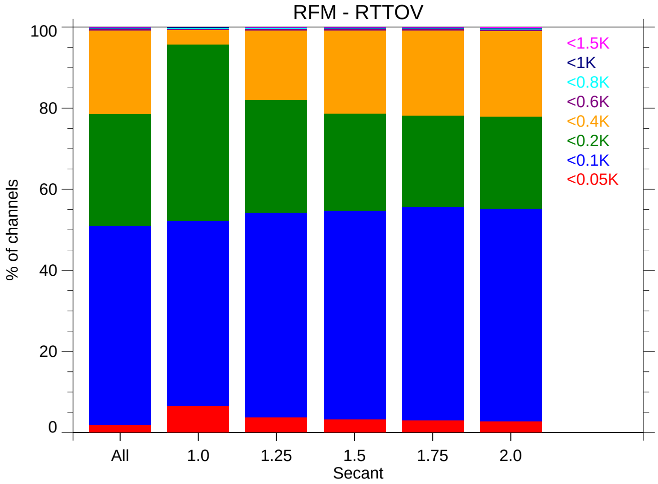

(a) RFM–RTTOV

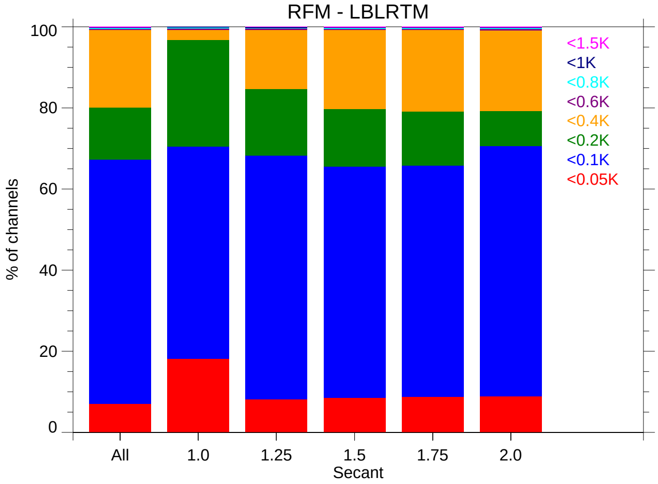

(b) RFM–LBLRTM

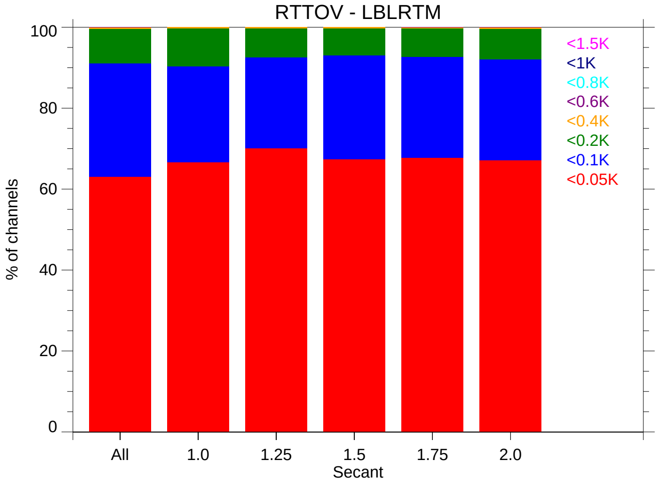

(c) RTTOV–LBLRTM

Figure 7.9: The percentage of channels with given RMS errors for all viewing angles combined and at each separate viewing angle.

7.2.3 Forward Model Error Propagation

Chapter 6 discussed the selection of a set of IASI channels that maximised the information contained within them whilst minimising the impact due to spectrally correlated errors, such as the atmospheric variability of interfering species. It was shown that all correlated measurement errors that can be represented by a combination of one or more statistically independent error vectors $\delta\mathbf{y}^j$, can be mapped into a corresponding retrieval error vector $\delta\mathbf{x}^j$ through

$$\delta\mathbf{x}^j = \mathbf{G}\delta\mathbf{y}^j + (\mathbf{I} - \mathbf{GK})\delta\mathbf{a}^j \tag{7.1}$$

where $\delta\mathbf{a}^j$ represent components of the same error j that contribute to the *a priori* estimate. These can in turn be combined in retrieval space to give a total retrieval error

$$\mathbf{S}_x^{\mathrm{tot}} = \mathbf{S}_x^{\mathrm{rnd}} + \sum_j (\delta\mathbf{x}^j)(\delta\mathbf{x}^j)^T \tag{7.2}$$

Here, the impact of including the error associated with the uncertainty in the radiative transfer models is assessed. First, the standard deviation of the difference between the radiative transfer models is represented as an additional noise term in the diagonal of the measurement covariance matrix, $\mathbf{S}_y$. This makes the assumption that the channel differences are spectrally uncorrelated with each other. Secondly, the bias is considered as a single error vector $\delta\mathbf{y}$ and mapped through the retrieval. The standard deviation cannot realistically be used in this way as it contains purely positive values and therefore eliminates any anticorrelation between channels. Ideally the matrix made up of the difference residuals would be decomposed into its separate spectrally correlated eigenfunctions, the first of which would be the bias; these would subsequently be mapped into independent error vectors in spectral space. Nevertheless, here we show only the simple cases as an example.

The effect upon vertical profiles of temperature, water vapour, and ozone, for the US standard atmosphere, viewed at nadir, are shown in figure 7.10. Results are not shown for trace gas retrievals since their uncertainties are dominated by the instrument noise. In each case the original profile error produced by the selected channels using the modified algorithm in chapter 6 is shown alongside how it is affected by both the addition of the forward model standard deviation as an additional noise term, and the forward model bias as a spectrally correlated error. The uncertainty from both RFM–RTTOV comparisons and LBLRTM–RTTOV comparisons are shown. The latter shows the effect upon a retrieval using a fast model as opposed to a line-by-line model, whereas the former shows the additional error caused by differences between the line-by-line models.

For temperature and water vapour the impact of the LBLRTM–RTTOV differences are almost negligible, with the inclusion as an 'error term' having a very small effect upon ozone. This is expected given the small bias found between the two models and shows that the fast model can recreate the line-by-line models with enough accuracy for use in retrievals. However, the difference between line-by-line models is much larger. The largest impact is to the temperature profile error which, given the large bias in the CO_2 ν_2 band, is unsurprising. Temperature is also the only example where the inclusion as added 'noise' has a noticeable impact, albeit still small. Slightly surprisingly, there is a large impact upon the water vapour profile through the inclusion as an 'error term' despite the bias across the water vapour band being small. This is due to the channels selected above $2000\,\mathrm{cm}^{-1}$ where the bias is larger; there will also be an effect from the CO_2 channels selected within the

ν_2 band.

Finally, it is noted that such ‘modelling’ errors could, in principle, be incorporated into the channel selection in order to minimise their impact.

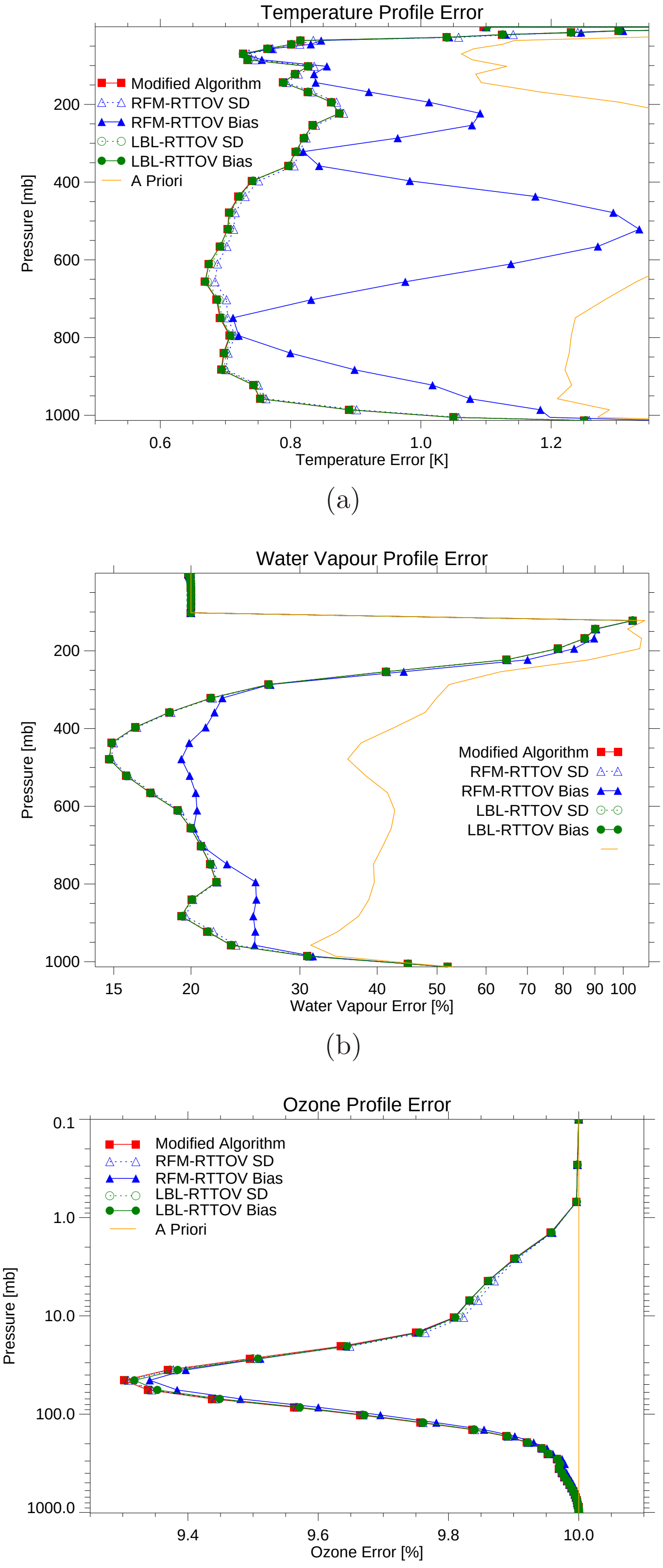

(a)

(b)

(c)

Figure 7.10: The effect of including an error due to forward model differences on the vertical error profiles of temperature, water vapour and ozone.

7.3 Comparison to IASI measurements

Having ascertained the RFM's ability to recreate synthetic IASI spectra, we finally examine how well it can recreate profiles coincident with IASI data. Comparisons to observations introduce complexity due to uncertainties in the atmospheric state, e.g surface properties or temperature profile.

7.3.1 Estimating the atmospheric state

Integral to the reproduction of IASI spectra is having a good estimate of the atmospheric state. The estimate of the atmospheric state for the location of the IASI spectra is taken from the ECMWF ERA-Interim dataset described by Dee et al. (2011), which does not include the assimilation of IASI data. ERA-Interim is the latest global atmospheric reanalysis produced by the ECMWF and covers the period from 1 January 1989 onwards. It provides a variety of gridded data products including 6-hourly parameters covering the surface, troposphere and stratosphere. Vertical profile data for temperature, water vapour and ozone are extracted from the dataset, along with surface temperature and pressure, at locations within the same latitude-longitude grid box used in the selection of the IASI spectra. The mean atmospheric state is calculated as the average of the ECMWF data points closest to the location of each IASI spectrum.

The vertical profile data in ERA-Interim is given on an altitude grid that only extends up to the stratopause ($\sim 1\,\mathrm{mb}$). As established in chapter 5 this is not adequate for fully simulating the high altitude spectral features in the IASI spectrum, therefore the altitude grid must be extended further. Assuming only mid-latitude regions, the mean atmospheric states are subsequently extrapolated up to 115 km by scaling towards the appropriate FASCODE atmospheric profile at altitudes above $\sim 1\,\mathrm{mb}$.

For atmospheric absorbers that are not found in the ERA-Interim archive, the initial estimate of their concentration is taken from the mean climatological profiles described in section 7.2.2 (and explained in detail by Matricardi (2008)).

7.3.2 Retrieval Theory

Chapter 3 introduced the concept of optimal estimation and its use as a method of retrieving an atmospheric state from satellite measurements. It was established that a solution for the state vector $\mathbf{x}$, containing n parameters, is found through the minimisation of the 'cost' function, χ^2,

$$\chi^2 = [\mathbf{y} - \mathbf{F}(\mathbf{x})]^{\mathrm{T}} \mathbf{S}_y^{-1} [\mathbf{y} - \mathbf{F}(\mathbf{x})] + [\mathbf{x} - \mathbf{a}]^{\mathrm{T}} \mathbf{S}_a^{-1} [\mathbf{x} - \mathbf{a}] + c_3 \tag{7.3}$$

where $\mathbf{y}$ and $\mathbf{S}_y^{-1}$ are the measurement vector and its associated error covariance matrix, $\mathbf{a}$ and $\mathbf{S}_a^{-1}$ are the *a priori* state vector and its associated error covariance matrix, $\mathbf{F}(\mathbf{x})$ is the forward model estimate of state $\mathbf{x}$ and c_3 is independent of x.

In the weakly non-linear limit the solution to finding the point at which the gradient of equation 7.3 equals zero can be found using Newtonian iteration. Ignoring second derivative terms under the assumption the problem is moderately linear, leads to the Gauss-Newton method, which gives

$$\mathbf{x}_{i+1} = \mathbf{x}_i + (\mathbf{S}_a^{-1} + \mathbf{K}_i^T \mathbf{S}_y^{-1} \mathbf{K}_i)^{-1} [\mathbf{K}_i^T \mathbf{S}_y^{-1} (\mathbf{y} - \mathbf{F}(\mathbf{x})_i) - \mathbf{S}_a^{-1} (\mathbf{x}_i - \mathbf{x}_a)] \tag{7.4}$$

where $\mathbf{K}_i = \mathbf{K}(\mathbf{x}_i)$. It is convenient to begin iterations using the *a priori* state vector as the 'first guess', i.e $\mathbf{x}_0 = \mathbf{x}_a$. For an exactly quadratic cost function, only one iteration would be required to find the cost function minimum. For non-quadratic cases, more iterations will be needed. The retrieval will stop when either the minimum is reached or a set criterion on the cost function is attained; in this case an imposed number of iterations. Nevertheless, if the initial guess lies sufficiently far from the solution, an iteration can in fact pull the result further from the truth and increase the residual. To solve this for a nonlinear least squares problem, the Levenberg–Marquardt method is used. Here a gamma factor, γ, is introduced which, at each step, is chosen to minimise the residual. A simplified version suggests the following,

$$\mathbf{x}_{i+1} = \mathbf{x}_i + ((1+\gamma)\mathbf{S}_a^{-1} + \mathbf{K}_i^T\mathbf{S}_y^{-1}\mathbf{K}_i)^{-1}[\mathbf{K}_i^T\mathbf{S}_y^{-1}(\mathbf{y} - \mathbf{F}(\mathbf{x})_i) - \mathbf{S}_a^{-1}(\mathbf{x}_i - \mathbf{x}_a)] \quad (7.5)$$

If χ^2 increases after a retrieval step, do not proceed to the next iteration, instead increase γ and retry. If χ^2 decreases, proceed to update $\mathbf{x}_i$ and decrease γ for the next iteration. Factors of 2 and 10 are chosen to increase and decrease γ respectively.

7.3.3 Selection of IASI data

For the comparison of IASI spectra to the simulations by the RFM, suitable data must be chosen. In order to minimise the uncertainties introduced by cloud, surface emissivity and non-local thermodynamic equilibrium only night-time cases over the ocean are considered.

Cloud flagging for the IASI instrument is non-trivial, especially given that for an instrument with a footprint of order 10 km, soundings where the atmosphere is completely free of clouds are rare (McNally and Watts, 2003). However, being able to remove cloudy scenes or simulate the effect of cloud correctly is extremely important given that the size of its impact upon a radiance signal can be tens of Kelvin. Techniques include using channels whose weighting functions peak above a diagnosed cloud top (e.g. McNally and Watts (2003) and Pavelin et al. (2008)), or using fully over cast scenes (McNally, 2009). However, dealing with multi layered cloud situations is less reliable.

Here a simple cloud flagging system is used to choose acceptable IASI spectra for inclusion in the comparison. Initially, within a 2° × 2° grid box, all IASI spectra are considered and the co-located ERA-Interim data are found. For all spectra that are considered by the ERA database to have zero total cloud cover a one iteration retrieval is carried out upon the surface temperature, with the ERA data providing the *a priori* value. If the retrieved value for surface temperature lies within 1K of the ERA-Interim value, the spectrum is considered to be clear.

All IASI spectra flagged to be clear within any 2° × 2° grid box are averaged to provide a mean spectrum. This aims to reduce the noise associated with each individual spectrum and it is this mean spectrum that the forward models aim to reproduce. Only regions that contain more than 15 suitable spectra are considered.

7.3.4 Reproducing IASI spectra

The following section contains comparisons between mean IASI measurement spectra and simulations calculated using ERA-Interim data as the input to the forward model. All ‘clear sky’ 2° × 2° grid boxes over the ocean for a single day, 5th January 2010, are considered and separated into latitudinal regions for comparison: the northern hemisphere (above 30°N), tropical (30°S–30°N) and the southern hemisphere (below 30°S). The mean difference (bias) between the averaged IASI measurements and simulated spectra can be seen, separated into the IASI bands, in figures 7.11,7.14 and 7.16.

However, one of the dominant sources of uncertainty in the simulation of the IASI spectrum is the knowledge of the atmospheric state. This is unavoidable for several reasons such as in-situ measurements not sampling the exact same spatial region or in the same time period. Because of this, as an example, a retrieval has been carried out for temperature and the primary absorbers, for one particular scene, in an attempt to optimise the specified atmospheric state before analysis of the residual from a comparison with IASI data, as is done by Alvarado et al. (2013). This method aims to reduce collocation errors introduced by the climatology.

The retrieval approach has been described in section 7.3.2 and is used to retrieve the following parameters: surface or 'skin' temperature (T_s) and vertical profiles of temperature (T), water vapour ($\mathrm{H_2O}$), ozone ($\mathrm{O_3}$), methane ($\mathrm{CH_4}$) and carbon monoxide (CO). The purpose of this section is not to test the retrieval method, merely to better constrain the atmospheric state and therefore in each case a maximum of 3 converging iterations are performed in order to improve the estimate.

The initial *a priori* values were described in section 7.3.1 and the *a priori* covariance's for each parameter are summarised in table 7.2. Absorbers whose *a priori* estimate is taken from the ERA-Interim database are given a larger variance above 0.1 mb due to the extrapolation of the profile above this level.

In sequence, the following retrievals are performed:

(a) T_s only

(b) a joint retrieval of T_s and T

Table 7.2: The *a priori* assumptions for each retrieved absorber

	Variance	Correlation length	Channels
T_s	1 K	No correlation assumed with lowest levels of T	252 selected in section 6.3
T	2 K (below 0.1mb) 5 K (above 0.1mb)	10 levels	252 selected in section 6.3
H_2O	20% (below 0.1mb) 50% (above 0.1mb)	10 levels	252 selected in section 6.3
O_3	20% (below 0.1mb) 50% (above 0.1mb)	10 levels	252 + 15 selected in section 6.5.1
CH_4	20%	10 levels	252 + 15 selected in section 6.5.2
CO	20%	10 levels	252 + 15 selected in section 6.5.3

(c) a joint retrieval of T_s, T and H_2O

(d) as (c) but additionally O_3

(e) as (c) but additionally CH_4

(f) as (c) but additionally CO

with the result from each retrieval becoming the first guess in the subsequent one.

The example shown is for the region [33.0–35.0S,125.0–127.0W] in the southern hemisphere over the ocean on 5th January 2010 and the residual between the final simulated spectrum and the averaged IASI spectrum can be seen, separated into the IASI bands, in figures 7.12,7.15 and 7.17.

IASI Band 1 (645–1200 cm^{-1})

The mean differences (bias) between RFM simulations and observed IASI measurements for IASI band 1, which contains the CO_2 ν_2 and the O_3 ν_3 absorption bands,

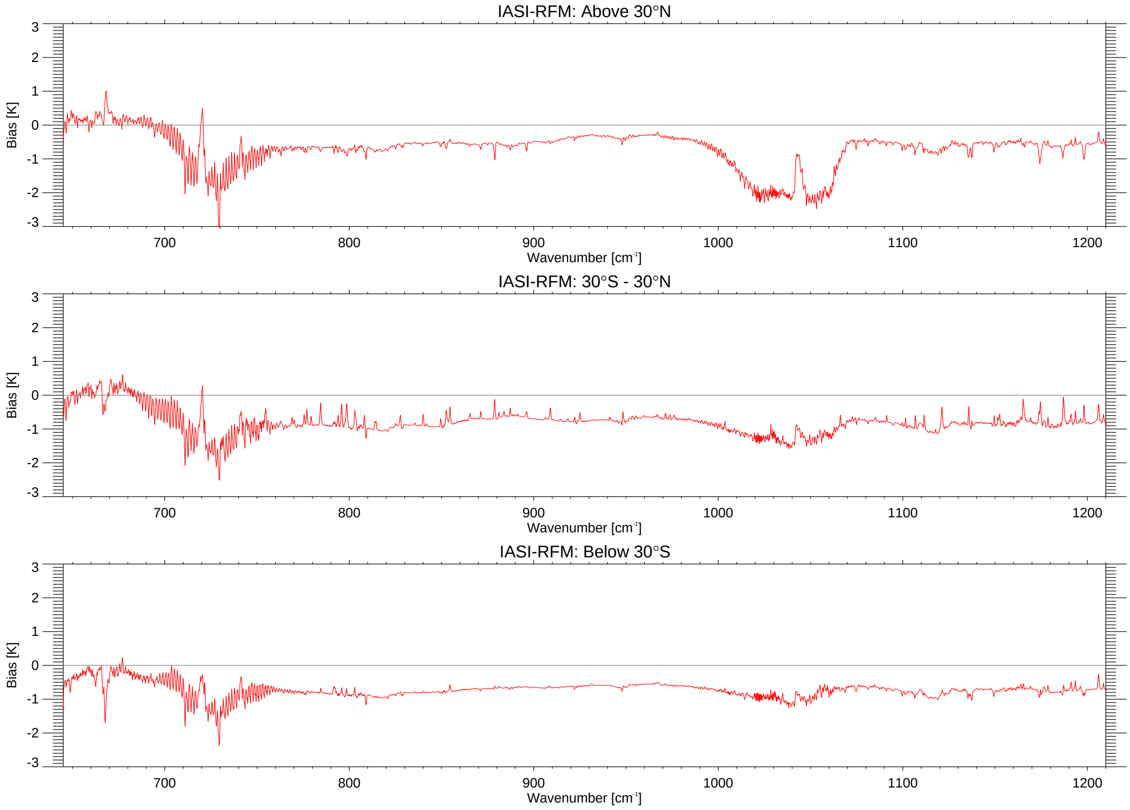

Figure 7.11: The mean value (bias) of the differences between observed and simulated IASI measurements for IASI band 1 are shown in brightness temperature for the latitudinal regions: below 30°S, 30°S–30°N and above 30°N.

are shown in figure 7.11 and the example residual after retrievals of the major absorbers have been performed is shown in figure 7.12, along with the noise associated with the mean spectrum (i.e. $\mathrm{SD}/\sqrt{n}$, where SD is the standard deviation of n spectra). A clear bias in the simulated surface temperature can be seen in the window region between 800–1000 cm^{-1} of ~ 0.7K in all latitude bands, however, after the retrieval it can be seen that throughout the majority of the band the simulated spectra agrees very well with the IASI measurements, with the window region differing by less than ~ 0.2K and the residual lying at the level of the noise or below. In the northern hemisphere, there is a large residual in the O_3 ν_3 band of up to 2K,

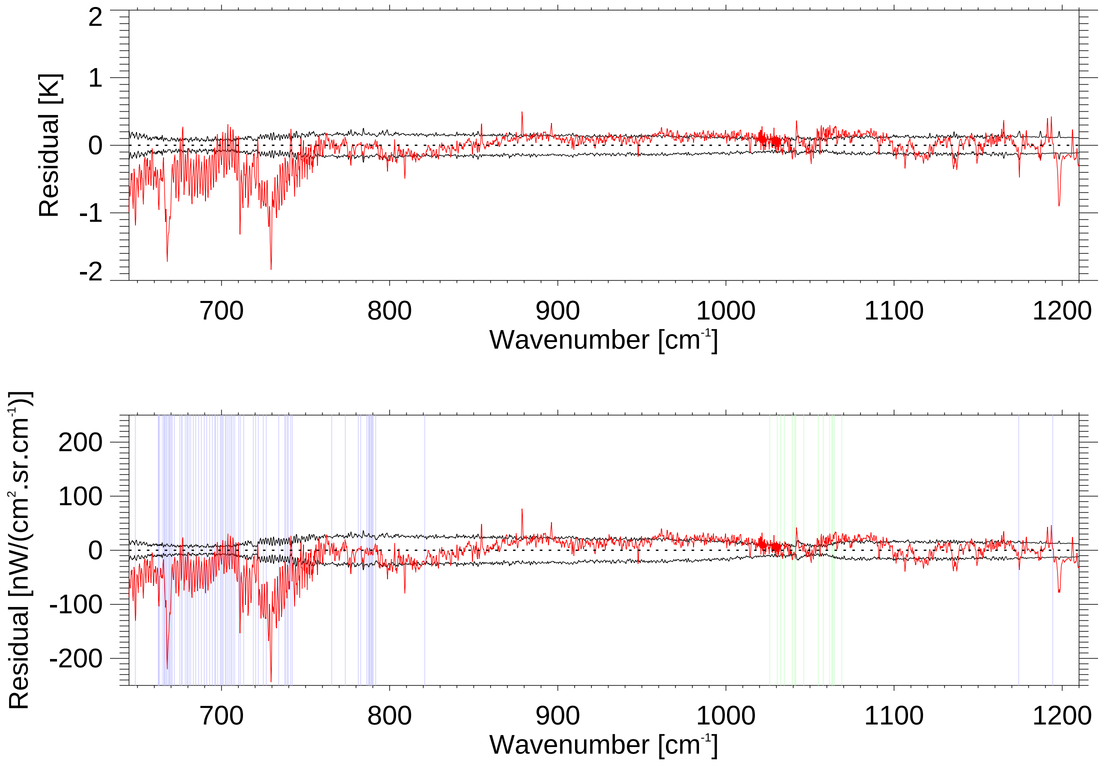

Figure 7.12: The difference between observed and computed IASI measurements for IASI band 1 (after the retrieval) is shown in both brightness temperature and radiance in red and the noise associated with the mean spectrum is plotted in black. Also shown are the locations of the channels used within each retrieval step, with those for the T_s, T and $\mathrm{H_2O}$ retrievals in blue and the additional channels used for the $\mathrm{O_3}$, $\mathrm{CH_4}$ and CO channels in green, purple and aqua respectively.

whereas in the tropical and southern hemisphere regions the residual is in line with the surface temperature offset. This suggests that the mid-latitude ozone profiles used are more accurate for the southern hemisphere, but is also an artefact due to the smaller number of suitable grid boxes in the northern hemisphere to include in the comparisons. After retrieval, small residuals are seen of less than 0.3K in this band; this result agrees with that shown by Alvarado et al. (2013) in comparisons of the LBLRTM with IASI measurements. The ‘spikes’ visible in the window region above the ozone band may be the effect of errors in the water vapour profiles in the lower troposphere near the surface, caused by the far wings of the H_2O ν_2 band.

The spectral range with the largest discrepancies across all latitudinal regions, and much larger than the noise even after retrieval, is that across the CO_2 ν_2 band (640–800 cm^{-1}) where the comparisons appear to have a bias of $\sim$ 2K; this is reduced to $\sim$ 0.5K after the temperature retrieval. Below $\sim$ 700cm^{-1} the retrieval has little effect upon the residual. One of the largest residuals (of over 1.5K) coincides with the Q-branch at 667 cm^{-1} and, given that channels in this branch are sensitive to high altitude emissions, this is expected to be caused by errors in the temperature profile in the stratosphere and mesosphere. This feature is not unexpected as it was also seen by both Alvarado et al. (2013) and Matricardi (2009) in comparisons to IASI data, but could also be due to the extrapolation of the ERA-Interim temperature profile to higher altitudes. The difference between the *a priori* profile estimates and the retrieved atmospheric profiles are shown in figure 7.13 and, in the case of temperature it can be seen that the largest changes occur above 0.1mb, the point at which the extrapolation begins. This suggests that an improved *a priori* estimate is needed for this region, which may, in turn, improve the retrieval across the whole profile. Conversely, the change in the ozone profile (see figure 7.13c) is greatest in the troposphere. Despite this, changes across the entire profile are very small and suggest that the initial estimate was good.

The large residuals around the Q-branch at 720 cm^{-1} feature in the same region as the large CO_2 residuals found in section 7.2, which were caused by the difference in CO_2 line mixing used in the compared models. This is expected to be one of the causes here as well. The RFM does not include P- and R-branch line coupling (by Niro et al. (2005) or more recently Lamouroux et al. (2010)) nor the associated adjustment to the CO_2 continuum. Both of these will have a large impact upon the residual and it is expected that their inclusion would improve the agreement with measurements as was shown by Alvarado et al. (2013).

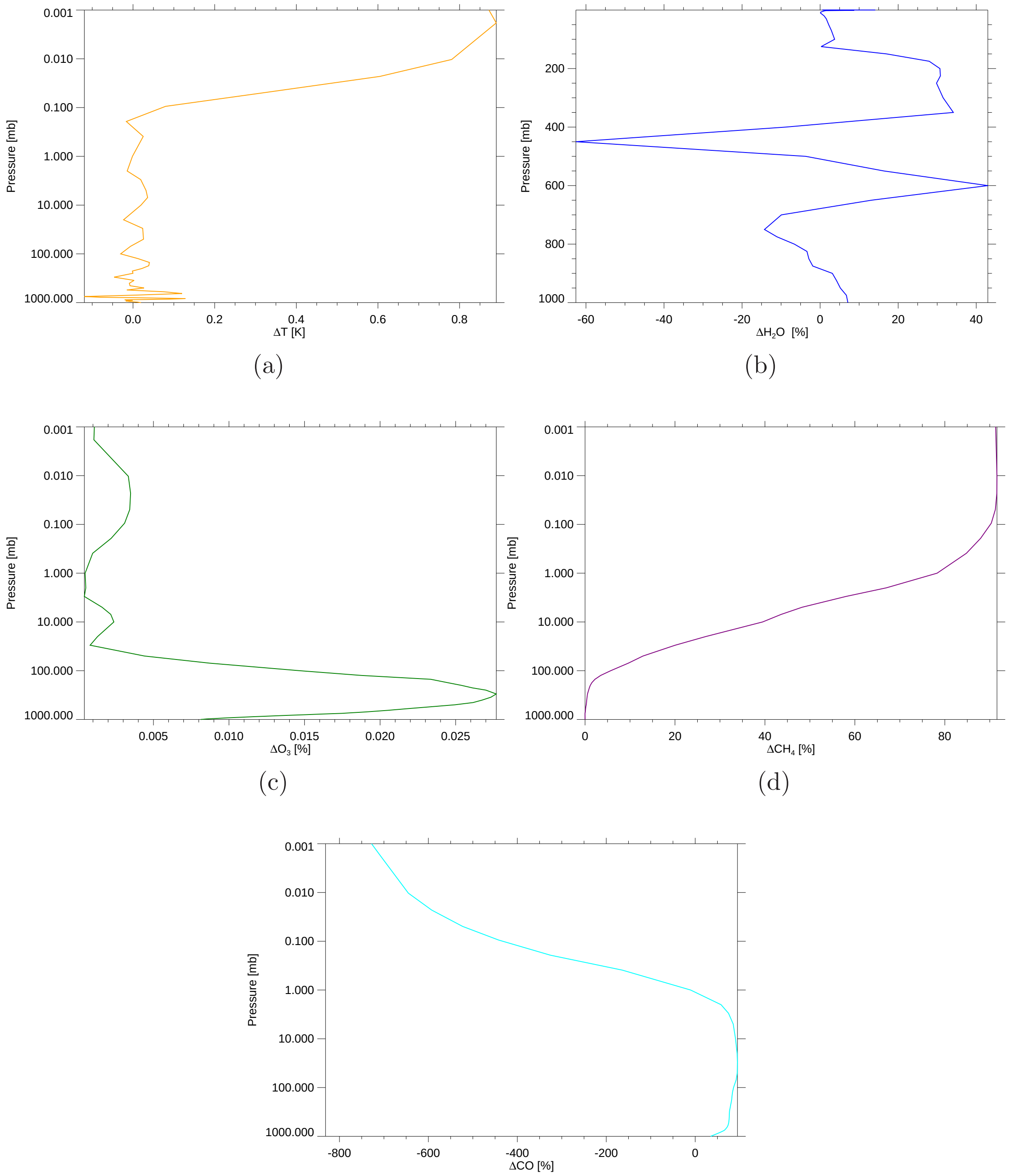

(a) (b)

(c) (d)

(e)

Figure 7.13: The difference between the retrieved vertical profiles and the *a priori* profile for each of the retrieved variables: Temperature, water vapour, ozone, methane and carbon monoxide

IASI Band 2 (1200–2000 cm^{-1})

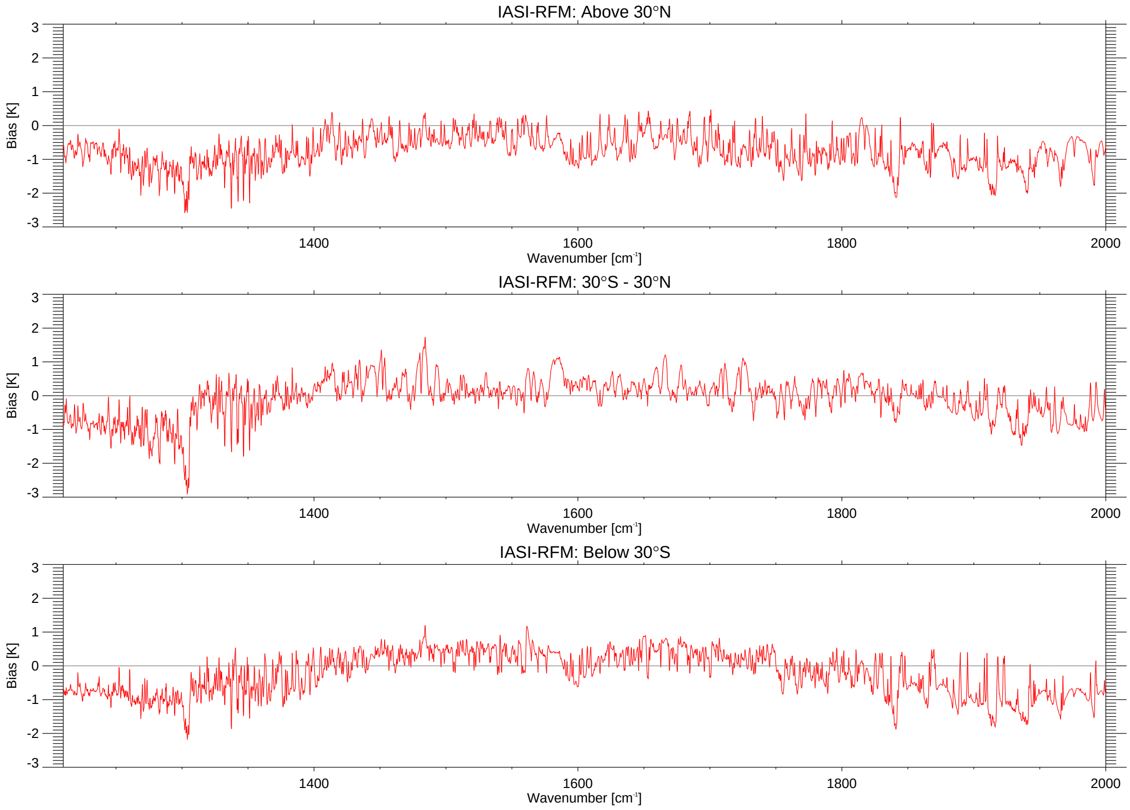

Figure 7.14: The mean value (bias) of the differences between observed and simulated IASI measurements for IASI band 2 are shown in brightness temperature for the latitudinal regions: below 30°S, 30°S–30°N and above 30°N.

Comparatively, the biases seen in band 2, which is dominated by the H_2O ν_2 absorption band, are much noisier than those in band 1 and can be seen in figure 7.14, with the residual after the retrieval in figure 7.15. The residual oscillates between $\sim \pm 1$K, increasing to ~ -2K towards the shorter wavelengths. Given that the major absorber within this band is water vapour, the residuals are largely caused by inaccuracies in its modelling and may reflect errors in both the line parameters and the water vapour continuum. The biases across the water vapour band are similar for all latitude bands and the retrieval removes the consistent offset seen.

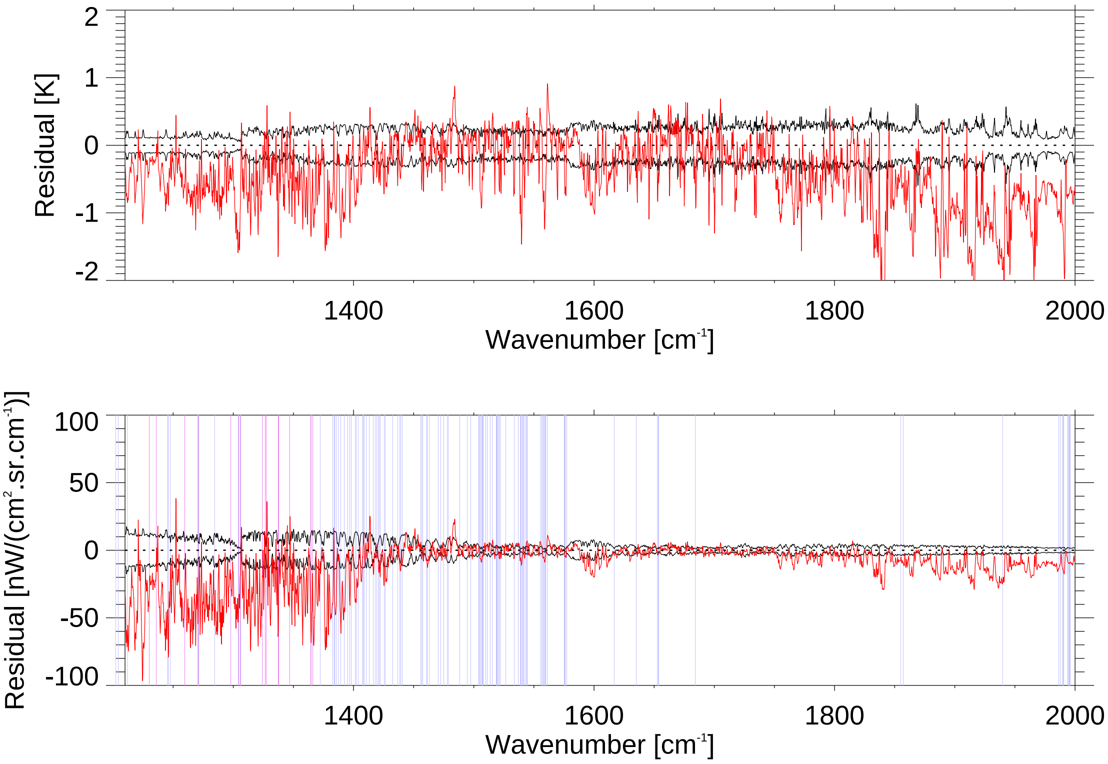

Figure 7.15: The difference between observed and computed IASI measurements for IASI band 2 (after the retrieval) is shown in both brightness temperature and radiance in red and the noise associated with the mean spectrum is plotted in black. Also shown are the locations of the channels used within each retrieval step, with those for the T_s, T and H_2O retrievals in blue and the additional channels used for the O_3, CH_4 and CO channels in green, purple and aqua respectively.

Errors in the water vapour line strength have a large impact upon the simulated spectrum and work carried out by Coudert et al. (2008) showed that The HITRAN 2004 database underestimated line intensities in the region of 1000–2000 $\mathrm{cm^{-1}}$ by $\sim$ 5–10%, however, the new parameters calculated by Coudert et al. (2008) were not adopted in HITRAN 2008, the database used for these retrievals. Alvarado et al. (2013) showed that simulations using HITRAN 2008 appeared to have an unphysical discontinuity in the spectra at 1750 $\mathrm{cm^{-1}}$ caused by the exclusion of these parameters: although the effect of including the Coudert et al. (2008) line intensities cannot explain all of the bias we observe here, the degradation in spectral fit between 1750–2000 cm^{-1} is clearly visible and the 'spikes' in the residual coincide with water vapour features. The largest differences between the *a priori* and retrieved water vapour profiles (see figure 7.13b) are located in the upper troposphere and, given the sharp features, may be masking problems with the spectroscopy across the band.

Another contributing factor to the bias in the spectral fit above 1850 cm^{-1} is the ability to model the CO_2 spectral features in this region. Similarly, inaccuracies in the retrieved estimate of the temperature profile will filter through the retrieval procedure and affect the modelling of water vapour.

The CH_4 ν_4 band below 1400 cm^{-1} shows biases of up to 3K, the largest of which is evident at the band centre, 1310 cm^{-1} in the tropical region. However, the northern hemisphere has a more consistently large bias across the whole of the band, pointing again to the poorer statistics in this region. After the retrieval the residual becomes ~ 0.5K, with the band centre still clearly visible. This may suggest errors in the spectroscopy, however, given the simplistic nature of the retrieval procedure used, the residuals may merely be due to mis-characterisation of the methane profile. Without co-located methane data, the *a priori* estimates for methane come from a climatology and errors may be introduced if the initial estimate is too far from the true state. Nevertheless, methane is considered to be well known within the troposphere and, given that the difference between the *a priori* and retrieved methane profile increases significantly with altitude, it is again expected that an improved estimate of the upper atmosphere is required to improve the residual.

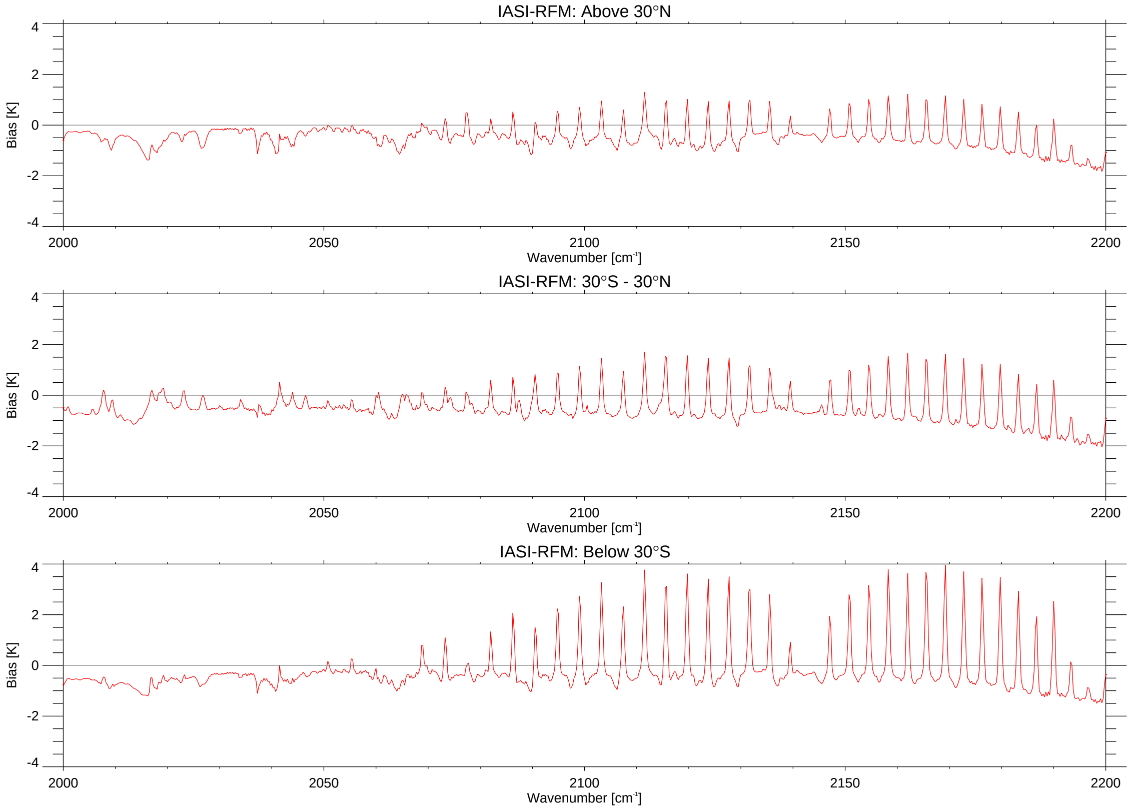

Figure 7.16: The mean value (bias) of the differences between observed and simulated IASI measurements for IASI band 3 are shown in brightness temperature for the latitudinal regions: below 30°S, 30°S–30°N and above 30°N.

IASI Band 3 (2000–2200 cm^{-1})

Figure 7.16 shows the biases between observed and computed IASI measurements for IASI band 3 up to 2200 cm^{-1} (the upper limit used throughout this work) and the result after the retrieval can be seen in figure 7.17. This region has major absorption features from CO, N_2O, H_2O and CO_2.

The biases in this band are much larger in all latitudinal regions than the previous two IASI bands. The offset due to inaccuracies in the surface temperature can again be seen across the whole band and the CO line structure is clearly visible in all cases. The largest biases are found in the southern hemisphere, however, the CO

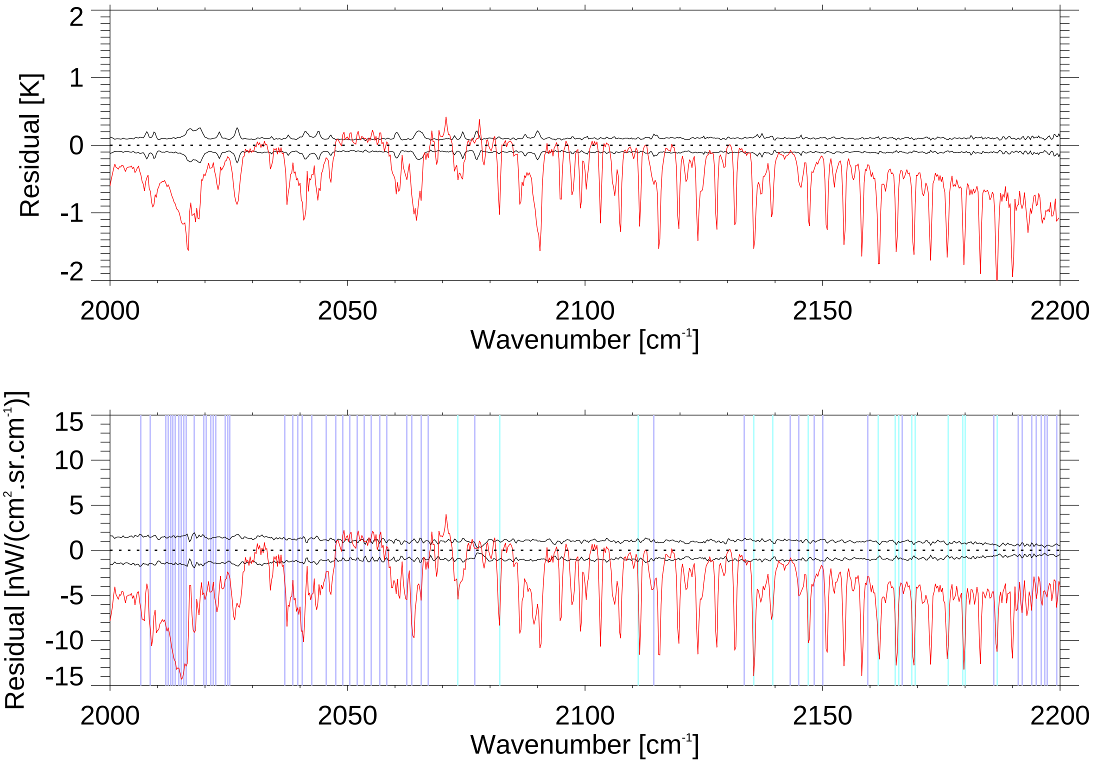

Figure 7.17: The difference between observed and computed IASI measurements for IASI band 3 (after the retrieval) is shown in both brightness temperature and radiance in red and the noise associated with the mean spectrum is plotted in black. Also shown are the locations of the channels used within each retrieval step, with those for the T_s, T and H_2O retrievals in blue and the additional channels used for the O_3, CH_4 and CO channels in green, purple and aqua respectively.

atmospheric profile used is clearly inadequate for all regions.

Having carried out the retrieval, hoping to improve the residual, it can be seen that following from band 2 there are visible ‘spikes’ in the residual up to 2100 cm^{-1} that coincide with water vapour features. These occur due to the reasons previously proposed; the lack of the Coudert et al. (2008) line parameters in HITRAN 2008 and inaccuracies in the temperature retrieval.

Between $\sim$ 2080–2200 cm^{-1} larger biases can still be seen, which are due to the poor performance of the CO retrieval. Due, in part, to the simplistic retrieval process implemented it was difficult to produce improved residuals for both water vapour and carbon monoxide, with, in the example shown, unphysically large values of water vapour required to improve the carbon monoxide retrieval. This has also been observed by Alvarado et al. (2013) and is attributed to the update to the H_2O self continuum in this region in the MT_CKD_2.5 continuum model, used by the RFM, being inconsistent with the spectroscopy of the H_2O ν_2 band. The update to the continuum model was implemented to improve residuals near the CO_2 ν_3 bandhead, however in doing this it has degraded the spectral fit for CO. The poor performance of the CO retrieval is also highlighted in how the *a priori* profile estimate is changed by the retrieval. Figure 7.13e shows that in the upper atmosphere the CO profile is adjusted by an extremely large percentage. This illustrates the problem with the *a priori* values being too far from the true values (causing a switch from a large over-estimation of CO to an under-estimation) or, is perhaps, compensation for problems with the spectroscopy.

Finally, above $2100\,\mathrm{cm}^{-1}$, on top of the CO spectral line features, there is a clear gradient in all the residuals, which corresponds to the wing of the N_2O band and therefore may indicate errors in the spectroscopy of N_2O. Despite having only used a climatological profile scaled to the appropriate year, N_2O does not vary significantly and therefore it is unlikely that this is caused by substantial errors in the N_2O estimate.

All Bands

The residuals associated with the RFM–IASI comparisons are much larger than those observed for RFM–RTTOV/RFM–LBLRTM comparisons (in sections 7.2.1

and 7.2.2) and this can be seen in figure 7.18, which shows the percentage of channels in each IASI band whose residual error from RFM–IASI comparison, after the retrieval, lies within certain binned values.

The agreement between IASI measurements and the simulated RFM spectrum is clearly much better in band 1 than in both bands 2 and 3, with the latter two producing similar results. The percentage of channels across all bands with residual < 0.05K is comparable to the percentage found in the forward model comparisons. However, there are significantly more channels with residual > 0.4K ($\sim 40\%$ compared to $\sim 1\%$ for RFM–LBLRTM comparisons) and in fact $\sim 10\%$ of channels have a residual > 1.5K. These larger values are expected given that the comparisons are no longer dealing with synthetic spectra and there is uncertainty in the atmospheric state.

Promisingly, the residuals observed here in the window regions and the O_3 ν_3 and H_2O ν_2 absorption bands compare well to the residuals observed by Alvarado et al. (2013) in comparisons of the LBLRTM to IASI measurements. However, the residuals seen in the longwave CO_2 band and the CO band are much larger. This is expected to be caused by insufficient *a priori* data and the simplistic nature of the retrieval procedure implemented.

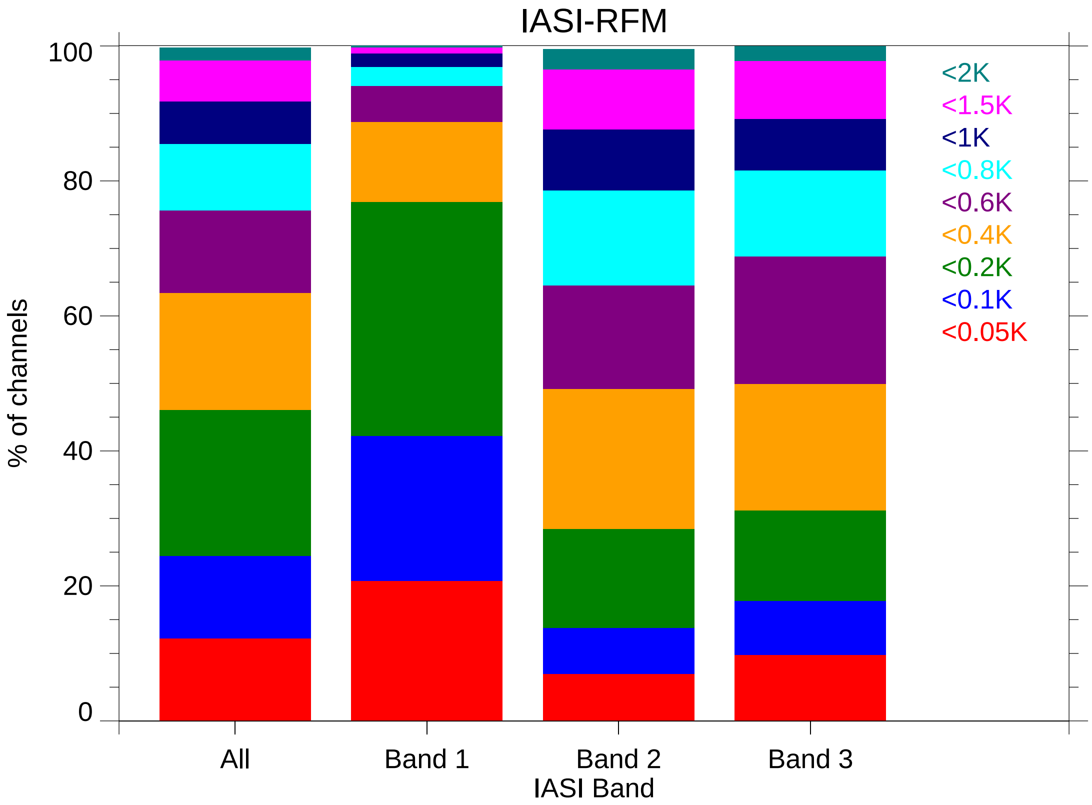

Figure 7.18: The percentage of channels with given residual errors for the whole spectrum and for each IASI band.

7.4 Summary

Three radiative transfer models (RFM, RTTOV and LBLRTM) have been compared to see if the differences in the outputs are significant or whether they can be considered negligible. Both a dependent and independent dataset of atmospheric profiles are used to compare the results from the RFM with those from RTTOV. For the independent selection the output from the LBLRTM, the line-by-line model used to train RTTOV, is also included in the comparisons to establish which discrepancies can be attributed to differences in the line-by-line models and which are due to the fundamental differences between monochromatic line-by-line models and fast band models.

The comparisons between the RFM and RTTOV for the dependent dataset showed good agreement across the ν_2 water vapour band with biases of $\sim 0.1\,\mathrm{K}$ and, outside of the CO_2 bands, the biases lying below the IASI noise. However, due to the inclusion of the P- and R- branch line coupling within the LBLRTM, which also causes a recalculation of the CO_2 continuum, large biases can be seen in the CO_2 ν_2 band and the CO_2 peak at $2400\,\mathrm{cm}^{-1}$. Spectral regions with large standard deviations were found to coincide with regions of interfering species, with updates to the H_2O self continuum in the MT_CKD_2.5 model likely to be responsible for the spread shown by the comparisons within the CO band.

Agreement of better than 0.4K in $\sim$ 95% of the channels was found, which compared favourably to the literature, where comparisons between RTTOV and the LBLRTM found that $\sim$ 98% of channels had rms values less than 0.1K.

A 3–way comparison was performed using an independent dataset between the RFM, RTTOV and the LBLRTM and it is shown that the RFM–RTTOV bias is almost entirely due to the bias between the line-by-line models and is caused by, for example, differences in the continua and CO_2 line parameters. There is also minimal difference between the bias seen using the dependent and independent profile sets, suggesting minimal sensitivity to the profile data set chosen. The RTTOV–LBLRTM bias is, by comparison, small, but the deviations show similar discrepancies to those in the RFM–RTTOV comparison. These deviations are expected to be caused by the formulation of coefficients in regions of interfering water vapour lines with the respective gases.

Agreement between the RFM and LBLRTM is encouragingly good, with $\sim$ 80% of channels having an rms error less than 0.2K and in the nadir case this value increases to $\sim 95\%$. The results are similar for the RFM–RTTOV comparison, with $\sim 80\%$ of channels having an rms error less than 0.2K.

The impact of including the error associated with the uncertainty in the radiative transfer models is assessed in two ways; by representing the standard deviation as an additional noise term in the diagonal of the measurement covariance matrix and by considering the bias to be a single error vector and mapping it through the retrieval. For temperature and water vapour the impact of the LBLRTM–RTTOV differences are almost negligible and show that fast models can recreate the line-by-line models with enough accuracy for use in retrievals. However, the difference between line-by-line models is much larger, most noticeably in the temperature profile error.

Finally, using a simple retrieval procedure, averaged IASI measurements are compared to a simulated spectrum to see how well the RFM is able to accurately model the IASI data. Good agreement can be seen in the window regions of IASI band 1 and across the O_3 ν_3 band, however larger biases occur in the temperature sounding band due to the lack of P- and R- branch line coupling in the simulations, as well as poor knowledge of the stratospheric temperature profile. Spectral features caused by the lack of P- and R- branch line coupling were also visible in IASI band 2, with errors in the temperature retrieval also propagating through the procedure and degrading the spectral fit within this band. Overall, the residual across the H_2O ν_2 band is good, oscillating between ±1K, however a systematic bias occurs in the CH_4 band. IASI Band 3 showed the poor performance of the CO retrieval caused by the incompatibility of updates to the H_2O self continuum in this region with the H_2O ν_2 band spectroscopy.

Promisingly, the residuals observed in the window regions and the O_3 ν_3 and H_2O ν_2 absorption bands compare well to the residuals observed by Alvarado et al. (2013)

in comparisons of the LBLRTM to IASI measurements. However, the residuals seen in the longwave CO_2 band and the CO band are much larger. This is expected to be caused by insufficient *a priori* data and the simplistic nature of the retrieval procedure implemented.

Chapter 8

Conclusion and Future Work

A fundamental part in the retrieval of atmospheric composition is the use of radiative transfer models (RTMs) to simulate observations. An accurate representation of the expected absorption spectrum measured by the satellite is essential in ascertaining the correct atmospheric composition providing the observed satellite radiances. Errors in the reproduced atmospheric spectra can propagate through a retrieval procedure and hence produce an incorrect estimate of the atmospheric state.

Different types of forward model were discussed in chapter 4 and chapter 5 presented the importance of the initial assumptions within the forward model. A summary of the key forward model parameters and the suggested settings required for general simulation of the IASI spectrum in the troposphere, along with the settings recommended for more accurate IASI calculations, was provided in table 5.18.

The approximations used in the spatial modelling within the RFM have been shown to be valid at all viewing angles. However, at larger scan angles a correction must be made to the zenith angle to fully capture the extended path length due to the curvature of the Earth. The importance of the vertical altitude grid spacing in the modelling of the atmosphere was examined, showing that both the troposphere and stratosphere must be well sampled in order to fully resolve water vapour and high altitude CO_2 or O_3 spectral features respectively. The implementation of the 'linear in τ' approximation is advised when there is only coarse vertical representation of the troposphere.

Within the RFM there are several optional spectral modelling parameters that all exhibit large residuals on their exclusion, and it is therefore advised that they be included in any calculations; The χ-factor and line mixing are crucial in fully capturing the behaviour of the CO_2 spectral features, whilst the molecular continua must be included in order to correctly model the full IASI spectrum. Despite this, it should be noted that there are continuous improvements to the water vapour continuum models available, and as was shown, large differences between versions; therefore discrepancies between RTMs often arise from their handling of the continua.

Some of the largest residuals observed configuring the RFM were those between spectroscopic databases, illustrating how significantly the input line parameters can affect the output spectra by RTMs and highlighting the importance of taking into account the spectroscopy when comparing such models.

Having established the importance in the ability of RTMs to recreate the IASI spectrum within the retrieval and assimilation process, the information gained from the IASI measurements is examined. Chapter 6 presented a new method for the selection of IASI channels. Through comparison with the algorithm used to select the currently operational NWP channels, it has been shown that the new algorithm maintains the same number of DFS whilst reducing the sensitivity of the channel set to unknown (or unspecified) spectral correlations. The methods are intrinsically the same in that the channels are selected based upon their contribution to the DFS, however, where the previous method only considers the random component of the error and fully excludes certain channels from being chosen, the new method incorporates, for example, the effects of species' atmospheric variability within the selection process as a 'systematic' error.

Initially carried out within an NWP context to allow comparison, the new selection method was generalised to the selection of channels for the retrieval of any species. In the case of minor species, there is only a small improvement by the modified algorithm due to the dominance of the random noise, however, with the modified algorithm a full error analysis is obtained. It has been shown that the precision in tropospheric column amount is generally improved to a far greater extent by a positive thermal contrast at the surface than by improved knowledge of the stratosphere. In essence, combining information from limb and nadir viewing instruments to improve the error in tropospheric column amount does not appear promising for species largely concentrated within the troposphere and that have large variability near the surface. However, for species such as O_3 that are largely concentrated in the stratosphere, greater knowledge of the stratosphere does provide additional information that can improve tropospheric estimates.

In chapter 6 the Collard selection was recreated using the RFM to avoid discrepancies due to the radiative transfer model that simulated the Jacobians used in the selection affecting the comparison to the modified method. Chapter 7 assesses whether these forward model differences are significant or whether they can be considered negligible. Both a dependent and independent dataset of atmospheric profiles are used to compare the results from the RFM with those from RTTOV.

For the independent selection the output from the LBLRTM, the line-by-line model used to train RTTOV, is also included in the comparisons to establish which discrepancies can be attributed to differences in the line-by-line models and which are due to the fundamental differences between monochromatic line-by-line models and fast band models.

For both datasets the comparisons between the RFM and RTTOV showed good agreement across the ν_2 water vapour band with biases of $\sim 0.1\,\mathrm{K}$ and, outside of the CO_2 bands, the biases lying below the IASI noise. However, due to the inclusion of the P- and R- branch line coupling within the LBLRTM, which also causes a recalculation of the CO_2 continuum, large biases can be seen between the RFM and both LBLRTM and RTTOV in the CO_2 absorption bands. Large standard deviations were also found in spectral regions that coincide with regions of interfering species.

The RFM–RTTOV bias is shown to be almost entirely due to the bias between the line-by-line models. The RTTOV–LBLRTM bias is, by comparison, small, but the deviations show similar discrepancies to those in the RFM–RTTOV comparison. These deviations are expected to be caused by the formulation of coefficients in regions of interfering water vapour lines with the respective gases. Agreement between the RFM and LBLRTM is encouragingly good, with $\sim 80\%$ of channels having an rms error less than 0.2K and in the nadir case this value increases to $\sim 95\%$.

The impact of including the error associated with the uncertainty in the RTMs is assessed; For temperature and water vapour the impact of the LBLRTM–RTTOV difference is almost negligible, showing that fast models can recreate the line-by-line models with enough accuracy for use in retrievals. However, the difference between line-by-line models is much larger, most noticeably in the temperature profile error.

Finally, using a simple retrieval procedure, averaged IASI measurements are compared to a simulated spectrum to see how well the RFM is able to accurately model the IASI data. Promisingly, the residuals observed in the window regions and the O_3 ν_3 and H_2O ν_2 absorption bands compare well to the residuals observed by Alvarado et al. (2013), who compared the LBLRTM to IASI measurements. However, larger biases occur in the temperature sounding band due to the lack of P- and R- branch line coupling in the simulations, as well as poor knowledge of the stratospheric temperature profile. The poor performance of the CO retrieval, which is expected to be caused by the incompatibility of updates to the H_2O self continuum in this region with the H_2O ν_2 band spectroscopy was also shown.

In conclusion, it has been shown that the configuration and choice of RTM used in retrievals is important for the correct modelling of the IASI spectrum. It has also been shown how to minimise the effects of spectral errors when selecting IASI channels for use in both NWP and trace gas retrievals. The RFM has been validated and shown to have good agreement with alternative RTM's and the causes of many discrepancies have been established. Finally, the RFM has been shown to be able to simulate IASI measurements well, and areas that need to be improved have been highlighted.

There are still many avenues following on from the work shown that would be interesting to explore in the future. These include:

- Liaising with NWP centres to include their specific error characterisation within the modified channel selection algorithm and evaluate the ratio of the channel set that would realistically be retained for use in the NWP assimilation process.

- Testing the capabilities of the modified channel selection method using correlated $\mathbf{S}_y$ matrices.
- Improve the modelling of CO_2 within the RFM, e.g. including CO_2 P- and R-branch line coupling and updating the CO_2 continuum .
- Calculating RTTOV regression coefficients using the RFM and comparing the model outputs.
- Repeating comparisons of the RFM to IASI measurements with an improved retrieval process and additionally with alternative spectroscopic databases, molecular continuum models and geographical locations.

Bibliography

AER, Atmospheric and Environmetal Research (2012). The line by line radiative transfer model, LBLRTM. `http://rtweb.aer.com/lblrtm.html`.

Alvarado, M. J., Payne, V. H., Mlawer, E. J., Uymin, G., Shephard, M. W., Cady-Pereira, K. E., Delamere, J. S., and Moncet, J.-L. (2013). Performance of the line-by-line radiative transfer model (LBLRTM) for temperature, water vapor, and trace gas retrievals: recent updates evaluated with IASI case studies. *Atmospheric Chemistry and Physics Discussions*, 13(1):79–144.

Atkinson, N. C., Hilton, F. I., Illingworth, S. M., Eyre, J. R., and Hultberg, T. (2010). Potential for the use of reconstructed IASI radiances in the detection of atmospheric trace gases. *Atmospheric Measurement Techniques*, 3(1):501–529.

Bernath, P. F., McElroy, C. T., Abrams, M. C., Boone, C. D., Butler, M., Camy-Peyret, C., Carleer, M., Clerbaux, C., Coheur, P.-F., Colin, R., DeCola, P., De-Mazière, M., Drummond, J. R., Dufour, D., Evans, W. F. J., Fast, H., Fussen, D., Gilbert, K., Jennings, D. E., Llewellyn, E. J., Lowe, R. P., Mahieu, E., McConnell, J. C., McHugh, M., McLeod, S. D., Michaud, R., Midwinter, C., Nassar, R., Nichitiu, F., Nowlan, C., Rinsland, C. P., Rochon, Y. J., Rowlands, N., Semeniuk, K., Simon, P., Skelton, R., Sloan, J. J., Soucy, M.-A., Strong, K., Tremblay, P., Turnbull, D., Walker, K. A., Walkty, I., Wardle, D. A., Wehrle, V., Zander, R., and Zou, J. (2005). Atmospheric chemistry experiment (ACE): Mission overview. *Geophysical Research Letters*, 32(15):n/a–n/a.

Bormann, N., Collard, A., and Bauer, P. (2010). Estimates of spatial and interchannel observation-error characteristics for current sounder radiances for numerical weather prediction. ii: Application to AIRS and IASI data. *Quarterly Journal of the Royal Meteorological Society*, 136(649):1051–1063.

Boynard, A., Clerbaux, C., Coheur, P.-F., Hurtmans, D., Turquety, S., George, M., Hadji-Lazaro, J., Keim, C., and Meyer-Arnek, J. (2009). Measurements of total and tropospheric ozone from IASI: comparison with correlative satellite, ground-based and ozonesonde observations. *Atmospheric Chemistry and Physics*, 9(16):6255–6271.

Buchwitz, M. (2013). The Greenhouse Gas Climate Change Initiative (GHG-CCI): comparison and quality assessment of near-surface-sensitive satellite-derived CO2 and CH4 global data sets. In *EGU General Assembly Conference Abstracts*, volume 15 of *EGU General Assembly Conference Abstracts*, page 1340.

Carboni, E., Grainger, R., Walker, J., Dudhia, A., and Siddans, R. (2012). A new scheme for sulphur dioxide retrieval from IASI measurements: application to the eyjafjallajokull eruption of april and may 2010. *Atmospheric Chemistry and Physics*, 12(23):11417–11434.

Chalon, G., Cayla, F., and Diebel, D. (2001). IASI: An advance sounder for operational meteorology. In *Proceedings of the 52nd Congress of IAF*.

Chevallier, F., Di Michele, S., and McNally, A. (2002). Sampled databases of 60-level atmospheric profiles from the ecmwf analyses. Technical Report NWPSAF–EC–TR–004, NWP SAF.

Chevallier, F., Di Michele, S., and McNally, A. (2006). Diverse profile datasets from the ECMWF 91-level short-range forecasts. Technical Report NWPSAF–EC–TR–010, NWP SAF.

Clarisse, L., Coheur, P. F., Prata, A. J., Hurtmans, D., Razavi, A., Phulpin, T., Hadji-Lazaro, J., and Clerbaux, C. (2008). Tracking and quantifying volcanic SO_2 with IASI, the September 2007 eruption at Jebel at Tair. *Atmospheric Chemistry and Physics*, 8(24):7723–7734.

Clarisse, L., Hurtmans, D., Clerbaux, C., Hadji-Lazaro, J., Ngadi, Y., and Coheur, P.-F. (2012). Retrieval of sulphur dioxide from the infrared atmospheric sounding interferometer (IASI). *Atmospheric Measurement Techniques*, 5(3):581–594.

Clarisse, L., Hurtmans, D., Prata, A. J., Karagulian, F., Clerbaux, C., Mazière, M. D., and Coheur, P.-F. (2010). Retrieving radius, concentration, optical depth, and mass of different types of aerosols from high-resolution infrared nadir spectra. *Appl. Opt.*, 49(19):3713–3722.

Clarmann, T., Höpfner, M., Funke, B., López-Puertas, M., Dudhia, A., Jay, V., Schreier, F., Ridolfi, M., Ceccherini, S., Kerridge, B., Reburn, J., and Siddans, R. (2003). Modelling of atmospheric mid-infrared radiative transfer: the AMIL2DA algorithm intercomparison experiment. *Journal of Quantitative Spectroscopy and Radiative Transfer*, 78(3-4):381 – 407.

Clerbaux, C., Hadji-Lazaro, J., Turquety, S., George, M., Coheur, P.-F., Hurtmans, D., Wespes, C., Herbin, H., Blumstein, D., Tourniers, B., and Phulpin, T. (2007). The IASI/MetOp1 mission: First observations and highlights of its potential contribution to GMES2. *Space Research Today*, 168:19–24.

Clough, S., Kneizys, F., and Davies, R. (1989). Line shape and the water vapor continuum. *Atmospheric Research*, 23(3–4):229 – 241.

Clough, S., Shephard, M., Mlawer, E., Delamere, J., Iacono, M., Cady-Pereira, K., Boukabara, S., and Brown, P. (2005). Atmospheric radiative transfer modeling: a summary of the AER codes. *Journal of Quantitative Spectroscopy and Radiative Transfer*, 91(2):233 – 244.

Clough, S. A., Iacono, M. J., and Moncet, J.-L. (1992). Line-by-line calculations of atmospheric fluxes and cooling rates: Application to water vapor. *Journal of Geophysical Research: Atmospheres*, 97(D14):15761–15785.

CNES (2009). IASI description by CNES. `http://smsc.cnes.fr/IASI/GP\_instrument.htm`.

Collard, A., McNally, T., Hilton, F., Healy, S., and Atkinson, N. (2010). The use of principal component analysis for the assimilation of high-resolution infrared sounder observations for numerical weather prediction. *Quarterly Journal o the Royal Meteorological Society*, 136:2038–2050.

Collard, A. D. (2007). Selection of IASI channels for use in numerical weather prediction. *Quarterly Journal of the Royal Meteorological Society*, 133(629):1977–1991.

Cortesi, U., Bertacci, G., Carli, B., Bianco, S. D., and Gai, M. (2009). First results of the KLIMA-IASI sensitivity study. In *International Workshop on Atmospheric Science from Space using Fourier Transform Spectrometry*.

Coudert, L., Wagner, G., Birk, M., Baranov, Y., Lafferty, W., and Flaud, J.-M. (2008). The H216O molecule: Line position and line intensity analyses up to the second triad. *Journal of Molecular Spectroscopy*, 251(1–2):339 – 357. Special issue dedicated to the pioneering work of Drs. Edward A. Cohen and Herbert M. Pickett on spectroscopy relevant to the Earth's atmosphere and astrophysics.

Cousin, C., Doucen, R. L., Boulet, C., and Henry, A. (1985). Temperature dependence of the absorption in the region beyond the 4.3-μm band head of CO2 . 2: N2 and O2 broadening. *Appl. Opt.*, 24(22):3899–3907.

Crevoisier, C., Chedin, A., and Scott, N. A. (2003). AIRS channel selection for CO2 and other trace-gas retrievals. *Quarterly Journal of the Royal Meteorological Society*, 129(593):2719–2740.

Crevoisier, C., Nobileau, D., Fiore, A. M., Armante, R., Chédin, A., and Scott, N. A. (2009). Tropospheric methane in the tropics – first year from IASI hyperspectral infrared observations. *Atmospheric Chemistry and Physics*, 9(17):6337–6350.

Dee, D. P., Uppala, S. M., Simmons, A. J., Berrisford, P., Poli, P., Kobayashi, S., Andrae, U., Balmaseda, M. A., Balsamo, G., Bauer, P., Bechtold, P., Beljaars, A. C. M., van de Berg, L., Bidlot, J., Bormann, N., Delsol, C., Dragani, R., Fuentes, M., Geer, A. J., Haimberger, L., Healy, S. B., Hersbach, H., Hólm, E. V., Isaksen, L., Kållberg, P., Köhler, M., Matricardi, M., McNally, A. P., Monge-Sanz, B. M., Morcrette, J.-J., Park, B.-K., Peubey, C., de Rosnay, P., Tavolato, C., Thépaut, J.-N., and Vitart, F. (2011). The ERA-Interim reanalysis: configuration and performance of the data assimilation system. *Quarterly Journal of the Royal Meteorological Society*, 137(656):553–597.

Doucen, R. L., Cousin, C., Boulet, C., and Henry, A. (1985). Temperature dependence of the absorption in the region beyond the 4.3-μm band head of CO2. 1: Pure CO2 case. *Appl. Opt.*, 24(6):897–906.

Dudhia, A. (2002). RFM, reference forward model. `http://www.atm.ox.ac.uk/RFM/`.

Dudhia, A., Jay, V. L., and Rodgers, C. D. (2002). Microwindow selection for high-spectral-resolution sounders. *Appl. Opt.*, 41(18):3665–3673.

Duflot, V., Hurtmans, D., Clarisse, L., R'honi, Y., Vigouroux, C., De Mazière, M., Mahieu, E., Servais, C., Clerbaux, C., and Coheur, P.-F. (2013). Measurements of hydrogen cyanide (HCN) and acetylene (C_2H_2) from the infrared atmospheric sounding interferometer (IASI). *Atmospheric Measurement Techniques*, 6(4):917–925.

Edwards, D. (1992). *GENLN2-A General Line-by-Line Atmospheric Transmittance and Radiance Model*.

Edwards, D. P., López-Puertas, M., and López-Valverde, M. A. (1993). Non-local thermodynamic equilibrium studies of the 15 μm bands of CO2 for atmospheric remote sensing. *Journal of Geophysical Research: Atmospheres*, 98(D8):14955–14977.

Eremenko, M., Dufour, G., Foret, G., Keim, C., Orphal, J., Beekmann, M., Bergametti, G., and Flaud, J. M. (2008). Tropospheric ozone distributions over europe during the heat wave in July 2007 observed from infrared nadir spectra recorded by IASI. *Geophysical Research Letters*, 35(18):0–4.

EUMETSAT (2009). EUMETSAT: IASI level 1 product guide. `http://oiswww.eumetsat.org/WEBOPS/eps-pg/IASI-L1/IASIL1-PG-0TOC.htm`.

Fischer, H., Birk, M., Blom, C., Carli, B., Carlotti, M., von Clarmann, T., Delbouille, L., Dudhia, A., Ehhalt, D., Endemann, M., Flaud, J. M., Gessner, R., Kleinert, A., Koopman, R., Langen, J., López-Puertas, M., Mosner, P., Nett, H., Oelhaf, H., Perron, G., Remedios, J., Ridolfi, M., Stiller, G., and Zander, R. (2008). MIPAS: an instrument for atmospheric and climate research. *Atmospheric Chemistry and Physics*, 8(8):2151–2188.

Flaud, J., Piccolo, C., and Carli, B. (2003). A Spectroscopic Database for MIPAS. In *ESA Special Publication*, volume 531 of *ESA Special Publication*.

Gambacorta, A. and Barnet, C. D. (2013). Methodology and information content of the NOAA NESDIS operational channel selection for the cross-track infrared sounder (CrIS). *IEEE T. Geoscience and Remote Sensing*, 51(6-1):3207–3216.

George, M., Clerbaux, C., Hurtmans, D., Turquety, S., Coheur, P.-F., Pommier, M., Hadji-Lazaro, J., Edwards, D. P., Worden, H., Luo, M., Rinsland, C., and McMillan, W. (2009). Carbon monoxide distributions from the IASI/METOP mission: evaluation with other space-borne remote sensors. *Atmospheric Chemistry and Physics*, 9(21):8317–8330.

Hartmann, J.-M., Tran, H., and Toon, G. C. (2009). Influence of line mixing on the retrievals of atmospheric co$_2$ from spectra in the 1.6 and 2.1 μm regions. *Atmospheric Chemistry and Physics*, 9(19):7303–7312.

Hébert, P., Blumstein, D., Buil, C., Carlier, T., Chalon, G., Astruc, P., Clauss, A., Siméoni, D., and Tournier, B. (2004). IASI instrument: technical description and measured performances. In B. Warmbein, editor, *5th International Conference on Space Optics*, volume 554 of *ESA Special Publication*, pages 49–56.

Hilton, F., Armante, R., August, T., Barnet, C., Bouchard, A., Camy-Peyret, C., Capelle, V., Clarisse, L., Clerbaux, C., Coheur, P., Collard, A., Crevoisier, C., Dufour, G., Edwards, D., Faijan, F., Fourrié, N., Gambacorta, A., Goldberg, M., Guidard, V., Hurtmans, D., Illingworth, S., Jacquinet-Husson, N., Kerzenmacher, T., Klaes, D., Lavanant, L., Masiello, G., Matricardi, M., McNally, A., Newman, S., Pavelin, E., Payan, S., Péquignot, E., Peyridieu, S., Phulpin, T., Remedios, J., Schlüssel, P., Serio, C., Strow, L., Stubenrauch, C., Taylor, J., Tobin, D., Wolf, W., and Zhou, D. (2012). Hyperspectral earth observation from IASI: Five years of accomplishments. *Bulletin of the American Meteorological Society*, 93(3):347–370.

Hilton, F., Atkinson, N. C., English, S. J., and Eyre, J. R. (2009a). Assimilation of IASI at the met office and assessment of its impact through observing system experiments. *Quarterly Journal of the Royal Meteorological Society*, 135(639):495–505.

Hilton, F., Atkinson, N. C., English, S. J., and Eyre, J. R. (2009b). Assimilation of IASI at the met office and assessment of its impact through observing system experiments. *Quarterly Journal of the Royal Meteorological Society*, 135(639):495–505.

Illingworth, S., Remedios, J., Boesch, H., Ho, S., Edwards, D., Palmer, P., and Gonzi, S. (2011). A comparison of OEM CO retrievals from the IASI and MOPITT instruments. *Atmospheric measurement techniques*, 4(5):775–793.

Illingworth, S. M., Remedios, J. J., and Parker, R. J. (2009). Intercomparison of integrated IASI and AATSR calibrated radiances at 11 and 12 νm. *Atmospheric Chemistry and Physics*, 9(18):6677–6683.

Jacquinet-Husson, N. (2009). GEISA-IASI 2009 spectroscopic database. `http://ether.ipsl.jussieu.fr/etherTypo/?id=1292\&L=0`.

Jacquinet-Husson, N., Scott, N., Chédin, A., Garceran, K., Armante, R., Chursin, A., Barbe, A., Birk, M., Brown, L., Camy-Peyret, C., Claveau, C., Clerbaux, C., Coheur, P., Dana, V., Daumont, L., Debacker-Barilly, M., Flaud, J., Goldman, A., Hamdouni, A., Hess, M., Jacquemart, D., Köpke, P., Mandin, J., Massie, S., Mikhailenko, S., Nemtchinov, V., Nikitin, A., Newnham, D., Perrin, A., Perevalov, V., Régalia-Jarlot, L., Rublev, A., Schreier, F., Schult, I., Smith, K., Tashkun, S., Teffo, J., Toth, R., Tyuterev, V., Auwera, J. V., Varanasi, P., and Wagner, G. (2005). The 2003 edition of the GEISA/IASI spectroscopic database. *Journal of Quantitative Spectroscopy and Radiative Transfer*, 95(4):429–467.

Keim, C., Eremenko, M., Orphal, J., Dufour, G., Flaud, J.-M., Höpfner, M., Boynard, A., Clerbaux, C., Payan, S., Coheur, P.-F., Hurtmans, D., Claude, H., Dier, H., Johnson, B., Kelder, H., Kivi, R., Koide, T., López Bartolomé, M., Lambkin, K., Moore, D., Schmidlin, F. J., and Stübi, R. (2009). Tropospheric ozone from IASI: comparison of different inversion algorithms and validation with ozone sondes in the northern middle latitudes. *Atmospheric Chemistry and Physics*, 9(24):9329–9347.

Kerzenmacher, T., Dils, B., Kumps, N., Blumenstock, T., Clerbaux, C., Coheur, P.-F., Demoulin, P., García, O., George, M., Griffith, D. W. T., Hase, F., Hadji-Lazaro, J., Hurtmans, D., Jones, N., Mahieu, E., Notholt, J., Paton-Walsh, C., Raffalski, U., Ridder, T., Schneider, M., Servais, C., and De Mazière, M. (2012). Validation of IASI FORLI carbon monoxide retrievals using FTIR data from NDACC. *Atmospheric Measurement Techniques*, 5(11):2751–2761.

Lafferty, W. J., Solodov, A. M., Weber, A., Olson, W. B., and Hartmann, J.-M. (1996). Infrared collision-induced absorption by N 2 near 4.3 μm for atmospheric applications: measurements and empirical modeling. *Applied Optics LP*, 35:5911–5917.

Lamouroux, J., Tran, H., Laraia, A., Gamache, R., Rothman, L., Gordon, I., and Hartmann, J.-M. (2010). Updated database plus software for line-mixing in co_2 infrared spectra and their test using laboratory spectra in the 1.5–2.3νm region. *Journal of Quantitative Spectroscopy and Radiative Transfer*, 111(15):2321 – 2331. ¡ce:title¿XVIth Symposium on High Resolution Molecular Spectroscopy (HighRus-2009)¡/ce:title¿ ¡xocs:full-name¿XVIth Symposium on High Resolution Molecular Spectroscopy¡/xocs:full-name¿.

Lubrano, A. M., Masiello, G., Matricardi, M., Serio, C., and Cuomo, V. (2004). Retrieving N2O from nadir-viewing infrared spectrometers. *Tellus B*, 56(3):249–261.

Matricardi, M. (2003). RTIASI-4, a new version of the ECMWF fast radiative transfer model for the infrared atmospheric sounding interferometer. `ECMWFTechnicalMemorandumNo.425`.

Matricardi, M. (2007). An inter-comparison of line-by-line radiative transfer models. Technical Memo 525, ECMWF.

Matricardi, M. (2008). The generation of RTTOV regression coefficients for IASI and AIRS using a new profile training set and a new line-by-line database. Technical Memo 564, ECMWF.

Matricardi, M. (2009). Technical note: An assessment of the accuracy of the RTTOV fast radiative transfer model using IASI data. *Atmospheric Chemistry and Physics*, 9(18):6899–6913.

Matricardi, M. (2010). A principal component based version of the RTTOV fast radiative transfer model. *Quarterly Journal of the Royal Meteorological Society*, 136(652):1823–1835.

Matricardi, M., Chevallier, F., Kelly, G., and Thépaut, J.-N. (2004). An improved general fast radiative transfer model for the assimilation of radiance observations. *Quarterly Journal of the Royal Meteorological Society*, 130(596):153–173.

Matricardi, M. and Saunders, R. (1999). Fast radiative transfer model for simulation of infrared atmospheric sounding interferometer radiances. *Appl. Opt.*, 38(27):5679–5691.

McNally, A. P. (2009). The direct assimilation of cloud-affected satellite infrared radiances in the ECMWF 4D-Var. *Quarterly Journal of the Royal Meteorological Society*, 135(642):1214–1229.

McNally, A. P. and Watts, P. D. (2003). A cloud detection algorithm for high-spectral-resolution infrared sounders. *Quarterly Journal of the Royal Meteorological Society*, 129(595):3411–3423.

Mlawer, E. J., Payne, V. H., Moncet, J.-L., Delamere, J. S., Alvarado, M. J., and Tobin, D. C. (2012). Development and recent evaluation of the MT_CKD model of continuum absorption. *Philosophical Transactions of the Royal Society A: Mathematical, Physical and Engineering Sciences*, 370(1968):2520–2556.

Niro, F., Jucks, K., and Hartmann, J.-M. (2005). Spectra calculations in central and wing regions of co2 ir bands. iv: software and database for the computation of atmospheric spectra. *Journal of Quantitative Spectroscopy and Radiative Transfer*, 95(4):469–481.

Pavelin, E., English, S., and Eyre, J. (2008). The assimilation of cloud-affected infrared satellite radiances for numerical weather prediction. *Quarterly Journal of the Royal Meteorological Society*, 134(632):737–749.

Pequignot, E. (2009). IASI/Metop PSF. `http://smsc.cnes.fr/IASI/IASI_PSF_format_description_v1.pdf`.

Prunet, P., Clerbaux, C., Dufour, E., Chimot, J., Lezeaux, O., and Phulpin, T. (2010). Principal component compression of IASI data:Impact on the exploitation of trace gases information for atmospheric chemistry. In *2nd IASI International Conference*.

Rabier, F., Fourrié, N., Chafäi, D., and Prunet, P. (2002). Channel selection methods for infrared atmospheric sounding interferometer radiances. *Quarterly Journal of the Royal Meteorological Society*, 128(581):1011–1027.

Razavi, A., Clerbaux, C., Wespes, C., Clarisse, L., Hurtmans, D., Payan, S., Camy-Peyret, C., and Coheur, P. F. (2009). Characterization of methane retrievals from the IASI space-borne sounder. *Atmospheric Chemistry and Physics*, 9(20):7889–7899.

Remedios, J. J., Leigh, R. J., Waterfall, A. M., Moore, D. P., Sembhi, H., Parkes, I., Greenhough, J., Chipperfield, M., and Hauglustaine, D. (2007). MIPAS reference atmospheres and comparisons to V4.61/V4.62 MIPAS level 2 geophysical data sets. *Atmospheric Chemistry and Physics Discussions*, 7(4):9973–10017.

Ricaud, P., Attié, J.-L., Teyssèdre, H., El Amraoui, L., Peuch, V.-H., Matricardi, M., and Schluessel, P. (2009). Equatorial total column of nitrous oxide as measured by IASI on MetOp-A: implications for transport processes. *Atmospheric Chemistry and Physics*, 9(12):3947–3956.

Rodgers, C. D. (1996). Information content and optimization of high-spectral-resolution measurements. *Society of Photo-Optical Instrumentation Engineers (SPIE) Conference Series*, 2830:136–147.

Rodgers, C. D. (2000). *Inverse methods for atmospheric sounding:Theory and practice*. World Scientific Publishing Co.

Rothman, L., Gordon, I., Barbe, A., Benner, D., Bernath, P., Birk, M., Boudon, V., Brown, L., Campargue, A., Champion, J.-P., Chance, K., Coudert, L., Dana, V., Devi, V., Fally, S., Flaud, J.-M., Gamache, R., Goldman, A., Jacquemart, D., Kleiner, I., Lacome, N., Lafferty, W., Mandin, J.-Y., Massie, S., Mikhailenko, S., Miller, C., Moazzen-Ahmadi, N., Naumenko, O., Nikitin, A., Orphal, J., Perevalov, V., Perrin, A., Predoi-Cross, A., Rinsland, C., Rotger, M., Simecková, M., Smith, M., Sung, K., Tashkun, S., Tennyson, J., Toth, R., Vandaele, A., and Auwera, J. V. (2009). The HITRAN 2008 molecular spectroscopic database. *Journal of Quantitative Spectroscopy and Radiative Transfer*, 110(9-10):533–572. HITRAN.

Rothman, L. S., Barbe, A., Benner, D. C., Brown, L. R., Camy-Peyret, C., Carleer, M. R., Chance, K., Clerbaux, C., Dana, V., Devi, V. M., Fayt, A., Flaud, J. M., Gamache, R. R., Goldman, A., Jacquemart, D., Jucks, K. W., Lafferty, W. J., Mandin, J. Y., Massie, S. T., Nemtchinov, V., Newnham, D. A., Perrin, A., Rinsland, C. P., Schroeder, J., Smith, K. M., Smith, M. A. H., Tang, K., Toth, R. A., Auwera, J. V., Varanasi, P., and Yoshino, K. (2003). The HITRAN molecular spectroscopic database: edition of 2000 including updates through 2001. *Journal of Quantitative Spectroscopy and Radiative Transfer*, 82(1-4):5–44. The HITRAN Molecular Spectroscopic Database: Edition of 2000 Including Updates of 2001.

Rothman, L. S., Jacquemart, D., Barbe, A., Chris Benner, D., Birk, M., Brown, L. R., Carleer, M. R., Chackerian, C., Chance, K., Coudert, L. H., Dana, V., Devi, V. M., Flaud, J., Gamache, R. R., Goldman, A., Hartmann, J., Jucks, K. W., Maki, A. G., Mandin, J., Massie, S. T., Orphal, J., Perrin, A., Rinsland, C. P., Smith, M. A. H., Tennyson, J., Tolchenov, R. N., Toth, R. A., Vander Auwera, J., Varanasi, P., and Wagner, G. (2005). The HITRAN 2004 molecular spectroscopic database. *Journal of Quantitative Spectroscopy and Radiative Transfer*, 96:139–204.

Russell, J. M., Gordley, L. L., Park, J. H., Drayson, S. R., Hesketh, W. D., Cicerone, R. J., Tuck, A. F., Frederick, J. E., Harries, J. E., and Crutzen, P. J. (1993). The halogen occultation experiment. *Journal of Geophysical Research: Atmospheres*, 98(D6):10777–10797.

Sangwon, J., Eyre, J., and Marriott, R. (2013). The impact of Metop and other satellite data within the Met Office global NWP system using an adjoint-based sensitivity method. *Monthly Weather Review*.

Saunders, R., Hocking, J., Rundle, D., Rayer, P., Matricardi, M., Geer, A., Lupu, C., Brunel, P., and Vidot, J. (2013). RTTOV-11 Science and Validation Report. Technical Report NWPSAF-MO-TV-032, EUMETSAT NWPSAF.

Saunders, R., Rayer, P., Brunel, P., von Engeln, A., Bormann, N., Strow, L., Hannon, S., Heilliette, S., Liu, X., Miskolczi, F., Han, Y., Masiello, G., Moncet, J.-L., Uymin, G., Sherlock, V., and Turner, D. S. (2007). A comparison of radiative transfer models for simulating atmospheric infrared sounder (airs) radiances. *Journal of Geophysical Research: Atmospheres*, 112(D1):n/a–n/a.

Sherlock, V. (1999). ISEM-6: Infrared Surface Emissivity Model for RTTOV-6. Technical memo, EUMETSAT NWPSAF.

Siméoni, D., Singer, C., and Chalon, G. (1997). Infrared atmospheric sounding interferometer. *Acta Astronautica*, 40(2-8):113–118. Enlarging The Scope of Space Applications.

Strow, L., Hannon, S., and Schou, P. (2010). Radiometric intercomparisons of AIRS and IASI for climate Monitoring applications. In *2nd IASI International Conference*.

Strow, L. L. and Reuter, D. (1988). Effect of line mixing on atmospheric brightness temperatures near 15 μm. *Appl. Opt.*, 27(5):872–878.

Strow, L. L., Tobin, D. C., and Hannon, S. E. (1994). A compilation of first-order line-mixing coefficients for CO2 Q-branches. *Journal of Quantitative Spectroscopy and Radiative Transfer*, 52(3-4):281 – 294. Special Issue Atmospheric Spectroscopy Applications.

Thibault, F., Menoux, V., Doucen, R. L., Rosenmann, L., Hartmann, J.-M., and Boulet, C. (1997). Infrared collision-induced absorption by o2 near 6.4 μm for atmospheric applications: measurements and empirical modeling. *Appl. Opt.*, 36(3):563–567.

Tjemkes, S., Patterson, T., Rizzi, R., Shephard, M., Clough, S., Matricardi, M., Haigh, J., Höpfner, M., Payan, S., Trotsenko, A., Scott, N., Rayer, P., Taylor, J., Clerbaux, C., Strow, L., DeSouza-Machado, S., Tobin, D., and Knuteson, R. (2003). The {ISSWG} line-by-line inter-comparison experiment. *Journal of Quantitative Spectroscopy and Radiative Transfer*, 77(4):433 – 453.

Turquety, S., Hadji-Lazaro, J., C.Clerbaux, Hauglustaine, D., Clough, S., Casse, V., Schlussel, P., and Megie, G. (2004). Operational trace gas retrieval algorithm for the infrared atmospheric sounding interferometer. *Journernel of Geophysical Research*, 109.

Turquety, S., Hurtmans, D., Hadji-Lazaro, J., Coheur, P.-F., Clerbaux, C., Josset, D., and Tsamalis, C. (2009). Tracking the emission and transport of pollution from wildfires using the IASI CO retrievals: analysis of the summer 2007 greek fires. *Atmospheric Chemistry and Physics*, 9(14):4897–4913.

Walker, J. and Dudhia, A. (2009). Use of the RFM to model IASI spectra. `http://www.atm.ox.ac.uk/user/walker/pdf/rfm\_iasi.pdf`.

Walker, J. C., Dudhia, A., and Carboni, E. (2011). An effective method for the detection of trace species demonstrated using the MetOp infrared atmospheric sounding interferometer. *Atmospheric Measurement Techniques*, 4(8):1567–1580.

Weston, P. (2011). Progress towards the Implementation of Correlated Observation Errors in 4D-Var. Forecasting Research Technical Report 560, UK Met Office.

Xiong, X., Barnet, C., Maddy, E. S., Gambacorta, A., King, T. S., and Wofsy, S. C. (2013). Mid-upper tropospheric methane retrieval from IASI and its validation. *Atmospheric Measurement Techniques Discussions*, 6(2):2501–2531.